Self-organized turbulent transport in fusion plasmas

Claudia Norscini

Thèse de doctorat
Université d'Aix-Marseille

École doctorale: *Physique et Sciences de la Matière*

Spécialité : **Energie, Rayonnement et Plasma**

Self-organized turbulent transport in fusion plasmas

Presentée par:
Claudia Norscini

Thèse soutenue publiquement le 20 novembre 2015 devant le jury composé de :

Pr. Pascale Hennequin	Rapporteur	Professeur à LPP Paris
Pr. Steve Tobias	Rapporteur	Professeur à l'Université de Leeds
Pr. Alberto Loarte	Examinateur	Coordinateur Scientifique à ITER
Pr. Alain Pocheau	Examinateur	Professeur à IRPHE Marseille
Pr. George Tynan	Examinateur	Professeur à UCSD California
Pr. Domiziano Mostacci	Examinateur	Professeur à l'Université de Bologna
Dr. Guilhem Dif-Pradalier	Examinateur	Chercheur CEA
Pr. Philippe Ghendrih	Directeur de thèse	Directeur de Recherche au CEA

Laboratoire d'accueil :
Institut de **R**echerche sur la **F**usion par confinement **M**agnétique
CEA – Cadarache
13108 Saint-Paul-lez-Durance, France

Nov 2012 – Nov 2015

A Nonno Ennio

Abstract

Transport barriers (TB) are a key element in controlling turbulent transport and achieving high performance burning plasmas. In the experimental procedures such self-organized structures are routinely obtained but appear to exhibit a variety of behavior and impact on the confinement improvement. Theoretical studies are addressing the turbulence self-regulation as a possible explanation for transport barrier formation but a complete understanding of such complex dynamics is still missing. In this context, we address self-organized turbulent transport in fusion plasmas with the aim of presenting a novel understanding of transport barriers dynamics. The numerical tools we use span simulations from the most complex gyrokinetic turbulence to simpler 2D fluid turbulence and predator-prey like models.

Two main features of turbulence self-organizations, avalanches and zonal flows, appear to control large scale transport. In the SOL (Scrape Off Layer) region, intermittent avalanche events do not allow for any time or space scale separation between mean fields and fluctuation terms. In the edge, where magnetic surfaces are closed, the generation of long living double shear layers in the profiles of the velocity tangent to the magnetic surfaces reduces radial turbulent transport. Such radially distributed barriers govern profile corrugations, namely a radial structure of localised increase of temperature gradient. A rich zonal flow and turbulence interplay has been observed and studied both in gyrokinetic and fluid model. The role of criticality has been further investigated for the latter case, proving that the so-called DIMITS shift is not driven by specific kinetic effects.

A 2D turbulent model for pedestal generation, which is not specific of Tokamak plasmas, has been developed, the pedestal being localized at the interface between regions with different zonal flow damping: the edge region, where zonal flows are weakly damped by collisions, and the SOL region characterized by zonal flow damping due to boundary conditions. Quasi-periodic relaxation events are studied reducing the model to three modes coupling to identify the interplay between streamers and zonal flows and the role of Reynolds stress in the generation and saturation of TBs. A 0D predator-prey model is developed that recovers the interaction between turbulence and zonal flows has been defined.

Finally, several generic properties of transitions from Low to High confinement has been identified in the model: (1) the generation of a pedestal at the separatrix location, (2)the occurrence of a gap in the turbulent spectrum between zonal flows and microturbulence and (3) the global quasi-periodic relaxation events governed by the collisional erosion.

Résumé

Les barrières de transport sont un élément clé dans le contrôle du transport turbulent, afin d'atteindre de hautes performances dans les plasmas de fusion. De telles structures auto-organisées sont régulièrement observées dans les expériences, mais semblent présenter une large variété de comportements et d'impacts sur l'amélioration du confinement. Des études théoriques suggèrent l'auto-organisation de la turbulence comme une explication possible pour la formation de barrières de transport, mais une compréhension complète de ces dynamiques complexes reste à développer. Dans ce contexte, nous traitons de l'auto-organisation du transport turbulent dans les plasmas de fusion dans le but d'améliorer la compréhension de la dynamique des barrières de transport. Les outils numériques que nous utilisons vont de simulations gyrocinétiques complexes de la turbulence, à des simulations numériques plus simples utilisant un modèle fluide 2D, ainsi que des modèles proie-prédateur.

Deux principales caractéristiques de la turbulence auto-organisée, les avalanches et les écoulements zonaux, semblent contrôler le transport à grande échelle. Dans la région à lignes de champs ouvertes (SOL, Scrape Of Layer), les avalanches, intermittentes, ne permettent pas une séparation d'échelles – en temps et en espace - entre champs moyens et fluctuations. Dans le bord, où les surfaces magnétiques sont fermées, la génération de couches de cisaillement doubles dans les profils de vitesse tangente aux surfaces magnétiques radiales réduisent le transport turbulent. Une riche interaction entre écoulements zonaux et turbulence a été observée et étudiée à la fois dans les modèles gyrocinétique et fluide. Le rôle de la criticité a été étudié de façon approfondie dans ce dernier cas, prouvant que le 'DIMITS shift' n'est pas généré par des effets cinétiques spécifiques.

Un modèle turbulent 2D pour la génération de piédestal, qui n'est pas spécifique aux plasmas de tokamak, a été mis au point, le piédestal étant localisé à l'interface entre les régions présentant différents niveaux d'amortissement des écoulement zonaux : la zone de bord, où les écoulements zonaux sont faiblement amortis par les collisions, et la SOL, caractérisée par un amortissement des écoulement zonaux en raison des conditions limites. Les événements de relaxation quasi-périodiques sont étudiés en réduisant le modèle à trois couplages entre modes afin d'identifier l'interaction entre les streamers et les écoulements zonaux, ainsi que le rôle du tenseur de Reynold dans la génération et la saturation des barrières de transport. Un modèle proie-prédateur 0D a été développé, permettant de retrouver l'interaction entre la turbulence et les écoulements zonaux.

Enfin, plusieurs propriétés génériques des transitions d'un régime de confinement faible (L-mode) à élevé (H-mode) ont été identifiées dans le modèle: (1) la génération d'un

piédestal à l'emplacement de la séparatrice, (2) l'apparition d'un vide dans le spectre turbulent entre les écoulements zonaux et la microturbulence et (3) les événements de relaxation quasi-périodiques globaux régis par l'érosion due aux collisions.

Acknowledgements

First off, I would like to thank the members of the jury, starting with the referees: Pascale Hennequin, who gave me a new perspective on this work thanks to her experimental background; Steve Tobias, who appreciated the effort of this work to go beyond the fusion plasma discipline. Thanks! I thank Alain Pocheau for presiding the jury and for his interest in the topic. I thank George Tynan to come from so far to participate to my defence and for his interest in my work and the fruitful conversations we had in EPS conference. I thank Alberto Loarte for his ITER oriented comments, his interest in the Dimits shift result and his point of view on the LH transition. I thank Guilhem Dif-Pradalier, that was not just a jury member but also a valuable help in these years (I will never forget his first explanations of turbulence self-organization). Finally Domiziano Mostacci, my university supervisor that proposed this first fruitful collaboration between the fusion group of Cadarache and Bologna University.

I would like to thank Philippe Ghendrih, in these years he gently led my research and helped me to become a young and curious researcher. He gave me the right freedom to express my ideas without feeling lost in such new and complex domain as plasma fusion. I hope I will keep his enthusiasm towards research always with me!

In addition, I thank the IRFM Institute. Particularly I am very grateful to the SIPP service, the chief Philippe Magaud who always supported my work and the secretaries Natalie and Laurance who helped to go through these three years full of bureaucratic challenges.

I would also like to acknowledge the GP2B group, I enjoy participating at the group meeting and I deeply appreciate the help and the "Italianità" of our chief Guido Ciraolo.

In these years, working with fluid and kinetic codes, I had the pleasure to collaborate with two different great teams: the GYSELA and EDGE (tokam) team. From both teams I learned a lot!

I started participating to the GYSELA meeting during my first year of PhD, I was an absolute beginner and Xavier Garbet, Yanick Sarazin, Guilhem Dif-Pradalier, Philippe Ghendrih, Virginie Grandgirard, Guillaume Latu and Chantal Passeron made me feel comfortable with many new concepts and vocabularies related to gyro-kinetic theory and French! Yanick was a pleasure to be your office neighbour and I really appreciated the morning 'Bonjour'! Virginie and Chantal with your female touch made your office as such a cozy place where I could always feel welcome with my 'J'ai une question', I often said to my friends that you are the researchers I aim to become.

In the edge team, I could finally feel home speaking about TOKAM2D, H-mode and pedestal. I had pleasure to collaborate with Patrick Tamain and Nicolas Fedorzak that showed me a gracious way to conjugate theory and experiments in plasma physics community!

During my PhD I also met an incredible amount of smart and funny guys that made me change the initial opinion I had about snob Frenches. I have to admit that I will miss Nicolas and Olivier with their stupid jokes, Hugo, Alexandre and Damien who entirely shared with me these three years, Clothilde and Fabien that appeared sporadically but shared similar mixed feelings about PhD, Charles, my fabulous officemate, Camille, - the one and only girl among the PhDs right now! - the elder ones, Francois, Didier, David (I know he is Spanish!), Jeremie, Hugo and Timothee, Gregoire, - I still remember the first PhD meeting, how scared I was! - the jounger ones, Julien, Axel and Laurent, the 'newly' french acquired Farah, - how much I enjoyed our chats! - Jae Heon, - my second favourite korean - Jorge -the nicest guy in the world that makes me feel always mean- and finally Thomas with whom I had the pleasure to share Philippe guidance - thank you for your help through many ups and downs of the thesis.

In these cosmopolitan world I had the pleasure to meet also a new foreign family that with me could understand the difficulties and advantages of being an expat, thanks Emelie, Aku, Olivier, Ronak, Adi, Jagruti, Felix, David and Pete. Finally Olivier that I still consider as a foreigner even if is 100% from Marseille.

I also would love to thank the "Italian mafia" that is growing year by year, from the 'veterani' like Gloria, Gerardo e Maurizio till the new arrivals like Christian, Davide, Alberto and Elisabetta. And thanks also to the participants of Tuesday Italian lunch: a weekly hour(s?) of chats and noise!

Finally I would love to thank my family, Mamma, Babbo, Giulia e Michele to be always with me in every important moment of my life, to always support and trust my choices, to give me the opportunity and above all the courage of travel, to meet new people and never be scared in front of the new challenges. In these years, I actually built up my new own little family: my husband Unkyu and my little dog Spritzy shared with me the difficulties and joys of these years and will share the future ones and the new adventures in Prague. I am sure that we will grow soon and you will be able to make me feel home wherever we will go!

Contents

Introduction

ITER is being built in Cadarache by seven partners China, Europe, India, Japan, Korea, Russia, United States. ITER is a large-scale scientific experiment intended to demonstrate the operation and control of a burning plasma, namely to reach a state such that most of the energy used to sustain the burning conditions is brought by the nuclear fusion reactions themselves. The project is extremely ambitious in all aspects, international organization, technology and physics. The physics basis of ITER stems from more than 50 years of worldwide research. With respect to JET, the European largest machine, the extrapolation in size is typically a factor two which is expected to drive an enhancement of performance by a factor 10 and open a novel era of nuclear fusion experiments. Three main challenges must be overcome to reach ITER nominal performance.

High temperatures and plasma conditions. To be a viable energy source, the fusion reactions require temperatures of the order of $150,000,000$ Kelvin to overcome the Coulomb repulsion between reacting nuclei. Although this corresponds to modest energies (in the range of 10 keV) when compared to present accelerators, such a temperature is larger than that of the sun. Under such conditions, electrons are separated from the nuclei, the lighter ions being fully stripped above some $100,000$ Kelvin. Such a state of matter is called a plasma.

Confinement performance: the energy confinement time τ_E. The plasma temperature has to be sustained by confining and controlling it in order to avoid excessive power losses. Following a fusion reaction, the ions must remain at high temperature at least until they can undergo a fusion reaction. Given the reaction probability, and the energy that can be transferred to the ions by the fusion reaction, this bounds the energy loss of the plasma under such burning conditions. The confinement time τ_E characterizes this energy loss: it is the characteristic decay time of the temperature once the heating is switched-off. A confinement time at least a factor five above present achievements is required in ITER. This figure of merit is crucial since its value governs the efficiency of the entire system. Moreover, the operational domain of ITER is very sensitive to small changes in τ_E. It appears that the confinement performance is controlled by turbulence. This turbulence governs transport from the hot core plasma to the outer plasma regions. Such turbulence degrades the very large insulation properties that have been reached when using large magnetic fields to confine the charged plasma particles.

Scrape-Off-Layer (SOL), its width and Plasma-Wall Interaction. No material can withstand the continuous exposure to hot plasma in burning conditions. Furthermore, despite plasma turbulence, the contact between the plasma and the solid state vessel that contains the plasma leads to a very thin boundary layer, the Scrape-Off Layer or SOL,

where all the power coupled to the plasma circulates to the Plasma Facing Components. Such a local power deposition is also a challenge for the cooling technology and solid state armor material. In that respect, the SOL width is a key parameter. Conversely to the core plasma, increasing the SOL width by reducing the confinement performance in the boundary layer is another challenge to be addressed on ITER.

Key aspects of ITER operation are thus governed by both plasma turbulence and the consequent turbulent transport. When designing ITER such an issue as been fully taken into account and empirical scaling laws have been used to determine ITER key parameters such as its size. However, changing operation conditions bring new insight and questions regarding such scaling laws. Furthermore, recent experiments, in particular in JET, indicate unexpected decrease in the confinement performance. A strong effort to better understand and control turbulent transport is thus mandatory to prepare experiments on ITER and achieve the nominal performance of this device. The present work aims at such a task. Our ambition has been to question key issues and concepts that underlie our present understanding of plasma turbulence.

How self-organization of turbulence in fusion plasmas occurs? Turbulence is characterized by the interplay between many different scales. There lies its complexity and the difficulty to represent it both in science and art. In the scientific point of view the various scales are understood as independent modes that interact following given laws. The transfer of energy between two modes can rely on two different mechanisms. The first involves the scale-by-scale transfer of energy. The second relies on direct transfer of energy from small to large scale or viceversa. We refer to this second mechanism as turbulence self-organization that appears to control the formation of large scale patterns observed in the fusion plasmas, such as avalanches and zonal flows (these will be described later). It has been observed both experimentally and numerically that avalanches govern the transport in the SOL. Conversely, in the confined region of the plasma, a strong interplay between avalanches and zonal flows occurs, which can eventually lead the formation of transport barriers that control the plasma confinement time. Two intuitive sketches of avalanches and zonal flows interplay in nature and in plasma are shown in fig.1

Can one define the turbulence threshold? The onset of turbulence is generally the balance between a drive and a damping mechanism. This is clearly illustrated in the Reynolds number $Re = UL/\nu$ where the system of size L is immersed in a fluid driven with a velocity U given a viscous damping ν. A transition to turbulence is observed when Re exceeds a critical value, the threshold to turbulence. Similarly, in plasma, different turbulent regimes have been observed by increasing the system forcing above the critical threshold. An intuitive picture, also sketched in fig.2, is used to explain these regimes: once the instability grows hence above the threshold, unstable modes (streamers) are excited; streamers transfer then their energy towards ZFs via a non linear coupling mechanism; turbulence is then damped, the zonal flows are excited. A specific role of the zonal flows is to inhibit turbulent transport and sometimes quench turbulence for instance by closing the valley followed by the avalanche, sketch on fig.1(b). Two possible regimes can then be observed. On one hand, turbulence is modified by the zonal flows but passes through. On

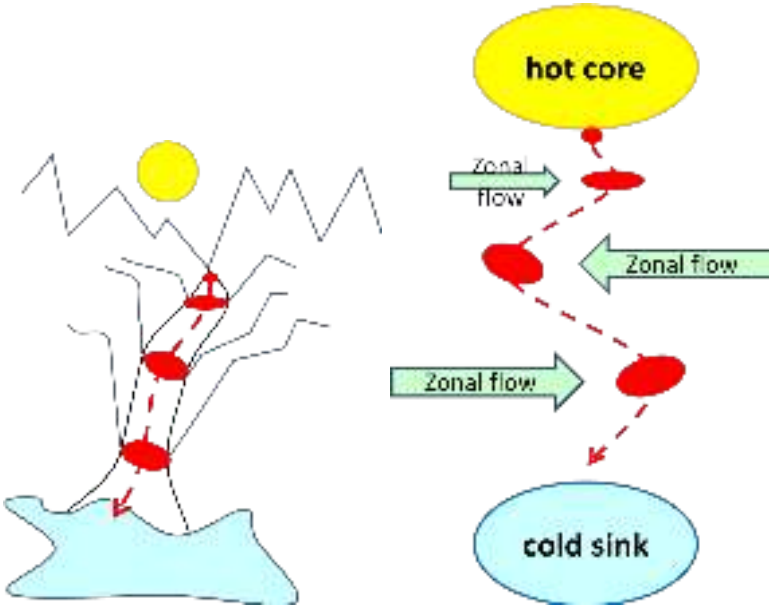

Figure 1: intuitive sketch on the role of zonal flows on the avalanche dynamic in nature (a) and in plasma (b)

the other hand turbulence is suppressed by the zonal flow, turbulence is quenched! One can then consider that a transport barrier has appeared, alternatively that the threshold to reach the turbulence regime has changed.

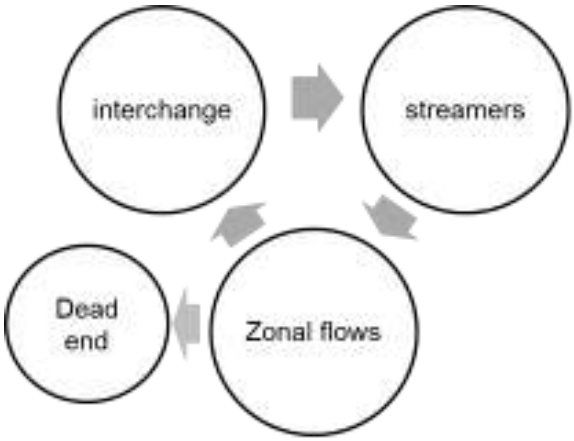

Figure 2: an intuitive sketch of the possible ZF and streamers dynamics

Which mechanism controls the barriers dynamics? Transport barriers do not appear to be stable. In particular they are prone to quasi-periodic relaxation effects. Turbulent transport bursts pass through the barriers and decrease the barrier efficiency. The dynamics of this relaxation appears to be controlled by an independent mechanism. By identifying the relaxation mechanism, it could be possible to determine a mean of controlling the resilience of transport barriers.

Are kinetics effects driving turbulence self-organization? Magnetically confined plasmas are characterized by very low density. As a consequence the collision mean free path is very long. The weak collision limit is therefore appropriate for these plasmas. Regarding the description of turbulence, kinetic description then appears to be better suited than the usual set of Navier Stokes equations. Although fluid and kinetic simulations appear to differ quantitatively, the understanding of these differences is unclear. Furthermore, one can ask oneself if fluid and kinetic simulations can exhibit qualitative similarity so that fluid simulations could be quite an effective reduced model allowing one to investigate plasma turbulence.

How the SOL width should be defined? In order to control plasma-wall interaction, defining transport in the Scrape Off Layer region, namely the region of open field lines, where the plasma touches the wall, is mandatory. Strong signatures of avalanche like behavior dominating the large scale transport have been observed in this region of the plasma. However the typical SOL width definition is usually associated to small steps random walk and not to avalanches that can propagate with ballistic motion over several SOL widths. Moreover the time associated to such long range radial transport can be shorter than the parallel transport time scale. These features thus contradict the properties usually attached to the common understanding of the SOL width.

Which are the key ingredient for the H-mode? The spontaneous generation of transport barriers via turbulence self-organization is a promising operational regime for future fusion reactors. In ITER, the reference scenario to achieve the nominal performance is based on an H-mode confinement characterized by a barrier. Achieving a fully self-consistent simulation able to address the turbulent transport at the interface between edge and SOL is crucial in order to answer to the many questions concerning the H-mode regime and the plasma wall interaction.

A sketch is presented on fig.9.1 to summarize the perspective of our work and identify their relevance in the context of ITER physics.

Figure 3: Thesis objectives

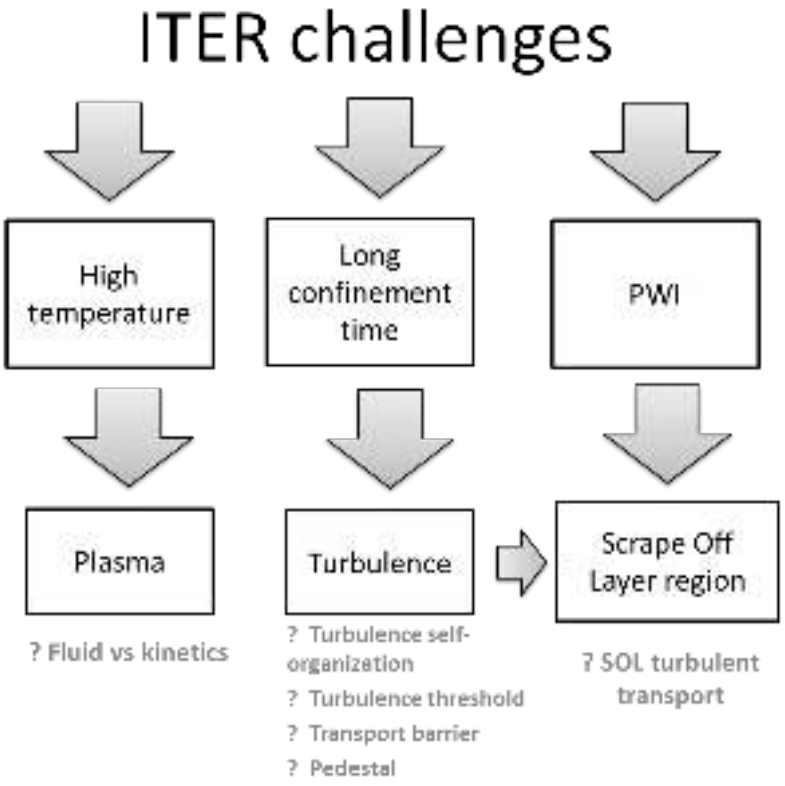

0.1 Manuscript outline

In Chapter 1, we introduce some basic aspects of fusion devices and the role of turbulent transport with respect to the operation and performance of these experiments.

In Chapter 2, we present the models we are going to use to study the turbulence of tokamak plasmas[1]. The equations solved by the numerical codes GYSELA and TOKAM2D, respectively based on the gyrokinetic and fluid model, are introduced.

In Chapter 3, we describe different self-organization patterns observed in turbulent transport simulations and their signature in terms of large scale feature. The consequence of such structures and the departure from the standard diffusive paradigm is presented.

In Chapter 4, the role of boundary condition and source driving the system out of equilibrium is addressed in order to identify the impact on turbulence self-organization in the SOL region.

In Chapter 5, the role of criticality on turbulence self-organization is discussed in detail. A study of the linear instability growthrate is presented and different regimes are observed depending on the distance from the threshold. The so-called Dimits shift has been recovered in the fluid framework.

In Chapter 6, the transport barriers generation and saturation dynamics is further analyzed in order to understand how the barriers interplay with the turbulence. The problem is reduced to three modes coupling model in order to investigate the zonal flows and streamer interplay. Comparison with the non linear simulations are then presented in order to define the role of non linear coupling in the transport barrier formation.

Finally, in Chapter 7, the formation of a transport barrier at the interface between open and closed field lines is presented. Such results are then compared with some experimental observation done in the transition from the LH regime. It is shown that such a behavior is not specific of tokamak plasmas and can be observed in numerous fields with quasi 2D turbulence.

[1] Although most of the properties of plasma turbulence are not specific of tokamaks, and can thus be relevant for stellarators or reversed field pinches, the two codes GYSELA & TOKAM2D have been developed for the tokamak geometry, hence the restriction to tokamak plasmas.

Chapter 1

Fusion basic concepts

The present chapter aims to introduce main fusion terminologies used throughout the thesis and to identify key issues related to turbulent transport.

Nuclear fusion reaction. Nuclear fusion is based on the production of energy through the fusion of two or more atomic nuclei. The mass of the resulting nucleus is lower than the sum of the separated nuclei. This mass difference is released in kinetic energy, according to Einstein's law $E = mc^2$. On fig.1.1 the binding energy per nucleus is shown. In the first portion of the graph, i.e. nuclei with lower mass than iron, the binding energy per nucleon increases on average with the mass number. The binding energy of the resulting nucleus is greater than the binding energy of each of the nuclei that fused to produce it. Hence, for light nuclei the fusion reaction is an esoenergetic process, i.e. energy is released. Note the remarkable peak for He that provides the largest gain when fusing neighboring nuclei. Conversely, for heavy nuclei the binding energy decreases. The energy can be released by the opposite nuclear reaction, nuclear fission. A heavy nucleus is split in two or more lighter nuclei with higher binding energy. Fusion process is more favorable than the fission process from an energetic point of view when measured per nuclei (hence per mass) and not per reaction.

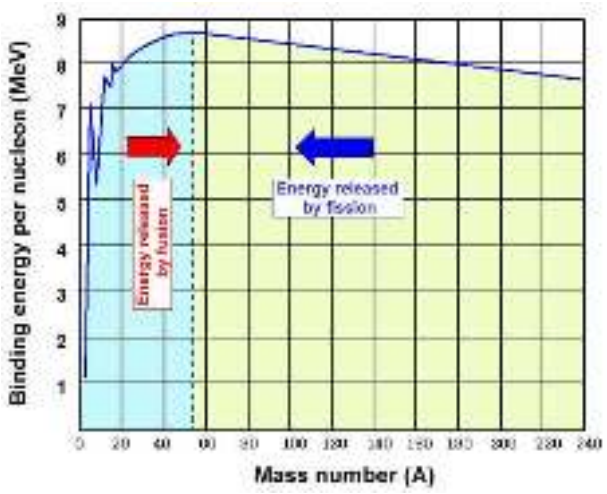

Figure 1.1: the binding energy per nucleon in function of the mass number

The hydrogen isotopes are currently considered to be the best candidates for physical reasons (released energy, cross section..) and practical ones (potential availability on the earth). As shown in fig.1.2 the most efficient fusion reaction is the Deuterium Tritium reaction, D-T fusion reaction.

$$ {}^{2}_{1}D + {}^{3}_{1}T \rightarrow {}^{4}_{2}He(3.5MeV) + {}^{1}_{0}n \tag{1.1} $$

The D-T fusion reaction produces the highest energy gain at the 'lowest' temperatures. It

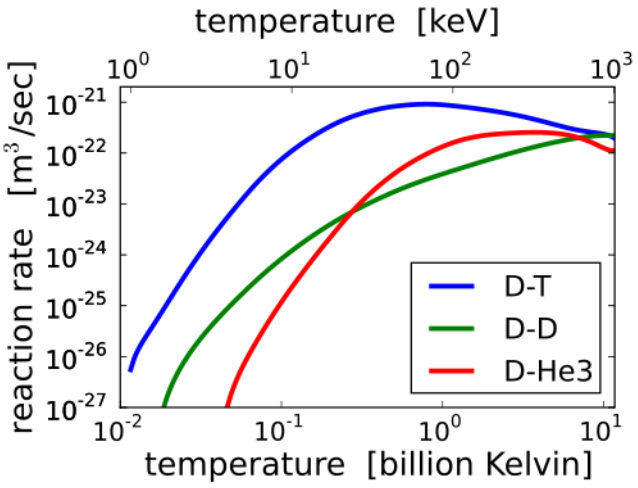

Figure 1.2: the reaction rate in function of temperature for the three most efficienfusion reactions (D-T,D-D,D-He3)

requires nonetheless temperatures of $150,000,000$ Kelvin to take place. The corresponding thermal energy is in the 10 keV range, hence much larger than the hydrogen ionization energy (13.6 eV).

Plasma magnetic confinement. At such extreme temperatures, it is no longer possible to confine the plasma solely with material walls, since no material would withstand the continued exposure to the hot plasma. Instead, plasma consists of charged particles, whose motion can be influenced by magnetic fields. By placing coils around the plasma, a strong magnetic field is imposed, which confines the plasma particles to helical orbits around the field by means of the Lorentz force. In a uniform magnetic field, the motion of a particle can be described by

- a free streaming motion in the direction parallel to the magnetic field lines
- a rapid cyclotron rotation around the magnetic field. All particles of a given species s will perform this rotation at the same gyrofrequency (or cyclotron frequency) $\Omega_s = e_s B/m_s$, where B is the intensity of the magnetic field, e_s and m_s are the species mass and charge. The radius of the cyclotron motion is the Larmor radius $\rho_c = m_s v_\perp/(e_s B)$, where $v_\perp$ is the velocity of the particle in the direction perpendicular to the magnetic field.

To contain the particles also along the field lines, a straightforward approach would be to close the magnetic field in a ring. Unfortunately, the resulting inhomogeneity of the

field leads to particle drifts, which make such a configuration unstable. By twisting the field lines into a helical shape, it is possible to overcome this problem and confine the hot plasma by a set of closed, toroidally nested, magnetic flux-surfaces.

This additional twisting of the field lines can be achieved by driving a current in the plasma, which induces an additional (poloidal) magnetic field B_θ, adding to the external (purely toroidal) field B_ϕ. To drive the current, usually the transformer principle is employed by placing the primary coil in the center of the plasma ring, and using the plasma itself as secondary coil. This approach is called the tokamak principle.

Magnetic configuration. Because of the pitch of the magnetic field lines $\mathbf{B} = \mathbf{B}_\theta + \mathbf{B}_\phi$, a field line which breaks the poloidal plane at one poloidal location will, on the next toroidal pass around the torus, usually cut that plane at a different poloidal location.

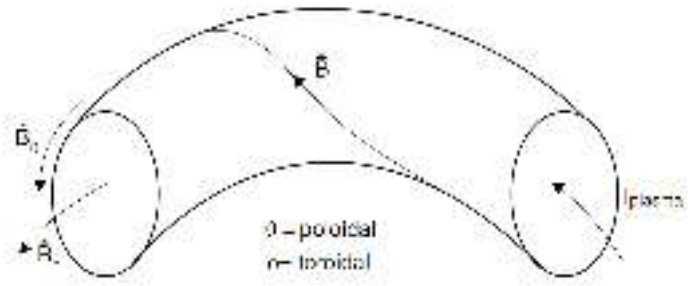

Figure 1.3: The toroidal direction ϕ is the long way around the polidal direction θ the short way

Although they remain on a given magnetic flux surface, most magnetic field lines never close on themselves, thus eventually mapping out the entire flux surface. A resonance exists if the safety factor q, :

$$q(r) = \frac{\mathbf{B} \cdot \nabla\phi}{\mathbf{B} \cdot \nabla\theta} \tag{1.2}$$

takes on rational values for a particular flux surface. Eq.(1.2) is the definition of safety factor q in the approximation of the circular concentric magnetic flux surfaces.

Plasma burning and ignition condition. The so-called Lawson criterion, is established in order to reach an energetically "profitable" nuclear fusion reaction. The Lawson criterion is a general measure that defines the conditions needed for a fusion reactor to produce more energy than it absorbs. The triple product of plasma temperature T_i, density n and confinement time τ_E has to exceed a critical value

$$nT_i\tau_E > 3.10^{21} keV.s.m^{-3} \tag{1.3}$$

where the confinement time $\tau_E = \frac{W}{E_{loss}}$ is the energy content W divided by the power loss E_{loss} and is defined as the necessary time for the plasma to cool down when all heat sources are switched off. The evaluation of τ_E is a crucial step in the ITER project since its value governs the efficiency of the entire system.

The energy gain factor Q is the ratio of fusion power produced in a nuclear fusion reactor P_{fus} to the power coming from external sources P_{heat} [1]:

$$Q = P_{fus}/P_{heat} \tag{1.4}$$

can be rewritten as function of the confinement time. Considering the energy balance equation inside the system in steady state condition

$$P_{heat} + P_{\alpha} = \frac{W}{\tau_E} \tag{1.5}$$

where P_{α} is equal to $\frac{P_{fus}}{5}$, i.e. the fraction of the fusion power contained in the α-particles. $\frac{4}{5}P_{fus}$ is transfered to the neutrons, which are not confined by the magnetic field but are absorbed in a surrounding walls (blanket) and are the key energy source when producing electrical power. Dividing each term per P_{heat}, the energy gain factor can be recovered as function of τ_E as

$$Q = \frac{5}{\frac{\tau_L}{\tau_E} - 1} \tag{1.6}$$

where $\tau_L = W \cdot (\frac{P_{fus}}{5})^{-1} = 5 \cdot 3nTV/P_{fus}$. Q equal to 1 represents the equilibrium condition, namely the power coming from external sources is equal to fusion power produced in a nuclear fusion reactor, but the process is not energetically profitable. The energy gain factor Q increases with the confinement time, until the ideal condition $\tau_E = \tau_L$. Q tends to infinity, namely it is no more necessary an external source, defined as ignition condition. $Q > 10$ is the goal of ITER, i.e. P_{α} is two times the power coming from external sources. One operates in condition of self-organized burning plasma. The ignition condition is not required in practical reactors. An external source power is used to control the fusion process. $Q > 40$ is the necessary condition to have economical profit by magnetic fusion [SGA+10].

Turbulence and scaling laws. Historically the first mechanism imagined to describe the perpendicular transport was based on existence of columbian collisions between particles. If two particles interact, we could observe a modification of their trajectory along the magnetic field lines. In this framework, taking in account of the curvature of the magnetic field lines, the so called neoclassical theory [HH76] has been developed to predict the transport in radial direction. Conversely, experimental observations demonstrated that the neoclassical theory could not explain the diffusion coefficient of several order of magnitudes larger than the theory, see fig.1.4. It has been claimed that the cause of this deviation can be explained via turbulent transport. Understanding the mechanism that drives the turbulence is then crucial to control the transport and therefore the confinement time.

At present, ITER reactor design studies rely on extrapolations of turbulent transport properties from present-day tokamak experiments to larger devices. These estimates are based in large part on some forms of empirical scaling, particularly device size scaling, for the global energy confinement time. In its standard form τ_E is expressed in terms of

[1] Note that in this definition P_{heat} is the plasma heating power and not the power required to operate these heating systems

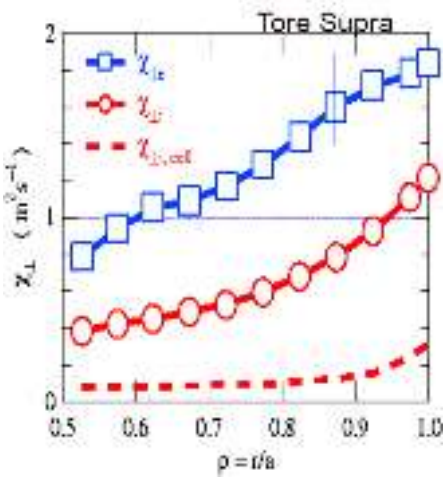

Figure 1.4: dashed lines, represents the transport diffusion coefficient predicted by the linear analysis, while the square and circle line represents respectively the diffusion transport coefficients recovered in the experiments fro electrons and ions obtained in Tore Supra experiments

products of so-called engineer parameters at some power:

$$\tau_E = \tau_0 \;\; I_{MA}^{\alpha_i} \;\; n_{19}^{\alpha_n} \;\; P_{MW}^{-\alpha_p} \;\; R_{SI}^{\alpha_r} \;\; A^{-\alpha_a} \;\; \kappa_a^{\alpha_k} \;\; M^{\alpha_m} \;\; B_{SI}^{\alpha_b} \tag{1.7}$$

Table 1.1: Exponents of the energy confinement time scaling

τ_0	α_i	α_n	α_p	α_r	α_a	α_k	α_m	α_b
0.0562	0.93	0.41	0.69	1.97	0.58	0.78	0.19	0.15

the values of the various exponents are given in table 1.1 and the subscripts indicate the normalisation of the various terms. Strangely enough, some parameters are already dimensionless such as the plasma elongation κ^{a}, the plasma aspect ratio A and the mass number M which is the mass of the ion species normalised by the nucleon mass. In this formulation, the various exponents, the α's, are defined in such a way that they are positive. The chosen parameters for this scaling law are the plasma current I, the plasma density n, the heating power P, the major radius R and the magnetic field amplitude B. As shown in fig.1.5, the value of τ_E is determined in ITER, according to the scaling law. One finds that τ_E is mostly dependent on the size of the toroidal fusion device.

The scaling law can be expressed in terms of dimensionless control parameters, namely ρ_*, β, i.e. the ratio of the plasma pressure to the magnetic pressure, and ν_*, i.e. collision-

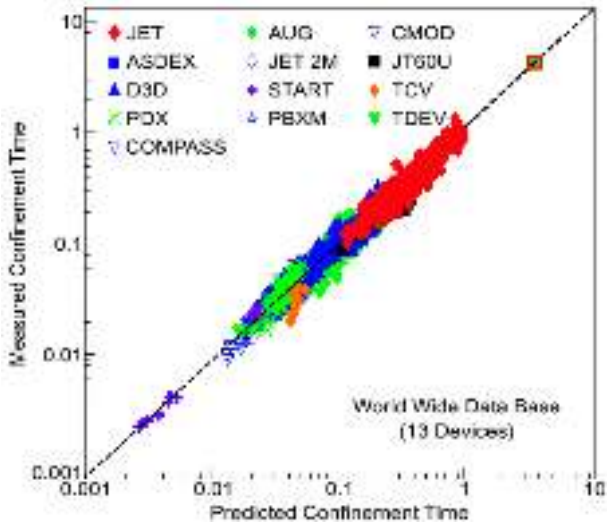

Figure 1.5: the scaling law of confinement time in function of machine size

ality. These parameters being defined as:

$$\rho_* = \frac{\rho_p}{a} = \frac{(T/m_p)^{1/2}}{a\ \Omega_p} \tag{1.8}$$

$$\nu_* \propto \frac{1}{\mathrm{L}_{coll}} \tag{1.9}$$

$$\beta = \frac{\langle p \rangle}{B^2/2\mu_0} \tag{1.10}$$

where a is the plasma minor radius, $a = R/A$, and where ρ_p, m_p and Ω_p are the proton Larmor radius, mass and cyclotron frequency respectively. The mass effect is not taken into account in this definition. The temperature T is the volume-average thermal energy per particle. L_{coll} is the particle mean free path. $< p >$ is the mean plasma pressure, and B the mean total field strength. When switching to dimensionless parameters, one finds:

$$\Omega_p \tau_E \propto \nu_*^{\alpha_\nu}\ \rho_*^{-\alpha_\rho}\ \beta^{\alpha_\beta}\ q_{cyl}^{\alpha_{qcyl}} A^{\alpha_A}\ (q/q_{cyl})^{\alpha_q}\ \kappa^{\mathrm{a}\alpha_\kappa}\ M^{\alpha_M} \tag{1.11}$$

In this expression the dependence on q_{cyl} the cylindrical value of the safety factor essentially accounts for the plasma current dependence and directly impacts the dependence on the aspect ratio A. The dependence on (q/q_{cyl}) is related to shaping properties similarly to that on the elongation κ. Here we concentrate on the leading dependence, namely the ρ_* dependence [MCT+07, SCM+07], one finds $\alpha_\rho \approx 2.68$, therefore $\Omega_p \tau_E \propto \rho_*^{-3}$[GDPN+14].

Turbulence modeling: local versus global. First theories [Hor99] and simulations (flux-tube)[DWBC96] used to predict the burning plasmas confinement time are based on the local assumption, i.e. fluctuations are assumed at microscopic scale and pressure gradient profile variations is ignored. This approach invokes a random walk type of picture for diffusive processes using the scale length of turbulent eddies as the step size and the linear growth time of the instability as the step time, hence local diffusion coefficient is defined as $\chi = \lambda_c^2/\tau_c^2$, where λ_c, τ_c are respectively the correlation time and space. One finds that λ_c scales with ρ_c and τ_c with a/c_s. The local diffusion can be rewritten as $\chi_{GB} = \rho_* \rho c_s$, also referred to as the gyro-Bohm scale. If τ_E can be rewritten by assuming

that the transport is gyro-Bohm, hence $\omega_i \tau_E = \omega_i a^2/\chi_{GB}$, one finds $\omega_i \tau_E = \rho_*^{-3}$ and can conclude that the scaling law based on the empirical fitting used to define τ_E, eq.(1.11), exhibits a gyro-Bohm scaling.

Conversely, experimental evidences have been accumulated about the breakdown of local approach. First observations of the violation of local gradient-flux relations have reported already in 1987 via a tracer encapsulated Solid pellet (TESPEL) injections[Gro87, GRB+95, ZGG+00]. Through these investigations, it has been shown that there are significant contributions of heat flux due to off-diagonal effects in the transport matrix and due to the non-local transport, which is not included in the local framework. Furthermore, global gyrokinetic simulations of electrostatic ion temperature gradient turbulence have shown that the fluctuation scale length is microscopic and independent of device size (gyro-Bohm), while the transport coefficient exhibits a gradual transition from a Bohm-like scaling, $\chi_B = \rho_s c_s$, for device sizes corresponding to present-day tokamak experiments to gyro-Bohm scaling for future larger devices [LEHT02, SGA+11, ITT+13], as shown in fig.1.6. If the confinement time is recalculated for the presents machine using the Bohm

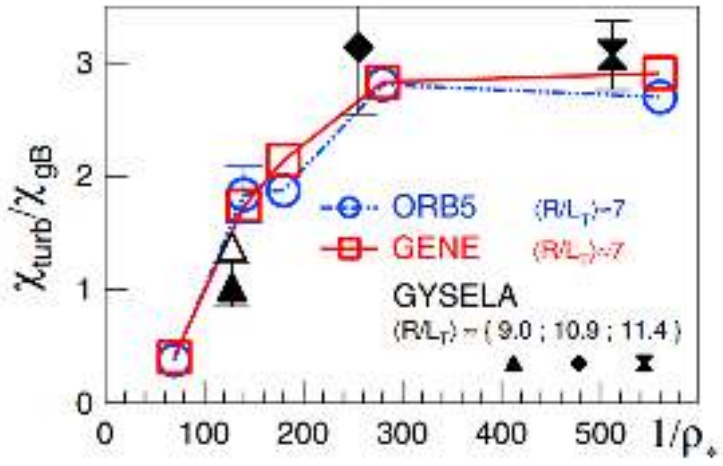

Figure 1.6: the transport coefficient in function of the Bohm scale compared for three different global ITG codes: GYSELA, GENE,ORB5

scaling, one finds that τ_E dependence of ρ_* is $\omega_i \tau_E = \rho_*^{-2}$. The scaling law predicts a ρ_* dependence $\omega_i \tau_E = \rho_*^{-2.8}$ in between Bohm and gyro-Bohm scaling.

A clear understanding of the role of non-local transport on the macroscopic transport is still missing. The study of meso- and macro-scale fluctuations, that appear to govern the turbulent transport in the global simulations[DPDG+10, GDPN+14], like avalanches and zonal flows, appear crucial to explain the contradictions between the local and global models.

Edge/SOL boundary layer and the pedestal formation. If we consider a poloidal cross section of the tokamak, two regions separated by the last closed flux-surface (LCFS) can be identified. As the name indicates the LCFS represents the transition between the regions of closed and open magnetic field lines, i.e. between the edge and SOL

regions. In general, the main plasma in a tokamak is confined within the LCFS (closed field lines region), but is surrounded by a relatively cold plasma, known as the scrape-off layer (SOL), which extends slightly beyond the LCFS (open field lines region). This surface can be created either by inserting a solid object, known as the limiter, into the plasma, or by shaping the poloidal magnetic field with external current carrying coils to create a poloidal field null, or X-point, and a magnetic separatrix , and thus to divert the SOL plasma into a specifically designed structure, known as the divertor.

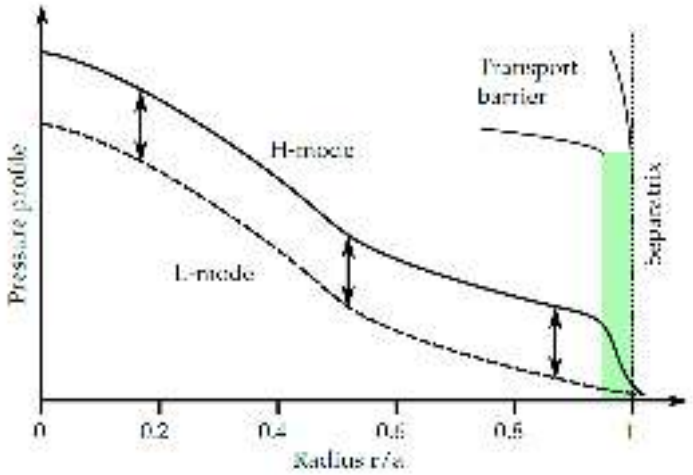

Figure 1.7: a schematic view of the pressure profile evolution during the LtoH transition

Studying and modeling the turbulent transport at the interface between edge and SOL is crucial in order to answer to the many questions concerning the dynamic of the H-mode (High-confinement) regime. The H-mode, which the plasma enters when the external heating power exceeds a given threshold value[WBB+82], represents a significant progress in the context of turbulence control. In this regime, the energy confinement time τ_E is roughly twice as large as in the Low-confinement regime, 'L-mode'. The improved confinement results from the formation of a transport barrier at the very edge of the plasma, which permits extremely steep temperature and density gradients in that region. The generally accepted picture of the H-mode barrier is that fast, sheared plasma flows suppress large-scale turbulence in the barrier region, which in turn leads to substantially reduced heat and particle transport, a schematic view of the LH transition is presented in fig.1.7. Conversely, in the SOL physics framework, turbulence is beneficial for broadening the deposition profiles and consequently reduces the power density load on the limiter/divertor plates.

Collisionality The collisionality term defines the interaction between the plasma particle. We define the typical particle mean free path, in the simplification assumption that there are no trapped particles, as

$$L_{coll} = \frac{Log\Lambda}{n\lambda_L^2} = \frac{Log\Lambda}{n(Ze^2/4\pi\epsilon)} \tag{1.12}$$

where $\Lambda = \lambda_D/\lambda_L$ is the plasma parameter, λ_D is Landau distance and λ_l the Debye length. We can define an adimensional collisionality term as the ratio between $L_{\|}$ and

L_{coll}, $L_{\|}$ is the parallel connection length defined as πqR, i.e. $\nu_* = L_{\|}/L_{coll}$.

By knowing the temperature and the density radial profile in the perpendicular direc-

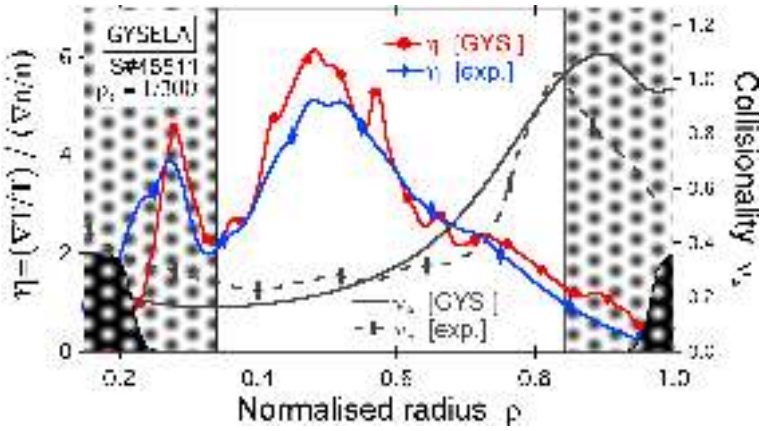

Figure 1.8: the collisional profile in TS (black line) and GYSELA (dashed line) and the $\eta = L_T/L_n$, where $L_T = -\nabla T/T, L_n = -\nabla n/n$ profiles in the TS (blue line) and GYSELA(red line)

tion, we can define the collisionality radial distribution. In fig.1.8, one can observe ν_* extrapolated by the experimental profiles of T and n for the machine TORESUPRA (TS) and reproduced by the GYSELA code. It has been observed that at the edge, where the density and temperature drop, the collisionality is increased.

Fluid versus kinetics. Two approaches are mainly used to model the turbulent transport in the fusion plasmas: (a) the kinetic approach, where the 6D distribution function $F_s(x, v, t)$ describes the probability to find a particle at given position and velocity; (b) the fluid model, derived by the so-called moments of the distribution function, calculated as the integer of f along the velocity space. The fluid model is reduced to 3 dimensions. In collisional media, fluid theories are robust and well established, because of the distribution function in the velocity space can be assumed Maxwellian, corresponding to the notion of local thermodynamical equilibrium. In low collisional media, fluid models have no universal validity. Kinetic description of particles position and velocity is a priori preferable but numerically more demanding. Fluid models can still be used in many circumstances, with some precautions, e.g. in the plasma edge.

First effort to compare the two approaches has been made by Dimits[DBB+00]. The comparison is carried out in the assumption that, at large scale, a Fourier law of diffusion can describe the macroscopic transport, i.e. the flux at large scale is proportional to the opposite of the pressure gradient $-\nabla P$, more specifically $-\nabla T$ for the ITG instability (or $-\nabla n$, in the interchange case). The proportionality coefficient χ_{eff} quantifies the microturbulence effect on the large scale transport (see fig.5.1(b)). According to Dimits paper, the fluid and kinetic prediction of the transport present strong discrepancies. Such difference in the prediction of turbulent transport between the two models appears to be related the presence of a non linear threshold, called Dimits upshift.

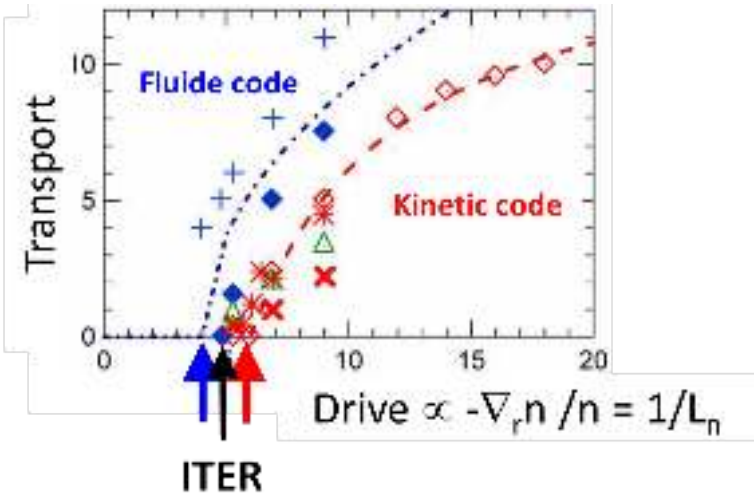

Figure 1.9: The turbulent trnasport in function of the pressure gradient xompared between the fluid(blue line) and kinetic models(red line)

Chapter 2

Turbulent transport models

Contents

This chapter introduces models which are used during the study of plasma turbulence in view of burning plasma conditions as foreseen in the tokamak ITER. We will address from a theoretical point of view GYSELA[GAB+15] code which is based on gyrokinetic description and TOKAM2D[SG98] code which is based on fluid description.

2.1 Plasma modeling approaches

Several approaches have been defined to model the plasma response to the dynamics of the electromagnetic fields. The three modeling approaches are listed here:

- **Particle model.** The trajectory of each particle is described by the classical motion equation for a charged particle, $m_\alpha d\mathbf{v}/dt = q_\alpha(\mathbf{E} + \mathbf{v}_\alpha \times \mathbf{B})$, where $\mathbf{E}$ & $\mathbf{B}$ are the external fields and the fields generated by plasma particles. To model the plasma response is then necessary to model the trajectory of 10^{23} particles. In case of ITER, such approach is numerically inaccessible, but the analytic study of the particle trajectory is important in defining the particle drifts and adiabatic invariants.

- **Kinetic model.** Using statistical description of the particle via probability distribution function, as it is not feasible to describe all particles trajectory, e.g. ITER. Using kinetic approach, the model can be reduced to six dimensions plus time as $F_s(x, v, t)$ describes the probability to find a particle at given position and velocity at a given time. Gyrokinetic model, which is based on kinetic approach, is reducing the model to five dimensions rather than six. Such an approach is based on the idea that scale separation can be performed in time between the cyclotronic frequency and the slow motion aligned with the magnetic field lines and the drifts.

- **Fluid model.** It describes the so-called moments of the distribution function, calculated as integrals of f along the velocity space. This model is then reduced to three dimensions plus time but the number of fields that account for the information in v-space is infinite. Reducing the number of coupled fields leads to the difficult problem of closure. When three moments are considered, closing the system to the Navier-Stokes equations, namely particle, momentum and energy balance, leads to the fluid description of the plasma. Disadvantage is that the change in particle response with particle energy, such as the specific effect of particle trapping or the change in the collision efficiency cannot be taken into account. Fluid model assumes that a system is highly collisional because the distribution of particle in velocity space is Maxwellian, hence defined by the density, mean velocity and temperature. Conversely, if the plasma is weakly collisional, the fluid description cannot capture the complexity of the various classes of particles. It is still the matter of discussion when it comes to the closure assumption required to truncate the fluid model.

It is then most important to quantify the information loss when stepping to a fluid model versus the difference in computer resources that are required and in terms of the efficiency to communicate the results [CM15]. The focus of the manuscript is on the description and understanding of the universal aspects of turbulence self-organization.

In the fusion community the fluid and kinetic models are addressed as incompatible scientific tools. However an appropriate analysis of model reduction leads to posing the problem as a trade-off between benefit and cost. Results, differences and similarities between the two models will be presented from the following chapters.

2.2 GYSELA: Gyrokinetic model

GYSELA uses gyrokinetic model. Advantage is that it reduces the kinetic model to five dimensions from six. Disadvantage is that the complexity of the equations increases. We will look into the analytical derivation of the gyrokinetic reduction in the context of particle trajectory. Then the GYSELA equations will be introduced. Finally, the modeling choices of the code are explained.

2.2.1 The scale separation on particle trajectories

In the non relativistic framework, we can determine the trajectory of particles of species α, charge q_α and mass m_α in an electromagnetic field as

$$\frac{d\mathbf{v}}{dt} = \mathbf{v} \times \frac{q_\alpha \mathbf{B}}{m_\alpha} + \frac{q_\alpha \mathbf{E}}{m_\alpha} \tag{2.1}$$

where $\mathbf{E}$ and $\mathbf{B}$ are respectively the electric and magnetic field. In the case of a strongly magnetized plasma we further assume that the magnetic field evolves slowly in time and space compared to the cyclotron motion frequency and scale. We define two time scales: a 'slow' time scale $\Omega = \partial_t \mathbf{B} \approx \partial_t \mathbf{E}$ and a 'fast' one $\Omega_c = q_\alpha B/m_\alpha$, i.e. the cyclotron frequency. And two space scales: a 'large' scale $\frac{B}{\nabla B}$ and a 'small' scale $\rho_c = m_\alpha v_\perp / q_\alpha B$, i.e. the Larmor radius.

$$\frac{v}{\rho_c} \approx \Omega_c \tag{2.2}$$

$$\frac{v}{a} \approx \frac{1}{\tau_\parallel} \tag{2.3}$$

$$\Omega_c \tau_\parallel \gg 1 \tag{2.4}$$

If we assume such scale separation, we can rewrite the physical quantities such as $\mathbf{v}, \mathbf{B}, \mathbf{E}$ as the sum of low frequency terms, the gyroaveraged (averaged along the cyclotron phase φ_G) component $\mathbf{v}_G, \mathbf{B}_G, \mathbf{E}_G$, and the high frequency motion term, $\tilde{\mathbf{v}}, \tilde{\mathbf{B}}, \tilde{\mathbf{E}}$.

Let us first focus on the high frequency motion. If we rewrite eq.2.1 in function of the fast dynamics $\tilde{\mathbf{v}}$, we assume that the magnetic field is the leading order contribution. Therefore we assume the electric field to be of order 0 compared to B of order 1. At lowest order, the equation is reduced to the high frequency dynamics:

$$m_\alpha \frac{d\tilde{\mathbf{v}}}{dt} = q_\alpha \tilde{\mathbf{v}} \times \mathbf{B}. \tag{2.5}$$

where, in first approximation, $\mathbf{B} \approx \mathbf{B}_G$. Since $\mathbf{B}_G$ does not depend on the high frequency component of the particle position. We can integrate the equation and define ρ_c such that $\tilde{\mathbf{v}} = \rho_c \times \Omega_c$ which defines the cyclotron motion.

Let us now focus on averaged motion, we rewrite the eq.2.1 as

$$m_\alpha \frac{d\mathbf{v}_G}{dt} = q_\alpha (\mathbf{E}_G + \mathbf{v}_G \times \mathbf{B}_G + < \tilde{\mathbf{v}} \times \tilde{\mathbf{B}} >) \tag{2.6}$$

where in the last term $< \tilde{\mathbf{v}} \times \tilde{\mathbf{B}} >$ we take into account self-correlation of the cyclotron motion. It can be rewritten as $\mu \nabla \mathbf{B}_G$ where $\mu = 1/2 m v_\perp^2 / B$ is an adiabatic invariant.

If we split the low frequency velocity in parallel and perpendicular component $\mathbf{v}_G = v_\parallel \mathbf{B}/B + \mathbf{v}_{G,\perp}$, we can define the velocity of the particles aligned with the magnetic field lines (parallel) and the transverse drifts (perpendicular) that cause the turbulent transport. The perpendicular contribution to the velocity can be rewritten as

$$\mathbf{v}_{G\perp} = \mathbf{v}_E + \mathbf{v}_{G,S} = \frac{\mathbf{E}\times\mathbf{B}}{B^2} + \frac{m_\alpha v_\parallel^2 + \mu_\alpha B}{q_\alpha B^3}\mathbf{B}\times\nabla B + \frac{m_\alpha v_\parallel^2}{q_\alpha B^2}\nabla\times\mathbf{B}\,|_\perp \tag{2.7}$$

where $\mathbf{v}_E$ corresponds to the electric drift while $\mathbf{v}_{G,S}$ is the magnetic contribution and is made of the so called *grad*-B and curvature drifts in the low β limit (the ratio β between the kinetic and the magnetic energy is typical of the order of few percents in tokamks). The first drift takes in account the effect of the electric field on particles. This term does not depend on the charge or mass of the particles therefore cannot generate current. The second term takes into account the variation of the magnetic filed in the radial direction. Because of such gradient the particle moves vertically and in opposite directions depending on charge sign. This leads to a vertical charge separation.

2.2.2 Equations in GYSELA

The scale separation and the gyroaveraged quantities defined in the framework of particle trajectories is then used in the kinetic description. Therefore, the original 6D distribution function f_α is gyro-averaged along the fast cyclotron motion scale $\bar{F}_G$ [BH07]. The problem is reduced to a 5D one, four slow variables and an adiabatic invariant $\bar{F}_G(x_G, v_G, v_\parallel, \mu)$. The reduced kinetic equation can be expressed as

$$\frac{d\bar{F}_S}{dt} = \partial_t \bar{F}_S + (\mathbf{v}_{G\perp}\cdot\nabla_\perp + v_\parallel\nabla_\parallel)\bar{F}_S + \dot{v}_\parallel\partial_{v_\parallel}\bar{F}_S = C(\bar{F}_S) \tag{2.8}$$

where the term $C(\bar{F}_S)$ on the right hand side is the gyro-averaged colllisions operator. In order to close the gyrokinetic system, the electric potential, that appears in the definition of the transverse drift has to be computed using Maxwell-Gauss equation. In the electrostatic limit we can rewrite the Poisson equation as

$$\nabla^2\phi = \frac{1}{\epsilon_o}\sum n_\alpha q_\alpha \tag{2.9}$$

In the quasi-neutrality limit this equation is reduced to

$$\sum n_\alpha q_\alpha = 0 \tag{2.10}$$

where n_α is the density of particles of species α. It is important to realize here that the densities appearing in Maxwell's equations are the densities of particles, rather than the densities of gyro-centers, namely the first moment of the distribution function evolved by the gyrokinetic Vlasov equation. By adding the polarization density $n_{pol,\alpha}$ we can calculate the density of particles n_α. This leads to $n_\alpha = n_{G,\alpha} + n_{pol,\alpha}$ where $n_{G,\alpha}$ is an integral in gyro-center phase-space and the polarization density $n_{pol,\alpha}$ is a function of the electric potential ϕ. The calculation of these two terms, not presented here but extensively detailed in [YSBOOK], leads to

$$n_{G,\alpha} = \int \mathcal{J}_v d\mu dv_{G\parallel} J\cdot\bar{F}_\alpha \tag{2.11}$$

$$n_{pol,\alpha} = \nabla\cdot\left(\frac{n_{eq,\alpha}m_\alpha}{q_\alpha B^2}\nabla_\perp\phi\right) \tag{2.12}$$

where $\mathcal{J}_v = 2\pi B^*_{||}/m_\alpha$ is the Jacobian in gyro-center velocity-space and J is the gyro-averaging operator.

Furthermore, one can assume that the electron parallel motion is fast enough for the electrons to have reached a Boltzmann equilibrium, they do not need to be treated kinetically. This approximation of the electron dynamic is often referred to as adiabatic electron response. Thus, the perturbed electron density in the quasi-neutrality equations reads as $\delta n_{eq} = \delta\Phi/T_e$. Moreover only one ion species is considered in the following. The gyrokinetic quasi-neutrality equation eq.2.11 can be rewritten in the form as $n_i - n_{eq} = \delta n_e$, such as:

$$\nabla \cdot (\frac{n_{eq} m}{B^2} \nabla_\perp \phi) + e \int \mathcal{J}_v d\mu dv_{G||} J \cdot (\bar{F} - \bar{F}_{eq}) = -\frac{n_{eq} e}{T} (\phi - < \phi >_{F.S.}) \tag{2.13}$$

where $\bar{F}_{eq}$ is the equilibrium gyrocenter distribution function associated with a vanishing potential and $< \cdot >_{F.S.}$ is the flux surface averaged electric potential.

2.2.3 Modeling choices behind the GYSELA code

In the context of gyrokinetic codes, some modeling choices can be made. The codes can be then distinguished in different classes: 'local' or 'global', 'full-f' or 'δf' and 'flux' or 'gradient' driven. GYSELA is a global, full-f, flux-driven code. We describe here the advantage and drawbacks of the different classes:

- **global versus local**. An important modeling choice is how to take into account the toroidal geometry. On one hand, we can take the advantage of the strong anisotropy between the perpendicular and parallel direction, $k_{||} \ll k_\perp$. In this context, if we use field aligned coordinate with the magnetic field line, we can reduce the simulation to the region in the neighborhood of the field line, such model is defined as local or 'flux tube'[CW03, GIVW10]. In such assumption we consider the mean gradient profile constant in time and we assume the radial perturbation periodic in time. In the flux tube approach we can reduce the numerical cost, but an implicit scale separation between mean profile and fluctuations is taken into account. On the other hand, in order to take into account the global aspect of transport, the global codes have been developed. With GYSELA, the simulation region can extend to all the core plasma, inside the last closed flux surface.

- **full-f versus δf**. Historically the distribution function is separated between equilibrium part and fluctuating perturbation, " $deltaf$ ". This procedure is based on the assumption that the equilibrium term of the distribution function evolves much slower than the fluctuating parts. Such constraint is relaxed in GYSELA, where no separation is made between the fluctuating and equilibrium profile. This method is defined as full-f. If the scale separation assumption presents a clear advantage from a computational point of view, it has some drawbacks such as keeping the turbulence drive constant, hence ruling out the feedback the fluctuations on the mean profile.

- **flux- versus gradient driven**. Another key difference between the different model describing the turbulent transport concerns the turbulent forcing. Two options are here detailed the flux driven and gradient driven assumption. In the gradient driven assumption, we consider the mean background profile as an input parameter. In

this way the constant gradient of the equilibrium profile drives the instabilities. The success of this approach is based on the idea that the temperature or density profile are known from experiments and this considered as input parameters, making easier a comparison between simulation and experiments. As second point is the fact that one can simulate steady state condition, skipping all the transient phase where the profile builds-up. The other possible forcing is the flux driven one. Forcing corresponds to a more realistic one, for a heat or particle source. In this case the profile is self-consistently generated. This leads to higher computational costs. On the other hand the mean profile is not constrained. In the gradient driven case to avoid profile relaxation, a Krook type of source is taken into account and the impact of such a constrain on the turbulence self-organization is open [GLB+11, IUAT09]. More details on the role of the driving terms will be discussed in Chapter 4.

The modeling choices taken in GYSELA, that strongly impact on the computational costs, give us the possibility of studying turbulence self-organization with no *a priori* assumption on fluctuation and equilibrium scales.

Here are the physical assumptions taken into account in order to simplify the model:

- gyrokinetic ordering, the reduction of phase-space from 6D to 5D by the gyro-center transform
- simplified magnetic geometry, we consider circular flux surfaces with a magnetic field given by an analytical expression [1]
- low plasma β limit (small ratio between kinetic and magnetic energy) leading to a simplified expression of the curvature drift,
- adiabatic electrons response, the electron follow a Boltzman response to the perturbation in the direction of the magnetic field,
- electrostatic turbulence, time variations of the magnetic field are ignored.

2.3 TOKAM2D: fluid model

TOKAM2D is a two-dimensional model for turbulent particle transport. TOKAM2D simulates the turbulent transport for the closed and open field lines region, i.e. the edge and the SOL. Benefit of TOKAM2D is that it reduces the computing time through simplified physic mechanism and providing sufficient overview of the turbulence organization in short amount of time. Also, some of the disadvantages due to simplification will be described.

2.3.1 TOKAM2D equations

TOKAM2D equation can be derived from the two first moments of the distribution functions[2]. The main assumptions of the model are:

- **Flute hypothesis.** Perturbations are constant along the field lines. This allows one to reduce the model to two dimensions, the radial direction x, $x = (r - a)/\rho_s$ where a is the plasma minor radius, r the radius of the considered magnetic surface

[1] the analytical expression of the magnetic field in GYSELA is treated in session 5.1.1
[2] In the Annex A, the derivation of TOKAM2D is treated in details

and ρ_s the hybrid Larmor radius, and an angle that describes the poloidal angle on the magnetic surface y, $y = a\theta/\rho_s$ where θ is the actual poloidal angle. The angle coordinate is periodic so that the average of any particle flux on a given magnetic surface yields the mean radial component of the flux.

- **Isothermal closure.** Assuming the temperature constant, we can close the fluid problem rewriting the third moment, the pressure tensor, in function of the density, i.e. $P = Tn \propto n$

- **Cold ion limit.** We assume that the ion temperature is much lower than the electron one $\tau = T_i \; T_e = 0$.

As in GYSELA, we assume the drift ordering that allows us to solve the momentum balance equation in term of the drift velocities.

The equations that govern the model are the particle balance equation for the electron density n and the charge conservation equation in the quasi-neutral asymptotic limit, which then restricts to $\mathrm{div}(\mathbf{j}) = 0$, $\mathbf{j}$ being the total current.

In the flux driven approach we assume that the density and the potential profile can fluctuate at all scales, i.e. the fluctuation size can be comparable to the size of the box. Such an assumption implies that the driving of the system is a particle source that is localized radially. In this way the initial profile is null and it will build-up through the source a density gradient that drives the bursts in the box. The equations solved by TOKAM2D are

$$\partial_t n + [\phi, n] = D_\perp \Delta_\perp n - \Gamma + S \tag{2.14}$$

$$\partial_t W + [\phi, W] + g\frac{\partial_y n}{n} = \nu_\perp \Delta_\perp W + j \tag{2.15}$$

where:

$$W = \nabla^2_\perp \phi \tag{2.16}$$

The particle balance equation Eq.(2.14) includes the leading order particle flux due to the electric drift velocity, which takes the form of the Poisson bracket, i.e. $[\Phi, f] = \partial_x(f(-\partial_y\Phi)) + \partial_y(f(\partial_x\Phi))$ between the normalized electric potential ϕ and the density $f = n$, together with a source term S, the parallel particle sink Γ and a small transverse diffusion $D_\perp$.

The charge balance equation Eq.(2.15) takes the form of the evolution equation of the vorticity W defined in eq.2.16, with an electric drift convection, the Poisson bracket term between the electric potential and the vorticity, i.e. $f = W$, together with a diffusive damping of the convective motion with diffusion coefficient $\nu_\perp$. Charge sources and sinks are due to the curvature drift, here simplified to a constant interchange term g. This g-term is the standard gravity term when addressing buoyancy effects in a neutral fluid. A similar term should be included in the density equation, however this term is a lower order term than the drift convection term that is only retained in the charge conservation equation because the latter only includes terms of this order, polarization current and parallel loss current J.

2.3.2 Closed and open field lines regions in TOKAM2D

The original version of TOKAM2D simulations address the turbulent transport only for the Scrape Off Layer region[SG98].

In the SOL region, we can consider the Bohm criterion to define the parallel particle and current losses and rewrite the sink terms such as:

$$\Gamma = \sigma_n\Big(n\ \exp(\Lambda-\phi)\Big) \tag{2.17}$$

$$J = \sigma_\phi\Big(1-\exp(\Lambda-\phi)\Big) \tag{2.18}$$

where σ_n is the particle lifetime in the SOL and σ_ϕ is the normalized sheath conductivity $\sigma_\phi = \rho_s/L_\parallel$, $L_\parallel$ is the connection length [3] and Λ is the floating potential.

A linearized version of the sink terms is used in this work, i.e. $\Gamma = \sigma_n n, j = \sigma_\phi\phi$, where Λ is set to zero, simplifying the σ-term to a linear drag term for the density and the vorticity[NGC+15].

In order to model the turbulent transport at the interface between open and closed field lines, the parallel loss terms (Γ and j) have been modified for the edge region. In this region the plasma is confined and moves in parallel direction along closed magnetic surface. One can then assume that the parallel particles transport do not contribute in the evolution of the density, the lines are closed in a loop, namely the particle will ideally move for an infinite time in the same region. Therefore we assume that if we average along the parallel direction, there is no loss of particles. The sink term for the density equation is set at zero in the edge, $\Gamma = 0$. For the parallel current, to take into account the closed field lines property, we assume that no net current can be generated along a closed field line, therefore the sink term j averaged along a given flux surface, namely the θ, ϕ plane, is set to zero. We redefine the sink terms for the TOKAM2D equations taking in account such constrains:

$$\Gamma = 0 \tag{2.19}$$

$$j = \sigma_\phi(\phi - <\phi>_y) \tag{2.20}$$

where $\sigma_\phi = 1/\eta$ represents the plasma conductivity.

In this work we do not consider different value of σ_ϕ for the SOL or edge region to avoid increasing the number of plasma parameters.

The new sink term is define such that

$$\Gamma \to \Gamma_{E,S} = (1-\chi(x))\sigma n \tag{2.21}$$

$$j \to j_{E,S} = \sigma(\phi - \chi(x) <\phi>_y) \tag{2.22}$$

where $\chi(x)$ is a mask function, $\chi(x > x_{Sep}) = 0$ and $\chi(x \leq x_{Sep}) = 1$, that accounts the for change in field line properties at the separatrix x_{sep}.

[3] In the SOL, the connection length associated with a given point is defined as the shortest distance from that point to any material surface measured along the field line through that point.

The edge and SOL difference is twofold. First the particle loss is localized in the SOL region. This has rather little effect on the turbulence but organizes the overall stratification of the system in the x direction Second, the change in j modifies the evolution equation for the zonal flow $V_z = \partial_x < \phi >_y$. The latter is governed by a balance between the non linear Reynolds stress source, and the loss terms: viscous damping at small scales, sink term $< J >_y$ at large scales. The edge constraint $< j >_y = 0$ favors the large scale zonal flow structures. Conversely, in the SOL, the current loss term $< j >_y = \sigma_\phi < \phi >_y$, is observed to damp the zonal flows.

2.3.3 Cons and pros of a reduced model

Various assumptions have been made to reduce the model. Let's look into the simplification assumptions and their impacts:

- **Fluid description.** The energy distribution function is assumed maxwellian, such assumption is not true for weakly collisionality plasma, but is considered valid for the edge;
- cold ions limit, we assume the ion temperature much smaller than the electron one. Only the electrons transport is modeled;
- **Particle transport only.** We assume a constant temperature as closure condition for the fluid model, the heat flux is assumed proportional with the particle flux;
- **Flute assumption.** We assume that the parallel transport periodic, this hypothesis is only true if the particles move in parallel direction much faster than in the perpendicular one ($\tau_\parallel \gg \tau_\perp$), where $\tau_\parallel$ and $\tau_\perp$ are respectively the parallel and transverse crocheters scales of turbulence;
- **Periodic boundary conditions.** In order to use a pseudo spectral method to numerically solve the problem, we consider the system periodic;

The strong simplifications adopted should not be seen as a limitation, but as an advantage. (1) the model presents strong analogies to other non linear dynamical systems, comparisons with other domains result easier. (2) Computing time reduces significantly due to the simplified equations. One can acquire results relatively quickly and grasp the idea of the turbulence self organization. (3) The model is suited to be used as reduced turbulent model to understand which are the key mechanism of plasma self-organization. Once the basic ideas are proven, then they can be implemented in more complex code such as GYSELA in order to see the more detailed analysis.

Chapter 3

Turbulence self-organization impact on plasma transport

Contents

The description of turbulent transport at large scale represents together with the understanding of turbulence a major scientific challenge. The problem is characterized by a large number of degrees of freedom with the strong interplay between all scales as exemplified by the turbulence spectra and our understanding of universal aspects associated to their slope in wave vector space. In such a framework, plasma turbulence appears to share some of the complexity of neutral fluid turbulence, combined so specific features such as weak collisions and the occurrence of instabilities as the main drive for turbulence.
A standard approach to separate microscopic and macroscopic properties is to introduce an averaging process. Such a step for a media that exhibits fluctuations appears quite natural. However, when considering its experimental counterpart, one finds that it is a very complex step, especially when investigating transport usually associated with inhomogeneity in time and space. Assuming that such a procedure can be determined, then microscopic and macroscopic scales can be identified, respectively for the fluctuating field $\tilde{f}$ and the averaged one $\bar{f}$. The conventional approach used to study turbulent transport is based on the assumption of a gap between these two scales, the evolution of $\bar{f}$ and $\tilde{f}$ can be studied separately, i.e. $\partial_x \tilde{f} \ / \ \tilde{f} \ll \partial_x \tilde{f} \ / \ \tilde{f} \longleftrightarrow kL_{\bar{f}} \ll 1$, where k is the characteristic wave-vector of the fluctuations and $L_{\bar{f}}$ the characteristic gradient length scale of the average field $\bar{f}$. In such a framework, the impact of the fluctuations on the mean-field evolution is usually reduced to an effective diffusion, D_{eff}. Once this effective diffusion coefficient is determined, most often based on empirical transport analysis, the dynamics of average profiles can be predicted.

In magnetic fusion plasmas, the scale separation assumption and its consequence in terms of diffusive transport properties, cannot be reconciled with experimental results [TFR87, GRB+95], where several transient transport phenomena appear to depart significantly from diffusive like transport.

Striking features of self-organization such as avalanches [DH95], staircases [DPDG+10] and transport barriers [SSZ+13], have been identified in plasma turbulence theory, via gyrokinetic models [CLL+15, GNCM+14, DPHG+15], like GYSELA, and reduced fluid models [CNLD96, SG98, Nau07], like TOKAM2D, have also been observed experimentally. Although transport barriers have been triggered in experiments, since the 1980's for external transport barriers, the H-mode [WBB+82], and the 90's for internal transport barriers [KKM+94], and easily identified due to their bifurcation nature and consequent improved confinement, measurements of other features are quite difficult to set-up and interpret [DPHG+15]. In this chapter, we describe different self-organization patterns observed in turbulent transport simulations and their signature in terms of large scale features, namely transport properties. The consequence of such structures and the departure from the standard diffusive paradigm they govern is the ultimate goal of this work. Since a global steady state averaged regime can always be reduced to an effective diffusive transport, linear by essence, our interest is to investigate the dynamics and non-linear features.

3.1 Non diffusive transport in a system driven away from equilibrium

In this Section, the aim of our analysis of turbulent models is to analyze the impact of turbulence non-linearity on large scale transport. According to a "local expression" of

the gradient-flux relation (see introduction), diffusive processes, Fourier law for heat, Fick law for particles, can describe the macroscopic transport, i.e. the flux at large scale is proportional to the opposite of the pressure gradient $-\nabla P$, more specifically $-\nabla T$ for heat (hot plasma ITG instability), or $-\nabla n$ for particles. In the thermodynamical framework we thus seek the relationship between the driving forces, here the gradients, and the restoring fluxes that tend to remove the gradients. In such a picture, the gradients are imposed to the system so that the latter is out of equilibrium, and consequently a flux is generated. A system in contact with two thermal baths with different temperatures is the idealized example of such a thermodynamical machine. In practice, and in particular for plasmas, such thermal baths must be replaced by a source, a driving flux, so that the gradients develop as a consequence of a form of resistivity of the media to transport. The proportionality coefficients χ_{eff} and D_{eff} between the flux and gradients, quantify in all cases the effect of micro-turbulence on large scale transport[DBB+00].

Given $\Gamma = -D_{eff}\ \partial_r n$, where Γ is the particle flux and $\partial_r n$ the density gradient, one can write that $\Gamma/n = G$ with $G = G(L_n^{-1})$, where $L_n^{-1} = -\partial_r n/n$. Via Taylor expansion, G can be rewritten as $G = G_0 + L_n^{-1}G^{(1)} + \frac{1}{2!}L_n^{-2}G^{(2)} + ...$ If G is amenable to the two first terms, which is consistent with a weak departure from equilibrium, $G^{(0)}$ and $G^{(1)}$, one has a local linear fit. Furthermore, if these two terms are close to constants, one obtains a relevant thermodynamical information namely a mean field diffusion coefficient. In most cases, it is argued that one cannot sustain a flux for a system in thermodynamical equilibrium so that $G \to 0$ when $1/L_n \to 0$, which enforces that $G^{(0)} = 0$ unless $G^{(0)}$ depends on another non-vanishing thermodynamical force present in the system.

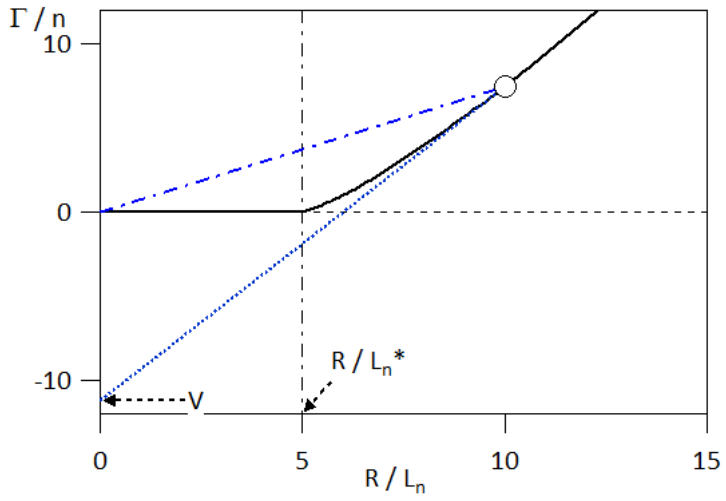

Figure 3.1: particle flux Γ/n in function of density gradient $1/L_n$ (black line) analyzed in term of diffusion coefficient D_{incr} and pinch velocity V (blue dotted line) or in term of a single point D_{bal}

For systems with a threshold for turbulence to grow, as is usually the case for plasma instabilities, the response is different see fig.3.1. Transport can then be analyzed in terms of incremental diffusion coefficients D_{incr} associated to a pinch velocity $\Gamma/n = -D_{incr}\ (-\partial_r n/n) + V$, where V, the pinch velocity can be determined by extrapolating

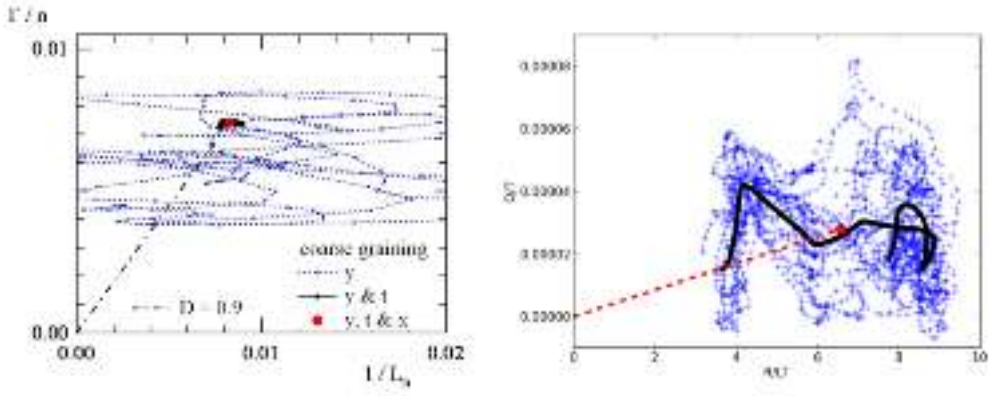

Figure 3.2: (a) particle flux Γ/n in function of density gradient $1/L_n$ in the SOL, y-averaged blue line, y- and t-averaged black dots, y-,x-,t-averaged red point, (b) heat flux Q/T in function of temperature gradient $1/L_T$ in the core, θ- and ϕ-averaged blue line, θ-, ϕ- and t-averaged black dots, θ-, ϕ-, t-, r-averaged red point

the linear fit to the axis $R/L_n = 0$, see fig.3.1. However, such a pinch velocity does not indicate that other thermodynamical forces are driving the system. There is also a clear difference with the value that would be defined knowing a single point $(R/L_n, \Gamma/n)$, the so-called balance determination $D_{bal} = -\Gamma/\partial_r n$, fig.3.1. Using GYSELA and TOKAM2D data, a comparable analysis has been carried out to define effective diffusion coefficients. The results summarized on fig.3.2 are difficult to reconcile with such a transport model:

- As shown in fig.3.2(a), no linear correlation between flux and pressure gradient can been defined, although both quantities are averaged on the flux surface (y-averaged in the TOKAM2D case). When one time-averages, the scatter of points is reduced, but one still cannot recover a monotonic linear correlation between flux and density gradient. Only when the quantities are averaged also in the radial direction, can one recover an effective diffusion coefficient. But the whole simulation region has been coarse-grained by the successive averaging procedures to a single point. Transport in such a region cannot be reduced to a linear diffusive transport model since a single scalar then characterizes the coarse grained transport. This characterization of transport is then equivalent to the use of the confinement time of the energy τ_E, as unique figure of merit. The coarse grained system is considered as a reservoir with global transport property and no insight on the existence of barriers, peaked profiles *etc.* that all contribute to the overall performance[GNH+12].

- The same analysis is performed with the GYSELA data, fig.3.2(b), here the x and y axes are respectively Q/T and R/L_T. The conclusion is then quite comparable. However, unlike the TOKAM2D case, a threshold in temperature gradient is readily observed. The boundary value for the region with transport corresponds to that predicted by the linear analysis, $R/L_T \approx 4$. The scatter in the heat flux exceeds a factor 5 while R/L_T changes by a factor 2 at most. Like for the TOKAM2D data, the time average considerably reduces the scatter, but a monotonic relationship is not obtained so that the incremental values of the transport coefficient have no meaning. It is interesting to see that the behavior with negative slop coincides with the Dimit's

shift region. In the core, as in the edge region, a linear diffusive transport relation can therefore only be defined by reducing the system to a single point.

The description of transport in terms of a diffusive process appears rather artificial since a strong coarse-graining procedure is required to recover a linear relation between the flux and gradients. Such a representation can be appropriate to describe steady states or adiabatic evolution. However, it does not yield any insight in the behavior of the system during transients nor on the underlying transport mechanisms when based on such an analysis, the Bohm or gyro-Bohm transport property can then be purely fortuitous. Finally most operating states that are presently foreseen for burning plasmas are associated to relaxation events such as sawtheet by ELMs so that the use of steady-state reduced features can be quite inappropriate.

3.2 Avalanche transport

3.2.1 Avalanche transport in the SOL

The non-diffusive feature of transport at macroscales appears to be governed by the avalanche like transport events. These are poloidally localized over-dense regions extending along the field lines. On average, these exhibit ballistic motion in the radial direction. Such intermittent events are observed in the Scrape Off Layer region of tokamaks, stellarators reversed field pinches, toroidal devices, etc. They appear to be propagating plasma filaments [Zwe89], [GHP+06, FLP+08] and have quite often been analyzed as "blobs" [MWS+03, RBM+02] following the theoretical investigation of a single over-dense region with radial displacement driven by interchange [KDM08].

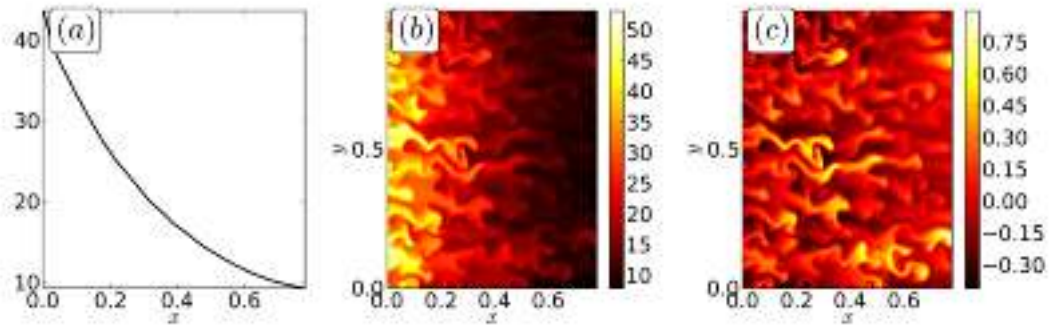

Figure 3.3: (a) $< n >_{y,t}$ profile, (b) 2D plot of $n(t_0, x, y)$ at arbitrary time t_0 in the non-linear region in function of $x = ((r-a)/(N_x\rho_s))$ and $y = \theta/2\pi$,(c) $\tilde{n}(t_0, x, y)/\bar{n}$

When analyzing the density fields in the SOL region determined by TOKAM2D (fig.3.3(b)), one can identify overdense patterns. Subtracting consecutive snapshots of the density fields allows one to identify front displacements. Analyzing the displacement of the fronts indicates that the latter move radially outward with ballistic motion (fig.3.4). One can then calculate the velocity of the front v_{front} since the radial displacement is typically of $1/\rho_s$ during time interval of $50/\omega_i$, hence $v_{front} = 0.02c_s$, a factor two smaller than the electric drift velocity in the radial direction $v_{E_x} = -\partial_y\Phi = 0.04$. These structures appear to be rather homogeneously distributed in the poloidal direction in line with the symmetry of the equation with respects to y. However, very long simulations are required

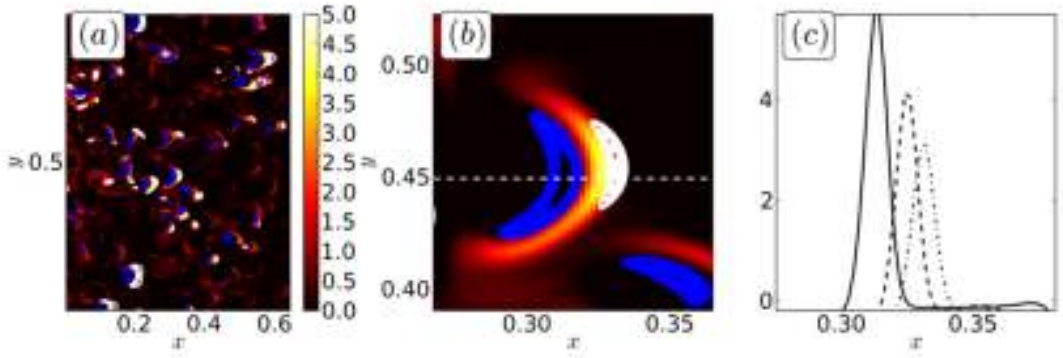

Figure 3.4: (a) $n(t_1), n(t_0) - n(t_1), n(t_2) - n(t_1)$ in function of $x = ((r-a)/(N_x \rho_s))$ and $y = \theta/2\pi$, at $t_0 = t0$ the fronts color is blue, at $t_1 = t_0 + 25/\omega_i$ red, at $t_2 = t_1 + 25/\omega_i$ white, (b) zoom of a single front displacement,(c) plot of a front displacement at $y = 0.45$

to achieve y-independent statistics. Two aspects govern such a feature. On the one hand, successive avalanches can propagate in the wake of the previous event, and, on the other hand very rare large avalanches occur. In both cases, such overloading events are rare but are so strong that they lead to long lasting distortion of the statistics. In the radial direction the symmetry is broken by the presence of a source, that is localized close to the origin[1]. Averaging the density distribution in time and poloidal direction, see fig.3.3(a), yields a near exponential radial profile. The instantaneous profile is markedly different from the mean one: i) it is non-monotonic, ii) the gradient length scales are much shorter that the e-folding length for both positive and negative gradients, iii) the departure from the mean profile is of the same order of magnitude as the mean value, see fig.3.3(c).

Considering the relative density fluctuation field, $\tilde{n}/\bar{n}$ where $\tilde{n} = (n - \bar{n})$, one finds that the fluctuation magnitude is uniformly distributed along the radial direction (until the non turbulent region is reached) as well as in the y-direction. The departure from the mean profile is quite significant since, one finds that $\tilde{n}/\bar{n}$ ranges from -0.6 to 0.8. The magnitude of the density fluctuations is thus comparable to the average value, fig.3.3(c). This property is recovered when considering the PDF of the density field at a given radial position, fig. 3.5. One finds that the PDF is close to a lognormal distribution as would be expected with large fluctuation to mean ratio. The width of the lognormal distribution is $n_+ - n_- = 2\, n_x \sinh(\Delta)$ where n_x is the most probable value of the density and $\Delta = 0.612$. Considering the lognormal fit one can compute the mean density $< n >\ = 1.196$ and the characteristic ratios for this PDF: $n_+/ < n >\ = 1.4$ and $n_-/ < n >\ = 0.4$.

The radial turbulent particle flux is $\Gamma_x = n v_{E_x}$, where the electric drift velocity in the radial direction is $v_{E_x} = -\partial_y \Phi$. One then finds that the maximum radial particle flux then favors the contribution of a maximum of the density at a maximum of the radial electric drift velocity. It is to be noted that $v_{E_x} = -\partial_y \Phi$ changes sign depending on the sign of the poloidal slop of the electric potential Φ. Furthermore, due to the fact that y is an angular quantity, one readily expects that $< v_{E_x} >_y = 0$, which is exactly obtained in the simulation where periodicity in y is considered. The mean radial particle flux

[1]The fluctuation regime being periodic, the source term is also periodic.

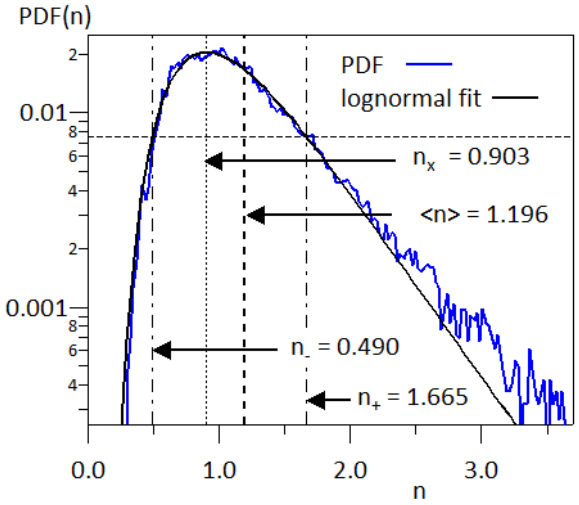

Figure 3.5: the PDFs of the density fluctuations

thus builds-up due to constructive interferences between the density and electric potential fluctuations.

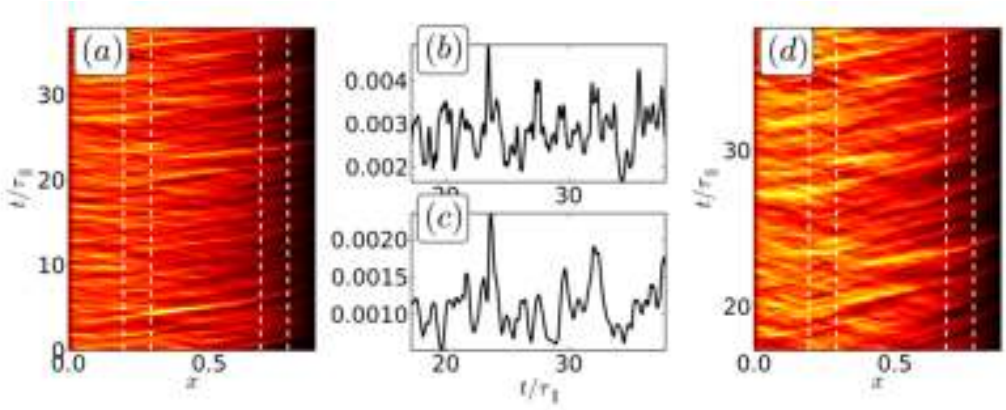

Figure 3.6: (a) turbulent flux $< \Gamma_x >_y /\bar{n}$ in function of radius $x = ((r-a)/(N_x \rho_s))$ and time $t/\tau_{\|}$, (b)-(c) $< \Gamma_x >_y /\bar{n}$ for two different radial intervals, (d) zoom of $< \Gamma_x >_y /\bar{n}$

In fig.3.6(a), where the 2D map of $< \Gamma_x >_y /\bar{n}$ is plotted versus the radial coordinate x, horizontal axis and time, vertical axis, one can readily notice that maxima of the particle flux are organized in a set of lines, which seem to appear quasi-periodically, and extend radially with a near constant slope. This corresponds to a ballistic motion with quasi-constant velocity $< v_a >$. Given the typical traces on fig.3.6(a), radial excursion of $\delta r = 256\rho_s$, the box width, during $\delta\tau = b\ \tau_{\|}$, with $b = 2$, one then estimates $< v_a >= 128\rho_s/\tau_{\|} = 0.02\ c_s$, where $\tau_{\|} = 1/\sigma_n = 1.510^{-5}\Omega_i$. This value is to be compared to the typical radial drift velocity $< |v_{E_x}| >= 0.04$.

One can also observe that the avalanche apparent frequency, at a given radial surface, exhibits a decrease with the distance from the source, see fig.3.6(c). This feature indicates

that the number of avalanches decreases radially and that the avalanche pattern appears to reorganize and to exhibit a slower averaged pace as the number of events decreases. As also show in fig.3.6(d), the avalanche transport is extremely rich: avalanches can move inward and outward, decay to smaller scale, or merge with other events. Only a few avalanches identified when considering $< \Gamma_x >_y / \bar{n}$ appear to cross the whole SOL. It is however to be underlined that the richness that is described here is simplified by the averaging process along y when compared to the local behavior of $\Gamma_x/\bar{n}$. This difference is quantified by the PDFs of Γ_x and $< \Gamma_x >_y$ that are analyzed in the following Section.

3.2.2 Quantifying avalanche transport

To further quantify the self-organization features, we use autocorrelations, namely the cross-correlation of a signal with itself at different points in time and space. This mathematical tool helps identifying repeated patterns, such as the presence of intermittent turbulent bursts observed in the flux Γ_x. In this particular case, we utilize a two dimensional autocorrelation in time and radial direction. One can then define and compare characteristic radial and time scales of avalanche transport. We define a limit for the autocorrelation, $c_{lim} = 0.3$, such that below c_{lim} a structure will not be considered as coherent. Given this 2D correlation function, fig.3.7(a), one can determine some statistical properties of avalanche transport. A first feature is the existence of a coherence between time and radial autocorrelation that is supported by the elongation of the correlation function along an axis in the δ_x, δ_t plane. We identify a coherent structure with characteristic correlation $\delta_t = 800\ \Omega_i^{-1}$ and $\delta_x = 32\ \rho_s$ in time and radial direction respectively. However, the correlation scale of Γ_x, $\delta_x = 32$, is much smaller than the correlation that one identifies with the eye for $< \Gamma_x >$ on fig.3.6(a). Furthermore, the autocorrelation threshold $c_{lim} = 0.3$ that we have used to identify δ_x is rather low. At higher values of c_{lim}, the elongation pattern is less clear. This feature, combined to the long range transport identified on fig.3.6(a) indicates that the avalanche motion is not aligned on the radial direction.

As shown on the sketch fig.3.8, an estimate of the mean angle made by the avalanche trajectory in the (x, y) plane is then $\theta_a \approx 17°$ assuming that the width of the avalanche is determined by half the wave length of the most unstable mode, typically $0.5(256/10)$. This geometrical analysis would then indicate that the correlation time is determined by the extent of the avalanche structure at any given time, which is quite different from the length and duration of the avalanche coherent motion. Given $< v_a >$ and δ_t one then obtains $\lambda_a =< v_a > \delta_t \approx \delta_x$ which indicates that the overdense region of the avalanche is rather symmetric in x and y. In this framework, the radial autocorrelation function is not a measure of the coherence of the avalanche motion in the radial direction, but that of the avalanche width, i.e. one is not measuring the length of the snake but its section, see sketch fig.3.8. As expected from the typical scaling of the interchange instability, the two correlation measurements can exhibit a scaling in ρ_s, while the mesoscale trajectory can have rather different dependencies, eventually a dependence on the minor radius a. As a consequence, the correlation length would exhibit the characteristic ρ^* scaling, consistently with gyroBohm confinement scaling, while the avalanche trajectory features could depart from the ρ^* scaling and govern Bohm scaling, eventually even degraded confinement with respect to Bohm.

Let us now consider the PDF of Γ_x, fig.3.7 (black curve). First, the negative values

of the particle flux account for a significant part of the data, hence driving particles from the sink towards the source. This result is in fact consistent with the properties of $E \times B$ eddy convection that does not discriminate directions. More unexpected is the fact that the most likely particle flux is negative, on the left hand side of the zero line (vertical dash-dot line). Second, one finds a heavy tail towards the large positive values of the particle flux. Since the small magnitude events are both positive and negative with high but nearly symmetric probability density, they tend to cancel out when addressing the mean value of the radial particle flux. From that point of view, one can state that the effective particle flux (the mean value) is essentially sustained by the heavy tail part of the PDF. This property is specific of flux driven system where the only constraint on the system is to ensure a balance, on average only, between the source and the sink. Regarding the negative particle flux events, only an averaging procedure allows one to recover the thermodynamically expected sign of the particle flux. In fact the y-average is found to be sufficient for this process as exemplified by the PDF of $< \Gamma_x >_y$ on fig.3.7(b), blue histogram upper scale. Only positive values are found for $< \Gamma_x >_y$ so that the PDF can be fitted with a lognormal PDF. More importantly is the strong change in the range of the fluctuations, typically a factor 10 between the lower and upper scale. For convenience the two PDF are centered at the same location of their mean value (which is of course identical). Despite the sharp drop in the fluctuation level, this PDF still exhibits a heavy tail. Consistently with the discussion of the PDF of Γ_x, one can consider that most of the data contributing to the PDF of $< \Gamma_x >_y$ must therefore stem from avalanche-like events.

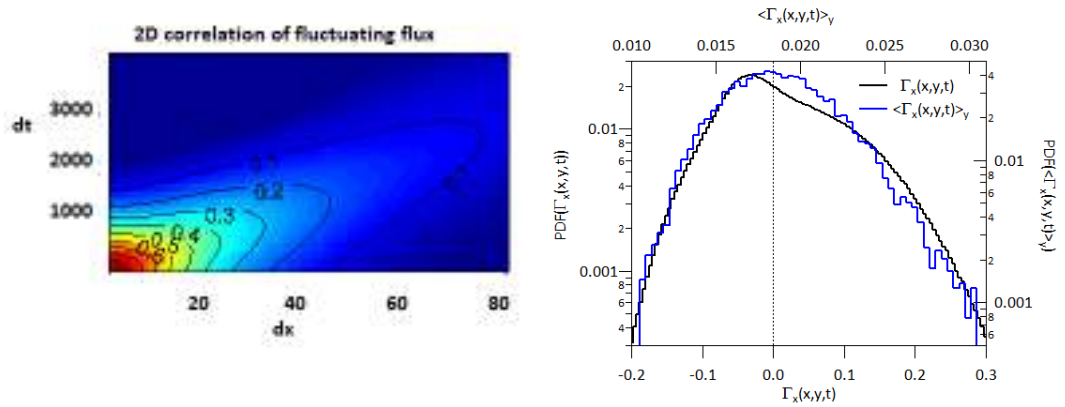

Figure 3.7: (a) 2D autocorrelation function of Γ_x, (b) PDF of the particle flux, black histogram Γ_x lower scale, blue histogram $< \Gamma_x >_y$ upper scale

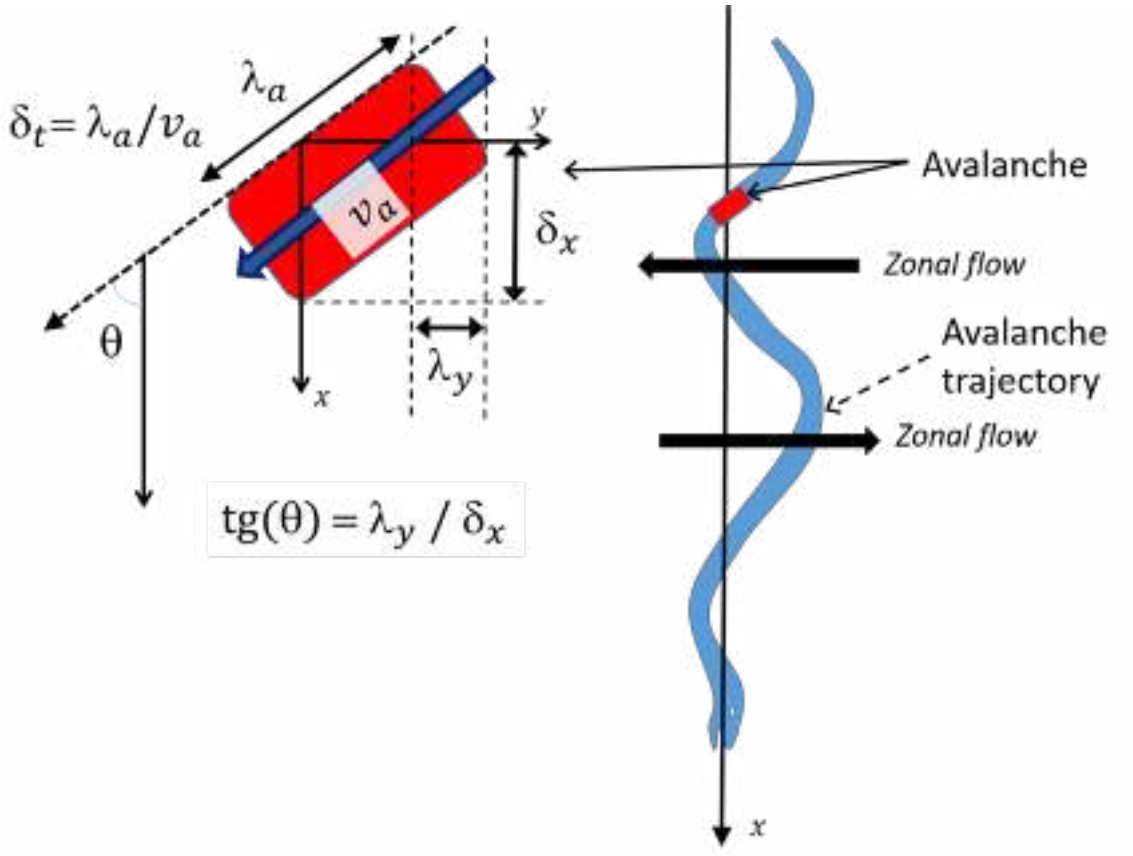

Figure 3.8: intuitive sketch of avalanche motion

3.3 Transport barriers

The transport barriers together with avalanche like transport events are clear signature of self-organization of turbulent transport. Their spontaneous generation is addressed both with GYSELA and TOKAM2D simulations. The turbulence transfers its energy via non linear coupling, Reynold Stress, (see Chapter 6) towards bigger and much more stable channels, zonal flows, where turbulent energy is stored. The key role of zonal flows as a stabilization mechanism leading to turbulent transport reduction has been proposed to improve plasma confinement[DIIH05, jKD03]. We distinguish here two different kinds of barriers: micro and macro barriers.

The micro barriers damp the transport in a weak fashion. They have been reported in core plasma simulations [DPDG$^+$10, VAB$^+$04] and observed to strongly interact with the avalanches dynamics. They are also observed to merge, and to be destroyed by a violent turbulent burst. Should the micro barrier structure scale a ρ_*, these would then ensure that the avalanche scaling would also exhibit this ρ_* scaling hence ensuring a global gyro-Bohm scaling for confinement. However, from an experimental point of view the observation of these structures is extremely challenging because of their small radial extent with respect to machine size and rich dynamics: micro barriers move radially, merge and fade away via interaction with the turbulent bursts. Recent analysis of well resolved radial correlations in Tore Supra plasmas appear to have been reported very recently by [DPHG$^+$15], here provided the first experimental evidence of such barriers.

A second class of transport barrier are reported in magnetic fusion experiments, the macro barriers. They are characterized by the development of very strong gradients. In the core plasma they are referred to as Internal Transport Barriers (ITB) [CFG$^+$04], while at the interface between open and closed field lines they are called External Transport Barriers (ETB) and are associated to H-mode confinement, [Wag07, CFG$^+$04]. The latter case is considered as the reference scenario for ITER [SCM$^+$07]. These barriers strongly damp turbulent transport. For the ETB, it causes the formation of a characteristic pedestal at the separatrix.

A strong difference between the macro and micro barriers is on the way the two kinds of barriers relax.

- Regarding macro barriers, the self-consistent generation and sustainment is still a matter of strong scientific debate. We have addressed this issue, Chapter 7. However, to study the dynamics between the turbulence and the barriers, artificial barriers can be triggered either by imposing an artificial shear flow, as shown in fig.3.9(a) [BBFC$^+$07] or by suppressing the turbulence [FCG$^+$13]. Beyer et al. have shown that artificial macro barriers quench the turbulence and then relax in a quasi periodic fashion. Consequently, the pedestal formed at the shear position relax (fig.3.9-(b)), and the temperature gradient drops (fig.3.9-(b)). This dynamics can be captured via a predator prey model: (1) the transport barriers are fed by the turbulence via Reynold stress, (2) consequently turbulence is quenched by the TB; (3) hence the TB can no more pump the energy from the turbulence and the TB eventually relaxes. Such relaxation dynamic is reminiscent of the ELMs (Energetic Localized Mode) [2]. Two possible damping mechanism control the relaxation: collisions or KH instability.

[2] For the ELMS case the role of magnetic field perturbation has to be taken into account.

The relation between collisionality and ELMs has been reported experimentally be Loarte[LSS+03]. The role of KH, a tertiary instability driven by the shear is less clear [DIIH05]. Very promising experimental results have shown that ELM-free regimes can be accessed during the H-mode confinement[SMC+03]. However, a consistent theory able to explain and predict the barriers self-organization and consequently ELM control is still lacking.

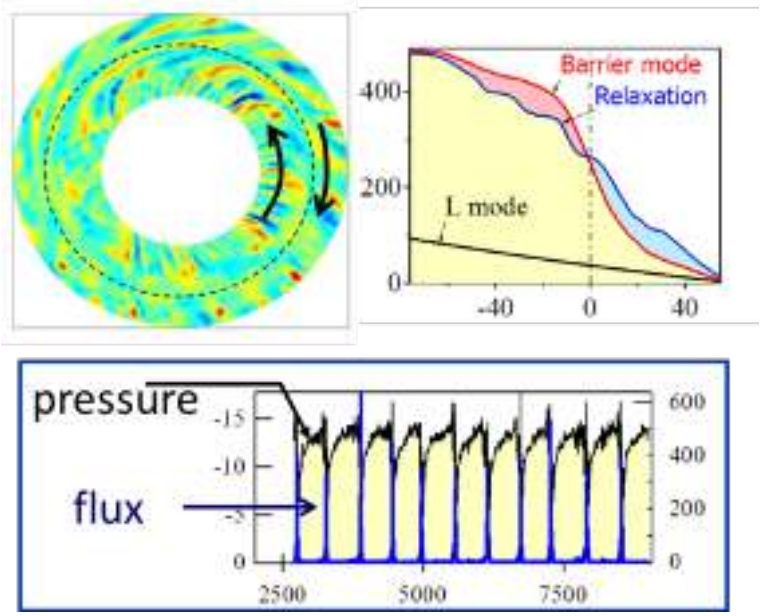

Figure 3.9: (a) artificial shear effect on the potential fluctuations (b) pressure profile during the barrier mode (red line) and relaxation (blue line), (c) quasi periodic transport barrier generation and relaxation: when the barrier relaxes the turbulent flux increases. Pictures from P. Beyer [BBFC+07]

- Micro barrier regimes have been observed in global ITG gyrokinetic simulation, where ExB shear flows self-organize in quasi regular patterns, as shown on fig.3.10(a). To identify the stopping capability of the micro-barriers, one can analyze the heat flux through the barrier, splitting it into the convective contribution dominated by the drift velocity v_x, $Q_{turb} = v_x T$ and the diffusive contribution $Q_{neo} = \chi_\perp \nabla_\perp T$, averaged along the flux surface in order to reduce the fluctuation range. The criterion R_b is then defined as the ratio of the surface averaged turbulent flux and the total flux, namely $R_b = Q_{turb}/Q_{tot}$ with $Q_{tot} = Q_{turb} + Q_{neo}$. One identifies two limits, the turbulent transport regime, $R_b \to 1$, and the quenched turbulence regime, $R_b \to 0$, where transport is neoclassical, i.e. via collisions, as shown in fig.3.10(c). Following R_b in time, one can observe that the turbulence is quenched at high values of the ExB shear, see fig.3.10(d). Furthermore no strong relaxation event is observed. Micro-barrier regimes appear favorable for the transport control, because turbulence is reduced by a series of barriers, hence with a distributed volumetric effect. Furthermore the relaxation events do not seem to effect all the barriers at a time so that a change in transport is moderate.

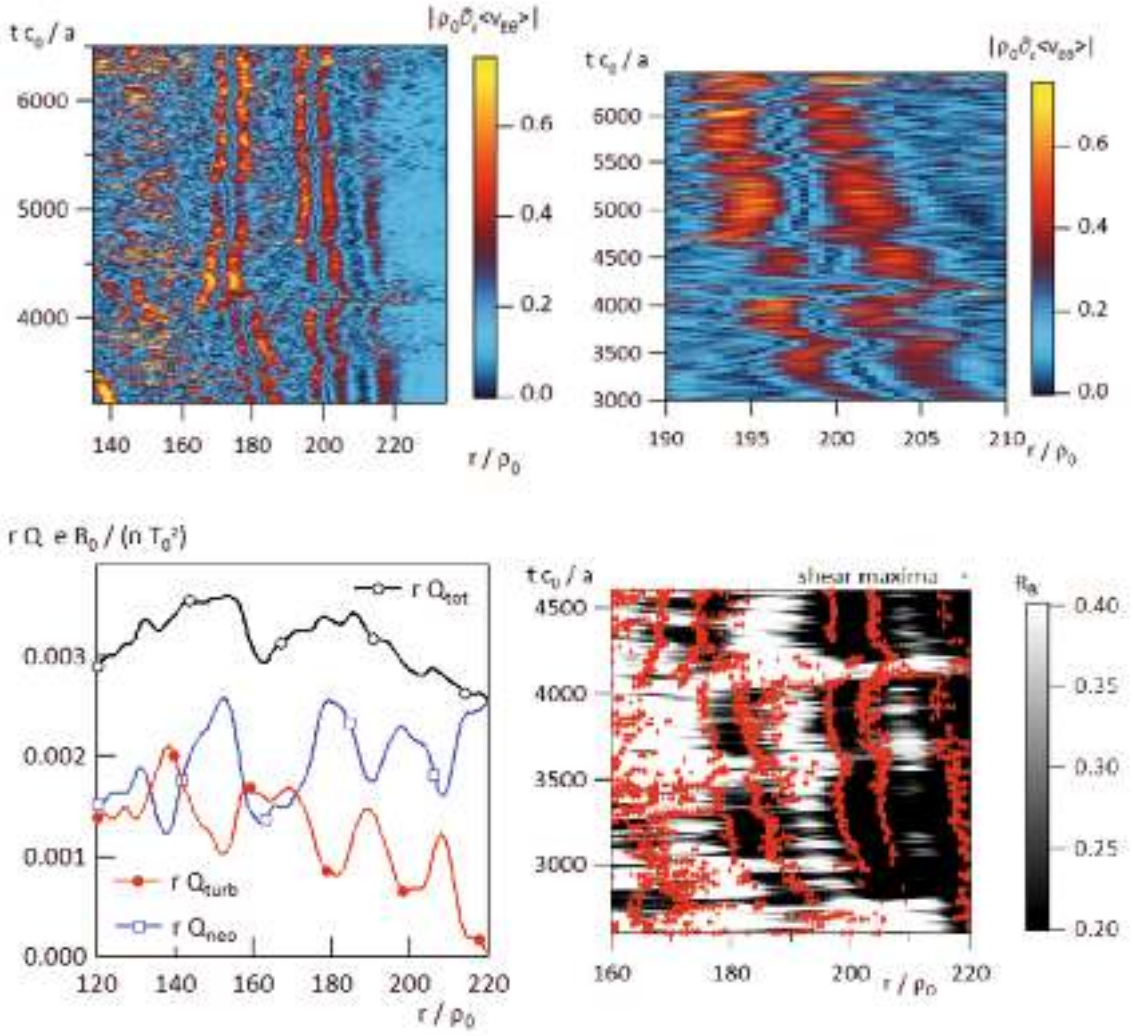

Figure 3.10: (a) the $E \times B$ shear distribution in time and radial direction (b) a zoom on a $E \times B$ staircase, the radial interval upstream this barrier is define as Δr_u, (c) the profile of turbulent Q_{turb}, neoclassical Q_{neo} and total Q_{tot} heat flux (d) R_b distribution in time and radial direction with the maxima of ExB shear superimposed (red lines)

Chapter 4

Non local transport properties of the SOL

Contents

We focus here on SOL physics characterized by large fluctuation levels in the range of 100%. The role of sources and boundary conditions (BC) is addressed in order to identify the non local properties of SOL transport. The concept of SOL width is questioned given the known properties of turbulence.

4.0.1 Definition of SOL width

The SOL transport governs the energy load on the first wall and defines the peak power density at the divertor plates. In that respect determining the exponential power fall-off length, λ_q, in the radial direction would be a crucial input. To define λ_q we consider the Bohm boundary conditions. The parallel heat flux at the divertor $q_{\|} \propto nT^{3/2}$, therefore $1/\lambda_q = -\partial_r q/q$ can be defined as

$$\lambda_q^{-1} = -\frac{n}{\partial_r n} - \frac{3}{2}\frac{T}{\partial_r T} = \lambda_n^{-1} + 3/2\lambda_T^{-1}. \tag{4.1}$$

λ_q can then be determined given the typical SOL widths for the density λ_n and temperature λ_T profiles. When assuming that the particle density and temperature profiles are described by an exponential fall-off, i.e. $f = f_0 e^{-x/L_f}$, λ_f^{-1} can be defined as $\lambda_f^{-1} = -\partial_r f/f = L_f^{-1}$, where $f = n, T$.

The SOL width is thus governed by the SOL transport. Furthermore, the standard definition is consistent with the concept of profiles, hence mean fields with only radial dependence, and its definition is still matter of discussion. In the TOKAM2D case, the temperature is assumed constant in the model, hence only λ_n can be defined. The density SOL width λ_n overestimates λ_q, $\lambda_q < \lambda_n$. The purpose of this work is then to investigate the typical transport features of the SOL and that are the main contribution to the physics.

In this chapter the definition of λ_n in a fluctuating media and the consequences on λ_q predictions are examined.

4.1 Breackdown of the Quasilinear theory in the SOL

The quasilinear (QL) theory describes with describing the slow evolution of $< f >$, taking in account the fluctuations feedback, $\tilde{f}$, via an effective diffusion like term. QL theory is, in some sense, the simplest possible theory of plasma turbulence and the methodology is broadly applied. In this section we are going to identify:

- **the key assumptions** that pave the way towards determining an effective diffusive transport;
- the issues related to **QL theory in the SOL transport** description, where the QL key assumptions are questioned.

To address the QL theory[1], a generic transport equation, akin to the particle balance equation of TOKAM2D, is used:

$$\frac{\partial f}{\partial \tau} + \big[\phi, f\big] - D\Delta f = -\sigma f \tag{4.2}$$

[1]In the Annex B a more detailed version of quasi linear theory is presented

For the sake of simplicity we consider 2D turbulent transport in the plane transverse to the magnetic field, the parallel transport being taken into account via the small loss term proportional to σ. The equation is normalised, time to $1/\Omega_i$, transverse scale to ρ_s and the potential to T_e/e so that the diffusion coefficient is normalised by the Bohm diffusion coefficient $D_B = \rho_s^2\Omega_i$. The equation is homogeneous in f so that the normalisation of f is arbitrary.

Average procedure. In a first step one assumes that f can be split into a mean and fluctuating part, $f = \bar{f} + \tilde{f}$. It leads to two coupled equations replacing (4.2).

$$\frac{\partial \bar{f}}{\partial \tau} + [\bar{\phi}, \bar{f}\,] + \Big\langle [\tilde{\phi}, \tilde{f}\,] \Big\rangle - D\Delta\bar{f} = -\sigma\bar{f} \tag{4.3a}$$

$$\frac{\partial \tilde{f}}{\partial \tau} + [\bar{\phi}, \tilde{f}\,] + [\tilde{\phi}, \bar{f}\,] + [\tilde{\phi}, \tilde{f}\,] - \Big\langle [\tilde{\phi}, \tilde{f}\,] \Big\rangle - D\Delta\tilde{f} = -\sigma\tilde{f} \tag{4.3b}$$

Ordering of the fluctuations. We introduce the parameter $\varepsilon = \tilde{f}|/|\bar{f}|$ where the symbol $|f|$ is an appropriate norm allowing one to characterise the magnitude of the fluctuations with respect to the mean. It is usually assumed that ε is small, however, in the SOL, one observes in the experiments [Zwe89, GHP+06], as well as in our simulations (see Section 3.2) that ε is of order one. Introducing ε in (4.3) to characterise the magnitude of all the fluctuating terms with respect to the mean terms, one obtains:

$$\frac{\partial \bar{f}}{\partial \tau} + [\bar{\phi}, \bar{f}\,] + \varepsilon^2\Big\langle [\tilde{\phi}, \tilde{f}\,] \Big\rangle - D\Delta\bar{f} = -\sigma\bar{f} \tag{4.4a}$$

$$\varepsilon\frac{\partial \tilde{f}}{\partial \tau} + \varepsilon[\bar{\phi}, \tilde{f}\,] + \varepsilon[\tilde{\phi}, \bar{f}\,] + \varepsilon^2[\tilde{\phi}, \tilde{f}\,] - \varepsilon^2\Big\langle [\tilde{\phi}, \tilde{f}\,] \Big\rangle - \varepsilon D\Delta\tilde{f} = -\varepsilon\sigma\tilde{f} \tag{4.4b}$$

Multiscale and averaging We now define the averaging process as an average over the high frequency variables, namely t, x, y, so that the mean fields only depend on T, X, Y, where τ_t is the relevant time scale of turbulent fluctuations $\tau_t = a/c_s$, hence $\rho_* = 1/(\Omega_i\tau_t)$ and τ_T is the relevant time scale of the diffusive transport.

In order to complete this ordering, one must determine the appropriate scaling properties of the diffusion coefficient D and of the parallel loss term σ. Regarding $\sigma = 1/(\Omega_i\tau_f)$ where τ_f is the characteristic life-time, one thus obtains:

$$\sigma = \frac{1}{\Omega_i\tau_f} = \frac{a}{\tau_f c_s}\rho_* \tag{4.5a}$$

$$D = \nu_D\rho_*^\alpha D_c \tag{4.5b}$$

Since the diffusion coefficient D is normalised by the Bohm diffusion coefficient D_B, $\alpha = 0$ corresponds to a Bohm-like diffusive transport while $\alpha = 1$ will lead to a gyro-Bohm like diffusive contribution to the transport. The parameter ν_D takes into account the smallness of the diffusive transport process. For collisional diffusion one has $\nu_D = \nu_*$ and $\alpha = 1$. Since $\tau_t = a/c_s$ as determined by the turbulence growth rate, the mean transport equation takes the form:

$$\begin{aligned}\frac{\partial \bar{f}}{\partial T} + \frac{\varepsilon^2}{\tau_t/\tau_T}\Big(- \partial_X\Big\langle \tilde{f}\,\partial_y\tilde{\phi}\Big\rangle + \partial_Y\Big\langle \tilde{f}\,\partial_x\tilde{\phi}\Big\rangle\Big) \\ + \frac{\rho_*}{\tau_t/\tau_T}\Big(- \partial_X\Big(\bar{f}\,\partial_Y\bar{\phi}\Big) + \partial_Y\Big(\bar{f}\,\partial_X\bar{\phi}\Big)\Big) \\ - \frac{\nu_D\rho_*^{1+\alpha}}{\tau_t/\tau_T}\,D_c\Delta_{X,Y}\bar{f} = -\frac{\tau_t/\tau_f}{\tau_t/\tau_T}\bar{f}\end{aligned} \tag{4.6}$$

One can then identify two transport regimes:

1. **Small fluctuations:** $\varepsilon^2 \ll \rho_* \ll 1$, so that one can set $\tau_t/\tau_T = \rho_*$, and consequently:

$$\frac{\partial \bar{f}}{\partial T} - \partial_X\Big(\bar{f}\partial_Y\bar{\phi}\Big) + \partial_Y\Big(\bar{f}\partial_X\bar{\phi}\Big) - \nu_D\rho_*^{\alpha}\ D_c\Delta_{X,Y}\bar{f} = -\frac{\tau_t/\tau_f}{\rho_*}\bar{f} \tag{4.7}$$

   In this regime the mean fields are decoupled from the fluctuations. The characteristic time scale of the parallel transport τ_f must be large enough, $\tau_T \leq \tau_f$, so that the transverse transport is adiabatic with respect to the parallel transport.

2. **Large fluctuations:** $\rho_*^{1/2} \ll \varepsilon$ so that one can set $\tau_t/\tau_T = \varepsilon^2$. The order one mean transport equation is then:

$$\frac{\partial \bar{f}}{\partial T} - \partial_X\Big\langle\tilde{f}\partial_y\tilde{\phi}\Big\rangle + \partial_Y\Big\langle\tilde{f}\partial_x\tilde{\phi}\Big\rangle - \frac{\nu_D\rho_*^{1+\alpha}}{\varepsilon^2}\ D_c\Delta_{X,Y}\bar{f} = -\frac{\tau_t/\tau_f}{\varepsilon^2}\bar{f} \tag{4.8}$$

   with the same condition on τ_f, $\tau_T \leq \tau_f$. In this regime, the mean field convective transport is governed by the coherent interferences between the fluctuations of f and of the electric drift velocities.

3. **Order one fluctuation transport:** $\varepsilon^2 = 1$. This case is in the same regime than defined by the previous item, however the condition $\tau_t/\tau_T = 1$ means that one cannot make a separation between turbulent and transport time scales $t \equiv T$. The lowest order mean transport equation then takes the form:

$$\frac{\partial \bar{f}}{\partial t} - \ \partial_X\Big\langle\tilde{f}\ \partial_y\tilde{\phi}\Big\rangle + \ \partial_Y\Big\langle\tilde{f}\ \partial_x\tilde{\phi}\Big\rangle - \nu_D\rho_*^{1+\alpha}\ D_c\Delta_{X,Y}\bar{f} = -\frac{\tau_t}{\tau_f}\bar{f} \tag{4.9}$$

Quasilinear framework, small amplitude fluctuations. Within the quasilinear framework, one neglects the quadratic terms with respect to the fluctuations. One thus requires that $\varepsilon \ll \rho_*$. Furthermore, to avoid issues regarding the ordering of the diffusive transport we shall assume that $\alpha = 1$, namely that the diffusion is gyro-Bohm. At lowest order one then obtains:

$$\frac{\partial \tilde{f}}{\partial t} + \partial_X\bar{\phi}\partial_y\tilde{f} - \partial_Y\bar{\phi}\partial_x\tilde{f} + \partial_x\tilde{\phi}\partial_Y\bar{f} - \partial_y\tilde{\phi}\partial_X\bar{f} - \nu_D D_c\Delta_{x,y}\tilde{f} = -\frac{\tau_t}{\tau_f}\tilde{f} \tag{4.10}$$

which is by construction linear with respect to the fluctuations and can therefore conveniently be Fourier expanded with respect to the high frequency variables, with no mode coupling. One can then determine $\tilde{f}$ in terms of $\tilde{\phi}$.

$$\hat{f}_{\omega,k_x,k_y} = -\frac{k_y\partial_X\bar{f} - k_x\partial_Y\bar{f}}{\omega + k_x\bar{V}_{Ex} + k_y\bar{V}_{Ey} + i\Big(\nu_D D_c k^2 + \frac{\tau_t}{\tau_f}\Big)}\hat{\phi}_{\omega,k_x,k_y} \tag{4.11}$$

In this expression we have introduced the following notations: $k^2 = k_x^2 + k_y^2$ and $\bar{V}_{Ex} = -\partial_Y\bar{\phi}$, $\bar{V}_{Ey} = \partial_X\bar{\phi}$ so that $k_x\bar{V}_{Ex} + k_y\bar{V}_{Ey} = \boldsymbol{k}\cdot\bar{\boldsymbol{V}}_E$ and therefore:

$$\hat{f}_{\omega,k_x,k_y} = -\frac{\omega + \boldsymbol{k}\cdot\bar{\boldsymbol{V}}_E - i\ \eta}{\big(\omega + \boldsymbol{k}\cdot\bar{\boldsymbol{V}}_E\big)^2 + \eta^2}\Big(k_y\partial_X\bar{f} - k_x\partial_Y\bar{f}\Big)\hat{\phi}_{\omega,k_x,k_y} \tag{4.12}$$

with $\eta = \nu_D D_c k^2 + \tau_t/\tau_f$.

One then find the quasilinear expression of the fluxes:

$$\mathbf{\Gamma} = \mathbb{D}_{QL} \cdot \boldsymbol{\nabla} \bar{f} \tag{4.13}$$

$$\mathbb{D}_{QL} = \sum_{\omega,k_x,k_y} |\hat{\phi}_{\omega,k_x,k_y}|^2 \, \frac{\eta}{\left(\omega + \boldsymbol{k} \cdot \bar{\boldsymbol{V}}_E\right)^2 + \eta^2} \begin{pmatrix} k_y^2 & -k_x k_y \\ -k_x k_y & k_x^2 \end{pmatrix} \tag{4.14}$$

The mean field evolution equation is then:

$$\frac{\partial \bar{f}}{\partial T} - \boldsymbol{\nabla} \cdot \left(\mathbb{D}_{QL} \cdot \boldsymbol{\nabla} \bar{f} \right) = -\frac{\tau_t/\tau_f}{\varepsilon^2} \bar{f} \tag{4.15}$$

Given the evolution with T the diffusion coefficient is normalised by $\rho_* D_B$ and is therefore gyro-Bohm.

One finds that for the SOL case, such that $\tau_f = \tau_t$, one must have ε of order 1, hence very large fluctuations which contradicts the quasilinear assumption regarding the quadratic contribution to the fluctuation evolution. Conversely, if the fluctuations are small, one must ensure that $\tau_t \ll \tau_f$, hence adiabatic transverse transport with respect to a slow parallel transport contribution.

Consequently: in the SOL case, one cannot apply a scale separation between fluctuations and mean profile, the QL theory is not valid.

4.2 The role of source and boundary conditions in SOL modeling

Different approaches can be used to drive the system out of equilibrium. We present here the sources and boundary conditions implemented in TOKAM2D used to study if turbulent transport in the SOL depends on them.

Two main approaches can be distinguished to model the turbulence: flux driven (FD) and gradient driven (GD) approach, already introduced in Session 2.2.3.

In the FD the turbulence is driven via a localized particle source that builds-up the steady state profile. In this FD case, no constraint or assumption is made on the mean profile.

The GD approach is a simplified version used to model the turbulence transport based on the assumption that, the mean profile evolution time is much slower compared to the characteristic fluctuations time see Section 4.1. This assumption requires the possibility of scale separation to model turbulence. Only the fluctuating terms are studied while the mean profile is considered to be constant. The advantages of this approach are:

- **Comparison between GD models and experiments** is more straightforward. Since the profiles extracted from the experimental measurements can be applied as input of GD simulation.

- **Turbulent time scale.** A GD system is assumed in steady state condition with respect to the mean field, reducing the computation times. The characteristic time needed to reach the confinement in FD simulations scale that is relevant in these simulations is that of turbulence.

Conversely, the drawback is that the key assumption of scale separation in the GD approach, however convenient, must be carefully assessed. Furthermore, considering the results obtained with the QL theory, in the previous section, one can consider that such a framework cannot hold for SOL physics.

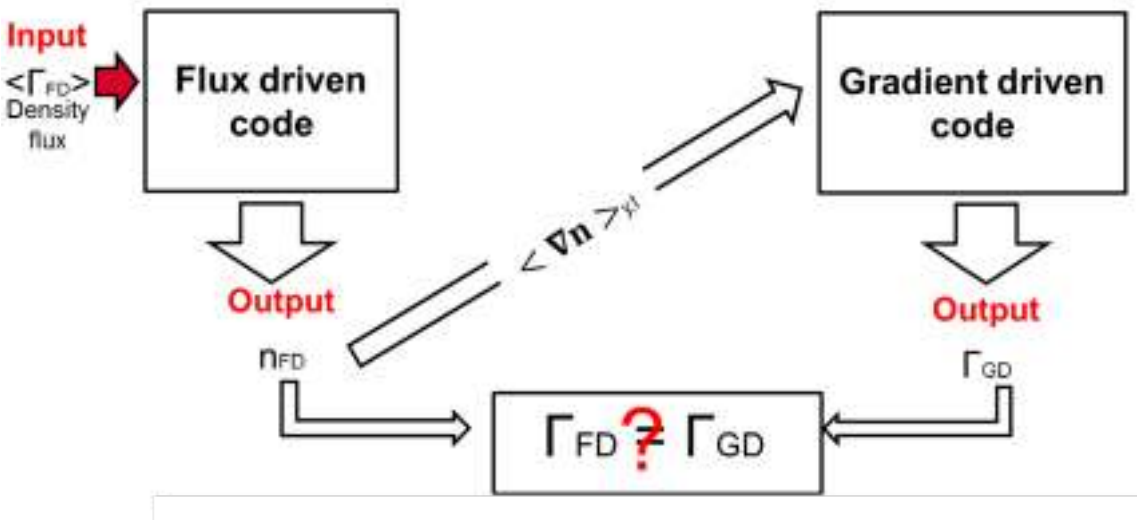

Figure 4.1: Computation procedure to compare FD and GD simulations

To compare the two approaches, we decide to follow the same process as applied to the comparison between experimental and numerical results. Namely one takes the steady state experimental density profile as input for the simulation in order to compare the flux produced by the two and benchmark the code. In this specific case we are supposing that the flux driven simulation will be compared to the fixed gradient one with the same approach, namely we run long FD simulation in order to define a steady state condition, then we calculate the mean density profile averaged in time and poloidal direction to smooth out the fluctuations. Such profiles or gradients of such profiles are the control parameters for GD simulations with zero source term, fig.4.1

4.2.1 FD: Source and periodic boundary condition

The equation solved in the FD approach, presented in Session 2.3.1, are here reintroduced.

$$\partial_t n + [\phi, n] = D_\perp \Delta_\perp n - \Gamma + S \tag{4.16}$$

$$\partial_t W + [\phi, W] + g\frac{\partial_y n}{n} = \nu_\perp \Delta_\perp W + j \tag{4.17}$$

where:

$$W = \nabla^2_\perp \phi \tag{4.18}$$

The source is localized at the origin $x = 0$ and is homogeneous in y. The boundary conditions are periodic. The typical mean density profile produced by the FD simulations is shown in fig.4.2.

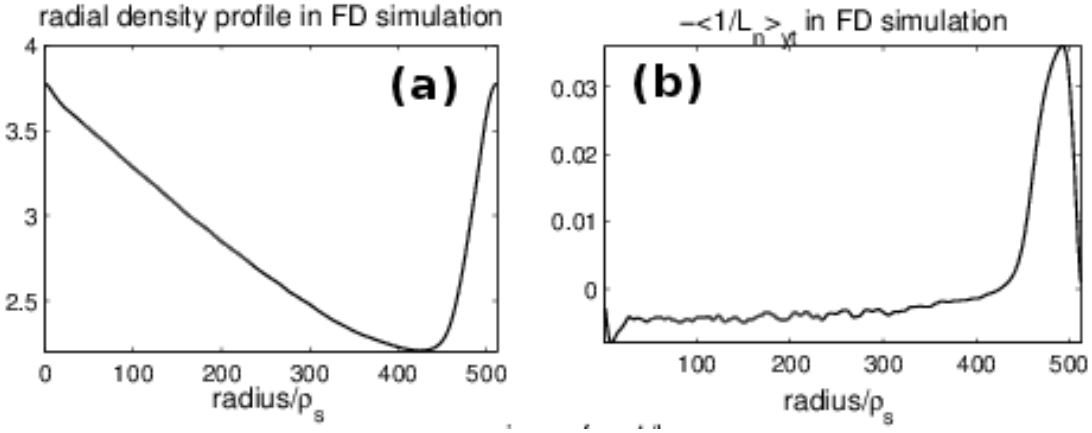

Figure 4.2: (a) mean density profile, (b) $< 1/L_n >_t$ in FD simulation of the SOL

In the FD case, the turbulent transport in the SOL is governed by avalanches. The analysis of the avalanches presented in the previous chapter has been achieved in FD TOKAM2D simulations.

4.2.2 GD: Profile driven and flux tube conditions

The gradient driven definition is often unclear. We present here two different kinds of approach: *profile driven* and *flux tube*.

Profile driven

In the profile driven (PD) case, a constant mean profile is defined as initial profile and enforced throughout the simulation. Different ways can be used to constrain the profile, either (1) removing the fluctuations feedback or (2) using a restoring term such as a Krook term [MJT+08]. We present here the modification made in the TOKAM2D equations to switch from FD to PD by removing the fluctuations feedback on the mean field.

In order to show how the model is modified from the flux driven to the gradient driven version, we first need to separate TOKAM2D equations in equilibrium and fluctuation equations. As in the previous section the fields are split into mean field and fluctuating field, namely $\bar{f} =< f >_y$ and $\tilde{f} = f - \bar{f}$. We further assume $< \Phi >_y$ is constant in time and radial direction and equal to $\bar{\Phi} = \Lambda$ and $< n >_y$ is constant in time and decreasing exponentially in the radial direction with an e-folding length equal to $1/L_n$.

Rewriting the TOKAM2D equations for the FD version averaged in the poloidal direction to define $\bar{\phi}$ and $\bar{n}$, one recovers the two following equations:

$$\partial_t \bar{n} + \left\langle \left[\tilde{\phi}, \tilde{n}\right] \right\rangle - D_\perp \Delta_\perp \bar{n} - \sigma_n \bar{n} = 0 \tag{4.19}$$

$$\partial_t \bar{W} + \left\langle [\tilde{\phi}, \tilde{W}] \right\rangle - \nu_\perp \Delta_\perp \bar{W} + \sigma_\phi \bar{J} = 0 \tag{4.20}$$

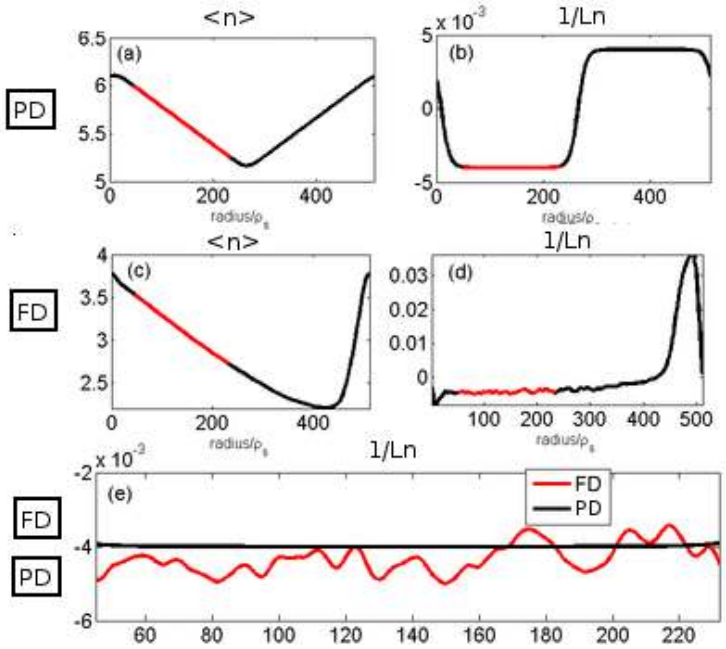

Figure 4.3: Density profile for GD (a) and FD case (c) $< 1/L_n >_t$ profile for GD (b) and FD case (d), (e) comparison between $1/L_n$ profiles for FD (red line) and GD (black line) simulation

One can readily observe that removing the poloidally averaged Poisson brackets term $\left\langle \left[\tilde{\phi}, \tilde{n}\right] \right\rangle$ from the first equation, one decouples the evolution of the mean density from that of the fluctuations. Furthermore defining the source term $\bar{S}$ such that:

$$-D_\perp \Delta_\perp \bar{n} - \sigma_n \bar{n} = \bar{S}(\bar{n}) \tag{4.21}$$

then the mean density field is a steady state of:

$$\partial_t \bar{n} - D_\perp \Delta_\perp \bar{n} - \sigma_n \bar{n} = \bar{S}(\bar{n}) \tag{4.22}$$

Modifying the density field equation in TOKAM2D to:

$$\partial_t \bar{n} + [\phi, n] - < [\phi, n] > -D_\perp \Delta_\perp \bar{n} - \sigma_n \bar{n} = \bar{S}(\bar{n}) \tag{4.23}$$

then allows the evolution of the full electric potential while the mean density field remains constant. Therefore, in the PD case, the density gradient profile set by the user will be constant during the simulation.

For this case we here define the density profile analytically. Using two hyperbolic tangent functions, we define the widths of unstable and stable regions as well the slope of the density field. As shown in fig.4.3, the value of L_n is chosen according to the results achieved by FD simulations.

Macroscopically, we recover similar results, namely in both case we obtain an avalanche like transport. However, we can observe that the turbulent flux structures do not have the same resilience in time and space, see fig.4.4(a)-(b). As introduceD before (Section

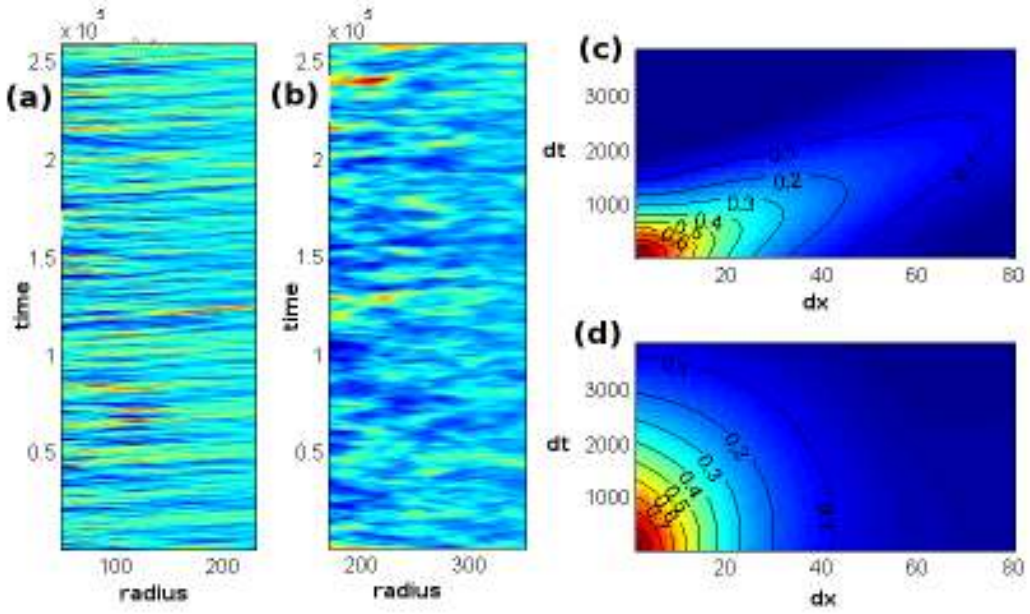

Figure 4.4: (a)$< \Gamma >_{y,t}$ in function of radius and time for the FD case, (b) for the GD case and the 2d correlation function of Γ for FD (c) and GD case (d)

3.2.2) in the definition on the typical scales in SOL region, a powerful tools to identify coherent structures is based on autocorrelation function. The result, that we can observe in fig.4.4(c)-(d), is characterized by clear differences in the pattern reorganization between the two models. In the GD case, the structures tend to last on longer time intervals, conversely they exhibit a more homogeneous structure compared to the FD case. One can identify that the characteristic velocity of such turbulent patterns in the radial direction is decreased by a factor 2 in the PD case, i.e $v_{FD} = 0.02c_s$ and $v_{GD} = 0.01c_s$.

Additionally, we can compare the density fluctuations via the PDF distribution at different radial positions for the two approaches, see fig.4.5. In both cases, we can observe a long tail on the positive side of the PDF that represents a signature of avalanche like intermittent behavior. Such long tails become more dominant far from the source. The skewness (measure of the asymmetry of the PDF) is reduced in the gradient driven case. This suggests a reduction of the ballistic transport when feedback loop of fluctuations of the mean density profile is removed. To conclude, on the one hand, the characteristic inhomogeneous turbulence distribution appears also in the PD case, on the other hand the effect of avalanche is underestimated with respect to the FD case.

Flux tube case

In the flux tube case, the profile is constrained by assuming that the density gradient is fixed not only in time but also in space. Namely we fix $1/L_n$ to a scalar value.

While this model should only solve the fluctuations fields, it is in practice generalized to the complete field. However the source is a volumetric term that corresponds to the Poisson bracket $[\phi, -\frac{x}{L_n} n_0]$. We rewrite then the TOKAM2D equations of density and

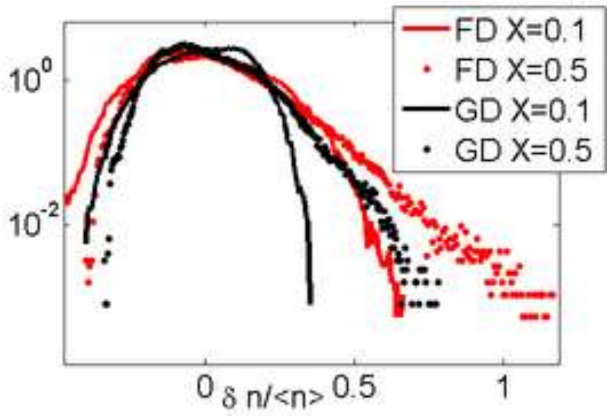

Figure 4.5: the PDFs of density fluctuations for FD (red) and GD (black) at $r/a = 0.1$ (line) and $r/a = 0.5$ (dots)

potential in function of $\tilde{f}$, where $f = n, \phi$. The equations solved by the code are then:

$$\partial_t n + [\phi, n] + [\phi, \bar{n}] = D_\perp \Delta_\perp n - \sigma_n n + \sigma_n \phi \tag{4.24}$$

$$\partial_t W + [\phi, W] = -g\frac{\partial_y n}{n_0} + \nu_\perp \Delta_\perp W + \sigma_\phi \phi. \tag{4.25}$$

given $\bar{n} = n_0(-x/L_n)$.

This approach is named flux tube, because it models the transport inside a small tube aligned with the magnetic field lines, where the gradient is considered constant and periodic BCs are imposed. This approach is then based on local assumption: namely that microturbulence only impacts locally the transport and not on macroscopic scales. The flux tube adds a further advantage to the FD approach since it introduces periodic boundary conditions in the radial direction and also more homogeneous radial properties due to the volumetric source. The setting is then particularly well suited for pseudo-spectral codes which also considerably simplifies the numerical solution of the Poisson equation $W = \Delta\phi$

4.3 Approaches to define the SOL transport

As observed in the previous chapter (Section 3.2.1), the SOL transport is governed by avalanches and the fluctuations effects are a constitutive features of the SOL concept. We have developed different approaches to reduce the SOL transport to macroscopic diffusion coefficient that would be consistent with the Fick and Fourier laws.

4.3.1 The modulation approach

With TOKAM2D, a source modulation has been used to quantify the turbulent transport. Experimental works have shown that the response of the turbulence to source modulation favor the identification of large scale transport parameters. The modulated source is localised in the same region as the main source, it is also constant along the y-direction and narrower in the x-direction, hence yielding a broad k_x spectrum. With the chosen value of the magnitude of the modulated source one identifies very well the density response at the source frequency ω_s, fig.4.6(a) [GNH+12]. One can then consider the transport equation

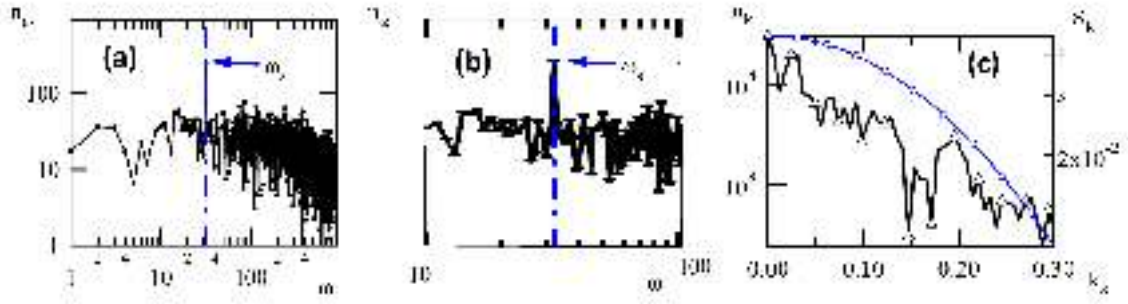

Figure 4.6: (a) the frequency spectrum for the density, (b) zoom of the frequency spectrum and (c) the ratio between source and density k_x spectrum

in Fourier space:

$$\sigma_n - i\omega_s + (D_{eff}k_x^2 + iV_{eff}k_x) = \frac{\hat{S}}{\hat{n}} \tag{4.26}$$

where we have assumed the macroscopic, or effective, transport to be of the standard form, $\Gamma = -D_{eff}\nabla_x n + V_{eff}n$. In such a framework the real part of the ratio $\hat{S}/\hat{n}$ should be a quadratic function of k_x while the imaginary part should be linear [2]. The frequency ω_s must be small enough to allow the transport wave to propagate from the source to a sufficiently large distance, but not that small that it only drives an adiabatic response of the system at quasiconstant profile but slowly varying particle content. A value comparable to σ_n thus appears to be optimum. At any rate, as exemplified on fig.4.6(a)-(b), it is not possible to find a frequency outside the broad range of the turbulence spectrum, since there is no obvious time separation between turbulence and transport. No correlation between the source and density k_x-spectra has been observed, see fig.4.6(c). In particular, a signature of diffusive transport would govern a quadratic shape of n_k for the small values of k, which is clearly not the case on fig.4.6(c), where the density spectrum is more exponential like.

4.3.2 Steady state versus fluctuating SOL

As shown in Session 3.1, a coarse graining approach with flux surface averages and long time averaging is required to determine large scale transport D_{eff} with an appropriate behavior. Furthermore, describing the large scale transport with D_{eff} reduced to a single value would require further coarse graining in the radial direction. Another possible transport law can be considered by combining a diffusion D_{incr} and a pinch velocity V, see Section 3.1.

$$\frac{< \Gamma_{turb} >_{t,y}}{\bar{n}} = -D_{incr}\frac{1}{L_n} + V \tag{4.27}$$

From fig.(4.7) one can define three different regions, already introduced in ref.[NGCM+14]

- **Flat top region**, namely region I, localized immediately after the source, in this region the flux is maximum and close to constant. In region I macroscopic transport is predominantly convective

[2] This procedure has been verified via a one dimensional code [HRG+15] where the transport is simply defined by a convection and diffusion term, where the exact values of V_{eff} and D_{eff} are recovered.

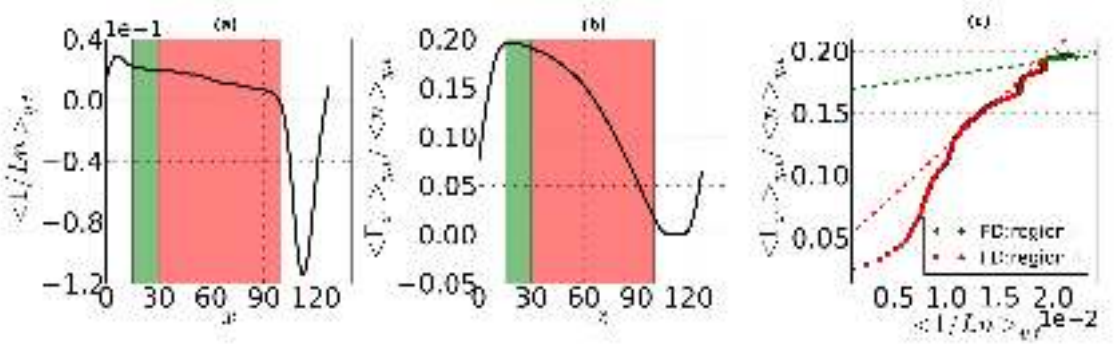

Figure 4.7: (a) Radial profiles of $< 1/L_n >_t$, (b) $< \Gamma >_{t,y} / < n >_{t,y}$ in radial direction, (c)$< \Gamma >_{t,y} / < n >_{t,y}$ in function of $< 1/L_n >_t$, the dashed lines identify two different regions,The turbulent flux Γ is normalized by $N_x/(2\pi)$ with $N_x = 128$

- **Main SOL**. Region II connects the first turbulent region to the stable last region. The flux starts decaying proportionally to $-1/L_n$.
- **Stable region**. Region III is necessary to maintain periodic profiles, the gradient of density is positive, turbulence stable and transport governed by the diffusion terms. This region does not have a physical relevance for SOL transport.

One can identify the incremental transport coefficients, in region I from $ix_1 = 15$ to $ix_2 = 30$, width $d_I = 15$, $D_I \approx 0.076$ and the outward pinch velocity $V_I \approx 0.008$, while in region II from ix_2 to $ix_3 = 80$, width $d_{II} = 50$, $D_{II} \approx 0.44$ and the outward pinch velocity is $V_{II} \approx 0.001$. Here the radial units are units of ρ_s, the pinch velocity in units of c_s, corresponding therefore to Mach numbers, and the diffusion coefficients are normalized to the Bohm diffusion coefficient, i.e. $\rho_s c_s$. The ratio $D/(dV)$ allows one to determine the dominant transport mechanism (since both act in the same direction). Hence, in region I, $D_I/(d_I V_I) \approx 0.625$ while in region II $D_{II}/(d_{II} V_{II}) \approx 8.8$; in the first region transport is governed by convection while in the second one the transport appears predominantly diffusive.

4.4 The issues of a fluctuating SOL

However via such a coarse graining procedure, the information retrieved through this approach can appear misleading. A difference should be made between steady SOL and a fluctuating SOL. If we define the SOL width as the radial distance such that $\Gamma(r_{SOL}) =< Gamma >_{max} /e$ and compare λ_{SOL} and $< \lambda_{SOL} >$ clear differences appear. Namely the value of $< \lambda_{SOL} >$ is approximately close to $15\rho_s$, however SOL width can actually oscillate from 0 to $60\rho_s$, hence four time the averaged calculated value, as shown in fig.4.8(a)-(b).

Three main issues can be identified with the definition of the SOL width based on the coarse grained profile:

- **Heat transport.** One can conclude that for an actively cooled component like the ITER divertor with time constant of about 5 seconds, the mean SOL width

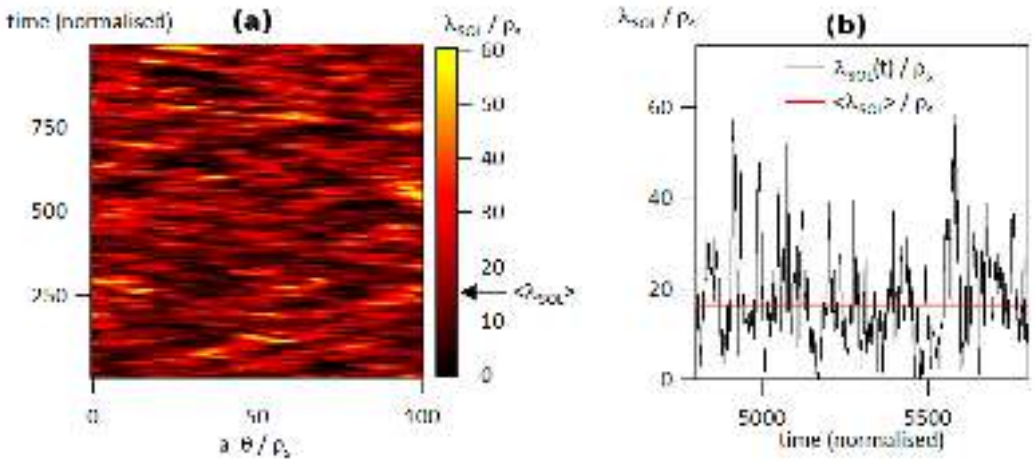

Figure 4.8: (a) λ_{SOL} fictuations in time and space, (b) λ_{SOL} time trace compare to steady $< \lambda_{SOL} >$

$< \lambda_{SOL} >$is relevant, hence the coarse grained λ_q. However, for a component at 1 λ_q from the separatrix such that the mean heat flux is strongly reduced, one can still have significant deposition, hence cycling of the surface temperature. This will become a problem if the chosen Plasma Facing Component has a much shorter thermal time constant or if the material is more sensitive to surface temperature excursions, for instance ITER main chamber wall with Berylium. Furthermore, when fluctuations are large, even if the component integrates the heat deposition, the fluctuations will govern important surface temperature excursions (the problem with ELMs). There is then a risk of exceeding critical surface temperatures as well as enhanced fatigue of the material during constant thermal cycling. However, it could also be that this constant temperature massaging of the surface has positive impact like self healing of cracks and Tritium extraction from the cracks [SCM+07].

- **Particles transport.** The problem can be more serious for particle transport since a significant fraction of the particles will recycle in the main chamber, out of reach of the divertor and the pumping system. This can have severe issues during long pulse operation with the loss of density control, drop out of the H-mode and possible ending in a disruption. Finally, ion heat transport can follow particle transport and lead to spurious energy deposition in the main chamber [GPR+11].

- **Divertor.** The SOL plasma acts as a lid that confines the neutral within the divertor volume. For a strongly fluctuating SOL, the lid can be on average closed. But most of the time it is open. Since the neutral characteristic time (time of flight) can be comparable to the turbulence time scale, the plasma lid can be considered to be ineffective.

Chapter 5

Turbulence self-organization close to criticality

Contents

Turbulent transport inside the tokamks is driven by instabilities. We focus here on instabilities of the interchange family, which govern both TOKAM2D and GYSELA models. The instability exists whenever there is a combination of a high plasma pressure gradient and magnetic field curvature. This instability presents a threshold that results from a balance between the force driving the system out of equilibrium and damping terms. By marginal stability or criticality, one defines the case where forcing and damping terms balance out so that the growthrate is equal to zero $\gamma = 0$.

It has been observed that close to criticality, large scale self-organized patterns develop in the case of flux driven simulations [NGCM+14, DPDG+10]. These large scale structures disappear when increasing the forcing. A plausible explanation for this transition is that an increase of the forcing corresponds to an increase of the number of unstable modes: (1) close to threshold, only few modes are unstable and the system has reduced number of degrees of freedom and regular patterns can appear; (2) far from criticality, the number of degrees of freedom of the system increases so that no clear signatures of regular reorganization can be observed.

In GD gyrokinetic simulations, by scanning the forcing, a new region has been identified close to criticality where, even if the system is linearly unstable, turbulence is quenched. In this region, the so-called Dimits shift region, it has been observed that ZFs quench the turbulence so that the radial transport is reduced to very low values,[DBB+00, RDK00].

The role of criticality in the interplay between streamers and ZF and in the turbulence self-organization appears to be crucial but still not fully understood. We present here a possible explanation to reconcile the Dimits shift observation for flux tube gyrokinetic collisionless models with other results obtained with FD codes, like GYSELA, or fluid codes, like TOKAM2D.

5.0.1 The Dimits upshift of turbulence threshold

In 2000 Dimits[DBB+00] presents an overview adressing turbulent transport at large scale and comparing the results of different types of turbulent transport models, gyrofluid and gyrokinetics, based on ITER relevant parameters (also known as CYCLONE base case parameters). The models that are compared are gradient driven and δf, flux tube models (see chapter 2). The aim of such a benchmark is to quantify linear and non linear turbulent transport prediction in an ITER like scenario.

From the linear analysis (see fig.5.1(a)), one can retrieve and compare the perturbation instability growthrate and frequency at given poloidal mode number. Via the linear analysis, one can obtain crucial information on the instability, such as the linear threshold, i.e. the minimum values of forcing for the perturbation to be linearly unstable, and the identification of the most unstable mode, often related with the characteristic turbulence size. In the next session, a comparable analysis is carried also for the TOKAM2D code.

In the non linear framework, the comparison is carried out taking for granted that, at large scale, a Fourier law of diffusion can describe the macroscopic transport, i.e. the flux at large scale is proportional to the opposite of the pressure gradient $-\nabla P$, more specifically $-\nabla T$ for the ITG instability (or $-\nabla n$, in the TOKAM2D case). The proportionality coefficient χ_{eff} quantifies the microturbulence effect on large scale transport (see

fig.5.1(b)). In the GD simulation case, where the pressure profile is an input parameter, it is possible to recover a clear dependence between turbulent flux and the forcing of the turbulence.

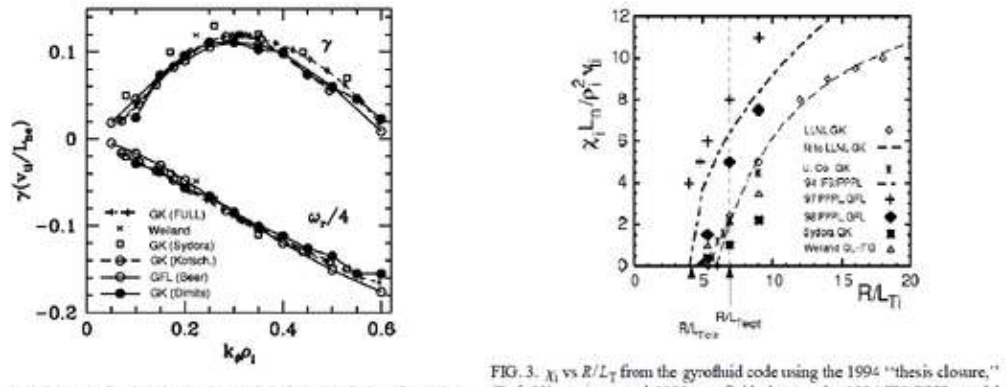

FIG. 1. γ and ω_r vs k_θ for the Sydora (global) and Dimits (flux-tube) nonlinear gyrokinetic codes, for the Kotschenreuther and Rewoldt (FULL) linear gyrokinetic codes, the Beer nonlinear gyrofluid code, and the Weiland fluid calculation.

FIG. 3. χ_i vs R/L_T from the gyrofluid code using the 1994 "thesis closure," (Ref. 23), an improved 1998 gyrofluid closure, the 1994 IFS-PPPL model (Ref. 8), the LLNL and U. Colorado flux-tube and UCLA (Sydora) global gyrokinetic codes, and the MMM model for the DIII-D base case.

Figure 5.1: Figures from the paper of Dimits[DBB+00]

An outstanding result is the presence of an upshift observed in many different gyrokinetic codes, also defined as Dimits shift, between the linear threshold $1/L_{Tc}$ (the minimum value of temperature gradient required for the perturbation to be linearly excited) and the non linear threshold (the value of $1/L_{Tnl}$ where the turbulent flux grows with the forcing). The Dimits region is of particular interest considering that in ITER, the temperature gradient $1/L_{Texp}$ should be close to the non linear threshold value $1/L_{Tnl}$.

The presence of this upshift is due to the transfer of energy from turbulence to the zonal flows. In the Dimits region, undamped zonal flows build-up until they quench the turbulence by ExB shear. When the forcing increases above another critical value $(1/L_T > 1/L_{Tnl})$, the shear of the zonal flows is no more capable to quench the turbulence, the ITG modes are then driven unstable so that a further increase of the temperature gradient governs an enhancement of the turbulent flux. [1]

Interestingly, such upshift is not reported in the fluid codes framework, where the onset of turbulent transport takes place at the linear threshold. It appears, from Dimits comparison, that the impact of zonal flows on turbulence is negligible in fluid simulations. The shift is driven by specific kinetic effects, in other words, according to such observations, a kinetic description is needed in order to observe the self-organized generation of patterns able to macroscopically quench the turbulence. Such results, that strongly influenced modeling choices, have been contradicted by the benchmark of European turbulent codes,[FSA+08], where the non linear upshift has been observed also for the fluid code ETAI3D[OM99].

The conditions for the appearance of the Dimits shift are still ambiguous and questions

[1] It is important to remind that the Dimits shift was observed in the collisionless configuration, the role of collisions is crucial in the Zonal flows dynamic and it will be treated extensively in Chapter 6.

on the general validity of this results and its relevance in predicting the transport have arose. We define here with the two models, GYSELA (kinetic, flux driven, simulating the close field line region only) and the reduced model TOKAM2D (fluid, flux and gradient driven, simulating open and close field lines region), which are the conditions required to recover the Dimits shift. In particular we focus on the two main constrains of Dimits result:

- **Fluid vs Kinetics.** According to Dimits results, the upshift appears only for kinetics codes, however new results contradict this constrain;
- **Flux Driven vs Gradient Driven.** In the flux driven models, evidence of the shift have not been found yet. However, the neighborhood of criticality for FD codes appears to favor turbulence self-organization, i.e. coalescence of stable and turbulent regions, leading to the micro barrier formation [DPDG+10]

5.1 Streamers and zonal flows: what do we learn from linear analysis?

To identify the conditions for which the transition to turbulence occurs, we first study how the instability driving the system can be linearly excited.

In the two models TOKAM2D and GYSELA the instabilities driving the system are referred as respectively the interchange[GLRS91] and ITG (Ion Temperature Gradient)[RB90]. Both instabilities are interchange-like instabilities. In TOKAM2D the magnetic field curvature is reduced to a scalar, namely the g-term, while in GYSELA the complete operator is considered. In the present analysis a simplified magnetic geometry is taken into account.

We compare here the results obtained by linear analysis in the two models. In particular, we focus on the streamers, linearly excited, and zonal flows, linearly or marginally stable. A point of interest is to understand if TOKAM2D contains all the features that are required to be a reduced model of GYSELA.

5.1.1 Linear analysis: The Ion Temperature Gradient instability in a global code

In the global gyrokinetic case, the linear reference value cannot be defined analytically, because the linear growthrate is influenced by global quantities, such as the temperature, density, safety factor profile or simulation size. Therefore a possible verification can be carried out only by comparing results coming from different gyrokinetic codes. We present here the results obtained in the effort of validating several European gyrokinetic codes, such as Eulerian Vlasov, Lagrangian PIC, and Semi-Lagrange codes.

In a global full-f code the definition of linear growthrate is still a quite complex procedure.

Here we present the comparison between the growthrate in function of the poloidal wave vector $k_\theta \rho_s$ for GENE and GYSELA. A good agreement is found between the two codes, see fig.5.2. In this case the physical parameters used are those presented in the Cyclone Base Case framework, CBC, detailed in Lapillone paper [LMG+10] and in the Annex D, where more technical information on the growthrate definition are detailed. The circular concentric magnetic equilibrium is defined with an aspect ratio of $R = 2.78a$ and

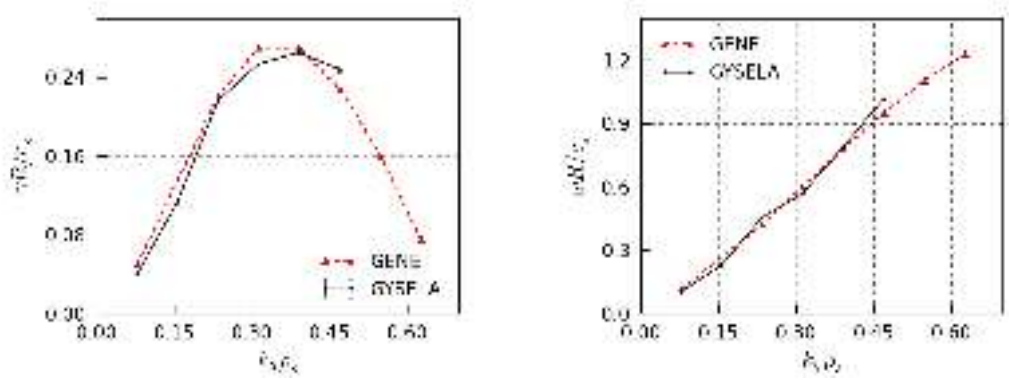

Figure 5.2: comparison between GENE (black line) and GYSELA (blue line) linear growthrate (a) and frequency (b)

a safety factor profile $q(r) = 0.86 - 0.16(r/a) + 2.526(r/a)^2$, as shown in fig.5.4(a). This corresponds to a local safety factor $q(r_{peak}) = 1.4$ and a local magnetic shear $s(r_{peak}) = 0.8$ with $r_{peak} = r_{min} + 0.5(r_{max} - r_{min})$. The initial density and temperature are defined with the radial form function $f(r) = \exp(\kappa_x \Delta_{r_x} tanh((r - r_{peak})/\Delta_{r_x})$. The parameters κ_x and Δ_{r_x} are chosen to obtain peaked gradient profiles at r_{peak}, the middle of the radial box r_{peak} with $\Delta_{n_{s0}} = \Delta_{T_{s0}} = 0.04$, $\kappa_{n_{s0}} = 2.2$ and $\kappa_{T_{s0}} = 7.1$, as shown in fig.5.4(b). To be consistent with the DIII-D reference shot of the initial Cyclone Base Case, ρ^* is chosen equal to 1/180.

The difficulty for GYSELA is that the CBC benchmark was historically designed for local δf code. Indeed, the first difficulty with a full-f code is that the separation between linear and non-linear terms is not trivial. Therefore the linear phase is extremely short because of non linear coupling between the modes. To increase the duration of the linear region, two possible methods are used. First, all the toroidal mode numbers n are filtered except the mode n_0 initialized as perturbation $F_S(t = 0) = (1 + \epsilon \sum_{m=0}^{m_{max}} cos(m\theta + n\phi + \delta_{mn}))$. Second, the initial size of the perturbation is set to $\epsilon \approx 10^{-6}$ to avoid any impact on the initial profile that should stay constant. Additionally if the perturbation amplitude grows above a given critical value, fixed at 10^{-4}, the perturbation is reinitialized with smaller magnitude. Besides, the global aspect of the code implies that large toroidal mode numbers n are hardly accessible because a large mesh discretization is then necessary. For these reasons, the linear analysis is limited to values of n ranging from 5 to 30.

However, the advantage of using a global description to study the linear benchmark is related to the other information we can get besides from the growthrate and the frequency. Namely, identifying the radial mode structure can be a good tool to verify the ballooning theory and provide a basis for some non-linear theories and simulations.
To investigate the three dimensional evolution of the perturbation and in particular the resonant featueres, a change of the poloidal coordinate is required from the geometrical poloidal coordinate θ to the straight field-line coordinates θ^* [DHCS91, X.L].

Global eigenmode

In the case of concentric, circular magnetic flux surfaces, corresponding to the geometry used in GYSELA, one can rewrite the magnetic field in toroidal coordinates according to

the following equation

$$\vec{B}_0 = \frac{R_0 B_{ref}}{R}[\vec{e}_\varphi + \frac{r}{R_0 \bar{q}}\vec{e}_\theta], \tag{5.1}$$

where B_{ref} is the magnetic field at the magnetic axes, $\bar{q}$ is called the cylindrical safety factor and $\vec{e}_\varphi$ and $\vec{e}_\theta$ are the unit vectors respectively in toroidal and poloidal direction. We can see that the magnetic field $\vec{B}$ has a toroidal and a poloidal component. The toroidal magnetic field decreases with $R = R_0 + r\cos\theta$ while the poloidal one with r. The safety factor that characterizes the helical winding of field lines on a given magnetic surface is defined as:

$$q(r) = \frac{1}{2\pi}\int_0^{2\pi} \frac{\vec{B}_0 \cdot \vec{\nabla}\Phi}{\vec{B}_0 \cdot \vec{\nabla}\theta}\, d\theta = \frac{\bar{q}(r)}{2\pi}\int_0^{2\pi} \frac{R_0 d\theta}{R_0 + r\cos\theta} = \frac{\bar{q}(r)}{\sqrt{1-\epsilon^2}} \tag{5.2}$$

where $\epsilon = r/R_0$ is the inverse of the aspect ratio. The safety factor is averaged along the poloidal direction, since the ratio between $\vec{B}_0 \cdot \vec{\nabla}\varphi$ and$\vec{B}_0 \cdot \vec{\nabla}\theta$ depends on θ. Defining a new coordinate θ^*, straight field line coordinate, such that the safety factor can be written directly as $\frac{\vec{B}_0 \cdot \vec{\nabla}\Phi}{\vec{B}_0 \cdot \vec{\nabla}\theta^*} = q$, it is not necessary to average along the poloidal direction, since q will be uniform along θ^* by definition. One can rewrite the relation between θ and θ^* according to $d\theta^*/d\theta = \vec{B}_0 \cdot \vec{\nabla}\Phi/(q\vec{B}_0 \cdot \vec{\nabla}\theta)$. Integrating over θ then yields:

$$\theta^*(r,\theta) = \frac{1}{q}\int_0^{\theta} \frac{\vec{B}_0 \cdot \vec{\nabla}\varphi}{\vec{B}_0 \cdot \vec{\nabla}\theta}\, d\theta = \frac{\bar{q}}{q}\int_0^{\theta} \frac{d\theta}{1+\epsilon\cos\theta} = 2atan(\frac{\sqrt{1-\epsilon^2}}{\sqrt{1+\epsilon^2}}tan\frac{\theta}{2}) \tag{5.3}$$

Once the potential $\Phi(r,\theta,\varphi)$ is expressed in function of the new coordinates system $\Phi(r,\theta^*,\varphi)$, one can identify the contribution of each poloidal mode $m = ak_\theta^*$, that satisfies the resonance condition $m = n/q$.

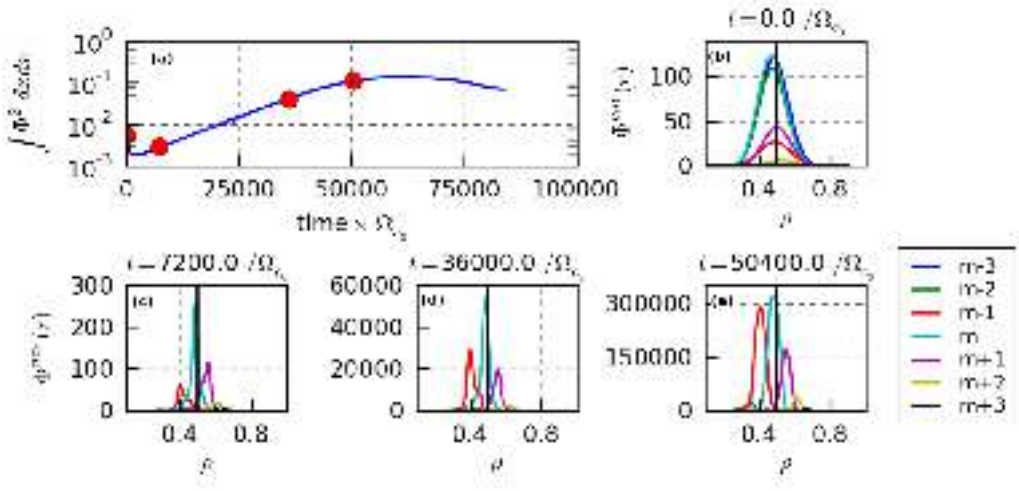

Figure 5.3: (a) the evolution in time of potential $< \Phi >_{\theta,\phi}$ at the midplane in logarithmic scale, (b)-(e) the poloidal modes $\hat{\Phi}_{n,m\pm\Delta m}$ distribution in the radial direction for different time step corresponding to the red dots in the fig.5.3(a), where $n = 5, m = 7, \Delta m = 3$

We present here, the global mode evolution for $n = 5$. We excite a band of modes with $(n,m) = (5, 7 \pm \Delta m)$, where $\Delta m = 3$ with random amplitude between $0 - \epsilon$. If we watch

at the linear growth rate of $\int \Phi d^3x d^3v$ from the initialization to the end of linear phase in fig.5.3(a), we can identify three regions:

1. **position-reorganization region**, damping proportional to $k_\parallel$ is very effective. This tends to localise the excited mode in the neighborhood of $k_\parallel = R^{-1}(n+m/q) = 0$ surfaces (resonant surfaces), in fig.5.3(c).

2. **amplitude-reorganization region**, each mode grows at different speed to converge towards a characteristic envelope with a characteristic growthrate, i.e. the global eigenmode of the system (see fig.5.3(e))

3. **saturation phase**, if the perturbation amplitude is big enough the perturbation modifies the mean profile and non linear effect should be taken into account (see fig.5.3(d)). The complexity of this problem is to ensure a long time window for the envelope to form. If phase(3) starts before phase (2), we cannot define a proper envelope growthrate.

The Cyclone Base case, on the other hand, takes into account only a specific set of parameters (safety factor, temperature, as shown in fig.5.4(a)-(b))), that often do not capture the ensemble of possible experimental results that are understood to be relevant for ITER operation. In order to understand how much the choice of the parameters can impact on the linear analysis, a comparison is carried out between the standard CBC (A) and two other cases, where the safety factor (B) or the temperature gradient profile (C) is modified. The envelope growthrate and shape vary with q and L_T profile, despite $q(r_{peak})$ and $L_T(r_{peak})$ is not varied from the reference case. However, the detailed comparison between the three cases is detailed in the Annex D.

The streamers: ITG unstable modes

The linear analysis is a powerful tool in the context of code verification, but also when analyzing nonlinear simulation.

One can observe that radially elongated structures, also called streamers, are linearly excited on the outboard midplane, see fig.5.4(a). The streamers orientation in the θ-plane is not uniform due to the magnetic shear effect[FGH+13]. The magnetic shear induces a continuous stretching of flux tubes following the parallel direction. On fig.5.4(b) one can notice that the structure of the electric potential has features that are similar to that of the most unstable eigenmode. A possible explanation is that in such flux driven simulations the system cycle from under to above the linear threshold. Accordingly it will experience the linear sequence as the temperature gradient increases above the critical value.

5.1.2 The Zonal Flows: marginaly stable modes

In contrast with the streamers modes, zonal flows are not linearly excited by the ITG instability. To study the ZF dynamic in GYSELA, we rewrite the Vlasov equation as:

$$\frac{d\bar{F}_S}{dt} = \partial_t \bar{F}_S + (\mathbf{v}_{G\perp} \cdot \nabla_\perp + v_\parallel \nabla_\parallel)\bar{F}_S + \dot{v}_\parallel \partial_{v_\parallel} \bar{F}_S = C(\bar{F}_S) \tag{5.4}$$

the system is driven by the electric and vertical drift velocities $\mathbf{v}_{G\perp} = \mathbf{v}_E + \mathbf{v}_{G,S}$, by the parallel force $v_\parallel$ and by collisions $C(\bar{F}_S)$ (as first approximation we assume that the

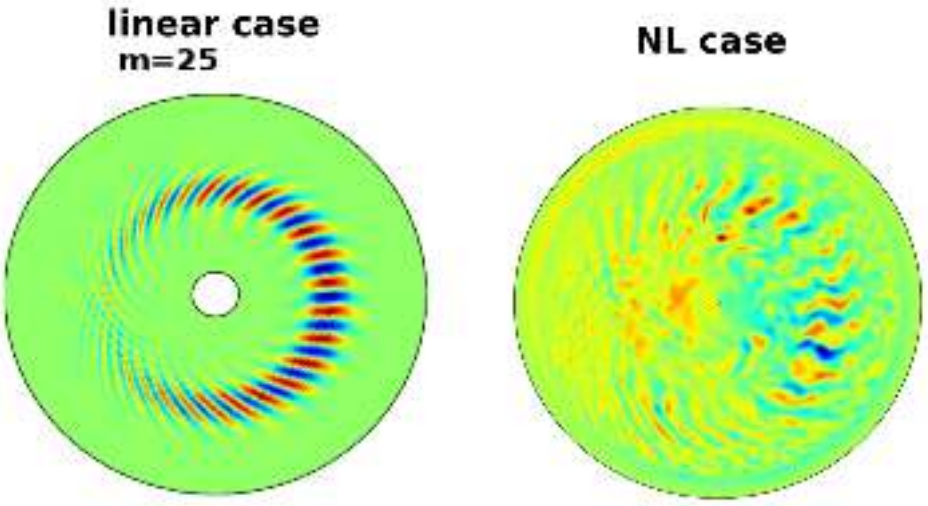

Figure 5.4: (a) safety factor q (b)R/L_T, (c) envelope distribution in the CBC case for $n = 20$ (b)the potential distribution along $r - \theta$

collisions term is equal to zero $C(\bar{F}_S) = 0$).

Note that both for the drift and the parallel force one must consider $J_0\phi$, hence a function of μB. Neglecting this aspect ($J_0 \approx 1$) and integrating along the velocity space, one recovers the fluid density conservation n

$$\partial_t n + [\phi, n] + \nabla \int \mathbf{v}_G f dv_{\parallel} = 0 \tag{5.5}$$

Given the quasi neutrality condition eq.2.13, the guiding center density n can be rewritten, assuming n_{eq}, B constant, as

$$\frac{n}{n_{eq}} = \frac{m}{eB^2}\Delta\phi + \frac{1}{T}(\phi - < \phi >_{F.S.}) + 1 \tag{5.6}$$

. Using the gyrokinetic equation and averaging along on flux surface, one can recover the zonal flow equations:

$$\partial_t \Delta\Phi_{ZF} + < [\Phi, \Delta\Phi] >_{F.S.} = 0 \tag{5.7}$$

where $\Phi_{ZF} =< \Phi >_{F.S}$. On a flux surface, the current due to the curvature drift must vanish for symmetry reasons. The ZF variation is governed by the non linear term. In the Dimits framework, the plasma is collisionless so that the zonal flows will only decay if $< [\Phi, \Delta\Phi] >_{F.S.} < 0$. Since the only variation is governed by non linear term, one thus find that V_z is marginal. The ZF are marginally stable: they are not excited by the linear instability but no linear damping acts to these structures, therefore once they are generated, they tend to live for longer time interval.

However, it has been observed that collisions act as ZF damping [RH98, HR99]. In the fluid model, such an effect is taken into account via viscosity term proportional to the

collisions frequency [DIIH05]. The zonal flows equation, where $\Delta\Phi_{ZF} = \partial_\Psi V_{ZF}$, can be then rewritten as:

$$\partial_t V_{ZF} = \partial_\psi < RS > -\nu\Delta V_{ZF} \tag{5.8}$$

.

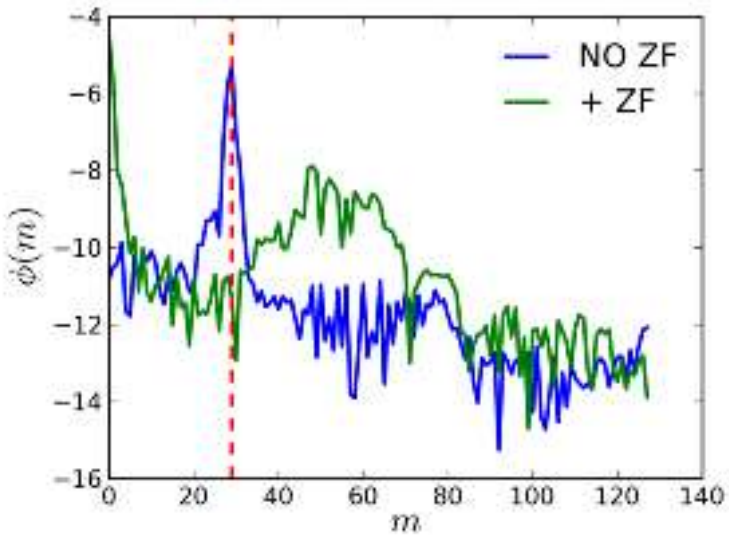

Figure 5.5: poloidal spectrum of potential fluctuations without (blue line) and with (green line) imposed ZFs, during the linear phase

To study the impact of ZF on the linear streamer like structure, we impose a constant ZF in the linear simulation. Without ZFs, if we excite the toroidal mode $n = 20$, a corresponding peak at poloidal mode $m = 28$ can be observed, see fig.5.5 (blue line). With ZFs the poloidal spectrum is changed, one can observe a peak for $m = 0$, i.e. the ZF mode, and a broad band of excited modes for $m > 28$. The ITG eigenmode is changed and now depends on higher mode numbers. ZFs quench the streamer like modes favoring smaller scale modes, that can grow in the reduced space bounded by the zonal flow structure and the boundary conditions.

5.1.3 TOKAM2D: a reduced model for streamers and ZFs dynamics

The advantage of using TOKAM2D is that a linear growthrate can be derived analytically and compared to the simulations results. A proper comparison can be done, when TOKAM2D is used as a flux tube code, see Section 4.2.2. In flux tube version, the driving term g/L_n is constant in time and space.

Analytical calculation of interchange growthrate for TOKAM2D

In TOKAM2D the growthrate in function of the radial and poloidal modes is known analytically for given value of density gradient at equilibrium state. Namely we define the equilibrium the density profile, only depending on the radial position, $\bar{n} = n(x) = n_0 exp(-x/L_n)$, and the electric potential profile constant in all directions and equal to Λ,

$\bar{\Phi} = \Lambda$. To study the linear growthrate of the interchange instability, one perturbs this reference equilibrium state with respect to

$$\tilde{n}_k = \tilde{n}_{k_x,k_y} \exp(i(k_x x + k_y y)) \exp(\Omega_k t) + cc \tag{5.9}$$

$$\tilde{\Phi}_k = \tilde{\Phi}_{k_x,k_y} e^{i\psi_k} \exp(i(k_x x + k_y y)) \exp(\Omega_k t) + cc \tag{5.10}$$

where ψ_k represents the phase shift between $\tilde{n}_k$ and $\tilde{\Phi}_k$, 'cc' means 'complex conjugates' and γ_k represents the real part of Ω_k. The perturbations will be excited if γ_k is positive, namely the system is unstable. We rewrite then the TOKAM2D equations of density and potential in function of $f = \bar{f} + \tilde{f}$, where $\bar{f} =< f >_y$, $\tilde{f} = f - < f >_y$ and $f = n, \Phi$:

$$\partial_t \bar{n} + \left\langle \left[\tilde{\phi}, \tilde{n}\right] \right\rangle + D_\perp \Delta_\perp \bar{n} - \sigma_n \bar{n} \tag{5.11}$$

$$\partial_t \bar{W} + \left\langle [\tilde{\phi}, \tilde{W}] \right\rangle = \nu_\perp \Delta_\perp \bar{W} + \sigma_\phi \bar{J} \tag{5.12}$$

$$\partial_t \tilde{n} + \left[\tilde{\phi}, \tilde{n}\right] - \left\langle \left[\tilde{\phi}, \tilde{n}\right] \right\rangle + \left[\tilde{\phi}, \bar{n}\right] \quad = D_\perp \Delta_\perp \tilde{n} - \sigma_n \tilde{n} + \sigma_n \tilde{\phi} \tag{5.13}$$

$$\partial_t \tilde{W} + \left[\tilde{\phi}, \tilde{W}\right] - \left\langle [\tilde{\phi}, \tilde{W}] \right\rangle \quad = -g\partial_y \tilde{n} + \nu_\perp \Delta_\perp \tilde{W} + \sigma_\phi \tilde{\phi}. \tag{5.14}$$

In the linear analysis framework, we assume that the perturbation are much smaller than the equilibrium terms $\tilde{f}/\bar{f} \approx \varepsilon$, therefore one neglects the quadratic contributions in the fluctuation equations, eqs.(5.13-5.14). The equations are then further simplified and rewritten as:

$$\partial_t \tilde{n} - \frac{\partial_y \phi}{L_n} \quad = D_\perp \Delta_\perp \tilde{n} - \sigma_n \tilde{n} + \sigma_n \tilde{\phi} \tag{5.15}$$

$$\partial_t \tilde{W} \quad = -g\partial_y \tilde{n} + \nu_\perp \Delta_\perp \tilde{W} + \sigma_\phi \tilde{\phi}. \tag{5.16}$$

given $\bar{n} = n_0(-x/L_n)$. Substituting eq.5.9-eq.5.10 in eq.5.15-eq.5.16, one obtains the following coupled equations:

$$(\Omega_k + Dk^2 + \sigma)\tilde{n} + (i\frac{k_y}{L_n} - \sigma))\tilde{\phi} = 0 \tag{5.17}$$

$$-ig\frac{k_y}{k^2}\tilde{n} + (\Omega_k + \nu k^2 + \frac{\sigma}{k^2})\tilde{n} = 0 \tag{5.18}$$

Note that to obtain this expression, one neglects the coupling between the equilibrium modes and the perturbations. Eq.5.17-eq.5.18 have a trivial solution $\tilde{n} = 0$ and $\tilde{\phi} = 0$. This solution is unique unless the determinant of this non linear system must vanish. This yields to a second order equation in function of Ω_k:

$$\Omega_k^2 + B_k \Omega_k + C_k = 0 \tag{5.19}$$

where $B_k = (D + \nu)k^2 + \sigma_n + \sigma_j k^{-2}$ and $C_k = (Dk^2 + \sigma_n)(\nu k^2 + \sigma_j k^{-2}) - \frac{gk_y^2}{L_n k^2} - i\sigma_j g\frac{k_y}{k^2}$.

As shown in fig.5.6(a), where the growthrate is plotted in function of k_y at $k_x = 0$, hence in the fixed gradient case, one finds that the most unstable mode corresponds to $(k_y = \bar{k},\ k_x = 0)$. The mode is extended in the radial direction with given poloidal width $L_y = 1/\bar{k}$. It exhibits the expected streamer like structure, with no radial structure due to the calculation for TOKAM2D in the flux tube geometry.

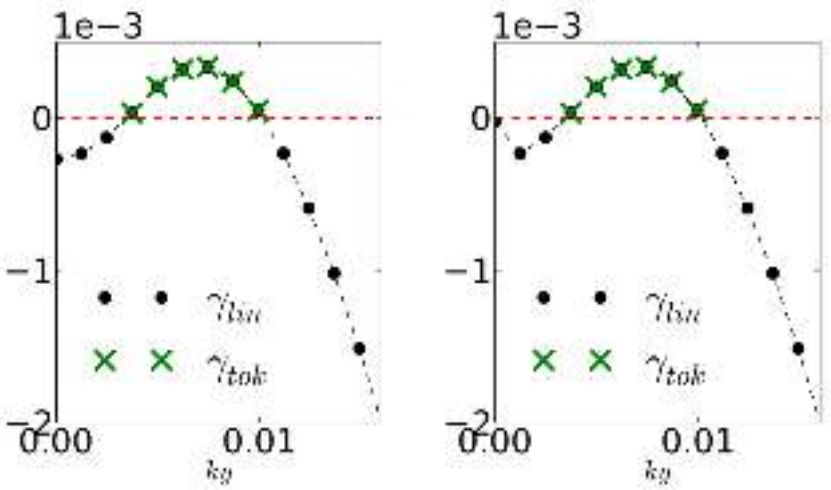

Figure 5.6: benchmark between the growthrate calculated analitically (black lines) and the results determined by TOKAM2D in the SOL for fixed $1/L_n$ (a) and edge (b) configuration (green dots)

The effect of the control parameters on the linear instability

Having an analytical expression for the linear growthrate allows one to: (1) verify implementation of the model in the code, at least regarding the linearised contribution, (2) analyze the impact of each control parameter on the linear growthrate, (3) investigate the geometrical effects introduced by boundary conditions when using TOKAM2D in standard condition (not flux tube). Obviously such results do not take into account the non linear terms, but a first picture of the effect of these parameters is useful for further analysis. In figure 5.7, we show how the growthrate changes with g, L_n, σ, ν, D:

- **forcing terms** (fig.5.7(a),(b)), we consider here two parameters, g and L_n, that act on the magnitude of the growthrate but with opposite effects. If one sets the damping terms equal to zero $\gamma \propto \sqrt{g/L_n}$, the damping terms, when taken into account, introduce a threshold on g/L_n. Regarding the comparison to experiments, one can consider that a variation of $g \propto \rho_s/R_0$ term will corresponds to a variation on the machine size R_0. As already discussed, L_n cannot be considered as a free control parameter in the FD framework.

- **small scales damping terms** (fig.5.7(c),(d)), the diffusivity and viscosity terms are acting in the same way on the growthrate, damping the small scale modes: in the asymptotic limit of $k \to +\infty$ the growthrate varies like $\gamma = -max(D, \nu)k^2$. The viscosity effect on large scale perturbations is small. For large values of D, one can observe a stabilizing effect also at the large scales due to the contribution $(D\sigma_\Phi)$ in C_k, eq.5.19.

- **drag terms** (fig.5.7(e),(f)), these terms are actually acting on the large scale, in the asymptotic limit of $k \to 0$ $\gamma = -\sigma_n - \sigma_\phi k^{-2}$ for the SOL or $\gamma = 0$ for the edge. The magnitude of γ is observed to vary with σ_n, while σ_ϕ plays a role both in the magnitude and the location of the maximum of γ. σ_n or σ_ϕ/k^2 are the characteristic evolution times. They should be used to normalize γ rather than Ω_i, hence $\gamma \propto \sigma_n$ or $\gamma \propto \sigma_\phi k^2$.

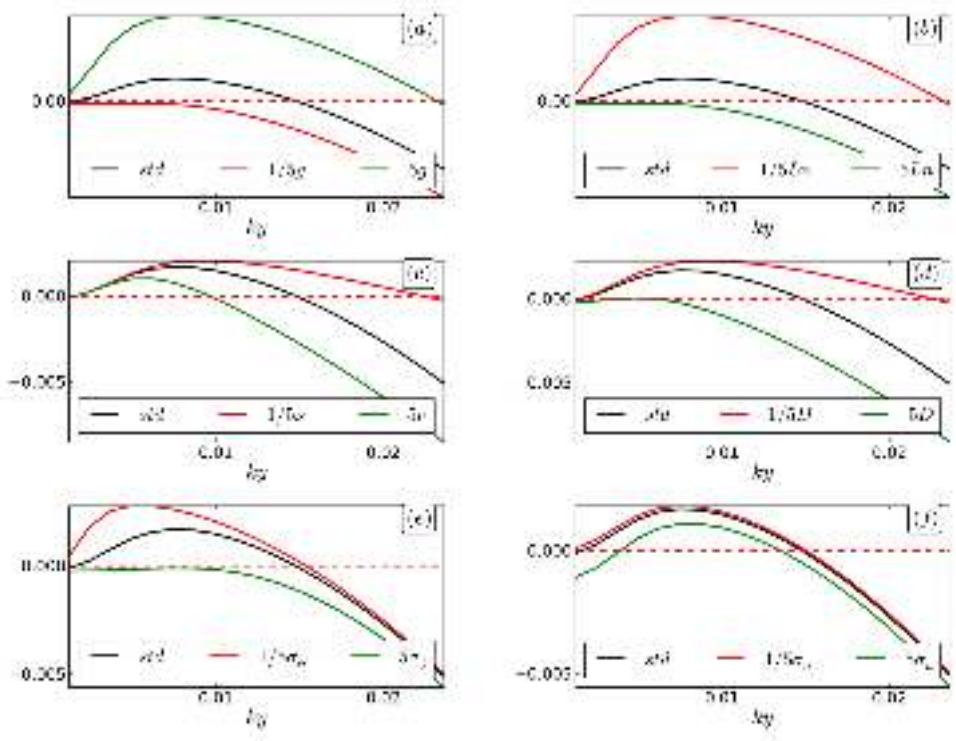

Figure 5.7: the linear dispersion relation in function of k_y for different values of g (a), L_n (b), ν (c), D (d), σ_ϕ (e), σ_n (f)

The role of these parameters on the behavior of turbulence is crucial in order to control the size and time scale of the turbulent structures. In annex C, we introduce a renormalization of the TOKAM2D equation to reduce the total number of independent control parameters, in case of linearised sheath loss terms.

ZF dynamic and drag term

When analyzing ZF dynamics in TOKAM2D, one can observe that the ZF are linearly damped by σ_ϕ in the SOL. In the new version of TOKAM2D, where the edge is modeled, the specific condition on σ_ϕ is changed so that zonal flows are marginally stable. The large scale damping is therefore set to zero. The viscous damping of zonal flows is kept to mimic collisional damping. It plays a role at small sales. With this choice of parameters in TOKAM2D, one can control the zonal flows to exhibit a comparable dynamics in GYSELA at non-vanishing collisionality.

The analytical study already presented for TOKAM2D does not take into account the changes of the σ terms in the edge region. Namely, if we consider no particle loss ($\sigma_n = 0$) and no current loss on the flux surface ($\sigma_\phi(k_y = 0) = 0$), the growthrate at $k_y = 0$ is changed, as shown in fig.5.6(b). Specifically, in the SOL case for $k_y = 0$, we expect $\gamma_{SOL} = -\sigma_n - \sigma_\phi/k_x^2$, while in the edge case $\gamma_{edge} = 0$. The change in parallel sink

terms is therefore:

$$\Gamma = \sigma_n n = 0 \tag{5.20}$$

$$J = \sigma_\Phi(\Phi - < \Phi >_y) = 0 \tag{5.21}$$

This yields the zonal flow equation:

$$\partial_t v_z + \partial_x < RS >_y - \nu \Delta_x v_z = 0 \tag{5.22}$$

where $< RS >_y = - < \partial_x \phi \partial_y \phi >_y$ is the Reynold stress non-linear contribution to the evolution of v_z. In the edge configuration, the streamer like modes are linearly excited, while the ZF modes are marginally stable (at first approximation the viscosity effect can be neglected for small k_x), the modes are not excited linearly or damped. The energy to the zonal flow can come from the non linear coupling only, the Reynold stress term. The latter is thus a key element in the interplay between turbulence and zonal flows.

In order to compare the numerical results with the analytical ones, we use a GD version of TOKAM2D, where the density gradient length is kept constant and equal to L_n, a free parameter. The equations solved by the code are eq.5.15-5.16, where the source is set to zero and the instability is driven directly by the L_n term[2]. A broad range of modes in k_x, k_y are inserted at small amplitude 10^{-4} as initial condition and the parameters used for the comparison are listed in the table below 5.1.

Table 5.1: parameter used in the following simulation both for flux and gradient driven case

$1/L_n$	g	D	ν	σ_n	σ_ϕ	N_x	N_y	L_x	L_y	t_{diag}
0.03	5E-4	1E-2	10E-2	6.1E-5	6.1E-5	128	128	128	128	32

The green points in fig.5.6(a)-(b) represent the growthrate of the excited modes for different values of k_y, given $k_x = 0$. A perfect agreement is found with the linear analysis both in the edge (a) and SOL (b) cases.

5.2 Recovering the Dimits shift

We first analyze FD and GD simulations both for GYSELA and TOKAM2D SOL-version, in order to compare how the two systems differ close to marginal stability. We then consider the edge version of TOKAM2D. In these simulations one recover the Dimits shift which thus tends to indicate that the Dimits shift is not a specific signature of kinetic problems. The impact of criticality on the self-organization dynamic can be investigated in the SOL and edge region and for gradient driven (flux tube) and flux driven versions of TOKAM2D.

The driving term in TOKAM2D directly depends on the density gradient and on the curvature term, via the combination $\frac{g}{L_n}$. In the GD framework, where the particle source is set to zero and L_n is a parameter, both values can actually be controlled by the user, while in the FD case, the control of the different regimes can only be achieved via the g-term.

[2]the GD approach is extensively explained in chapter 3

5.2.1 Gradient driven versus Flux driven

To study the Dimits shift, we first present the results obtained with GYSELA. The effective diffusion coefficient χ of FD global simulations are compared to the Dimits results. Even if the definition of linear threshold is unclear in the framework of global codes like GYSELA, the transition region from laminar to turbulent transport can be obtained by reducing the source amplitude [SGA+10] or increasing the machine aspect ratio. In the GYSELA case, it has been observed that a decrease of the heat source, that actually controls indirectly the temperature gradient, enhances the microbarriers [DPDG+10].

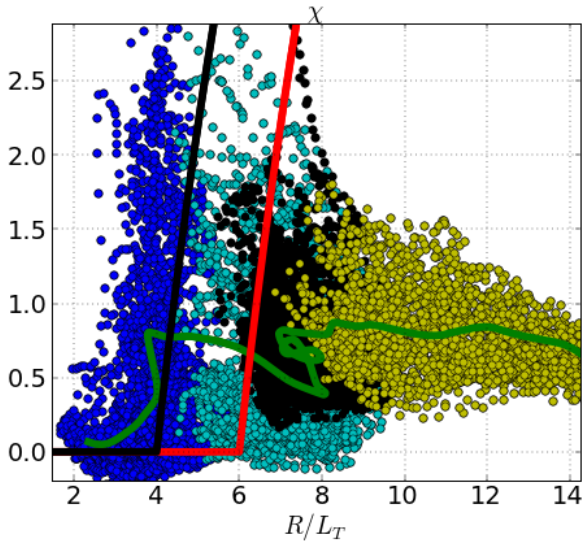

Figure 5.8: Dots: $\chi = < Q_{turb} >_{\theta,\phi} / < \nabla T >_{\theta,\phi}$ in function of R/L_T where $1/L_T = - < \nabla T >_{\theta,\phi} / < T >_{\theta,\phi}$. (blue dots: for $0.1 < \rho < 0.35$; cyan dots: for $0.35 < \rho < 0.4$; black dots: for $0.4 < \rho < 0.8$; yellow dots: for $0.8 < \rho < 1$). Green line: $< \chi >_t$ in function of $< R/L_T >_t$; Red and black line: fit of the flux tube data from gyrokinetic (red line) and fluid (black line) codes proposed in Dimits reference paper [DBB+00].

We now insert the GYSELA non linear simulation data, where microbarriers are present, in the plot $< Q_{turb} >_{\theta,\phi} /(n(\psi) < \nabla T >_{\theta,\phi}) = \chi$ versus R/L_T where $1/L_T = - < \nabla T >_{\theta,\phi} / < T >_{\theta,\phi}$, fig.5.8. Note that both χ and R/L_T are function of radial position and time, as can be observed on the time traces and radial profiles of $< Q_{turb} >_{\theta,\phi}$ and R/L_T of fig.5.9-5.10.

In the FD framework different transport regimes observed with different conditions in the flux tube simulation are recovered in a single simulation with self-consistent organization in time and space. However, no abrupt transition of the turbulent transport takes place at a critical value of R/L_T. The phenomenology of the Dimits shift does not occur in global FD simulations.

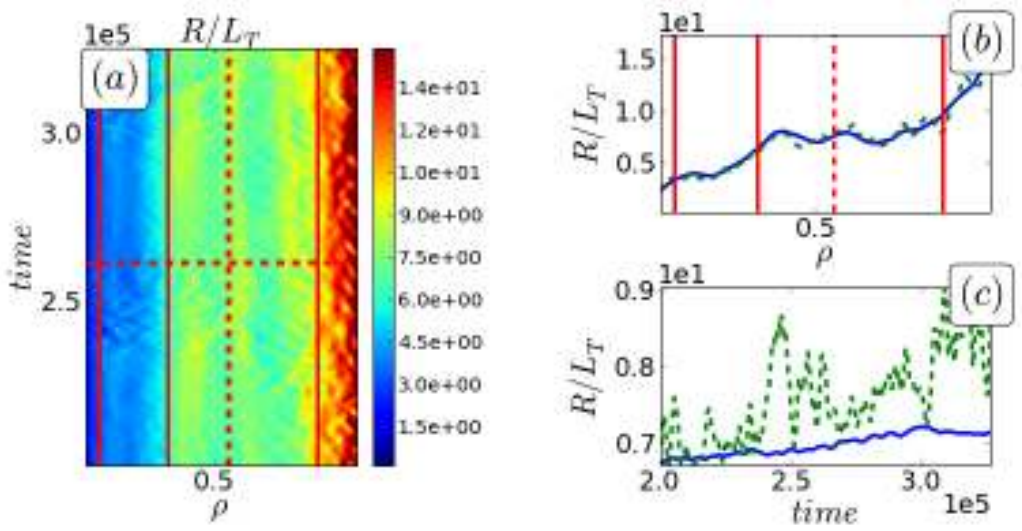

Figure 5.9: (a) R/L_T in function of time and radius averaged in ϕ, θ, (b) $< R/L_T >_t$ &$R/L_T(t_0)$ (blue & green dashed lines)) radial profiles, (c) $< R/L_T >_r$ &$R/L_T(\rho = 0.5)$ time traces (blue & green dashed lines)

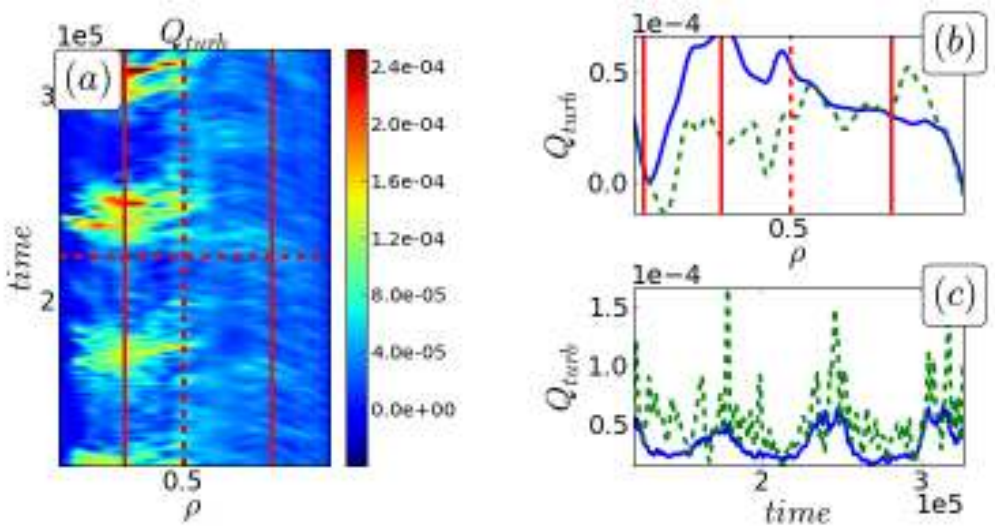

Figure 5.10: $< Q_{turb} >_{\theta,\phi}$ in function of time and radius, (b) $< Q_{turb} >_{\theta,\phi,t}$ & $< Q_{turb} >_{\theta,\phi}$ (t_0) (blue & green dashed lines) radial profiles, (c) $< Q_{turb} >_{\theta,\phi,r}$ & $< Q_{turb} >_{\theta,\phi}$ $(\rho = 0.5)$ (blue & green dashed lines) time traces

To localize and compare the different transport regimes of GYSELA, one can separate the data plotted in fig.5.8 in four radial intervals: core region (blue dots), for $0.1 < \rho < 0.35$, corrugation I & II region (respectively cyan and black dots), for $0.35 < \rho < 0.8$, and edge region (yellow dots), for $0.8 < \rho < 1$. The main features of these regions are:

- **Core**, turbulence is mostly localized below the ITG linear threshold.
- **Corrugation I**, for $\rho < 0.5$. Turbulence is controlled by quasi-periodically radial bursts that transport the particles efficiently from the core to corrugation II, as displayed in fig.5.10.

- **Corrugation II**, for $\rho > 0.5$. The microbarriers govern the transport. The flux is decreasing while R/L_T exhibits a corrugated profile, fig.5.9-5.10. The bursts coming from corrugation I region appears to be confined here.

- **Edge**, R/L_T grows radially and the heat flux can be quantified by a constant large scale diffusion coefficient χ.

5.2.2 Fluid versus kinetic

To study if the role of ZF can be identified also for fluid models, the results obtained with TOKAM2D in two regions with different ZFs dynamics, edge and SOL region, are presented here.

The 'reverse-Dimits' shift in the SOL

Let us first investigate the transition from stable to unstable state in the SOL region. There, transport is governed by avalanche like ballistic events. GD and FD are compared through the transition.
In the first case, the g parameter is set at $g = 2.\ 10^{-4}$, while the other parameters are unchanged and given in table 5.1. In the GD case the gradient $1/L_n$ for each simulation is assumed constant in the domain, therefore we perform a scan also in $1/L_n$, with $1/L_n$ varying from 0.015 to 0.04, where $1/L_n^* = 0.0197$ is the critical threshold given by the linear analysis. The chosen range of $1/L_n$ values set by the minimum and maximum value reached by $1/L_n$ in the corresponding FD simulation.

In fig.5.11(c) the two coarse grained curves of turbulent flux $< \Gamma_x >_{CG}$ versus the driving term $< 1/L_n >_{CG}$ are displayed. For the FD case, the coarse graining procedure consists of averaging the flux and density gradient on poloidal direction and time, ($< \Gamma_x >_y$ / $< n >_{y,t}$ and $< 1/L_n >_{y,t}$) to filter out the fluctuations. The curves with and without coarse graining are displayed in fig.5.11(a). For the GD case, each points of the coarse grained curve is calculated by averaging the radial flux in all directions, i.e. $< \Gamma_x >_{x,y,t}$. The level of fluctuations of $< \Gamma_x >_y$ at given $1/L_n$ is displayed in fig.5.11(b).

One finds an unexpected feature of the local (fixed gradient) approach. Just above the threshold, in the region that would correspond to the Dimits region [DBB+00], the system is linearly unstable but the flux is not governed by the conventional Fick's law since it first decays as the drive is increased. The system only recovers the standard behavior with increasing $1/L_n$ when the latter exceeds $2.5\ 10^{-4}$.

In this 'Dimits region', the turbulent flux exhibits a maximum. At given $1/L_n$, the flux evolution presents a quasi-periodic behavior: the flux grows with time and then collapse to zero close to a cyclic fashion. This cycle can be analyzed in terms of predator prey mechanism. Let us consider that in the critical region only a few modes are linearly excited, hence elongated structures in the radial direction. These streamers are the 'prey'. They grow until they couple non linearly with other modes, in particular the zonal flow mode. This mode is linearly stable and acts as a 'predator'. The energy of the streamers is transferred to the zonal flow, causing the flux collapse. This cyclic pattern can be understood as a signature of a secondary instability, which governs the zonal flows generation. The existence of a cycle is strongly linked to the zonal flows damping. This is one of the key parameters of the overall behavior. Changing the distance to criticality allows one to

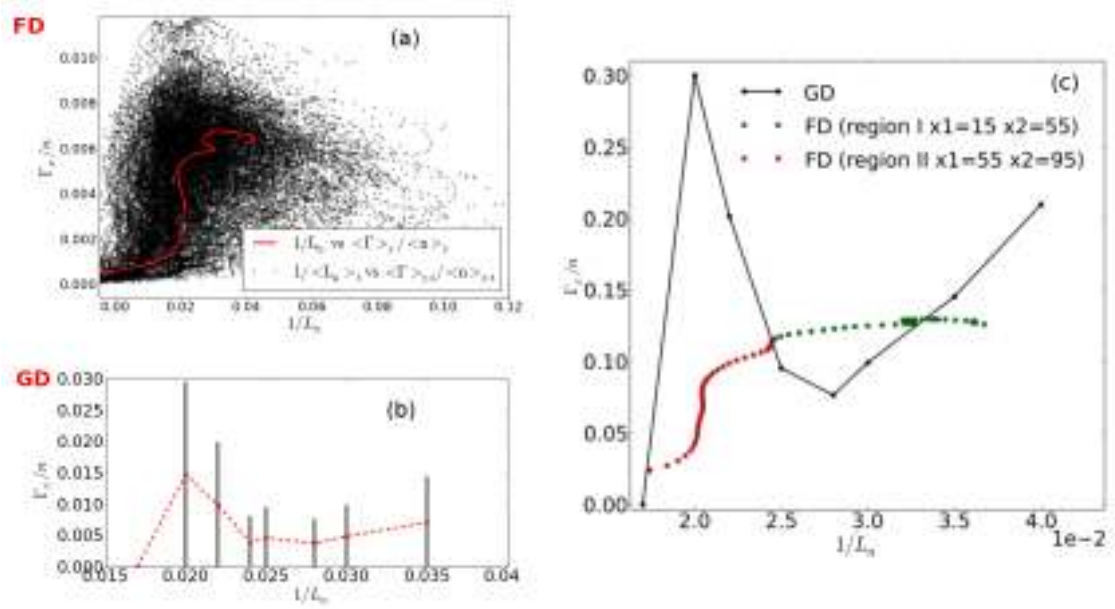

Figure 5.11: (a) FD case: $< \Gamma_x >_y / < n >_{y,t}$ in function of the forcing $< 1/L_n >_{y,t}$ (coarse grained curve, red line), $< \Gamma_x >_y / < n >_y$ in function of the forcing $< 1/L_n >_y$ (black +), (b) GD case: $< \Gamma_x >_{y,x,t}$ in function of different$1/L_n$ (coarse grained curve, red line), with the errorbar the minimum and maximum fluctuations of $< \Gamma_x >_y$ for each simulation at given $1/L_n$, (c) the two coarse grained curves for FD and GD case are compared

control the other characteristic time scale. In fig.5.15 such predator-prey mechanism can be observed (until $t = 5000 c_s/\rho_s$).

Further increasing $1/L_n$ generates more linearly unstable modes until the interchange instability becomes dominant and the system is fully turbulent. Increasing the range of unstable modes generates multiple cycles zonal flows-turbulence with enhanced frequency, until the latter can no more be identified as specific relaxation event.

To explain the flux discontinuity at $1/L_n = 2.8$, fig.5.11(c), we propose here a preliminary study on the interplay between the interchange instability (first instability) that excites the streamers favoring the increase of radial flux with the forcing, and the secondary instability that grows from a developed nonlinear state and depends on the magnitude of the linear perturbation, fig.5.12. The zonal flow mode $\phi_{ZF}(0, k_x)$ is generated by the coupling between two modes, a streamer mode $\phi_s(k_y 1, 0)$ and a turbulent mode $\phi_T(-k_y 1, k_x)$. Such a turbulent mode can be excited by the primary or the secondary instability according to the value of $1/L_n$:

- $1/L_n < 1/L_{n_{nl}}$ **region.** Only the streamer mode is linearly excited, the turbulent mode can be excited non linearly by the secondary instability that is proportional with streamer magnitude, fig.5.12(a)-(b). Once ϕ_s grows higher than a critical threshold ϕ_s^*, the turbulent mode starts growing and the energy is transferred from the streamer to zonal flow mode. By increasing the forcing, the primary instability magnitude grows and the time for the secondary instability to become unstable is reduced. The predator-prey cycle frequency increases and the flux is reduced.

- $1/L_n > 1/L_{n_{nl}}$ **region.** Streamer and turbulent modes are linearly excited. The zonal flow couples with streamer modes immediately, fig.5.12(c). There is no more a time interval governed by streamer modes only. The predator-prey mechanism cannot be distinguished. By further increasing the forcing, we favor the turbulence driven by interchange instability.

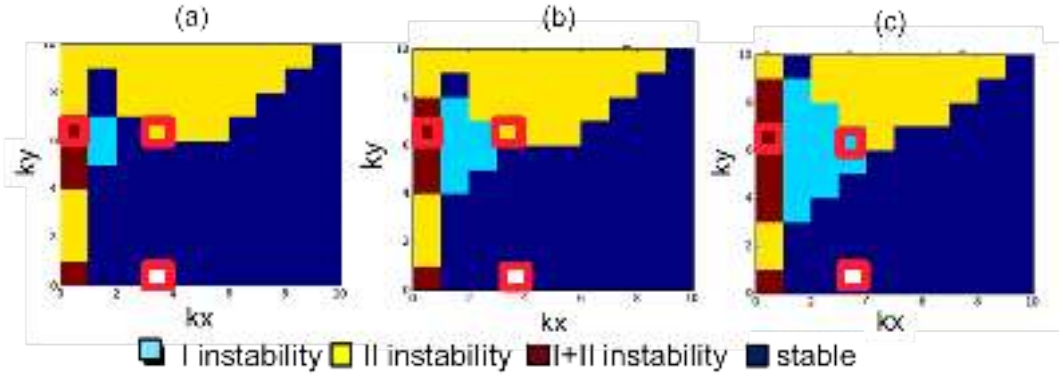

Figure 5.12: Study of instabilities governing GD simulations at (a)$1/L_n = 0.22$, (a)$1/L_n = 0.25$, (a)$1/L_n = 0.3$. The three coupled modes $(\phi_{ZF}, \phi_S, \phi_T)$ are identified by a red frame.

This particular behavior of the threshold region is not observed in the flux driven simulations, see fig 5.11(c). The behavior in the vicinity of the threshold is altogether different in the flux driven case. First, a non vanishing flux is obtained below the critical density gradient length L_n^*. This reduced flow can be related to turbulence spreading into stable region. Above the threshold the mean particle flux exhibits a sharp increases and the flattens out at the largest values of $1/L_n$ in region II.

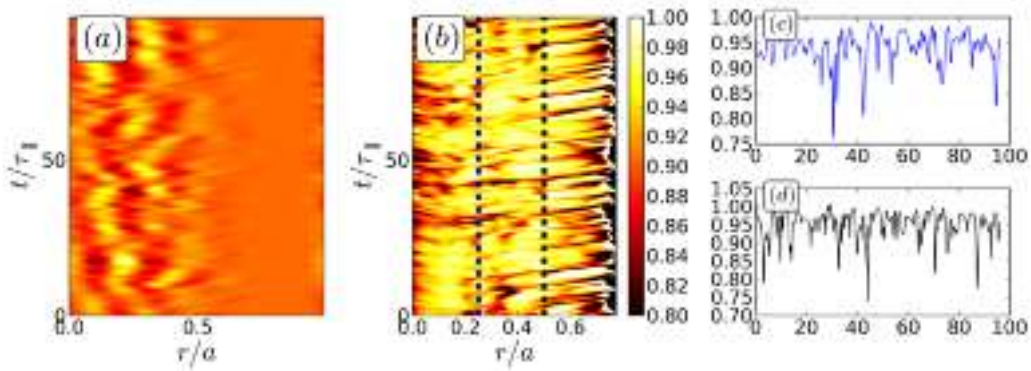

Figure 5.13: (a)the potential averaged in y versus time and radial direction,(b) the Rb quantity in the same interval in time and space, (c) & (d) time traces of R_b at different radial position

In the FD case, one can readily observe that close to criticality the system reorganizes with structures that resembles staircases, see fig.5.13(a). A predator-prey cycle between turbulence and zonal flows can be identified only close to the linear threshold. Even if a clear separation between the streamers and the zonal flows regime as in the GD case

cannot be observed, however one can still identify the generation of intermittent patterns in the potential: signature of a zonal flows cycle.

In order to study the actual impact of zonal flows on the turbulent transport, we are going to use R_b criteria, as previously introduced, Section 3.3. Although the electric potential exhibits a structure that is reminiscent of the microbarriers, the amplitude of these zonal flow patterns is too small to actually stop the avalanches, fig.5.13(b),(c),(d). When considering the pattern of the R_b index, it appears that the regions with reduced transport do not constrain the avalanches. On the contrary, it seems that the avalanches drag the small region of transport barriers. The latter are then slaved to the avalanches and in continuous reshaping.

Dimits shift in the plasma edge

In the closed field lines region, the zonal flows dynamics is modified by changing their drag term. The large scale loss term is set to zero just for the zonal flows. In the fusion machines, such variation can be related to the different condition on the parallel current between open and closed field lines (see Chapter 1).

In order to understand how the transport is impacted in this specific zonal flow regime, we first analyze the local flux tube case. The parameter g/L_n driving force term for the interchange instability is then controlled. This parameter can be then used to monitor the zonal flow generation.

Let us now analyze the difference in bahavior between the SOL $\sigma_\phi \neq 0$ for $k_y = 0$ and the edge such that $\sigma_\phi = 0$ for $k_y = 0$, see figure 5.15:

- **Until time step** $t = 5000 c_s/\rho_s$, open field line conditios are used and one recovers a quasi-periodic predator-prey behavior. The streamers turbulence pattern transfers its energy to the zonal flows. The ZFs have no source of energy once the turbulence is damped away. They are then damped also allowing he onset of new cycle. When analyzing the predator-prey cycle, most of the time is spent in the streamers regime. This time appears to increase as $1/L_n$ is reduced towards the critical value

- **At time** $t = 5000 c_s/\rho_s$, the TOKAM2D equations are changed to the closed field line configuration. The system then locks in the zonal flow configuration. The sink of the zonal flows is strongly reduced since we set $\sigma_\Phi = 0$ for $k_y = 0$. Once ZFs are the dominating modes, turbulence is quenched. A drop of the turbulent flux then occurs, due to the stopping capability of the shear layer.

The analysis of the turbulent flux and density gradient shown in the previous section, different from the results obtained by Dimits, is performed again, see fig.5.14(a). A comparable upshift is then observed between the linear prediction and the nonlinear results.

As shown in fig.5.14(b)-(d), there is more then a change in transport. Indeed the electric potential patterns characteristic time and size are also increased.

The shearing rate of the zonal flows tends to reorganize the transport in staircases and the width of the transport barrier can be controlled by the forcing parameter,[CMGS+14]: increasing g/L_n, the width of the barrier is decreased. It becomes less efficient and turbulent bursts can pass through. If one scans the turbulent flux in function of $1/L_n$, where

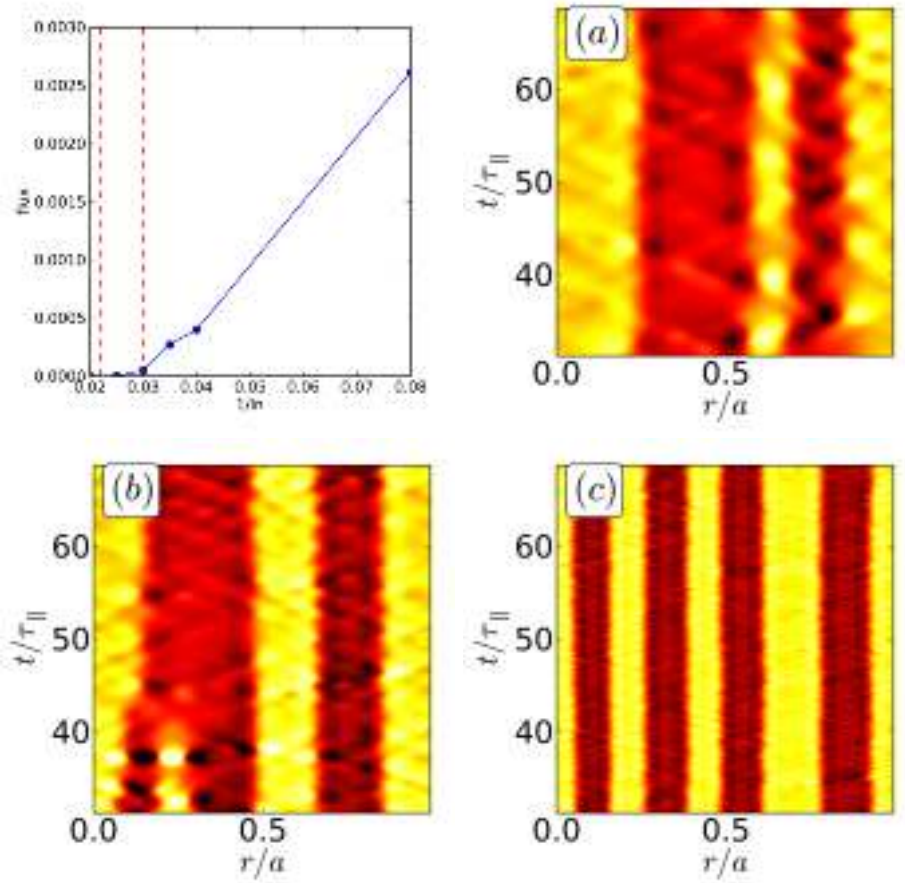

Figure 5.14: Particle flux in function of density gradient in the GD simulation.The potential averaged along y in time and radius direction for different values of L_n, i.e. (b) $1/L_n = 0.03$, (c) $1/L_n = 0.04$ and (d) $1/L_n = 0.08$

$1/L_n > 1/L_{n_{nl}}$, one recovers a direct dependence as already observed in the SOL. Conversely, in the range $1/L_{n_c} < 1/L_n < 1/L_{n_{nl}}$, the flux is constant and does not depend on the density gradient. This region corresponds to the Dimits shift region, where the impact of the zonal flows on the transport is so strong that no bursts can cross the transport barriers.

The dynamics of these patterns is quite rich and complex, they can vary with the forcing term and also move in time and space. Comparing the case in fig.5.14(c)-(d), we observe that

- **the number of staircase is proportional to the density gradient amplitude**, the number of zonal flows doubles from 2 to 4, once increasing $1/L_n$ from $1/L_n = 0.04$ to 0.08.
- **two staircases can merge and collapse in one**, see fig.5.14(b)
- **the position is independent from the number of staircases**, in fig.5.14(b) and (c), for a given number of staircases, their position and width is changed.

5.3 Dimits shift: a limit case

We can conclude that we are now able to retrieve the Dimits shift in the framework of fluid model, identifying the key role of the zonal flows. Namely we found that the transition region from laminar to turbulent transport is always dominated by a predator-prey dynamic.

Such mechanism is clearer in GD simulations where the instability drive is constrained to a constant value in time and space. In the FD case the dynamic is more complex because of the variation of the effective density gradient driving the system is both in time and space.

Such predator-prey cycle is strongly linked to the zonal flow damping that is governed by the drag term σ_ϕ. Therefore, in the SOL, where the zonal flows are damped by σ_ϕ, most of time is spent in the streamers, i.e. prey, regime. Conversely, in the edge, where σ_ϕ is equal to zero for $k_y = 0$, most of the time is spent in the ZF, i.e. predator, regime.

Finally, in the FD version, we cannot obtain the same behavior because the system is not locked in one of the two scenarios. The two regions below and above the Dimits non-linear threshold interact. The Dimits shift cannot be recovered in the experiments since the pressure profile changes in time and space. However it gives us useful information on the streamer and ZF dynamics close to criticality. The analysis of the system near the threshold proves to be most important to isolate the various aspects of the mechanisms that come to play in the model from quasi-periodic relaxation to barrier formation.

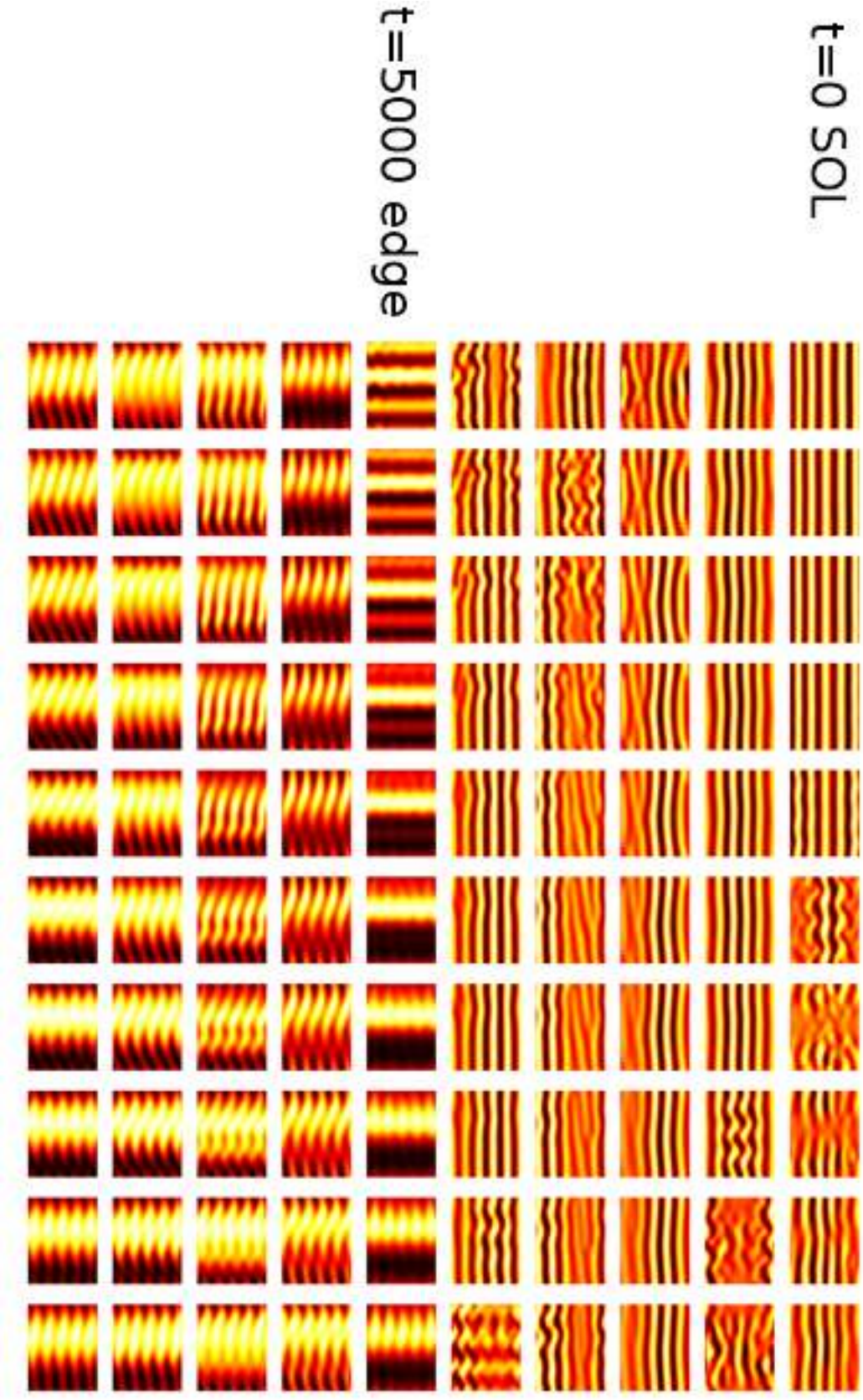

Figure 5.15: the time lapse of potential: for $t < t = 5000c_s/\rho_s$ the system is in the SOL configuration, for $t > t = 5000c_s/\rho_s$ in the edge configuration

Chapter 6

Turbulence and zonal flows

Contents

In this chapter we present a novel understanding of the mechanism regulating the energy transfer between turbulence and zonal flow. The parameters controlling such mechanism and consequently the transition from the *ZF-dominated*, strong ZF and weak turbulence, to *turbulence-dominated* regime, weak ZF and strong turbulence are identified. The transition observed in TOKAM2D is then compared with the one observed in other fluid-dynamical systems, based on the Hagesawa-Mima model (HMB).

The evolution of zonal flows is governed by two mechanisms, linear damping and three waves coupling via the divergence of the Reynold stress. The latter can be a sink, typically by Kelvin-Helmoltz (KH) instability [GFC+99, DIIH05] or a source by constructive interferences of turbulent modes. To study under which condition the sign of $\partial_x RS$ changes, we present a three modes model where the energy transfer between zonal flows and streamers is addressed analytically.

The turbulence injection scale $\bar{k}$ is identified as the control parameter for the transition from the *ZF-dominated* to *turbulence-dominated* regime. Two types of modes are defined: B-modes (Big scale modes) and S-modes(Small-scale modes). If the B-modes dominate, the system is governed by turbulence, otherwise if S-modes dominate, the turbulence is quenched and the ZFs govern the transport.

Comparison between TOKAM2D and Hagesawa-Mima models exhibits many similarities. However the mechanism driving the transition between the *ZF-dominated* and *turbulence-dominated* regime appears to be different. In the framework of HMB models, one refers to *ZF-dominated* and *turbulence-dominated* respectively as zonation and friction-dominated regime. These regimes are identified via a non-dimensional parameter R_β, defined by Galperin as the zonostrophy index [GSD08, GSD10]. The zonostrophy criteria can be redefined in the framework of TOKAM2D, but it does not govern a comparable change in regime.

6.1 Mechanism driving the ZF dynamics

In this section the mechanism that controls the ZF generation and relaxation is explained in the context of TOKAM2D. The aim is to identify how the energy is exchanged between turbulence and ZF.

The ZF relaxation can be controlled by: (1) KH instability, a tertiary instability driven by the ZF, that controls the transfer of energy from zonal flow to turbulence; (2) by collisions,[LHL+99, KR12], taken into account by a viscosity term ν, that acts as a damping term for the ZF.

The sign of the divergence of RS, $\partial_x RS$, is crucial to identify if RS is acting as a source or as a sink for zonal flow. However, its sign fluctuates in time and space, see fig.6.1 [1]. One cannot clearly identify in which conditions the RS term favors or disfavors the zonal

[1] $\partial_x RS$ plotted in fig.6.1 is defined as

$$\partial_x RS = V_{RS}(K_{ZF}) = \sum_{k_x,k_y} ik_y k_x k_{ZF} \phi(k_{ZF} - k_x, k_y)\phi(k_x, -k_y) \tag{6.1}$$

in order to study the effect of RS at given zonal flow mode

flow generation.

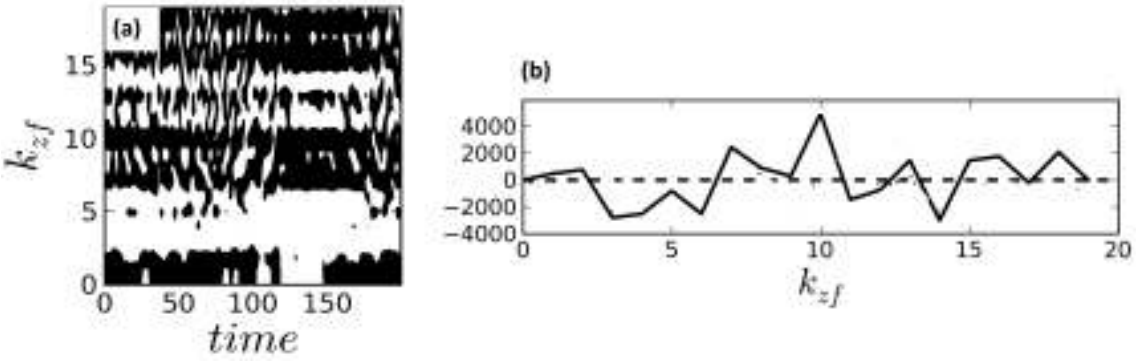

Figure 6.1: (a) $\partial_x RS$ in function of time and zonal flows modes k_{ZF},if $\partial_x RS > 0$ is colored in black, if $\partial_x RS < 0$ in black, (b) $\partial_x RS$ at given time in function of k_{ZF}

6.1.1 KH instability and collisions in the ZF relaxation process

We prove here the dominant role of collisions compared to KH instability in the ZF relaxation. To tackle this topic we need first to identify under which conditions the KH instability is excited and then compare the role of KH and collisions term in a ZF relaxation.

Through the study of the growth rate of two perturbed modes $k_1 = (k_x, k_y)$, $k_2 = (k_x - \kappa, k_y)$ coupled to the zonal flow κ, one defines a dispersion relation that takes into account the contribution of both interchange and Kelvin Helmoltz instability. Let us consider an equilibrium density profile equivalent to the one defined in the previous chapter in the interchange linear analysis framework $\bar{n} = n(x) = n_0 exp(-x/L_n)$ and a potential profile fluctuating along x such as $V_z = \partial_x < \Phi >_y = \partial_x(\Phi_z \cos(\kappa x))$.To study the linear growthrate of the two instabilities, we insert in the system two small fluctuations in density and potential field coupled to the zonal flow mode, $n_1(k_x, k_y)$, $n_2(k_x - \kappa, k_y)$, $\Phi_1(k_x, k_y)$, $\Phi_2(k_x - \kappa, k_y)$. Linearizing the TOKAM2D equations around the equilibrium, one obtains the following linear system of equations

$$\begin{pmatrix} \Omega_1^n & V_z k_y & 1/L_{n_1} & 0 \\ -V_z k_y' & \Omega_2^n & 0 & 1/L_{n_2} \\ k_y g & 0 & \Omega_2^W & V_1 V_z k_y \\ 0 & k_y g & V_1' V_Z k_y & \Omega_2^W \end{pmatrix} \begin{pmatrix} n_l \\ n_2 \\ W_1 \\ W_2 \end{pmatrix} = 0$$

where $\Omega^l = \gamma_+ \gamma^l$ with l corresponding to n or W, respectively $\gamma_i^n = D k_i^2$, and $\gamma_i^W = \nu k_i^2 + \sigma/k_i^2$, $V_1 = \left(k_1^2 - \kappa^2\right)/k_2^2$, $V_1' = \left(k_2^2 - \kappa^2\right)/k_1^2$ for the two coupled instabilities modes $1, 2$. The dispersion relation, a fourth order equation for γ is then:

$$\begin{aligned} &(\Omega_1^n \Omega_1^w - k_y G_1)(\Omega_2^n \Omega_2^w - k_y G_2) + \\ &+ k y^2 V_z^2 [\Omega_1^W \Omega_2^W + k_y^2 V_z^2 V_1 V_1' + \Omega_1^n \Omega_2^n V_1 V_1' + \\ &+ k_y V_1' G_1 + k_y V_1 G_2] = 0 \end{aligned} \tag{6.2}$$

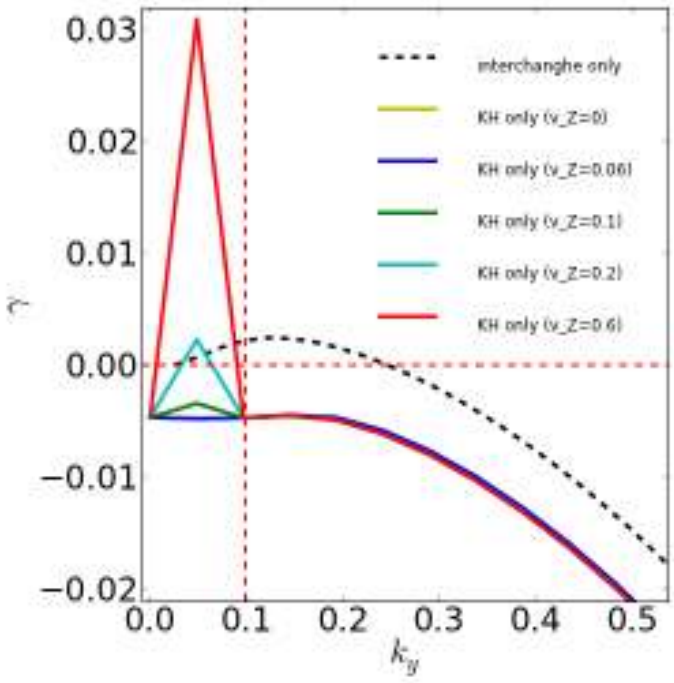

Figure 6.2: the interchange (dashed black line) and KH growthrate for different values of V_z at given $\kappa = 0.1$ in function of k_y

From eq.6.1.1 three different contributions to the growthrate can be distinguished:

- **Interchange terms.** The terms on the first line, red font, are related to the standard interchange instability. If one assumes that there are no zonal flows $V_z = 0$, the interchange forcing term defined as $Gi = (k_y g)/(k^2 L_n \sigma)$ controls the growthrate instability.

- **KH terms.** The terms on the second line, black font, identify the terms related to the pure KH instability, i.e. in case $V_z \neq 0$ and $G_I = 0$. One can readily observe that the KH instability growthrate depends on the amplitude of the ZF, $V_z = \kappa \Phi_z(kx)$ and only the region of the spectrum, where the condition $V_1 V_1' < 0$ is true, is Kelvin-Helmoltx unstable.

- **Interchange + KH terms.** The terms on the third line take into account the interplay between the interchange and KH instabilities. Interchange mechanism, G terms, can actually destabilize the ZF if the $G_i < 0$, namely on the high field side of the tokamak, where both the curvature force and pressure gradient are point outward of the plasma. In this region, the standard interchange modes are stable.

We present in fig.6.2 how the growthrate in function of k_y is changed, if the interchange or KH alone is the driving instability. The growthrate due to interchange instability is calculated using the reference parameters (tab.5.1) and the equation presented in Section 5.1.3. The KH instability growthrate is calculated for different values of V_z. If $V_z < 0.2$ the KH instability appears to be negligible compared to interchange. If $V_z > 0.2$, a new

region of the spectrum is linearly excited by the KH instability contribution, i.e. the region $k_y < \kappa$.

From the definition of KH instability growthrate, one expects that if KH modes are destabilized during the relaxation, a signature of KH instability on the potential fluctuations spectra can be identified. As predicted by the linear analysis, shown in fig.6.2, a peak at largest scale, $k_y < \kappa$, should appear. Conversely, in fig.6.3, where the spectrum of the potential fluctuations are compared during the generation and relaxation of the barrier, no increase of the KH modes is observed during the relaxation phase. The spectrum shrinks and expands respectively before and during the turbulent burst, as an 'umbrella effect'. It appears that when the barrier is ON, the spectrum shrinks transferring its energy to the zonal flows. Additionally, by calculating the KH growthrate, taking into account the simulation parameters (tab 5.1) and the maximum value of V_{ZF}, $V_{ZF} = 0.06$, one finds that the KH modes are linearly stable, see fig.6.2 (blue line)

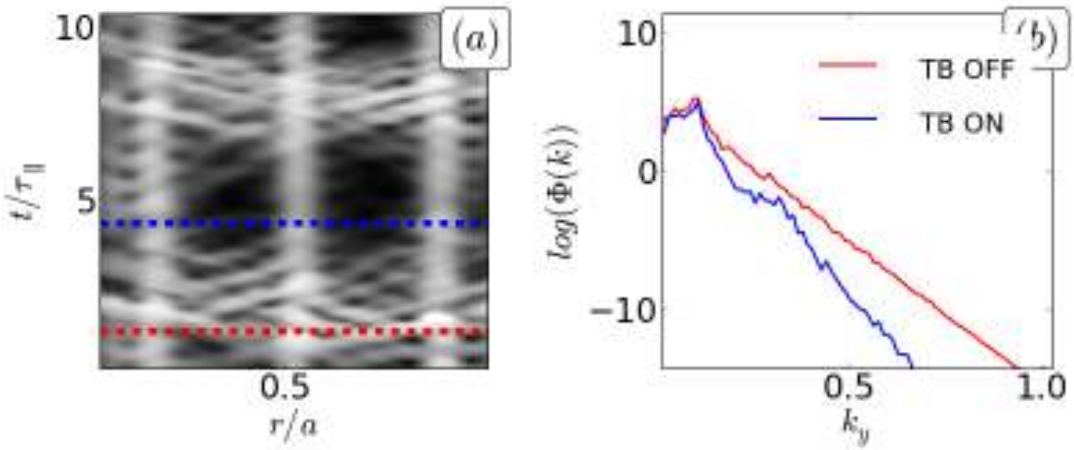

Figure 6.3: (a) R_b in function of time and radial direction. (b) Potential spectrum in function of k_y during the the barrier relaxation (TB OFF, red line) and generation (TB ON, blue line)

Finally, two different limit cases have been defined in order to better identify the role of KH instability.

1. **Collisionless ZF:** one assumes that viscosity ν is set to zero only for the ZF modes, i.e. $\nu_{k_y=0} = 0$. The only possible way for the zonal flow to relax is via KH instability.

2. **Quenched interchange:** the curvature term g is set equal to zero before the transport barrier relaxation, in such a way that the impact of the interchange and KH on the potential spectrum can be separated.

In both cases, we can conclude that the role of KH in damping the ZF is negligible.

For case (1), i.e. collisionless ZF, if the viscosity term is set to zero, $\nu_{k_y=0} = 0$, the system is locked in the zonal flow regime until the turbulence is totally suppressed. For the chose case, the ZF sink is controlled by the viscosity term. The resilience time of the

zonal flows is defined by the viscosity term.

For case (2), i.e. quenched interchange, once the driving force is switched off, $g = 0$, turbulence starts decaying. When the turbulence is linearly suppressed, one can observe that the most excited modes in the spectrum corresponds to the one excited by KH, as foreseen by the linear analysis (see fig.6.4). The KH instability impact on the spectrum is negligible compared to that of interchange instability. Only by suppressing the interchange drive, can one observe the KH modes appearing.

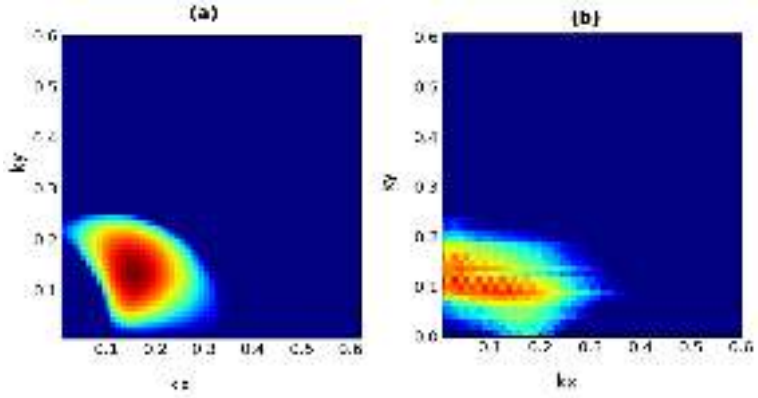

Figure 6.4: (a) the KH instability growthrate calculated by the linear analysis in function of k_x, k_y, (b) the potential spectrum in function of k_x, k_y after switching off the turbulence driving

6.1.2 RS sink or source of ZF: study of three modes coupling

In this section, we address the role of non linear coupling as zonal flows source and sink.

Starting from the TOKAM2D equations and assuming the absence of interchange forcing, the vorticity equation is derived as following

$$\partial_t W \quad + \quad [\phi, W] + g\partial_y n = \nu_\perp \Delta_\perp W + j \tag{6.3}$$

where W is the vorticity $W = \Delta_\perp \Phi$, x and y, the space coordinates corresponds to the poloidal angle and radial direction, g is the curvature term and j is the parallel current loss. The convective turbulent transport $[\Phi, W] = \partial_x(W(-\partial_y \Phi)) + \partial_y(W(\partial_x \Phi))$ competes with the small scale diffusive transport with coefficient ν. The loss term is defined such that $< j >_y = 0$. Averaging along the flux surfaces, there is no current loss in parallel direction and the zonal flows $V_z = \partial_x < \Phi >_y$ evolution can than be rewritten as

$$\partial_t V_z + \partial_x RS - \nu \Delta_x V_z = 0 \tag{6.4}$$

where $RS(x) =< \partial_x \tilde{\Phi} \partial_y \tilde{\Phi} >_y$ is the Reynold stress term and $\tilde{\Phi} = \Phi - < \Phi >_y$ is the potential fluctuations.

The interplay between zonal and turbulent modes can be addressed in the framework of non linear three mode coupling: the zonal flow, the streamer and the more homogeneous turbulent mode, respectively $\Phi_z(\kappa, 0), \Phi_s(0, k_s), \Phi_t(\kappa, k_s)$.

Two cases of study are proposed, comparable to the regimes previously mentioned:

(a) **The condensation of the ZF.** In the case where the streamer Φ_s represents the equilibrium profile and Φ_z, Φ_t are the small amplitude perturbations. If the growthrate is positive the turbulence is transferring energy to ZFs.

(b) **The Kelvin Helmoltz (KH) instability.** The ZF mode is the equilibrium profile and Φ_z, Φ_t are the perturbations. Positive growthrate means that the ZF is transferring energy to turbulence.

Let us first consider the case (b) where the Kelvin Helmoltz instability is the primary focus. We can study such instability in a more general way defining the perturbations as $\phi_l(k_{xl}, k_y)$, $\phi_{l+1}(k_{xl+1}, k_y)$, where $k_{xl} = l\kappa$ with $l = [0, \text{inf}]$ with $l \in \mathbb{N}$, the dispersion relation can be rewritten as

$$[\gamma + \frac{\gamma_l + \gamma_{l+1}}{2}]^2 = -V_l V_l' k_y^2 \kappa^2 |\Phi_z|^2 - \gamma_l \gamma_{l+1} + \frac{(\gamma_l + \gamma_{l+1})^2}{4} \tag{6.5}$$

where $\gamma_i = \nu k_i^2 + \sigma/k_i^2$, $k_i^2 = k_{xi}^2 + k_y^2$ with $i = l, l+1$ and coupling terms are $V_l = \left(k_l^2 - \kappa^2\right)/k_{l+1}^2$, $V_l' = \left(k_{l+1}^2 - \kappa^2\right)/k_l^2$. The instability condition is then $-V_l V_l' k_y^2 \kappa^2 |\Phi_z|^2 - \gamma_1 \gamma_{l+1} > 0$. If we define $R_l = -\frac{V_l V_l' k_y^2 \kappa^2 |\Phi_z|^2}{\gamma_l \gamma_{l+1}}$, then $R_l > 1$ is the instability condition, which leads to define three new variables X_l, Y_l, Z_l such that $X^2 = \frac{k_{xl}^2 + k_y^2}{K^2}$, $Y_l = \frac{k_{xl}}{\kappa}$ and $Z_l^2 = X_l^2 - Y_l^2 = \frac{k_{yl}^2}{\kappa^2}$. Let be $\bar{k}$ such that $\nu \bar{k}^2 = \frac{\sigma}{\bar{k}^2}$. In this way we rewrite $R_l = h^2 F(x, y, l)/H(X, y, l)$ such that

$$F = -V_l V_l' \Big(\frac{|\Phi_z| \kappa^4}{k_l k_{l+1}}\Big)^2 = (X_l^2 - Y_l^2)(X_l^2 - 1)(X_l^2 + 2Y_l) \tag{6.6a}$$

$$H = \gamma_1 \gamma_2 \Big(\frac{\sigma}{k_l k_{l+1}}\Big)^2 = \Big(\frac{k_l^4}{\bar{k}^4} + 1\Big)\Big(\frac{k_{l+1}^4}{\bar{k}^4} + 1\Big) \; ; \; h^2 = |\Phi_z|^2 \frac{\kappa^8}{\sigma^2} \tag{6.6b}$$

By definition H and h^2 are positive and $X_l^2 \geq Y_l^2$, therefore R_l is positive if $(X_l^2 - 1)(X_l^2 + 2Y_l) < 0$, which corresponds to two possible cases

$$Y_l^2 + Z_l^2 < 1 \;\; \cap \;\; (Y_l + 1)^2 + Z_l^2 > 1 \quad or \quad Y_l^2 + Z_l^2 > 1 \;\; \cap \;\; (Y_l + 1)^2 + Z_l^2 < 1 \tag{6.7}$$

In fig.6.5(a) the growthrate amplitude in function of the perturbation wave number is plotted. Additionally, more one couple of modes can be taken into account. The following linear system is derived set of coupled equations then describes the system:

$$\begin{pmatrix} \Omega_1 & V_1 & 0 & \cdots & 0 \\ -V_1' & \Omega_2 & V_2 & \cdots & 0 \\ 0 & \ddots & \ddots & \ddots & V_n \\ 0 & 0 & \cdots & V_n' & \Omega_n \end{pmatrix} \begin{pmatrix} \Phi_l \\ \Phi_2 \\ \vdots \\ \Phi_n \end{pmatrix} = 0$$

Solving the dispersion relation, one observes that the unstable spectrum region is expands in k_x the number of coupled perturbations increases. Conversely, the condition $\gamma > 0 \Rightarrow |k_y|/|\kappa| < 1$ still holds (see fig.6.5(b)-(d), where $\gamma \tau_{\|}$ is plotted in function of k_x, k_y respectively in the case of three, four and five modes contribution).

If the same procedure is repeated but considering the streamers as equilibrium condition and Φ_z, Φ_t as perturbations (case (a)), the opposite condition is recovered: the region

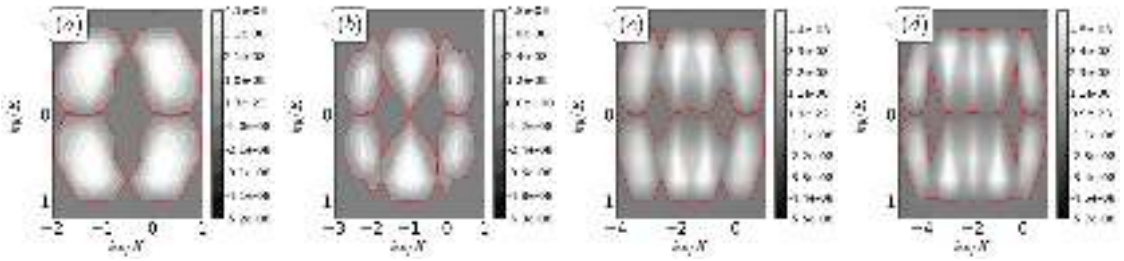

Figure 6.5: (a)the linear growthrate $\gamma\tau_{\|}$ in function of k_y and k_x in case of 2 coupled modes, (b) 3 modes, (c) 4 modes and (d) 5 modes

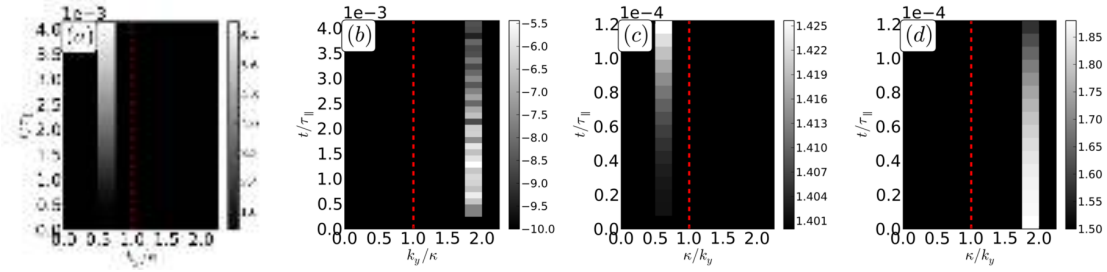

Figure 6.6: (a) evolution in time of the poloidal spectrum k_y if a streamer Φ_{s1} or (b) Φ_{s2} is perturbed,(c) evolution in time of the radial spectrum k_x if a zonal flow Φ_{z1} or (d) Φ_{z2} is perturbed.

of spectrum of positive growthrate is constrained by $|k_y|/|\kappa| > 1$.

To verify the analytical observation, the two regimes are now modeled. For (b) case, a equilibrium profile $\Phi_z(\kappa = 0.024, 0)$ is assumed and two cases with different streamer perturbation are considered $\Phi_l = \Phi_{s1}(0, \kappa/2), \Phi_{l+1} = \Phi_{s2}(0, 7/4\kappa)$. From fig.6.6(a)-(b) we can observe that the perturbation Φ_l is growing according to the linear analysis prediction, i.e. the growthrate is approximately $\gamma\tau_{\|} \approx 4 \cdot 10^{-8}$. Conversely, the streamers with poloidal size smaller than the ZF radial width is damped.

If one considers the streamers like mode $\Phi_s(0, k_s = 0.024)$ as equilibrium condition and two cases with different zonal flows perturbations, respectively $\Phi_{z1}(k_s/2, 0), \Phi_{z2}(7/4k_s, 0)$. One can observe that the zonal flow is excited only if its radial width is larger than the poloidal width of the streamer, fig.6.6(c)-(d).

One can then separate the streamers modes into two different groups, the 'B-modes region' and 'S-modes region'. 'B-modes' represent the big scales structures, i.e. the modes such that $k_y < \kappa$. The B-modes cannot act as a source for zonal flows. The 'S-mode' represent the small scale structures, such that $k_y > \kappa$, the S-modes transfer energy to the zonal flows and cannot act as a sink for zonal flows.

6.2 Control of the transition from *turbulence-dominated* to *ZF-dominated* regime

We present here the transport regimes accessed by the TOKAM2D model, namely *turbulence-dominated* and *ZF-dominated* regime. The key parameter controlling the transition is

defined.

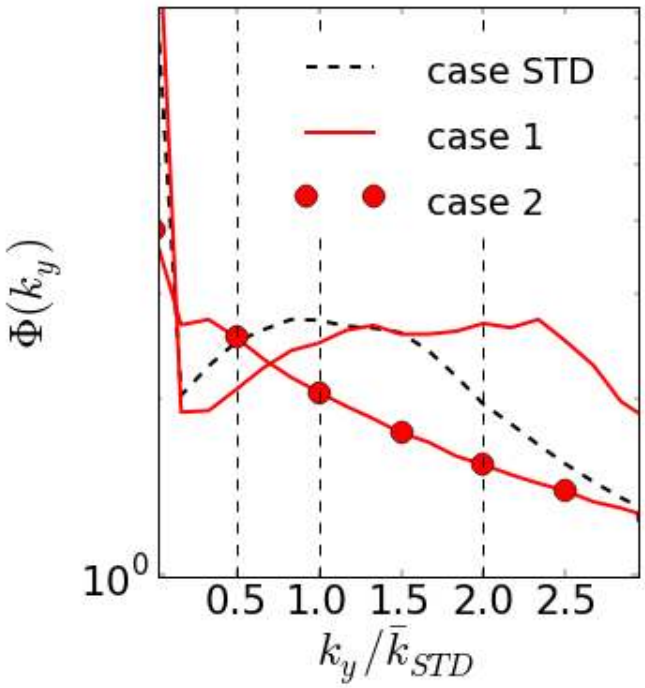

Figure 6.7: potential spectrum variation for the standard case (black line), case(1) (red line) and case(2)(red dotted line)

Departing from the analytical works, detailed in the previous section, one can now identify in TOKAM2D the impact of B-modes and S-modes in the interplay between zonal flows and turbulence. The respective importance of the S-modes and B-modes regions can be controlled via $\bar{k} = (\sigma/2\nu)^{1/4}$, the least damped mode. If the S-modes, namely the source for zonal flows, is dominant, the zonal flows govern the transport properties. Conversely, if the B-modes are dominant, turbulence then characterizes transport.

Two extreme cases from the standard case, where the value of σ has been varied in order to modifies the size of the most unstable mode, are compared with the reference case. In case (1), we increase the value of σ such that $\sigma_1 = \sigma_{std} \cdot 16$ and the most unstable wave vector is varied from $\bar{k}_{std}$ to $\bar{k}_1 = \bar{k}_{std} \cdot 2$, where *std* stands for reference (standard) case defined in the table 5.1. The potential fluctuations spectrum is plotted on in fig.6.7 (black line).

In case (2), σ is reduced such that $\sigma_2 = \sigma_{std}/16$, so that the most unstable wave vector is decreased to $\bar{k}_2 = \bar{k}_{std}/2$. Comparing the potential fluctuation spectrum with case (1), the typical turbulence size is increased as well as the ratio between B and S modes. From the definition of B-modes and S-modes, one expects that in case (1) the transfer of energy from turbulence to ZF is increased from standard case, while decreasing for case (2).

A good agreement is found between the simulation and the analytical work. The y-

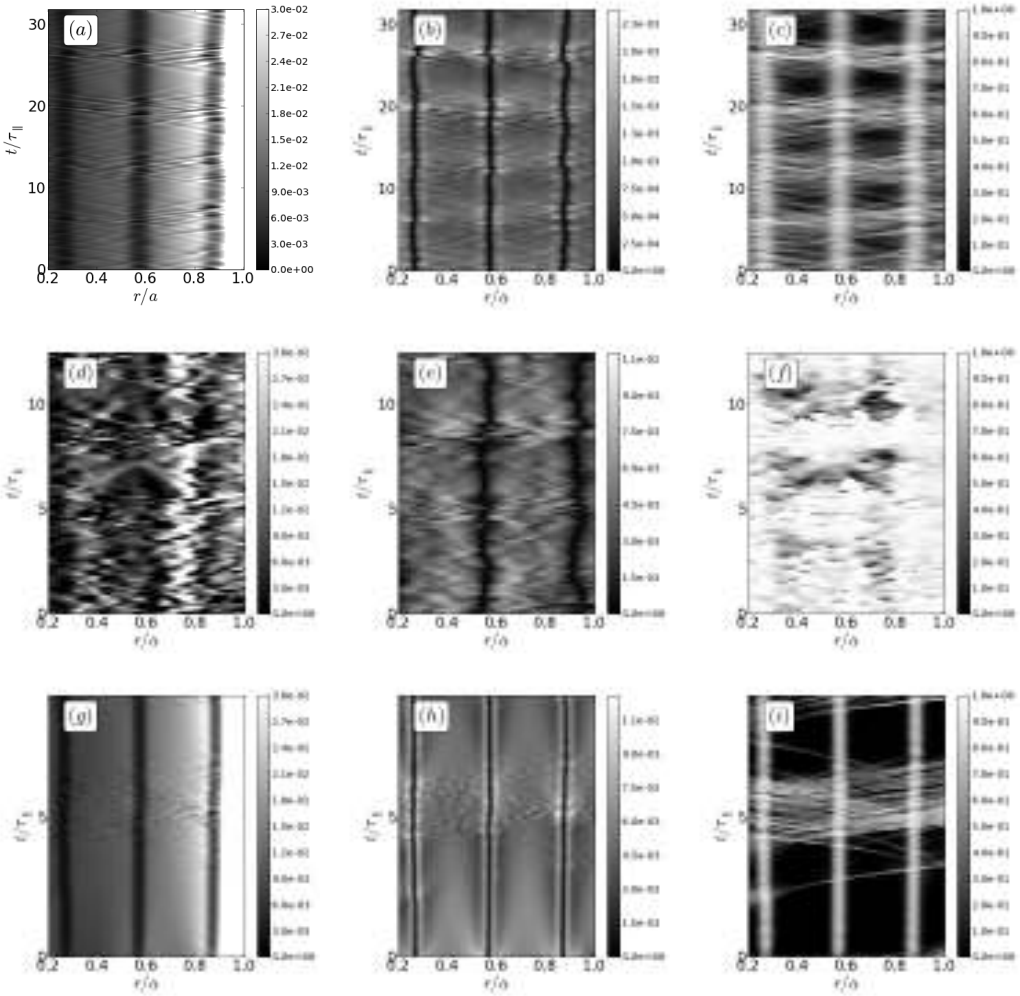

Figure 6.8: (a) $1/L_n$, (b) W, (c) R_b (withe color corresponds to $R_b = 1$, black to $R_b = 0$) for the standard case, (d) $1/L_n$, (e) W, (f) R_b at large injection scale (case 2), (g) $1/L_n$, (h) W, (i) R_b at small injection scale (case 1).

averaged density gradient $1/L_n$, fig.6.8(a)-(d)-(g), and the y-averaged vorticity $< W >= -\partial_x V_z$, fig.6.8(b)-(e)-(h), of the three cases are shown. One can readily observe how the resilience time of the barrier is strongly effected. In case where S modes dominate (case 1), one can identify the large scale patterns that govern the transport properties. One turbulent burst event is detected and stable jets develop. The position of the latter does not vary in time. On the contrary for case (2), when the B modes dominate, no sharp variation of the density gradient can be identified and the ExB shear patterns are continuously reorganized, so that no isolated relaxation event can be identified. Even if signatures of large scale reorganization still appear, one can observe that these resilient structures are not able to deplete all the turbulence energy. Finally comparing the barrier efficiency R_b, fig.6.8(c)-(f)-(i), we can see that, in the regime dominated by the S modes, the turbulence is suppressed by the ZF stopping capability, while in the other case the turbulence is the main feature of transport.

6.3 TOKAM2D versus Hagesawa Mima

Hagesawa Mima Based model and TOKAM2D models present strong similarities in terms of large scale pattern formation. However a proper comparison of these models has not been undertaken yet. In this section, we address the mechanism controlling the transition from *turbulence-dominated* to *ZF-dominated*.

In the astrophysics and geophysics framework, the jets-like dynamics [MBS05, VS05, PK13, TM13, SP08] are often studied via two dimensional equations based on the Hagesawa Mima model. Such equations present also strong similarities with the TOKAM2D model, if we assume that the density and electric potential fields are proportional to each other, i.e. $n \propto \phi$, which is the case for adiabatic electrons.

Let us consider the case with energy injection at small scales, linear damping by friction, barotropic, 2D vorticity for a fluid on a rotating sphere,

$$\partial_t W + [\Phi, W] + \beta \partial_x (\nabla^{-2} W) = D + \xi \tag{6.8}$$

where W is the vorticity, D the sink term, including large- and small-scale and ξ is a forcing at prescribed wavelength. Considering that a coupling term with the pressure equation is not included in the model, an ad-hoc forcing is used to inject energy into the system. In most of cases $D = \nu\nabla^2\zeta + \lambda\zeta$, namely the large scale drag is linear (i.e. comparing the following equation with the TOKAM2D vorticity equation, one can recover that the small scale friction λ corresponds to $\sigma\nabla^{-2}$). The β-term, representing the gradient of the Coriolis parameter, corresponds to the curvature term g in TOKAM2D. With this notation the x axis corresponds to the y axis in TOKAM2D and viceversa.

In such model that can be seen as a simplified version of TOKAM2D, the system can shift between two regimes: friction-dominated regime and zonation or zonostrophic regime, dominated respectively by isotropic turbulence and by jet-like patterns.

Given the energy spectrum defined by:

$$E(n) = \sum_{m=-n}^{n} \varepsilon(n,m) = \frac{n(n+1)}{4} \sum_{m=-n}^{n} < |\phi_n^m|^2 > \tag{6.9}$$

where $\varepsilon(n,m)$ the energy density spectrum for mode (n,m), being n the zonal wavenumber and m the total wavenumber, respectively k_x, k_y in TOKAM2D. The energy density spectrum for zonal flow modes is defined by $E_Z = \varepsilon(n,0)$ (zonal energy), hence the energy for the non zonal or residual mode as $E_R(n) = E(n) - E_Z$ (residual energy).

Two different energy spectra have been identified for the zonation and friction-dominated regime. On one hand, the energy spectrum of the zonostrophic regime presents two different slopes describing the inverse cascade, which are labeled the isotropic and anisotropic slopes (see fig.6.9) [SGD02]. The two slopes are due to different dominant modes in the two regions of the spectrum, namely the zonal E_z and residual modes E_r.
On the other hand, if the spectrum follows the classical Kolgomorow power law $n^{-5/3}$, the system is in the friction dominated regime.

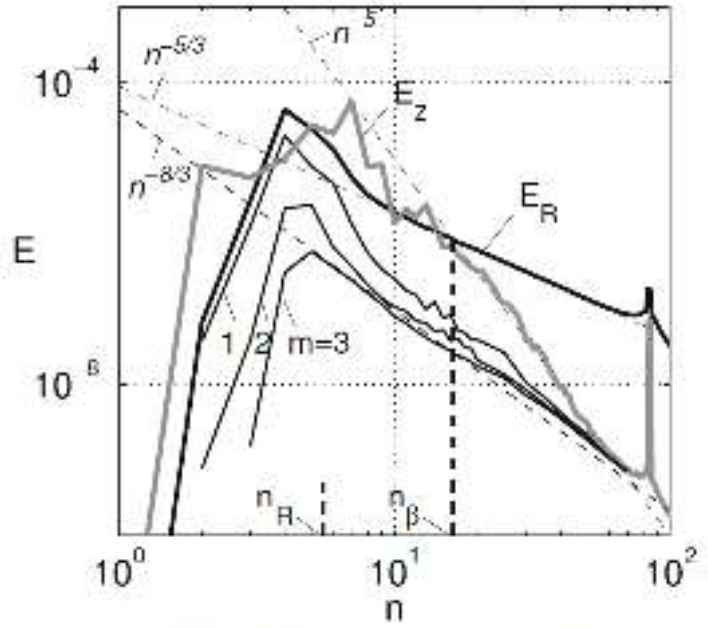

Fig. 6 The kinetic energy spectra for a zonostrophic regime ($n_R = 5.5$, $n_\beta = 16.2$). The *thick gray and black solid lines* show the zonal and nonzonal spectra, $E_Z(n)$ and $E_{NZ}(n)$, respectively, while the *thin lines* show the modal spectra, $\mathcal{E}(n, m)$. The values of m are shown near the *lines*. The *dashed straight lines* correspond to the spectra 15a, 15b, and 11

Figure 6.9: the Galperin energy spectrum for the zonostrophic regime [GSD10]

In order to move from one regime to the other, three key dimensional parameters depending on the input parameters are defined: the Rhines scale n_R, the β-scale n_β and the source scale n_ξ.

n_R characterizes the large-scale flow, i.e. in the zonostrophic regime it would correspond to the typical width of the zonal jets. It is defined as $n_R = \sqrt{\beta/(2v_{rms}}$ and thus gives the ratio between the non linear and the linear β term. Such a definition does not take into account the large scale dissipation that actually is a key parameter in setting an upper bound to the inverse cascade. One can then redefine $v_{rms} = \sqrt{2E}$, where the energy level can be rewritten in function of the control parameter such as $E = \epsilon/2\lambda$, being ϵ the energy injection rate, and the Rhines number [VM93] as

$$n_R = \beta^{1/2}(\lambda/4\epsilon)^{1/4} \tag{6.10}$$

Another important scale is n_β that characterizes the anisotropization threshold of the inverse cascade, defined as

$$n_\beta = 0.5(\beta^3/\epsilon)^{1/5} \tag{6.11}$$

Finally n_ξ represents the scale of the injected energy, in this case an input parameter.

An accurate criteria is used to define the transport regime: if $R_B = n_\beta/n_R$, named as Zonostrophy index, is larger than 2.5, corresponds to the zonostrophic regime or zonation,

i.e. governed by zonal flows. Such a necessary condition can be rewritten as $n_R < n_\beta < n_\xi$, namely the energy is injected at small scales, then by inverse cascade it yields the isotropic spectrum from n_β to n_ξ. It is there necessary a range of modes in the zonostrophic range, the anisotropic region($n_R - n_\beta$), to access the zonation regime.

6.3.1 Comparison between Hagesawa Mima Based models and TOKAM2D

To analyze the TOKAM2D results given the analysis of the HMB model, we present here a comparison between the zonation and friction-dominated regimes observed in the HMB context and the *ZF-dominated* and *turbulence-dominated* regimes in TOKAM2D.

We first present the energy spectrum and the zonostrophic index as introduced in the previous section. We choose the two simulations that characterize the *turbulence-dominated* and *ZF-dominated* (fig.6.8).

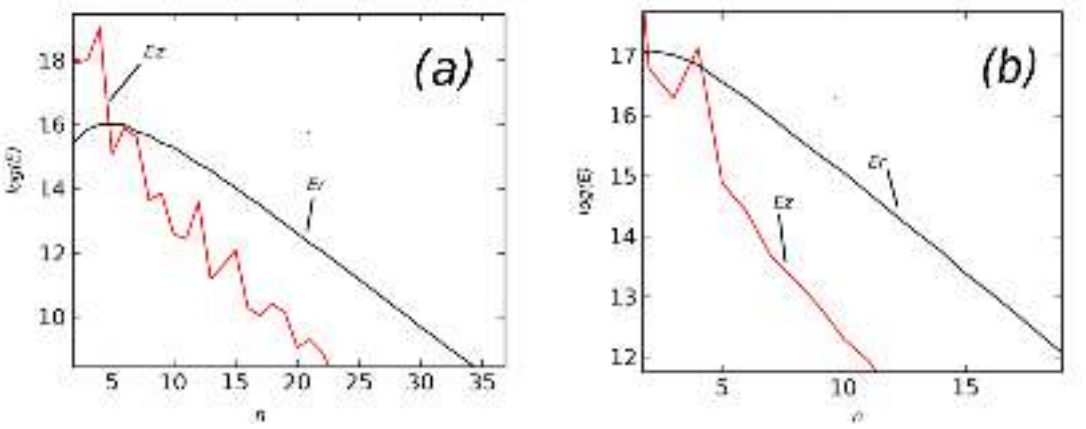

Figure 6.10: the zonal (red) and residual (black) energy spectrum for zonation (a) and fully turbulent (b) regime in the edge in function of the zonal wave number n, i.e. k_x

Splitting the energy spectrum in zonal flow $E_Z(k_x)$ and residual $E_r(k_x)$ contributions, fig.6.10(a)-(b), one can observe how the zonal and residual energy spectra change with σ. In the first case, fig.6.10(a), the energy in the zonal flow spectrum slope becomes larger than that of the residual at large scale, as predicted for the zonation regime. In the second case, fig.6.10(b), reducing σ, the residual energy remains larger than $E_z(k_x)$ until the largest scale $k_x = 2\pi/L_x$.

On one hand, we can observe a good agreement between the spectrum predicted by Sukoriansky [SGD02] for the HMB case and the TOKAM2D case. For the *ZF-dominated* regimes, the spectrum is governed by two different slopes. For the *turbulence-dominated* regime, a single slope governs the transport.

On the other hand, one can observe that at largest scale the zonal energy spectrum is higher than the residual one in both cases in the limit of $k_x \to 0$. Such result is due to the fact that, in the edge, no damping term is acting on the ZF mode.

We list here the differences between TOKAM2D and HMB model that have to be taken into account in order to rewrite n_R, n_β and the consequent zonostrophic index R_β :

- **Drag term.** It is not linear, the so-called hypofriction term does not act in the same way for all modes, but act selectively on the smallest modes of the system and then yields to a dissipation free region.

- **No ad-hoc vorticity source.** The energy is injected via the $g\partial_y n$ term, which couples the vorticity with the density equation. The energy injection rate ϵ is not a free parameter.

- **No large scale damping for the ZF.** The Rhines scale, controlling the halting scale of the inverse cascade is equal to zero for the ZFs, $n_R = 0$.

- **Anysotropic injection scale.** We need to take into account that the energy injection $n_\xi = \bar{k}$ typical scale is much larger that the one used in the HMB model, additionally the forcing is already anisotropic. Therefore we assume that n_β can be defined as $n_\beta = n_\xi = 1/\bar{k} = (\nu/2\sigma)^{1/4}$, the energy injection scale

The Rhines scale is calculated near marginal instability as the balance between g and dissipation scale, i.e. $n_R = (\nu\sigma_\phi)/g$. The zonostrophic index can be then calculated as $R_\beta = g\sigma^{-3/4}\nu^{-5/4}$. The transition from turbulent to zonation regime should then be achieved either by decreasing the g term or increasing the dissipation.

According to the R_β definition, by increasing σ, the zonation index is decreased and the system moves towards a fully turbulent regime. Conversely, the transition observed in TOKAM2D shows that the fully turbulent regime can be accessed only by decreasing σ. The definition of R_β is not valid to classify the different regimes accessed in TOKAM2D.

One can expect that such contradiction is related to the ZF condition: by varying σ, both the anysotropization scale and Rhines scale are changed, except for the ZFs, where the Rhines scale is constrained to be zero. Considering n_R as constant, we expect to control the transition by varying n_β. Such observation is consistent with the energy transfer mechanism we previously presented and the definition of the B and S-modes: by increasing n_β, which corresponds to increasing σ, the inverse cascade region that favors the transfer of energy from turbulence to zonal flows, is larger and the zonal flows dominate transport. Even if R_β cannot be used as valid index to identify the two regimes, an agreement on the crucial role of n_β for our model is found.

6.3.2 Zonation vs *ZF-dominated* regime

The transition from *turbulence-* to *ZF-dominated* can be achieved in the edge and is controlled by the typical forcing scale $\bar{k}$. If the forcing scale is decreased, the confinement is improved and the *ZF-dominated* regime is accessed. Conversely, decreasing the forcing scale, the system is governed by turbulence.

The R_β index definition appears no more valid in the framework of TOKAM2D model both in the edge and SOL (detailed in the Annex E). Such classification appears then to be correct only in the framework of an ad-hoc forcing term, decoupled by the system. In TOKAM2D model, the drag term controls not only the large scales damping, as in the Hagesawa Mima case, but also the injection scale $n_\xi = \bar{k} = \sqrt{\sigma/2\nu}$. The forcing is not decoupled from the system. However, for the edge region, the zonal flows are no more

dependent on σ. Hence, the zonation regime is achieved only by constraining the zonal flow drag term to zero, i.e. $\sigma(\Phi - < \Phi >_y)$.

An ad-hoc forcing should be implemented in TOKAM2D in order to properly verify the zonostrophic index and better identify the role of the forcing in accessing the zonation regime.

Chapter 7

Transport barrier generation in region of different zonal flow dynamics: comparison with experiments

Contents

It has been observed that a transport barrier can self-generate at the edge of the plasma, improving the confinement property of the machine [WBB+82]. The pressure is confined by the barrier inside the separatrix, i.e. at the interface between open and closed field lines. A steep gradient of the pressure profile, also known as pedestal, appears there. This regime is named H-mode, where H stands for High confinement. Compared to the L-mode regime, Low confinement regime, where no barrier appears at the separatrix, the confinement time is doubled.

The transition from L- to H-mode appears to be controlled by the injected power. The power threshold is defined by an empirical scaling law. A complete understanding of the mechanism driving the transition is still missing. It has been admitted within the fusion community that the pedestal development should be addressed by taking into account the real geometry of a Tokamak and accurate particle sources. These considerably increase the complexity of the model and the computational effort and narrow the relevance of this physics to Tokamak plasmas.

We present here a self-organized pedestal formation in order to seek for the simplest possible model isolating the crucial elements of the underlying mechanism. The result is a universal transition from turbulent (L-mode) to ZF-dominated regime (H-mode). In the H-mode, the pedestal is localized at the interface between regions where different zonal flow damping appears, i.e. between edge and SOL. The model provides the key elements to understand the mechanism of LH transition and gives a new tool to answer some of the main questions related to the H-mode, such as:

Can a 2D model be sufficient to simulate the pedestal formation? We identify the necessary elements to model the pedestal via a 2D turbulent code. A rich dynamics is observed in the model, with turbulence and transport barrier interplay.

Can the LH transition be accessed by the model? The conditions for the barrier to be generated are identified and the parameters that govern the energy exchange from turbulence to the ZF are defined. The pedestal height and width are analyzed, one finds in particular that the barrier expands on both sides of the interface.

Are the numerical results comparable with experimental observations? Characteristic properties of the LH transition observed experimentally are found in TOKAM2D model. The power threshold scaling is rewritten in function of the model parameters to identify if the LH transition controlling parameters found in the model agrees with the empirical law.

7.1 Can a 2D model be sufficient to simulate the pedestal formation?

The key features that make TOKAM2D suitable for the study of the pedestal formation are presented here. The dynamics of pedestal generation and saturation are introduced.

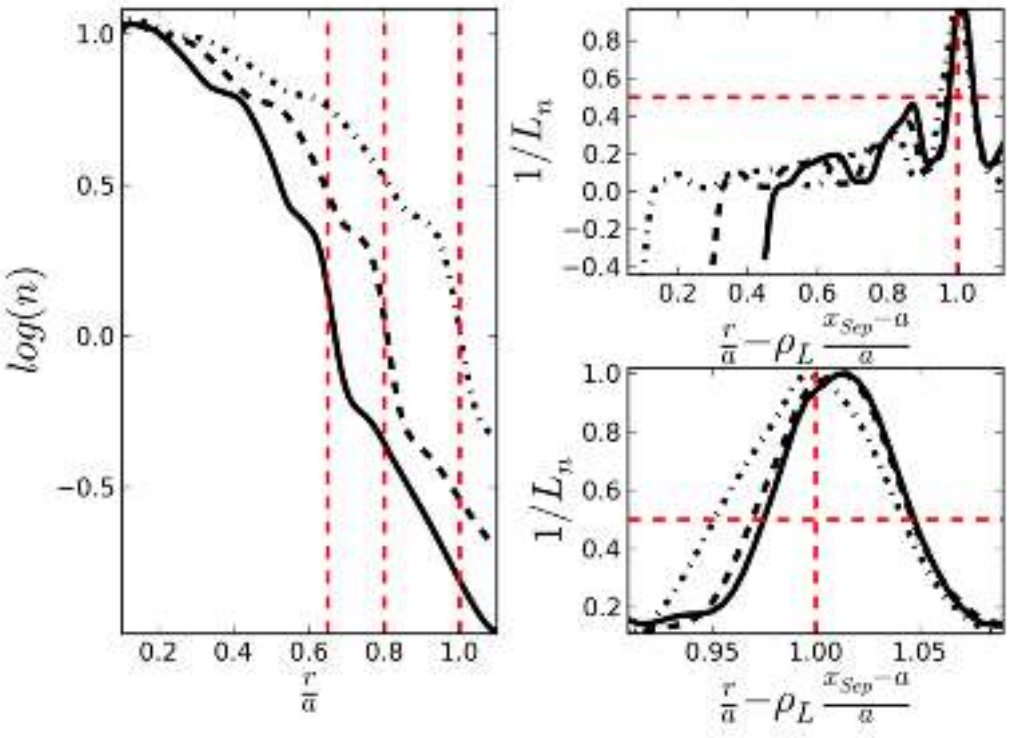

Figure 7.1: (a) pedestal formation in density profile for different positions of the separatrix, plain $x_{Sep} = 110$, dashed $x_{Sep} = 140$, desh-dotted $x_{Sep} = 180$(b) the density gradient profile of the shifterd radius ,(c)a zoom on the pedestal region

7.1.1 The pedestal at edge-SOL interface

TOKAM2D can model the transport in the edge and SOL regions. The change in field line properties at the separatrix is taken into account by a mask function $\chi(x)$, $\chi(x > x_{Sep}) = 0$ and $\chi(x \leq x_{Sep}) = 1$, acting on the parallel transport terms, see Section 2.3.

We present here the first simulations of TOKAM2D edge & SOL, where closed (edge) and open filed lines (SOL) region are simulated together. A barrier is readily observed at the interface between the two regions, fig.7.1(a).

In order to verify the consistency of the pedestal position, three different density profiles averaged in time and poloidal direction are shown on fig.7.1(a)) where only the position of the separatrix x_{Sep} is modified in the simulations, i.e. $x_{Sep} = 0.6\ x_a$ (continuous line), $x_{Sep} = 0.8\ x_a$ (dashed line) and $x_{Sep} = x_a$, (dash-dot line). One readily observes 4 common features for the different simulations: (1) the barrier characterized by a steep gradient is localized at the separatrix (2) the density e-folding length in the SOL is unchanged, (3) the pedestal region with increased density gradient at the separatrix extends both in the edge and in the SOL region, (4) other regions in the density profile exhibits corrugations (enhanced gradients) in the edge region which drive staircase like profiles [DPDG+10, DPHG+15]. In order to quantify the extent of the barrier in the edge &

SOL regions, we shift the profiles to the same separatrix position and compare the density gradient profiles $1/L_n = -\partial_x n \ / \ n$, fig.7.1(b). The strong density drop observed in the pedestal leads to a marked peak in the profile of $1/L_n$ localized at the separatrix. The barrier extends into both the edge and SOL region and its width is observed to range between 5 % and 10 % of the minor radius in these simulations, fig.7.1(c).

SOL-transport with the present model is comparable to that previously reported when only the SOL region was addressed [SG98, GNH+12] and described in Chapters 3&4. It is characterized by avalanche transport, hence ballistic propagation of fronts and holes, the so-called 'blobs' or filaments. Density and potential fluctuations are large but the mean value of the latter weakly departs from the equilibrium value.

Conversely, transport in the edge region appears to be controlled by the zonal flows. These generate transport barriers (TBs), where the transverse turbulent avalanches are damped and where the background diffusive transport governs a larger fraction of the particle outflux. Regions with large zonal flows shear are correlated with the corrugation of the profile, see fig.7.2(a)&(b). They are characterized by a stopping capability of most of the avalanches both overdense from uphill and holes from downhill. The simulation is characterized by a slow reorganization of the zonal flow pattern as readily observed on the contour plot of the zonal flow shear superimposed on the 2D plot of $1/L_n$, fig.7.2(b).

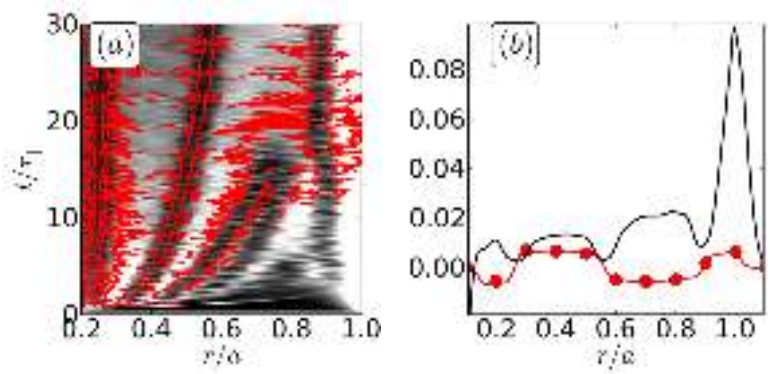

Figure 7.2: (a) $1/L_n$ (gray colormap) and ExB shear (red contour) reorganization in time and space and (b) time and y-averaged profile of the ExB shear (plain black) and density gradient $1/L_n$ (red circles)

Two features are outstanding, the evolution towards a dipolar structure of $< \Phi >_y$ in the edge region while the structure of the maximum value at the separatrix weakly evolves. When a statistical steady state is reached, one can average the profiles over time, fig.7.2(b) and fig.7.3(b). One can see that the total flux Γ_{tot} is radially constant in the edge and decays in the SOL. The turbulent contribution Γ_{turb} exhibits well defined minima, and conversely large values of the diffusive flux Γ_{dif}, of $1/L_n$ and of the zonal flow shear. Narrow regions with strong turbulent transport are localized in the vicinity of the zero shear of zonal flow layers.

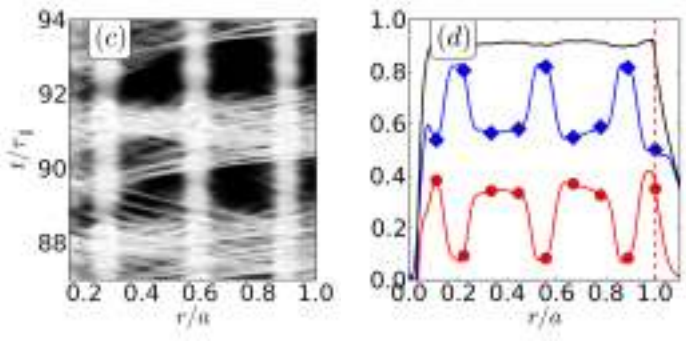

Figure 7.3: (c) parameter R_b used as figure of merit for the transport barriers (white corresponds to $R_b = 1$, no barrier, black to $R_b = 0$, barrier),(d) Radial flux profiles of total flux (black plain line), turbulent flux (blue line & diamonds) and diffusive flux (red line & circles)

7.1.2 Quasi periodic barrier relaxation

In steady state condition, a quasi periodic relaxation of the barriers is observed. We analyze here the barrier relaxation dynamic in time and space.

To quantify the transport barriers stopping capabilities, one defines the ratio between the y-averaged particle fluxes $R_b = \Gamma_{turb}/\Gamma_{tot}$ [FCG+13]. R_b varies between 0 and 1 in steady state and is a measure of the effectiveness of the barrier in reducing turbulent transport. One readily observes on fig.7.3(c) that R_b changes in time and space (x-direction). In space, one finds a dipolar structure with four transport barrier regions, a pedestal at the separatrix that is relatively narrow, two broad barriers in the edge and finally a small transport barrier towards the source region that is strongly linked to the boundary conditions of the model. In time, one can observe quasi-periodic relaxation events characterized by strong turbulent transport across all the barriers. While these events are globally quasi-periodic, the detailed time evolution is specific of each event made of consecutive avalanches that do not extend throughout the edge region[KDK+14, RM11].

The relaxation processes in the edge are also correlated with the large transport bursts in the SOL region, see fig.7.4(a). As can be observed on the time traces, the edge region exhibits a sawtooth structure corresponding to storage and release process by the TB while the SOL region exhibits a pulse-like variation since the SOL acts as the sink for the particles released at each relaxation, fig.7.4(b)&(c).

7.2 Can the LH transition be accessed by the model?

We present here (1) which are the parameters controlling the pedestal height. Furthermore, (2) via a 0-D model, the dynamics of turbulence and zonal flows is characterized and impact of the control parameters on the transition from L to H regimes is investigated.

7.2.1 The condition for pedestal generation

An intuitive scheme to understand how the turbulence interacts with the zonal flows is introduced in fig.7.5. It summarizes the main features observed in the previous chapter and

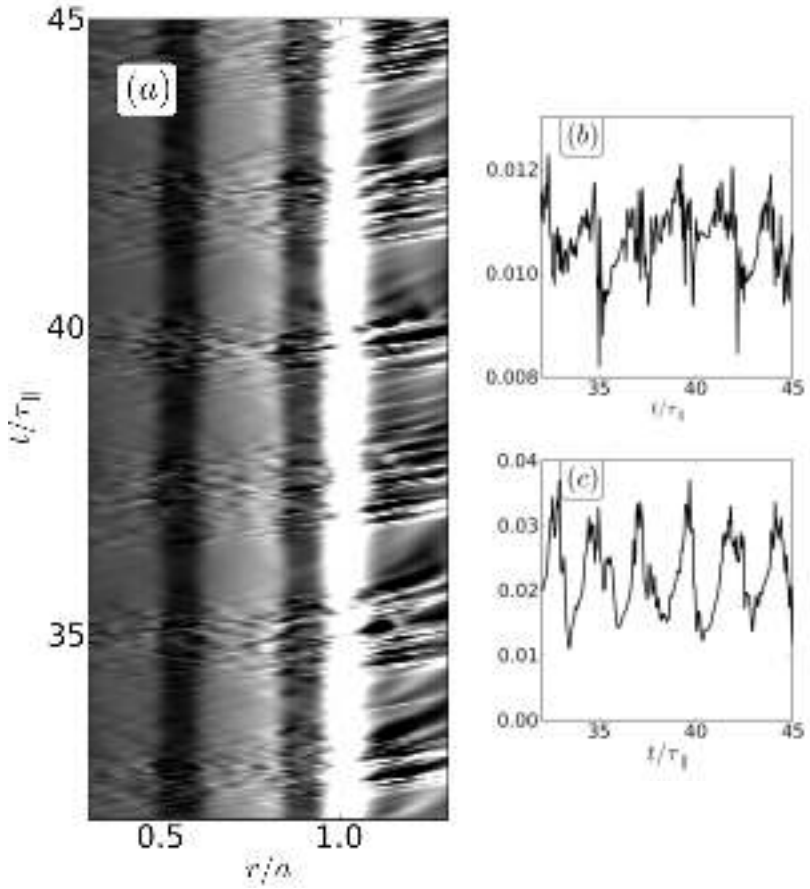

Figure 7.4: (a) $1/L_n$ evolution in time and radial direction: the different transport reorganization in SOL and edge region, evolution of $1/L_n$ in time at given radial positions in the edge (b), and SOL (c).

describes the energy transfer between turbulence and ZFs. The driving of the turbulence drive is controlled by the density gradient (L_n). Increasing the density gradient, turbulence is increased and consequently the Reynolds stress term, responsible for the energy transfer between turbulent and zonal modes. Here a bifurcation appears, the turbulence can be dominated by the large scale B modes or the small scale S modes. One one hand, the S modes act as source of zonal flows, the exchange energy is then from S modes to ZF, the S modes are damped by the transport barrier and the zonal flow energy increases. On the other hand, the B-modes energy cannot be transferred to ZF modes, but only an inverse exchange is allowed, i.e. from ZF to B modes. In our simulation we do not observe the latter energy exchange, because it requires very large ZF shear that do not develop. This is due to two different aspects. The ZF source saturates prior to the threshold and the viscosity governs a large enough damping of the ZF to prevent a gradual build up of the ZF amplitude. The 0-D model also requires that, one determines the interaction rule between the ZF and B-modes, the two classes of modes having comparable size in the radial direction. One can show that the shearing rate capability requires larger and larger shearing rate as the mode to be stabilized is more extended. One can then define the S modes as the class of modes that are stabilized by the zonal flows and thus set therefore the energy gained by the zonal flows, by definition too small to stabilize the B modes.

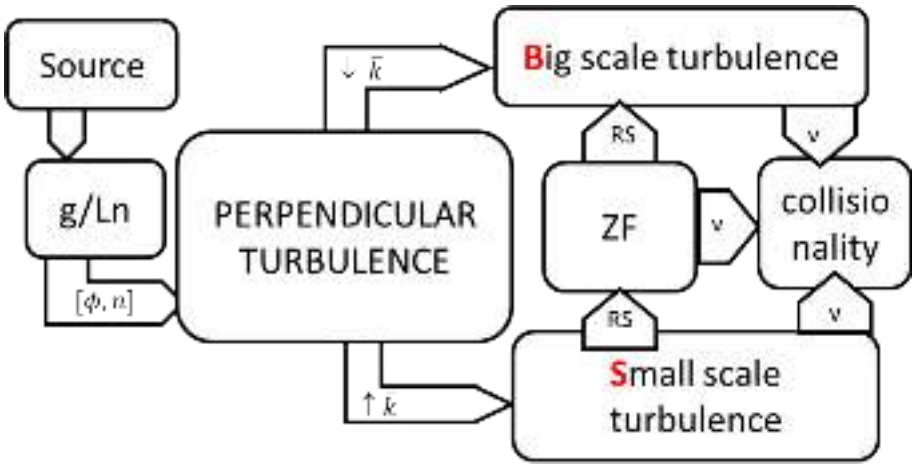

Figure 7.5: Intuitive scheme to explain the exchange of energy from the interchange driven turbulence to the zonal flows

The pedestal generation appears to be connected with the turbulence dominating scale:

- **S modes dominating.** If the spectrum (black line in fig.7.6(b))is characterized by a gap between S and ZF modes, hence with weak B-modes turbulence. The S-region transfers energy via non linear coupling towards the ZF, which tends to store the energy and quench the turbulent transport dominated by S-modes. The ZF are gradually damped by the viscosity, until a relaxation event is triggered and the TB relaxes. ZFs are regenerated by the S-modes turbulent activity and the TBs relax in a quasi-periodic fashion. In this regime, **ZF-dominated**, the ZF damping rate is much smaller than the ZF growth rate. Averaging along several relaxation events, one can observe that turbulence is quenched by the ZF and a pedestal is formed at the separatrix, fig.7.6(a).

- **B modes dominating.** If the gap between S and ZF regions is reduced, hence increasing the B-modes amplitude, (red line in fig.7.6(b)), the system enters in the *turbulence-dominated* regime. The B-modes turbulent activity is not affected by ZF shearing. There is then an increase of the frequency of the turbulent bursts to the point where they cannot be isolated from the steady state transport activity and the pedestal is smeared-out.

If in the edge the *ZF-dominated* regime can be accessed, the pedestal is formed. One can then identify this regime comparable to the H-mode. Conversely, if the edge regime is *turbulence-dominated*, the pedestal is not formed, the regime is L-mode like. The pedestal appears at the interface between two regions with different ZFs dynamic: edge, where ZF can govern the transport, and SOL, where ZF are damped and turbulence governs the transport properties. When turbulence governs the transport also in the edge, no clear interface between edge and SOL can be defined, no pedestal is formed. To move from one regime to the other we need then to control the ratio between S and B modes, namely the turbulence injection scale that is defined by $\bar{k} = (\sigma/\nu)^{1/4}$.

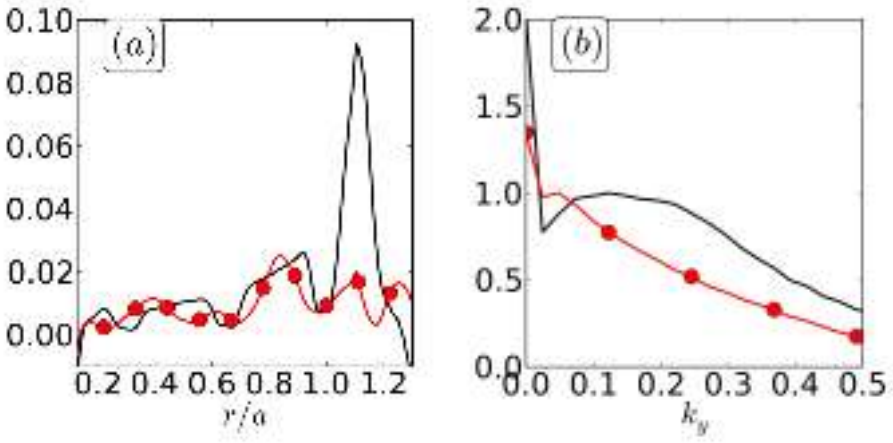

Figure 7.6: (a) Density gradient profile and (b) electric potential spectrum : *zonation-dominated* regime (black plain) and *turbulent-dominated* regime (red circles).

7.2.2 A reduced model to identify the key feature of the transition

The dynamics between zonal flows and turbulence energy exchange is conventionally captured by a 0-D predator-prey model [KD03].As shown in fig.7.10(a), in TOKAM2D simulations such predator-prey dynamics between turbulence and ZF can be also identified.

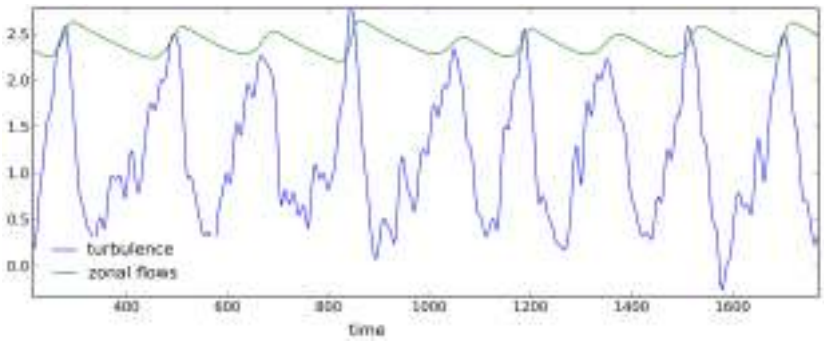

Figure 7.7: Time trace of zonal flows $ZF = |FT(V_Z)|$ (green line) and turbulence $T = \sqrt{|FT(RS)|}$(blue line), FT stands for Fourier Transform

The predator prey approach is equivalent to a reservoir model. Each reservoir, and similarly each species, are then assigned a particular function in the overall pattern of exchange. The basic model is an interplay between turbulence T and the gradient ∇n in the case of TOKAM2D. Since the zonal flows are generated by the turbulence and control the turbulence, we add them as particular species, ZF. Finally we split the turbulence T into two subspecies S and B that have a different interaction with the ZFs. Indeed, the interplay with the ZF is restricted to S, the B modes being the turbulent modes that weakly interact with the ZF. The model thus couples the gradient ∇n, the ZF and the S and B modes. The gradient ∇n is governed by a balance between the source P and transport, both turbulent $T = B + S$ and collisional T^*. The growth rates for S and B modes are γ_s and γ_b respectively and exhibit a threshold in the gradient, ∇n^*. Non-linear saturation of these modes are used, proportional to α_s and α_b. The control parameter of

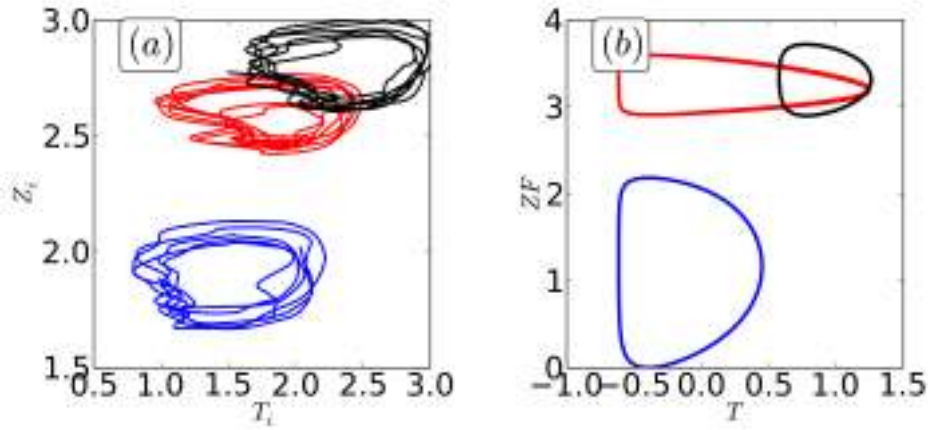

Figure 7.8: Limit cycles: (a) 2D simulation, (b) 0-D model

ZF generation by S is β. The B modes take part in the saturation mechanisms given the $1/T$ dependence of ZF generation and ZF shearing capability. The ZF sink is governed by the viscosity ν.

$$\frac{\partial_t \nabla n}{\nabla n} = \frac{P}{\nabla n} - (T + T^*) \tag{7.1a}$$

$$\frac{\partial_t ZF}{ZF} = \beta \frac{S}{T} - \nu \tag{7.1b}$$

$$\frac{\partial_t S}{S} = \gamma_s (\nabla n - \nabla n^*)(1 - \alpha_s S) - \beta \frac{ZF}{T} \tag{7.1c}$$

$$\frac{\partial_t B}{B} = \gamma_b (\nabla n - \nabla n^*)(1 - \alpha_b B) \tag{7.1d}$$

The limit cycles of the ZF-T interplay in simulations and 0-D model are compared in the $ZF - T$ plane, fig.7.8. ZF and T are readily determined by eq.(7.1) for the 0-D model. For the simulation output of the interchange turbulence, we define $ZF_i = |FT(V_z)|$ and $T_i^2 = |FT(RS)|$, where FT is the 2D Fourier mode energy of the zonal flow velocity V_z and Reynolds stress RS respectively.

The different positions of the cycles in the ZF-T plane are determined by the control parameters: from a reference case, blue trace, increasing the curvature term g, red trace, or decreasing σ, black trace, fig.7.8(a). Increasing g in the simulation leads to an increase of both turbulence and zonal flows. The latter increase being more important, the ratio of ZF_i/T_i also increases, fig.7.8(a) (red line)). A comparable behavior is obtained by increasing γ_s and γ_b, namely the growth rate of the interchange instability -governed by g - fig.7.8(b) (red line). Decreasing σ governs a decrease of $\bar{k}$ so that the spectrum maximum shifts towards the low k_y values, reducing the ZF-S gap. The turbulence amplitude is increased as well as the ratio between B and S modes, fig.7.8(a) (black line). Consistently, this behavior is recovered in the 0-D model by reducing α_s and α_b, the non-linear turbulence saturation, as well as the critical gradient ∇n^*. A similar effect can be obtained by reducing the critical gradient, ∇n_*

7.3 Are numerical results comparable with experimental observations?

We compare here some features of the LH transition observed both in the model and in experiments, such as (1) the spectrum condensation and (2) the LCO cycle. Finally (3) a comparison between the parameters governing the transition found empirically and in TOKAM2D model is carried out.

7.3.1 The spectrum gap

Let us considered here the observation made on the H1 stellarator at a transition from L to H confinement [SXP05]. As shown in fig.7.9, the system reorganizes spontaneously from the L-mode (1) broad spectrum of fluctuations, which extends from small to large scale, to H-mode, the turbulence spectrum shrinks towards a unique injection energy scale and the energy is stored at largest scale possible (ZF). These changes present strong similarity with that observed in TOKAM2D regarding the transition from no-pedestal to pedestal. Indeed, in the latter case, large scale of zonal flows only occurs if a gap between the fluctuation spectrum and that of the the poloidal flows is observed.

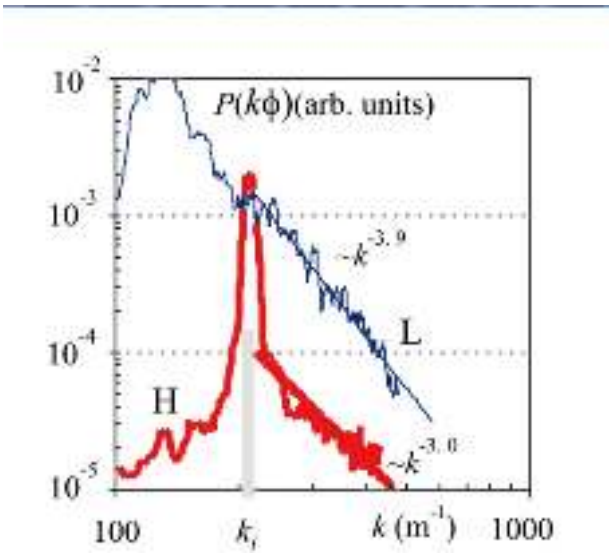

Figure 7.9: Spectrum of the electric potential in function of k in the L-mode (blue line) and H-mode with the evidence of the characteristic gap (red line) [SXP05]

7.3.2 LCO regime: predator-prey dynamics between turbulence and ZF

Predator-prey dynamics between turbulence and ZF have been observed in NSTX, AUG [CAR+11], in TJ-II [EHH+10], DIII-D [SZR+12] and EAST [XSL+14]. In these experiments, the temporal dynamics of the turbulence-flow interaction is defined as Limit Cycle Oscillation (LCO) regime. This regime is observed at transition between L and H mode and is defined as I-phase [XSL+14].

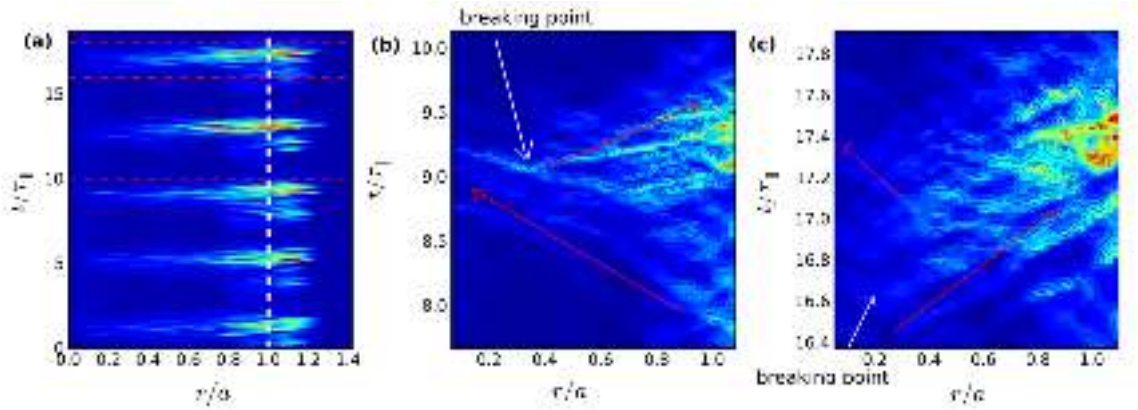

Figure 7.10: (a) turbulent flux normalized by the density in function of time and radius, (b) time interval from $t/\tau_{\|} = 8$ to 10, with turbulence propagating from separatrix towards the edge and viceversa, (c) from $t/\tau_{\|} = 16$ to 18, where flux is moving only from the edge towards the separatrix

The LCO observation made by the gas puff imaging in EAST [XSL+14] shows that the turbulence recovery appears to originate in the vicinity of the separatrix with clear wave fronts propagating both outwards into the far scrape-off layer (SOL) and inwards into the core plasma. In TOKAM2D simulations, fig.7.10, a peak of turbulence originating from the vicinity of the separatrix has also been observed. It appears that the turbulence from the separatrix can move outwards into the SOL. However it can only propagate inward once the barrier has relaxed. The turbulent burst generated at the separatrix does not appear to generate a barrier relaxation from its position. Rather, it appears to trigger the barrier disruption further into the plasma edge. However, the breaking point can change from relaxation to relaxation, as shown in fig.7.10(b)-(c), where the two relaxation events present different dynamics.

7.3.3 Impact of plasma resistivity on the power threshold

The issue is now understanding how the condition for the pedestal appearance can be achieved in fusion machines. In experiments the transition from L to H regime is mostly characterized by an power input threshold.

In TOKAM2D, the transition from L- to H-mode appears to be controlled via an increase of $\sigma\nu = \bar{k}^4$. The resistivity $1/\sigma$ and viscosity ν are a simplified measure of the collisionality respectively in the parallel and perpendicular directions [1]. By decreasing the collisionality, i.e. increasing $\bar{k}$, the transition from L to H is favored. Such observations goes along with the experimental results. The injected power is increased to access the H mode, therefore the temperature is increased and consequently the collisionality decreased.

In the experiments, several empirical laws to determine the power threshold required

[1] One can assume that ν is experimentally much smaller than the one used in the model, the amplitude of this term is constrained by numerical reasons. To study the LH transition, we focus only on the resistivity term.

for the LH transition in multi-machines have been found. We present here two such scaling laws. In the first case the dependence of power threshold on the effective charge, Z_{eff}, is studied [mPTDWGpbTT04]. While in the second scaling, a fitting expression for the input power in function of various parameters has been obtained [MTtICHmTDWG08].

The Z_{eff} scaling

The role of Z_{eff} in the power threshold scaling have been studied, because of the surprising results obtained in several machines, such as JET [MDH+12] and AUG [RRO+13]. Once the carbon walls of the machines have been replaced with Tungsten, a decrease of power threshold to achieve the LH transition has been observed. Hence, a dependence between the effective charge Z_{eff} and the LH power threshold has been found: $P_{thr} \propto Z_{eff}^{0.7}$ [mPTDWGpbTT04]. In the plasma the resistivity $\eta = 1/\sigma$ into parallel direction is proportional to Z_{eff}, $\eta \propto Z_{eff}$[ZMB+90]. This experimental result thus seems to suggest that lowering the plasma resistivity tends to also lower the H-mode power threshold. However, it does no explain why the confinement improvement of these H-modes is reduced compared to the experiments with carbon target plates.

7.3.4 Power threshold derivation from TOKAM2D vorticity equation

We consider the vorticity equation for the edge region

$$\partial_t \Delta\phi + [\phi, \Delta\phi] \quad - \quad \nu_\perp \Delta^2 \phi + \quad g\partial_y n - \sigma_\phi(\phi - < \phi >) = 0 \tag{7.2}$$

, i let us assume a scale separation such as $\phi = (\tilde{\phi} + \bar{\phi})$, where $\bar{\phi} =< \phi >_y$ and $\tilde{\phi} = \phi - \bar{\phi}$, consequently the velocity can be rewritten as $\nabla\bar{\phi} = v_Z$ and$\nabla\tilde{\phi} = v_F$, where F and Z stands respectively for fluctuation and zonal component. We define the kinetic energy of the fluctuation and zonal component as $\varepsilon_Z = v_Z^2$ and $\varepsilon_F = v_F^2$. The vorticity equation can be rewritten as

$$\partial_t v_Z = \partial_x < RS >_y - \nu_\perp \Delta v_Z \tag{7.3}$$

$$\partial_t \nabla v_F = [\tilde{\phi}, \tilde{W}] - \nu_\perp \Delta \nabla v_F - g\partial_y n - \sigma\tilde{\phi} \tag{7.4}$$

where $RS = -\partial_x\phi\partial_y\phi$. If one multiply the eq.7.3-7.4 respectively for v_Z and v_F, one can rewrite the two equations in function of ε_Z and ε_F

$$\partial_t \varepsilon_Z = \partial_x < RS >_y v_Z \quad - \quad \nu_\perp \Delta \varepsilon_Z \tag{7.5}$$

$$\partial_t \varepsilon_F = -P_{F\to Z} \quad - \quad (\gamma - \gamma_W)\varepsilon_F \tag{7.6}$$

where if we assume $\partial_y n = \partial_y \phi$, the forcing term $v_F g\partial_y n$ can be rewritten as $\gamma\varepsilon_F$ considering $\gamma = \sqrt{g}$, while $\gamma_W = \nu\Delta + \sigma/\nabla$ includes the damping terms. The non linear term are defined by $P_{F\to Z}$ but I do not have any idea what is inside.

If we assume a gap between the zonal flow and fluctuation scale as observed during the H mode (a gap appears between fluctuation and zonal mode and represent a necessary

condition for the sustainability of H mode) one can solve the two equations independently. We define the conditions for the H mode to be stable as:

$$\partial_t \varepsilon_Z = 0 \tag{7.7}$$
$$\partial_t \varepsilon_F < 0 \tag{7.8}$$

with the first condition $\partial_t \varepsilon_Z = 0$ the zonal flow energy to be stable (damping and forcing tem are balancing out) and with the second condition $\partial_t \varepsilon_F < 0$ we assume that flucutations should dissipate. One can rewrite the H mode condition as

$$\partial_x < RS >_y v_Z = \nu_\perp \Delta \varepsilon_Z \tag{7.9}$$
$$-P_{F\to Z} > (\gamma - \gamma_W)\varepsilon_F \tag{7.10}$$

If we assume that $-P_{F\to Z} = \partial_x < RS >_y v_Z$ one can reduce the conditions to one

$$\nu_\perp \Delta \varepsilon_Z > (\gamma - \gamma_W)\varepsilon_F \tag{7.11}$$

$$\rho_*^2 > \nu^* \frac{a\frac{\gamma}{c_s}}{a^2\kappa^2} \tag{7.12}$$

where $\frac{a\frac{\gamma}{c_s}}{a^2\kappa^2}$ is of order one. This condition is in agreement with the experimental power threshold law of Suttrop and Martin, if we rewrite the law in function of ν^* and ρ_* one obtain

$$\frac{P}{P_{thr}} \propto \rho_*^{0.9085} \beta^{1.856} \nu^{*-0.5018} \tag{7.13}$$

Considering that in our model the magnetic effects are not taken into account, if we neglect the β effect one can recover a comparable relation between ρ_*, ν^* with the theoretical one $\rho_* > \nu^{*0.55}$.

7.4 Pros and Cons of reduced model

In Chapter 2, where TOKAM2D model have been introduced, pros and cons of such a reduced model have been listed. Here, in the last chapter, we present the same section with the target of summarize the results achieved, the advantages and disadvantages of such a reduced model in the context of LH transition study.

The role of two regions interface with different ZF dynamics appears to be crucial to explain the pedestal generation during the LH transition. The TB dynamics is quite complex, namely the barriers can merge, move and finally condense. In space we can observe the coalescence of different transport regimes, turbulent and diffusive regions alternate. Also in time a quasi periodic relaxation of barriers appears to be controlled by a predator-prey mechanism.

With the advantage of using a reduced modes, we are now able to compare our results with a 0-D model, taking in account the role of turbulence either as sink or source of ZF. A new mechanism is described to explain the role of RS in ZF cycle. The dynamic

observed in TOKAM2D gives us a new understanding of the transition. A comparison with experiments are carried out, in particular strong similarities are found by comparing the spectrum of potential fluctuations between L and H mode.

However, TOKAM2D does not fit for a comprehensive comparison with experiments. New ideas can be developed in TOKAM2D to be then implemented in more complex models. In this framework, the implementation of new boundary conditions taking into account SOL physics is progressing in GYSELA.

Chapter 8

Conclusions

In this thesis, we have studied the self-organization of turbulent transport to understand and control confinement performance in fusion devices, with a strong emphasis towards the understanding of transport barrier generation.

On the nature of turbulent transport. A standard approach to model the turbulence in fusion plasmas is based on scale separation between microscopic and macroscopic properties, according to the underlying assumption that a gap exists between these two scales. Their evolution can then be studied separately, taking into account the impact of the fluctuations on the mean-field evolution via an effective diffusion, D_{eff}. A first aspect of the work is to investigate the validity of such an assumption using GYSELA, a gyrokinetic model of ion heat transport in the core plasma, and TOKAM2D, a reduced fluid model used to investigate particle transport in the edge plasma. Both models are dedicated to global and flux driven simulations. The definition of a large scale effective diffusion coefficient appears then rather artificial for both models, since a strong coarse-graining procedure is required to recover a linear relation between the flux and gradients. Furthermore, such a representation does not yield any insight in the behavior of the system during transients nor on the underlying transport mechanisms.
A diffusive description does not contain the sufficient information to model the turbulent transport contribution on the overall confinement time.

Self-organization of turbulence in fusion plasmas. The different self-organization patterns observed in turbulent transport simulations and their signature in terms of large scale features, namely transport properties, have been described. Striking features of self-organization such as (1) avalanches and (2) transport barriers have been investigated via GYSELA and TOKAM2D. A key aspect of the work is to investigate the role of the boundary conditions, understood here as the means to drive the system out of the equilibrium, in the self-organized properties. Regarding the transport barriers it is clear that self-generated flows are a key aspect that should be addressed in a global configuration without prescribed gradients, therefore flux driven. The case of avalanches is different since these are reported in flux tube simulations. We have thus developed TOKAM2D simulations with two different kinds of gradient driven turbulence: profile driven, such that a prescribed profile is imposed in the system, and flux tube. In the former case the equations are modified so that the chosen profile is an equilibrium solution, while in the flux tube case periodic radial boundary conditions are assumed and linear volumetric source drives the turbulence. We have shown that avalanches in flux driven are different

from those in gradient driven simulations.
The symmetry breaking that governs the transport from a source to a sink leads to a stratified media such that the turbulent burst of the avalanche is not homogeneous and exhibits faster dynamics with shorter life time at a given radius.

Turbulence threshold definition. In gradient driven simulations, by scanning the forcing, a new region has been identified close to criticality where, even if the system is linearly unstable, turbulence is quenched. In this region, the so-called Dimits shift region, it has been observed that zonal flows quench the turbulence so that the radial transport is reduced to very low values. We investigate here the role of criticality in the interplay between turbulence and zonal flows and in turbulence self-organization in the framework of flux driven simulation. In the flux driven case, the pressure gradient evolves self-consistently in time and space via the turbulence feedback. Hence, a more complex dynamics is found close to criticality: different transport regimes observed with different conditions in the flux tube simulation are recovered in a single simulation with self-consistent organization in time and space. No abrupt transition of the turbulent transport takes place at a critical value of R/L_T.
The phenomenology of the Dimits shift is not relevant in global FD simulations and most likely in experiments where the gradients are not monitored.

The SOL width definition. In the SOL region, transport is governed by avalanches that exhibit ballistic motion in the radial direction. The transport is then driven by such large scale events. We then show that the Quasi Linear theory, where the underlying assumption is that fluctuations scale is much smaller than the mean profile, is no more valid for the SOL. Furthermore, a difference should be made between steady SOL $< \lambda_{SOL} >$ and a fluctuating SOL λ_{SOL}. The standard definition of $< \lambda_{SOL} >$ can be still relevant for an actively cooled component like the ITER divertor, but is an issue for the physics that exhibit a comparable time scale.
The definition of SOL width must be associated with a characteristic time scale, the steady-state SOL does not give sufficient information to properly address the plasma wall interaction issues.

The kinetics effects driving turbulence self-organization. Turbulence self-organization is being investigated with the gyrokinetics code GYSELA. Spontaneous generation of large scale flow shears occurs. These persistent and coherent structures damp most of the turbulent bursts and form small barriers that govern a local increase of the radial temperature gradient, so called corrugations, and lead to a staircase like temperature profile. If the complexity of the 5D gyrokinetic models give us (1) the advantage of mimicking realistic plasma parameters of the tokamak, it also present some limitations, (2) large computational effort are required for these studies and (3) the identification of the non linear dynamics driving the self-organization is extremely challenging. In the TOKAM2D framework, the circumstance is inverted. We do not aim at realistic simulation of the plasma transport in the fusion device but at the simplest possible model in order to isolate the crucial elements of the self-organized dynamics of transport barrier formation. The result is that avalanches and barriers interplay can then be studied via such a reduced models, where a rich non linear dynamics is observed by properly taking into account the impact of collisions on the zonal flows evolution.
There is no evidence that self-organized turbulence is a specific kinetic effect.

The mechanism controlling the barriers dynamics. The energy transfer between turbulence and zonal flows have been identified and a general mechanism controlling the barriers relaxation and generation is proposed. An effort is done towards the definition and identification of the Reynolds Stress as zonal flows source and sink. The transfer of energy from turbulence to zonal flows and viceversa has been investigated via a three modes coupling model where the energy transfer between zonal flows and streamers is addressed analytically. Two different groups of turbulent modes has been individuated: Big scale modes and Small scale modes. One one hand, the Small modes act as source of zonal flows, the exchange energy is then from Small modes to zonal flow, the Small modes are damped by the transport barrier and the zonal flow energy is increased. On the other hand, the Big modes energy cannot from the zonal flow modes. Large scale turbulent structures (Big modes) are not quenched by zonal flows, but zonal flows can be quenched by the Big modes. By varying the forcing scale, one varies the turbulence dominating scale, namely the ratio between Big and Small modes.
A transition from turbulence dominated to zonal flows dominated regime is achieved and controlled by the typical forcing scale.

The key ingredient for the H-mode. A novel understanding of transport barriers associated to the interface between two regions with different zonal flows regimes is proposed. This model captures the universal features of the H-mode regime in tokamak plasmas and relates it to other fields where turbulence self-organization yields zonal flows dominated regimes. The zonal flow dominated regime is shown to be controlled by the occurrence of a gap in the turbulent spectrum between the wave vector of the peak of the spectrum and that of the zonal flow. Such a regime develops in the closed field line region, leading to small transport barriers. A large pedestal region is found to build-up overlapping the edge region, where zonal flows are weakly damped by collisions, and the SOL region characterized by large scale zonal flow damping. Indeed, the latter is governed by plasma-wall interaction, that constrains the plasma current pattern. Further in the SOL the turbulent transport is weakly modified by the pedestal. Although the TOKAM2D model is not fit for a comprehensive comparison to experimental evidence, it is characterized by several generic properties of such transitions: (1) the occurrence of a gap in the turbulent spectrum has been reported in the investigation of the enhanced plasma confinement of a stellarator, (2) this mechanism bridges the various fields where the zonal flow-dominated regime is discussed, (3) the edge-SOL interface is found to generate a strong barrier with large gradients, (4) this explains the specific location of the pedestal, (5) in this flux-driven model, the barrier gradients build-up until a relaxation burst of turbulence reinitiates the process, (6) the onset of this quasi-periodic relaxation is governed by the collisional erosion of the zonal flows which thus control the relaxation frequency and stored energy in the barrier.
A novel understanding of the pedestal generation at the interface between edge and SOL is presented.

Generic features of transport barrier at the interface between different zonal flow damping regions Barriers and zonation regimes, namely the spontaneous generation of a low turbulence regime with well-established patterns of large scale flows, the zonal flows, appear in many dynamical systems including geophysics (1) oceans, (2) planetary atmospheres as well as (3) plasmas. However, it has been admitted within the

fusion community that the pedestal development, the edge transport barrier (or H-mode), should be addressed by taking into account the real geometry of a tokamak and accurate particle sources. These considerably increase the complexity of the model and the computational effort and narrow the relevance of this physics to tokamak plasmas. We present a novel point of view developing a minimum model of pedestal generation, which is not specific of tokamak plasmas. The result is a universal transition from turbulent to zonation regimes, the pedestal being localized at the interface between regions with different zonal flow damping.
In a two-dimensional fluid model comparable to that of the Rayleigh Bénard instability, we introduce (1) the main ingredients to simulate plasma confinement and (2) appropriate drive out of equilibrium to allow turbulence self-organization.

My point of view on the future work

Two are then the main conclusions of this work: (1) It is not mandatory to increase the codes complexity to identify the turbulence self-organization. Such results represent then a major improvement, considering the numerical constrains of the more complex codes. (2) The key aspects that control the barrier dynamics have been identified via such a reduced model. By controlling the barrier, hence the plasma confinement, new scaling law relevant for ITER design, not only based on the empirical laws, can be now proposed.

The biggest achievement of this work is to open new perspectives on the exploitation of reduced models to study complex non linear dynamics. The art of empirical science like physics is to capture large body of experimental facts with the same model and allow the model to be simple enough to be taught in standard university training so that it can be used practically.

In this spirit I am going to address my future work, namely by using my understanding of self-organization to investigate the experimental observations and hopefully improve the machine performances. In particular, a consistent technique to identify the signatures of self-organized large scale patterns, such as avalanches and transport barriers, and their impact on the turbulent transport is still missing. Small tokamak machines devoted on the identification of turbulent transport through many different diagnostics (Langmuir reciprocating probes, Gas Puff Imaging) represent a perfect platform to develop new tools and validate the results we obtained via turbulent models. The idea is to build a minimum turbulent model with all the key ingredients to predict and understand the transport inside the machine. To do so, I first need to identify the key issues to be addressed for a conclusive comparison between the model and experimental results:

- **Characterize the SOL width.** Quantifying the steady and fluctuating SOL width represents my first objective. Via such analysis, one can calibrate the coefficients used in the model equations with the experimental ones and verify if the model predictions can be exported to the experiments. This has also very strong engineering consequences regarding the design of Plasma Facing Components.

- **Characterize the transport barriers and large scale flows.** How to identify large scale patterns in the experimental results represents still an open issue. However, with reciprocating probes, the Reynold stress can be quantified. By studying

how the Reynold stress varies in space and in time (during barrier relaxation and generation) one can characterize the barriers time and space scales.

- **Characterize the LH transition.** The main control parameter for the transition from turbulence to zonal flows dominated regime appears to be related to the turbulence characteristic scale. It would be interesting to verify if the parameters that control the turbulence injection scale and consequently the Big and Small modes dynamic are found in the experiments. Once the turbulence injection scale is controlled, one can finally verify if, by reducing the poloidal size of turbulent structures, the transition from L to H mode is favored.

- **Characterize the barrier relaxations.** It is crucial to better identify the barriers relaxation mechanism. In my opinion, it would be interesting to find a mean to generate numerous small relaxation driven by turbulence that avoid the MHD ELMs. If the procedure is efficient one would be able to do without RMPs and use the H-mode in DEMO.

The final aim is to furnish a more complete understanding and experimental studying of turbulent transport self-organization in Big & Small devices to the fabulous and demanding experiment of ITER.

.

Chapter 9

Résumé étendu

Le Tokamak International ITER est en construction à Cadarache. Le projet est porté par sept partenaires, la Chine; la Corée, l'Europe, l'Inde, le Japon, la Russie et les Etats-Unis. ITER est un très grand équipement destiné à apporter une démonstration expérimentale de l'opération et du contrôle des plasmas en combustion. A cette fin, .il faut que les conditions obtenues dans ITER soient telles que l'essentiel de l'énergie nécessaire à entretenir cette phase de combustion soit dû aux réactions de fusion nucléaires elles-mêmes. Ce projet est extrêmement ambitieux sur tous les plans, l'organisation internationale, la technologie ainsi que la physique des plasmas mise en œuvre. La base physique d'ITER repose sur plus de 50 années de recherche à travers le monde. Par rapport à JET, le tokamak européen situé au Royaume-Uni, et la plus grande machine en opération, l'extrapolation en rayon est typiquement d'un facteur 2. Cette augmentation de taille doit se traduire par une augmentation des performances d'un facteur 10 pour atteindre le régime de combustion thermonucléaire et ainsi ouvrir une nouvelle phase dans la recherche sur l'utilisation de la fusion thermonucléaire à des fins pacifiques. Trois défis devront être surmontés pour qu'ITER atteigne son régime de performance nominal.

Le défi des fortes températures du plasma. Le régime des plasmas en combustion doit atteindre des températures de l'ordre de 150.000.000 Kelvins afin de vaincre avec une probabilité suffisante les répulsions coulombiennes entre les noyaux. Bien que les énergies en jeu, de l'ordre de 10 keV, soient très modestes au regard de celles atteintes par les accélérateurs de particules, cette énergie thermique correspond à une température supérieure à celle du soleil. Ce point donne en lui-même une bonne mesure du défi que représente ITER. Dans ces conditions, les électrons ne sont plus liés aux noyaux. En effet, pour les isotopes de l'hydrogène le seuil d'ionisation bien connu est de 13,6 eV, ce qui correspond à une énergie thermique inférieure à 10 eV, typiquement 7 eV, car il faut alors prendre en compte le pouvoir ionisant important des électrons suprathermiques. Cet état de la matière constitué d'un gaz d'électrons et d'ions est appelé plasma, terme introduit par Langmuir en 1928 en s'inspirant du terme médical. Il est à noter que dans ITER les atomes les plus légers seront totalement ionisés au cœur du plasma alors que les éléments lourds comme le tungstène, numéro atomique 74, ne seront que partiellement ionisé avec un état d'ionisation supérieur à 60%.

Performance de confinement : le temps de confinement de l'énergie τ_E. Pour atteindre ces températures le plasma doit être chauffé pour équilibrer les pertes d'énergie due au pouvoir d'isolation fini qui peut être mis en œuvre. Pour atteindre un

régime de réactions de fusion autoentretenues avec un faible apport d'énergie extérieur, les ions doivent maintenir leur énergie thermique jusqu'à subir une réaction de fusion. En combinant l'énergie produite par réaction, le temps caractéristique des réactions de fusion nucléaire et l'énergie interne du plasma, on peut évaluer le pouvoir isolant nécessaire à travers le temps de confinement de l'énergie τ_E. Ce temps donne un critère de performance des dispositifs de confinement. Dans la pratique, ce temps correspond au temps caractéristique de décroissance de la température du plasma lorsque la puissance de chauffage est arrêtée. Une amélioration du temps de confinement d'un facteur 5 par rapport aux expériences actuelles est nécessaire dans ITER. Pour les dispositifs de confinement magnétique, il est important de remarquer que ce temps est court par rapport à la durée de la phase de combustion. De ce point de vue, on se rapproche ainsi d'un fonctionnement en continu. Dans les dispositifs tels que les tokamaks, la limitation des performances de confinement est dominée par la turbulence. Cette dernière assure un transport entre le cœur thermonucléaire et la périphérie du plasma. Déclenchée par l'important écart à l'équilibre qui est réalisé, elle tend à limiter l'accroissement des performances au-delà d'un seuil de l'écart à l'équilibre.

La couche limite appelée Scrape-Off-Layer (SOL), sa largeur et l'interaction plasma-paroi. L'interaction du plasma avec un solide en régime stationnaire, conduit à un processus d'équilibre dynamique où le solide neutralise continuellement le flux de plasma qui l'atteint et où l'énergie cédée par le plasma à sa surface du solide est évacuée. Le régime d'interaction peut conduire à une érosion de la surface du solide et donc à une détérioration graduelle de ce dernier. Dans les conditions du plasma en combustion aucun solide ne peut être maintenu durablement en contact avec le plasma. L'interaction ne peut être maintenue que dans des conditions de plasma à plus faible température ce qui fait que l'écart à l'équilibre thermodynamique déjà évoqué doit se faire pour l'essentiel dans le plasma. Malgré la turbulence qui se développe dans un tel scénario, l'écart entre les conditions plasma et celles du solide est réalisé dans une couche limite de très faible extension par rapport à l'échelle du plasma. Cette région cruciale pour le contrôle de l'interaction plasma-paroi est appelée Scrape-Off puis Scrape-Off Layer ou SOL. La traduction à acronyme constant, Section à l'Ombre du Limiteur, ne rend pas compte du rôle de cette région du plasma et restreint l'usage de cette notion à l'existence d'un limiteur. En fait on peut considérer que la SOL est une couche limite dans laquelle le plasma dépose tout le flux d'énergie sortant aux éléments solides, les Plasmas Facing Components ou PFC qui l'entourent. La largeur de la SOL est un paramètre clef. Si l'épaisseur est très faible, la concentration du dépôt d'énergie est extrême et il devient très difficile de réaliser des composants pouvant fonctionner sans élévation continuelle de leur température. La maîtrise de l'interaction plasma-paroi avec la mise en œuvre d'une largeur de SOL effective compatible avec les limites technologiques actuelles que ce soit pour le refroidissement ou la tenue du matériau de protection en contact avec le plasma, est un enjeu important dans ITER. A l'inverse des contraintes du plasma central, les conditions de bord conduisent à rechercher une baisse des performances de confinement dans la couche limite.

La turbulence média des performances dans ITER. La turbulence, et en conséquence le transport turbulent, apparaissent comme des éléments clefs dans plusieurs des défis qui

attendent la physique dans ITER. Elle apparait d'ailleurs comme un élément décisif dans le dimensionnement d'ITER à travers la loi d'échelle empirique qui relie le temps de confinement de l'énergie aux principaux paramètres qui définissent la machine. C'est le cas en particulier du volume d'ITER qui d'après la loi d'échelle est l'élément le plus déterminant pour augmenter les performances. Il faut cependant constater que les changements dans les conditions d'opération des tokamaks apportent un nouvel éclairage et conduisent à s'interroger sur le sens de ces lois d'échelle. Ainsi, les expériences récentes de JET avec du tungstène comme matériaux de surface indiquent une baisse inattendue des performances en termes de confinement de l'énergie. Un effort pour mieux comprendre et contrôler la turbulence reste à l'ordre du jour pour préparer les expériences dans ITER et permettre d'atteindre avec efficacité le régime de plasmas en combustion. Notre ambition a été d'étudier les éléments clefs et les concepts qui fondent notre compréhension de la turbulence dans les plasmas de fusion.

Comment se développe l'auto-organisation de la turbulence dans les plasmas de fusion ? La turbulence se caractérise par l'interaction entre de très nombreuses échelles couvrant un grand domaine de taille. C'est cet aspect qui conduit à sa complexité et aux difficultés de représentation aussi bien dans les arts que dans les sciences. Du point de vue scientifique, les différentes échelles sont comprises comme autant de modes indépendants qui interagissent selon des lois spécifiques. On peut montrer que le transfert d'énergie entre deux modes se fait selon deux mécanismes. Le premier correspond à un transfert entre échelles voisines. Le second est basé sur un transfert direct entre échelles différentes, des petites échelles vers les grandes échelles ou vice-versa. Par auto-organisation de la turbulence nous désignons essentiellement ce second mécanisme qui permet le couplage entre des échelles lointaines. L'auto-organisation se traduit alors par la formation de structures à grandes échelles. Ila été montré aussi bien numériquement qu'expérimentalement que le transport par avalanche est prépondérant dans la SOL. A l'inversement dans la région confinée du plasma, in existe une interaction forte entre écoulement zonaux et avalanches, ce qui peut dans certains cas se traduire par la formation de barrières de transport. Ces dernières conduisent à une augmentation significative du temps de confinement (facteur pouvant atteindre 2, nettement supérieur aux dégradations des lois d'échelle évoquées ci-dessus, de l'ordre de 20%).

Peut-on prédire et définir le seuil de transport turbulent ? Le seuil d'apparition de la turbulence est en général défini comme résultant de la compétition entre les forces tendant à générer la turbulence et les mécanismes d'amortissement. Cet aspect est clairement illustré par le nombre de Reynolds $Re = UL/\nu$ caractérisant un système de taille L plongé dans un fluide porté à une vitesse U dont la viscosité est ν. Une transition vers la turbulence est observée lorsque Re dépasse une valeur critique, le seuil de la turbulence. De manière identique, différents phases de turbulence sont observées lorsque l'on augmente le forçage du système, en pratique l'écart à l'équilibre thermodynamique, au-dessus d'un seuil. Une image intuitive du processus dans les plasmas est la suivante :

1. Au-delà du seuil une instabilité croit dans tout le domaine où le forçage est appliqué. Cette instabilité est caractérisée par un nombre d'onde qui indique la formation d'une structure périodique là où préexistait un milieu constant. Le système perd ainsi une symétrie initiale (rupture de symétrie). Ces structures, dont la géométrie est proche des modes propres de la phase linéaire de l'instabilité sont appelés 'streamers'.

2. Dans la phase non-linéaire du développement de ces streamers, le couplage entre écoulements opposés génère un écoulement transverse aux streamers, et constant dans la direction de symétrie initiale. Cet écoulement appelé écoulement zonal ou 'zonal flow' tend ainsi à régénérer l'équilibre avant l'apparition de la turbulence. Il conduit à une baisse de la turbulence et un affaiblissement du transport turbulent. Ce deuxième stade peut lui-même bifurquer vers deux états :

    - La turbulence bien que modifiée par les écoulements zonaux maintient un transport turbulent qui s'oppose à l'écart à l'équilibre. Le système se stabilise alors dans un état d'équilibre statistique entre des événements de transport et des évènements renforçant les écoulements zonaux.
    - Les écoulements zonaux se renforcent jusqu'à supprimer la turbulence et bloquer le transport turbulent. Ce stade correspond à l'apparition d'une barrière de transport. L'augmentation du forçage conduira à terme à une nouvelle instabilité, et ainsi à un phénomène de relaxation. Si l'énergie libérée lors de la relaxation reste faible, et donc les relaxations fréquentes, le système peut se maintenir dans ce système cyclique, au contraire si la relaxation est trop forte, prenant donc la forme d'un évènement rare, le système n'est plus contrôlé et un changement d'état peut intervenir.

Quels mécanismes contrôlent la dynamique des barrières ? Dans de nombreuses situations, les barrières présentent des instabilités conduisant à une dynamique turbulente et le déclanchement de transport turbulent à travers la barrière. L'origine de ce phénomène de relaxation semble dans bien des cas indépendant du mécanisme conduisant à l'apparition de la barrière. En identifiant ces mécanismes, on peut espérer introduire un contrôle des barrières de transport, soit pour les renforcer, soit pour déclencher des relaxations quasi-périodiques de faibles amplitudes et éviter ainsi des relaxations fortes qui posent inévitablement des problèmes de recyclage et de contrôle.

Quel est le rôle des effets cinétiques dans l'auto-organisation de la turbulence ? Les plasmas magnétisés sont caractérisés par de faibles densités. Le libre parcours moyen est alors très grand, de loin supérieur aux tailles du dispositif de confinement. La limite dite de faible collisionnalité doit alors être considérée pour décrire ces plasmas. En pratique, les équations cinétiques semblent donc préférables pour étudier la turbulence plasma par rapport à la description fluide de type Navier-Stokes où l'on considère implicitement une réduction du nombre de champs indépendants liée à des effets collisionnels. Bien que les descriptions fluides et cinétiques de la turbulence plasma diffèrent quantitativement, la compréhension et la signification de ces différences restent incertaines. Par ailleurs, on peut s'interroger sur la possibilité d'un accord qualitatif entre ces approches permettant de les réconcilier par un ajustement empirique des fermetures inhérentes à la description fluide. Le bénéfice en termes de coûts numériques et d'interprétation des résultats est suffisamment important pour donner toute sa place à cette interrogation, sans compter avec la finalité objective de la physique qui est d'établir des moyens d'agir sur notre environnement sur la base d'une description la plus concise et efficace possible.

Comment définir la largeur de la SOL ? Pour contrôler l'interaction plasma-paroi, il est impératif de réguler le transport dans la région de lignes de champ ouvertes, la SOL, où le plasma entre en contact avec la paroi en suivant un écoulement parallèle aux lignes de champ. Ce transport n'est pas réguler par le champ magnétique autrement que par

la géométrie des lignes de champ. De ce fait, le temps de confinement dans la SOL est très court et son volume restreint. Dans le sens transversal aux lignes de champ l'écart à l'équilibre thermodynamique peut alors être considérablement amplifié les paramètres plasmas comme la densité ou l'énergie interne devenant très faible sur une distance très courte. Les signatures d'un transport dominé par des avalanches, donc balistique dans la direction transverse aux lignes de champ ainsi que des niveaux de fluctuations approchant de l'unité sont observés dans la SOL. Malgré cela, le paradigme dominant dans la SOL est celui d'une marche au hasard constitué de pas transverses microscopiques en compétition avec un transport parallèle très rapide et rapidement dominant. A l'opposé de ce paradigme, on constate que le transport balistique est suffisamment rapide pour couvrir des distances mésoscopiques sur des temps courts par rapport aux temps du transport parallèle au champ magnétique. Ces approches contradictoires font de l'analyse de la largeur de la SOL, la fine couche limite du plasma, un enjeu de recherche considérable dont les enjeux sont cruciaux pour ITER.

Quels sont les éléments déterminants dans l'établissement du mode-H, le mode de confinement de référence dans ITER ? L'apparition spontanée d'une barrière de transport, par auto-organisation de la turbulence est le régime de référence pour l'opération d'ITER. La réalisation de simulations auto-consistantes conduisant au développement d'une barrière de transport à l'interface du bord du plasma, où les surfaces magnétiques sont fermées, et la SOL est cruciale pour déterminer les propriétés essentielles du mode-H et améliorer son contrôle. Ceci est d'autant plus important que la proximité entre la barrière du mode-H et de la SOL modifie considérablement les propriétés de l'interaction plasma-paroi. Concilier l'amélioration du confinement du plasma central et la maitrise de l'interaction plasma-paroi est un enjeu considérable dont la mise en œuvre sera grandement simplifié si les mécanismes clefs de cette transitions sont identifiés.

Le sketch suivant reprend les interrogations qui président à ce travail de recherche et qui font l'objet des chapitres de thèse résumés dans la suite. Les implications pour ITER sont au cœur de notre démarche.

Figure 9.1: Thesis objectives

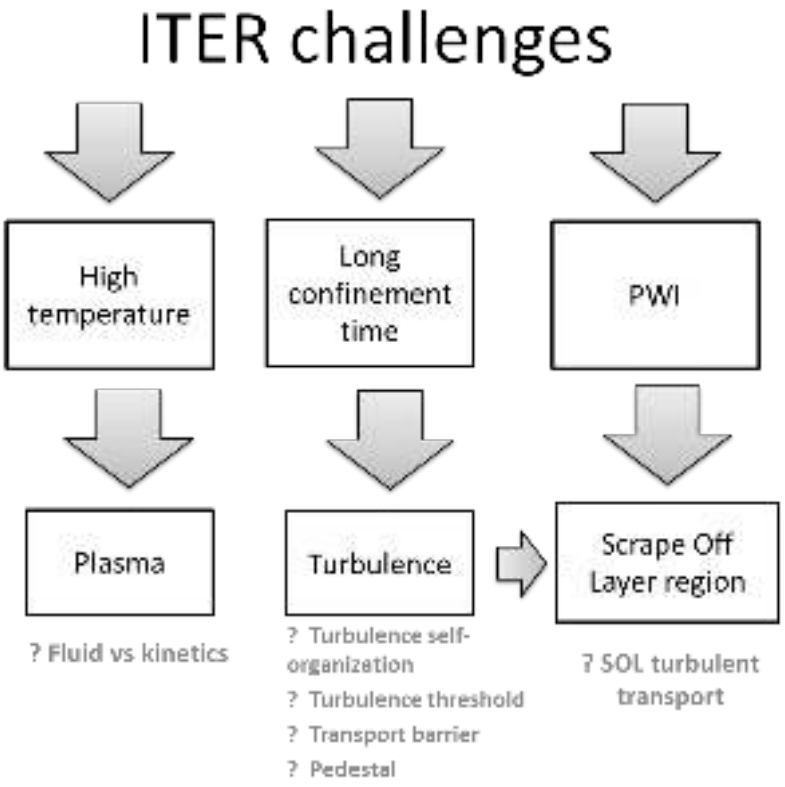

Les principaux objectifs scientifiques sont associés à l'étude du transport turbulent et l'auto-organisation de la turbulence. Le but est la compréhension et le contrôle que celle-ci permet de mettre en œuvre. Les enjeux apparaissent dans plusieurs facettes de la recherche de performance dans ITER où la turbulence est le média entre différentes régions du plasma. L'étude de ces phénomènes non-linéaire fait appel à deux outils numériques, le code TOKAM2D utilisant un formalisme fluide en dimension réduite et le code GYSELA, un code cinétique 5D qui est un outil complet pour l'étude de la turbulence mais dont l'utilisation et l'interprétation des résultats demandent un investissement considérable.

Dans le Chapitre 1, nous introduisons les éléments de base des dispositifs de fusion magnétique et le rôle du transport turbulent dans l'opération et les performances des expériences en cours ainsi que projetées dans ITER.

Dans le Chapitre 2, les deux outils numériques, GYSELA et TOKAM2D, sont présentés. Les principaux choix présidant aux différences entre ces deux approches de la modélisation des plasmas sont mis en avant. Les forces et faiblesses de chacune des approches sont analysées. Le modèle utilisé dans le code cinétique GYSELA est l'approche la plus directe. Elle est basée sur un minimum d'hypothèse et vise à réduire au maximum les paramètres libres pour se rapprocher des conditions de simulations ab-initio. Les limites de cette approche sont le coût de ces simulations, qui limitent en conséquence les domaines étudiés. Par ailleurs, l'identification et l'analyse des dynamiques non-linéaires qui conduisent à l'auto-organisation est particulièrement difficile, rejoignant par certains aspects les conditions expérimentales où seule une information parcellaire est réellement accessible. Dans le cas de TOKAM2D, les attendus sont inversés. Le modèle ne vise pas une simulation complète, potentiellement réaliste du transport plasma dans les tokamaks. Au contraire, nous avons recherché la simplification maximale qui contienne encore les éléments cruciaux de l'auto-organisation de la turbulence. Cette démarche nous permet d'aborder le problème dans une plus grande généralité et de retrouver des problèmes et des comportements génériques à d'autres champs de la physique comme l'océanographie ou la physique des atmosphères.

Dans le Chapitre 3, les modèles d'auto-organisation à grande échelle, observés expérimentalement et par l'intermédiaire des simulations du transport turbulent, sont présentés. Leur impact sur le transport à grande échelle est quantifié.

L'approche standard pour modéliser la turbulence dans les plasmas de fusion est basée sur la description par un transport diffusif de la turbulence. Un premier point de questionnement est celui de la validité d'un tel principe en utilisant GYSELA et TOKAM2D. Ces deux modèles sont dédiés à des simulations globales, permettant de ne pas faire d'hypothèse de séparation d'échelle et dans des conditions de forçage par le flux, c'est-à-dire avec comme seule contrainte de stationnarité celle d'assurer le transport d'un flux moyen, en temps et en espace, identique au flux de forçage. Dans ces conditions de réalisation, la définition d'un coefficient de diffusion effectif à grande échelle apparaît assez artificielle pour ces deux modèles. En effet, pour retrouver un comportement en accord avec le principe d'un transport diffusif, nous sommes conduits à une procédure de moyenne à gros grains. C'est seulement dans cette limite que l'on retrouve une relation linéaire entre les flux et les gradients. En outre, une telle représentation ne donne aucune indication sur le comportement du système lors des transitoires, ni sur les mécanismes de transport sous-jacents.

On arrive alors à une description analogue à celle conduisant au temps de confinement de l'énergie des lois d'échelle, sans gains significatifs permettant de construire une description plus fine basée sur la dynamique des profils.

Les avalanches et les barrières de transport sont caractéristiques de l'auto-organisation de la turbulence. Les propriétés de ces motifs auto-organisés sont décrites et quantifiées. Nous retrouvons que les avalanches régissent le transport SOL (où les lignes de champ sont ouvertes). Dans cette région, le transport est dominé par ces événements de grande amplitude. Pour leur analyse nous avons eu recours à différents d'outils mathématiques, telles que les densités de probabilité et les fonctions d'autocorrélation. Dans la région 'bord' où les lignes de champ sont fermées, une forte synergie entre la turbulence et les écoulements zonaux est identifiée. Elle peut conduire à la formation de barrières de transport. La dynamique de formation et d'évolution des différentes barrières de transport observées, les macro-barrières et les micro-barrières, est présentée. Les macro-barrières modifient globalement les propriétés de confinement. En revanche, elles sont régies par un comportement de relaxations quasi-périodiques potentiellement incompatible avec les conditions d'opération souhaitées. Les micro-barrières, sont essentiellement locales et peuvent évoluer rapidement par micro-relaxation, déplacement, voire fusion ou disruption définitive ou temporaire. Cette dynamique rapide, associée à une densité radiale assez importante, instaure une amélioration volumique du confinement avec une réorganisation régulière sans évènement de relaxation majeur. Cependant, nous n'avons pas pu établir les conditions favorisant un type de barrière plutôt qu'un autre.

Dans le Chapitre 4, nous étudions l'impact du transport intermittent sur la notion de largeur de SOL.

La définition de la largeur caractéristique de la SOL dépend fortement du problème que l'on souhaite traiter. En effet, dans un système où les fluctuations sont de l'ordre de l'unité, l'échelle de temps caractéristique joue un rôle crucial. Un des points importants de la physique de l'interaction plasma paroi est celui du dépôt d'énergie. On est alors amené à considérer deux régimes en fonction du temps de mise à l'équilibre thermique des composants face au plasma, typiquement 6 secondes dans ITER. Du point de vue de l'extraction de chaleur, la notion de largeur de SOL intègre donc les propriétés du transport turbulent sur des temps longs par rapport aux temps de la turbulence. On peut alors considérer une largeur moyenne malgré l'importance des fluctuations. En revanche, si l'on s'intéresse au cyclage thermique de la surface du composant, une analyse plus fine des fluctuations induites par la turbulence devra être considérée.

Dans la SOL, l'analyse du transport par la théorie quasilinéaire permet de montrer que la séparation entre parti fluctuante et partie moyenne n'est pas possible. En effet, le temps de confinement de la SOL, qui permet de définir la notion de moyenne est comparable au temps caractéristique d'évolution de la turbulence. Le développement en échelle multiple dans ce cas de figure montre que les fluctuations sont d'ordre 1, ce qui ne permet pas de poursuivre l'analyse quasilinéaire et la dérivation d'un coefficient de diffusion du transport turbulent.

Par ailleurs, les conditions de forçage du système hors équilibre influent sur le transport turbulent dans la SOL. Deux types de forçage par un gradient ont été développés pour

analyser ce point. Dans le cas le plus simple et le plus généralement considéré, on suppose qu'un gradient fixe est imposé dans tout le système. Cette solution, combinée à des conditions périodiques dans la direction radiale, correspond aux conditions de simulation appelées flux tube. Ce type de forçage n'est pas cohérent avec les conditions de la SOL. Par ailleurs, le transport généré par la turbulence n'est pas pris en compte et le gradient de forçage est invariant. Cela nous amené à un deuxième type de forçage où l'on prescrit un profil et l'on modifie les équations de telle sorteque ce profil soit une solution stationnaire des équations. Le comportement de ces deux types de forçage est difficilement comparable. En effet les simulations flux tube génère des conditions de forçage volumiques, homogènes dans le temps et l'espace, totalement indépendantes de la réponse plasma. En revanche, les simulations à profils stationnaires fixés introduisent plus de contraintes dans le système. Nous avons comparé le transport à flux fixé au régime à profil fixé en introduisant comme profil de forçage le profil moyen obtenu dans le cas du forçage par le flux. Dans les deux cas on observe un transport par avalanche. Cependant celui à profil fixé est caractérisé par une dynamique plus lente et un transport radial moins efficace.

Chapitre 5, l'étude des instabilités est approfondie dans ce chapitre. Deux types de conditions initiales, supposées varier de façon adiabatique, sont considérés. Le premier cas est le cas linéaire usuel où l'équilibre est la solution stationnaire homogène dans la direction angulaire. Dans le second cas on considère comme état de départ un régime de streamer ou de zonal flow développé caractérisé par un nombre d'onde donné. Le couplage avec d'autres modes, à travers les termes non-linéaires, produit également des instabilités.

L'instabilité d'interchange à l'origine des modes ITG pour Ion Temperature Gradient est étudiée dans GYSELA. Nous avons développé une procédure de fonctionnement du code qui permet d'étudier les modes propres et les valeurs propres dans le cadre des simulations globales propres à GYSELA. On retrouve ainsi des modes globaux dont la structure est ballonnée dans la direction poloïdale du tokamak et où la structure radiale dépend fortement des profils de température et du paramètre de sécurité. Cette étude permet de connaitre la structure des modes linéaires et donc celle des streamers qui peuvent se développer pendant les différentes phases d'évolution de la turbulence.

L'étude linéaire de TOKAM2D est présentée pour analyser le couplage à trois modes entre streamer, écoulement zonaux et mode turbulent. Un choix des modes est effectué en utilisant les contraintes propres aux streamer et aux écoulements zonaux. L'analyse peut alors être menée soit dans le cas de streamers développés, permettant le développement des perturbations de turbulence et d'écoulements zonaux, soit dans le cas d'écoulements zonaux développés soutenant le développement de streamers et de modes turbulents. Un accord qualitatif est trouvé sur la dynamique des écoulements zonaux et de la turbulence.

Dans les simulations flux tube gyrocinétiques, un nouveau régime de transport a été identifié juste au-dessus du seuil de turbulence. Dans cette région, appelé Dimits shift region, le développement des écoulements zonaux est tel que la turbulence ne peut se développer. Au-dessus du seuil linéaire de turbulence, les écoulements zonaux générés par la turbulence déplacent le seuil de transport turbulent vers des gradients de température plus élevés. Ce résultat a été considérés comme très positif pour ITER dans la mesure où le gradient de température attendu se trouve dans cette zone sans transport turbulent. Le rôle de cette région proche du seuil de la turbulence a été étudié avec soin. En premier lieu, les simulations flux tube avec le code TOKAM2D ont permis de retrouver le régime

de Dimits indiquant clairement que cette propriété n'est pas liée à des effets cinétiques. Par ailleurs dans le cas d'un forçage par un gradient, on observe aussi bien dans GYSELA que dans TOKAM2D que cette région de gradient de température sans transport turbulent n'existe pas. Les simulations sont alors caractérisées par dans l'espace gradient de température transport turbulent dès que le seuil linéaire est franchi. Le Dimits shift en tant que région sans transport turbulent n'est donc pas un régime cohérent avec le mode de fonctionnement d'une machine. En revanche, on observe que le régime de micro-barrières tend à se développer au voisinage du seuil de la turbulence.

Dans le Chapitre 6, le mécanisme contrôlant la dynamique des barrières de transport et le transfert d'énergie entre la turbulence et les écoulements zonaux est étudié avec le modèle de couplage 3 modes afin de déterminer analytiquement le rôle de l'instabilité de Kelvin-Helmholtz dans l'amortissement des écoulements zonaux qui détermine les cycles de relaxation turbulente observées dans les barrières de transport.

L'étude nous conduit à considérer deux groupes de modes turbulents en fonction de leur échelle et des spécificités de leur couplage aux écoulements zonaux. Les petits modes 'S-modes' agissent comme source de flux zonaux. Ce transfert d'énergie entre échelles disjointes détermine un amortissement des S-modes. D'autre part, les grands modes 'B-modes' trouvent leur énergie soit directement par les instabilités soit par couplage avec les petits modes de manière consistante avec les cascade d'énergie dans les spectres. En revanche les B-modes de tailles comparables aux écoulements zonaux ne sont pas stabilisés par ces derniers. La transition d'un régime dominé par les écoulements zonaux à un régime turbulent est alors déterminée par l'échelle contrôlant la source d'énergie dans le spectre, soit directement par l'échelle d'injection d'énergie soit par l'échelle limitant la cascade inverse.

Une comparaison est effectuée avec d'autres modèles réduits utilisés pour étudier les systèmes turbulents (océanographie, physique des atmosphères) où des transitions comparables ont été observées. Le mécanisme de contrôle des régimes dominés par les écoulements zonaux obtenus dans TOKAM2D diffère de ceux étudiés avec le modèle d'Hagesawa-Mima dans la mesure où dans ce dernier modèle l'échelle d'injection de l'énergie n'est pas auto-consistant mais correspond à un paramètre libre du modèle. Le phénomène de limitation de la cascade inverse devient alors l'élément crucial dans la description du régime dominé par les écoulements zonaux.

Chapitre 7. La formation d'un piédestal à l'interface entre les lignes de champ fermées et ouvertes est étudiée avec TOKAM2D en lien notamment avec la physique du mode-H.

Bien que le modèle ne soit pas adapté à une comparaison exhaustive avec les expériences, il est caractérisé par plusieurs propriétés génériques des transitions vers des régimes avec barrières de transport. On peut citer l'apparition d'un creux dans le spectre turbulent entre le pic de turbulence et la composante des écoulements zonaux. Cette signature a été observée dans l'étude des régimes de confinement d'un stellarator. L'interface bord-SOL sépare la région SOL où le profil de potentiel électrique moyen est fortement contraint par les conditions limites de gaine, et le bord du plasma où le potentiel électrique est quasi-libre avec cependant une double contrainte. D'abord la contrainte physique de conservation de l'impulsion qui impose une structure dont la moyenne est nulle, structure dipolaire si la

cascade inverse permet d'atteindre cette échelle. La courbure du potentiel électrique à l'interface de la SOL et du bord génère spontanément une barrière de transport à cet endroit. Le modèle de barrière est également caractérisé par des relaxations consécutives à l'érosion collisionnelle des écoulements zonaux. Les phases de turbulence qui caractérisent ces relaxations permettent de régénérer les écoulements zonaux.

Appendix A

Derivation of TOKAM2D equations

A.1 Fluid equations

The two first moments of the distribution function for species s are essentially definitions:

$$\frac{\partial\, n_s}{\partial t} + \boldsymbol{\nabla}\cdot(n_s\mathbf{u_s}) = 0 \tag{A.1}$$

$$\frac{\partial\,(m_s n_s \mathbf{u}_s)}{\partial t} + \boldsymbol{\nabla}\cdot\mathbb{P}_s = q_s n_s\,(\mathbf{E}+\mathbf{u}_s\times\mathbf{B}) \tag{A.2}$$

where the particle flux $\boldsymbol{\Gamma}_s$ and momentum flux $\mathbb{P}_s$ are defined as:

$$\boldsymbol{\Gamma}_s = n_s\mathbf{u_s} \tag{A.3}$$

$$\mathbb{P}_s = p_{\perp s}\mathbb{I} + (p_{\parallel s}-p_{\perp s})\mathbf{b}\otimes\mathbf{b} + m_s n_s \mathbf{u}_s\otimes\mathbf{u}_s + \Pi_s \tag{A.4}$$

For a two species plasmas, one can introduce the charge balance equation and the total plasma momentum balance:

$$\frac{\partial\,\rho_c}{\partial t} + \boldsymbol{\nabla}\cdot\mathbf{j} = 0 \tag{A.5}$$

$$\frac{\partial\,(m_i n_i \mathbf{u}_i + m_e n_e \mathbf{u}_e)}{\partial t} + \boldsymbol{\nabla}\cdot(\mathbb{P}_i+\mathbb{P}_e) = \rho_c\mathbf{E}+\mathbf{j}\times\mathbf{B} \tag{A.6}$$

In the quasineutral limit with $\rho_c = 0$, one obtains therefore:

$$\boldsymbol{\nabla}\cdot\mathbf{j} = 0 \tag{A.7}$$

$$\frac{\partial\,(m_i n\ \mathbf{u}_i + m_e n\ \mathbf{u}_e)}{\partial t} + \boldsymbol{\nabla}\cdot(\mathbb{P}_i+\mathbb{P}_e) = \mathbf{j}\times\mathbf{B} \tag{A.8}$$

In the vanishing mass ratio limit and drift ordering one then obtains for the total plasma momentum balance:

$$\frac{\partial\,(m_i n\ \mathbf{u}_i)}{\partial t} + \boldsymbol{\nabla}\cdot\left(p_\perp\mathbb{I} + (p_\parallel - p_\perp)\mathbf{b}\otimes\mathbf{b} + m_i n\mathbf{u}_i\otimes\mathbf{u}_i + \Pi\right) = \mathbf{j}\times\mathbf{B} \tag{A.9a}$$

$$p_\perp = p_{\perp i} + p_{\perp e} \quad ; \quad p_\parallel = p_{\parallel i} + p_{\parallel e} \quad ; \quad \Pi = \Pi_i + \Pi_e \tag{A.9b}$$

A.2 Diamagnetic cancellation

We consider the fluid hierarchy given the Vlasov-Landau kinetic equation.

$$\partial_t f + \boldsymbol{\nabla}\cdot\Big(\boldsymbol{v} f\Big) + \frac{q}{M}\boldsymbol{\partial}_v\cdot\Big(\big(\boldsymbol{E}+\boldsymbol{v}\times\boldsymbol{B}\big)f\Big) = C(f) \tag{A.10}$$

where $C(f)$ stands for the collision operator. We then consider the moment of $G(\boldsymbol{v})$ defined by:

$$\int d^3v\ f\ G(\boldsymbol{v}) = \big\langle G\ \big\rangle \tag{A.11}$$

In the large magnetic field approximation, i.e. in the drift approximation, the magnetic field dependent term in (A.10) is the largest the contribution so that $\big\langle v_i\partial_{vj}G\ \big\rangle$ can be determined from:

$$\frac{\partial}{v_j}\Big(\epsilon_{ijk}\ B_k v_i f\Big) = \partial_t f + \boldsymbol{\nabla}\cdot\big(\boldsymbol{v} f\big) + \frac{q}{M}\boldsymbol{\partial}_v\cdot\big(\boldsymbol{E} f\big) - C(f) \tag{A.12}$$

One then obtains the drift-like expression of $\big\langle G\ \big\rangle$:

$$\Big\langle v_i\frac{\partial}{\partial v_j}G\ \Big\rangle = -\frac{M}{q\ B^2}\ \epsilon_{ijk}\ B_k\ \ \Big(\mathcal{K}(G)+\mathcal{P}(G)\Big) \tag{A.13}$$

where one can readily identify the operators $\mathcal{L}$ and $\mathcal{N}$:

$$\mathcal{K}(G) = \partial_t\big\langle G\big\rangle - \frac{q}{M}E_m\Big\langle\frac{\partial}{\partial v_m}G\Big\rangle - R(G) \tag{A.14}$$

$$\mathcal{P}(G) = \nabla_m\big\langle v_m\ G\big\rangle \tag{A.15}$$

and where the collisional contribution is defined by:

$$R(G) = \int d^3v\ C(f)\ G(\boldsymbol{v}) \tag{A.16}$$

The drift-like expression of G is thus characterised by 2 contributions: the operator $\mathcal{K}$ depending on polarisation aspects with the time derivative (A.14) and the drift induced by the applied forces, the electric field and collision term, as well as a the diamagnetic like operator $\mathcal{P}$ that depends on the gradient and on a higher moment $v_m\ G$, (A.15). It is to be noted that the diamagnetic contribution is expressed in fact in terms of a higher moment in the fluid hierarchy. A proper closure, consistent with the drift expansion must therefore be considered.

Let us now be more specific regarding the structure of the function G by defining it as:

$$G = \prod_{m=1}^{3} v_m^{\alpha_m} \tag{A.17}$$

One then readily obtains the identity:

$$v_i\ G = \frac{v_i}{\alpha_j+1}\ \partial_{v_j}\Big(v_j\ G\Big) = v_j\frac{\partial}{\partial v_j}F \tag{A.18}$$

with $F = v_j\ G/(\alpha_j+1)$. One can then rewrite the diamagnetic contribution $\nabla_m\langle v_m\ G\ \rangle$ in (A.13) as:

$$\begin{aligned}\mathcal{P}(G) &= \nabla_m\langle v_m\ G\rangle = \nabla_m\langle v_m\frac{\partial}{\partial v_j}F\ \rangle \\ &= \varepsilon\ C_n\ \mathcal{K}\big(v_n\ G\big) + \varepsilon\ C_n\ \mathcal{P}\big(v_n\ G\big)\end{aligned} \tag{A.19}$$

where we have introduced the vector operator:

$$C_n = \frac{M}{q}\ \frac{\epsilon_{nmr}}{\alpha_n+1}\nabla_m\ \frac{B_r}{\varepsilon\ B^2} \tag{A.20}$$

Given $\mathcal{P}\big(v_n\ G\big)$ (A.19):

$$\mathcal{P}\big(v_n\ G\big) = \nabla_s\big\langle v_s\ (v_nG)\big\rangle \quad = \quad \varepsilon\ C_\ell\ \mathcal{K}\big(v_\ell v_n\ G\big) + \varepsilon\ C_\ell\ \nabla_s\big\langle v_s v_\ell v_n\ G\big\rangle \tag{A.21}$$

In this expression we use the parameter ε such that $\varepsilon\ B \sim 1$ to underline the large B expansion that is automatically generated when higher and higher moments of the fluid hierarchy are considered. One can then expand $\big(\mathcal{L}+\mathcal{N}\big)(G)$ (A.13):

$$\begin{aligned}\big(\mathcal{K}+\mathcal{P}\big)(G) &= \mathcal{K}(G) + \varepsilon\ C_n\mathcal{K}(v_nG) + \varepsilon^2\ C_nC_t\mathcal{K}(v_tv_nG) \\ &\quad +\varepsilon^2\ C_nC_\ell\mathcal{P}(v_sv_\ell v_n\ G)\end{aligned} \tag{A.22}$$

so that one readily obtains:

$$\big(\mathcal{K}+\mathcal{P}\big)(G) \quad = \quad \sum_{\ell=0}^{+\infty}\varepsilon^\ell\Big(\prod_{k=0}^{\ell}\ C_{m_k}\Big)\mathcal{K}\bigg(\Big(\prod_{k=0}^{\ell}v_{m_k}\Big)G\bigg) \tag{A.23}$$

As a consequence one can write the moment of G, (A.13) solely in terms of the operator $\mathcal{K}$ with no diamagnetic contribution due to the operator $\mathcal{P}$.

$$\Big\langle v_i\frac{\partial}{\partial v_j}G\ \Big\rangle = -\varepsilon\ \frac{M}{q}\ \epsilon_{ijk}\ \frac{B_k}{\varepsilon\ B^2}\ \sum_{\ell=0}^{+\infty}\varepsilon^\ell\Big(\prod_{k=0}^{\ell}\ C_{m_k}\Big)\mathcal{K}\bigg(\Big(\prod_{k=0}^{\ell}v_{m_k}\Big)G\bigg) \tag{A.24}$$

The way of solving the fluid equations using the Laplace large force to compute directly explicit contributions, in the spirit of the drift ordering, does not drive diamagnetic cancellations but rather leads to an expression that does not dependent on these diamagnetic effect as readily observed in (A.24). To be fully consistent with this approach we must assume that the contribution depending on the ∂_t in the operator $\mathcal{K}$ is small typically of order ε. We thus extend (A.24) by introducing an expansion of $\mathcal{K}$ of the form:

$$\mathcal{K} = \mathcal{K}^{(0)} + \varepsilon\ \mathcal{K}^{(1)} \tag{A.25}$$

So that can write the general expression of the moment $v_i\ \partial G/\partial v_j$.

$$\begin{aligned}\Big\langle v_i\frac{\partial}{\partial v_j}G\ \Big\rangle = &-\varepsilon\ \frac{M}{q}\ \epsilon_{ijk}\ \frac{B_k}{\varepsilon\ B^2}\ \sum_{\ell=0}^{+\infty}\varepsilon^\ell\Big(\prod_{k=0}^{\ell}\ C_{m_k}\Big)\mathcal{K}^{(0)}\bigg(\Big(\prod_{k=0}^{\ell}v_{m_k}\Big)G\bigg) \\ &-\varepsilon^2\ \frac{M}{q}\ \epsilon_{ijk}\ \frac{B_k}{\varepsilon\ B^2}\ \sum_{\ell=0}^{+\infty}\varepsilon^\ell\Big(\prod_{k=0}^{\ell}\ C_{m_k}\Big)\mathcal{K}^{(1)}\bigg(\Big(\prod_{k=0}^{\ell}v_{m_k}\Big)G\bigg)\end{aligned} \tag{A.26}$$

Let us now address the specific case of $G = v_j$, hence $\langle v_i \frac{\partial}{\partial v_j} G \Big\rangle = \langle v_i \rangle = n u_{\perp i}$.

$$
\begin{aligned}
n u_{\perp i} = & -\varepsilon \, \frac{M}{q} \, \epsilon_{ijk} \, \frac{B_k}{\varepsilon \, B^2} \, \sum_{\ell=0}^{+\infty} \varepsilon^\ell \Big(\prod_{k=0}^{\ell} \, C_{m_k} \Big) \mathcal{K}^{(0)} \left(\Big(\prod_{k=0}^{\ell} v_{m_k} \Big) v_j \right) \\
& - \varepsilon^2 \, \frac{M}{q} \, \epsilon_{ijk} \, \frac{B_k}{\varepsilon \, B^2} \, \sum_{\ell=0}^{+\infty} \varepsilon^\ell \Big(\prod_{k=0}^{\ell} \, C_{m_k} \Big) \mathcal{K}^{(1)} \left(\Big(\prod_{k=0}^{\ell} v_{m_k} \Big) v_j \right)
\end{aligned} \tag{A.27}
$$

At lowest order in ϵ, namely at order 1, one then finds the very straightforward result:

$$
\begin{aligned}
n u_{\perp i}^{(1)} &= - \frac{M}{q} \, \epsilon_{ijk} \, \frac{B_k}{\varepsilon \, B^2} \, \mathcal{K}^{(0)}(v_j) \\
&= \frac{M}{q} \, \epsilon_{ijk} \, \frac{B_k}{\varepsilon \, B^2} \left(\frac{q}{M} E_m \Big\langle \frac{\partial}{\partial v_m} v_j \Big\rangle + R(v_j) \right) \\
&= \frac{n}{\varepsilon \, B^2} \epsilon_{ijk} \left(E_j + \frac{M}{n \, q} R(v_j) \right) B_k
\end{aligned} \tag{A.28}
$$

Summing the transverse current over all species a one recovers the ambipolarity constraint

$$
\begin{aligned}
\sum_a \, q_a n_a u_{\perp i,a}^{(1)} &= \sum_a \, q_a n_a \, \frac{1}{\varepsilon \, B^2} \, \epsilon_{ijk} \, E_j \, B_k \\
&\quad + \frac{1}{\varepsilon \, B^2} \epsilon_{ijk} \sum_a \, M_a \, R_a(v_j) \, B_k
\end{aligned} \tag{A.29}
$$

where both term are equal to zero, the former via the quasineutrality limit and the latter via the action-reaction balance of collisional momentum exchange. The order 2 in ε is also readily determined:

$$
n u_{\perp i}^{(2)} = - \frac{M}{q} \, \epsilon_{ijk} \, \frac{B_k}{\varepsilon \, B^2} \, \mathcal{K}^{(1)}(v_j) - \frac{M}{q} \, \epsilon_{ijk} \, \frac{B_k}{\varepsilon \, B^2} \, C_m \mathcal{K}^{(0)}(v_m v_j) \tag{A.30}
$$

and therefore:

$$
\begin{aligned}
n u_{\perp i}^{(2)} = & - \frac{1}{q} \, \epsilon_{ijk} \, \partial_t \Big(n \, M \, u_{\perp j}^{(1)} \Big) \, \frac{B_k}{\varepsilon \, B^2} \\
& + \frac{M}{q} \, \epsilon_{ijk} \, \frac{B_k}{\varepsilon \, B^2} \left(\frac{M}{q} \, \frac{\epsilon_{nmr}}{\alpha_n + 1} \nabla_m \, \left(\frac{B_r}{\varepsilon \, B^2} \frac{q}{M} E_m \Big\langle \frac{\partial}{\partial v_m} v_n v_j \Big\rangle \right) \right) \\
& + \frac{M}{q} \, \epsilon_{ijk} \, \frac{B_k}{\varepsilon \, B^2} \left(\frac{M}{q} \, \frac{\epsilon_{nmr}}{\alpha_n + 1} \nabla_m \, \left(\frac{B_r}{\varepsilon \, B^2} R(v_n v_j) \right) \right)
\end{aligned} \tag{A.31}
$$

For simplicity, the collisional contribution is neglected from now on so that:

$$
\begin{aligned}
n u_{\perp i}^{(2)} = & - \frac{M}{q} \, \epsilon_{ijk} \, \partial_t \Big(\epsilon_{j\ell m} \frac{n}{\varepsilon \, B^2} E_\ell B_m \Big) \, \frac{B_k}{\varepsilon \, B^2} \\
& + \frac{M}{q} \, \epsilon_{ijk} \, \frac{B_k}{\varepsilon \, B^2} \left(\frac{\epsilon_{nmr}}{1+1} \nabla_m \, \left(\frac{n \, B_r}{\varepsilon \, B^2} (E_n u_j + E_j u_n) \right) \right)
\end{aligned} \tag{A.32}
$$

A.3 Ordering of the main terms of the conservation equations

We introduce characteristic time scale τ, perpendicular length scale $L_\perp$, parallel length scale $L_\parallel$, perpendicular velocity $V_\perp$ and parallel velocity $V_\parallel$. Similarly, N, T, U, B are the characteristic density, temperature, electric potential and magnetic field respectively, so that:

$$\left\{\frac{N}{\tau}\right\}\frac{\partial\, n_s}{\partial t}+\left\{\frac{NV_\perp}{L_\perp}\right\}\boldsymbol{\nabla}_\perp\cdot(n_s\mathbf{u}_{\perp s})+\left\{\frac{NV_\parallel}{L_\parallel}\right\}\boldsymbol{\nabla}_\parallel\cdot\left(n_s\mathbf{u}_{\parallel s}\right)=0 \tag{A.33}$$

$$\perp\quad\left\{\frac{m_im_s/m_iNV_\perp}{\tau}\right\}\frac{\partial\left(m_sn_s\mathbf{u}_s\right)}{\partial t}+\left\{\frac{NT}{L_\perp}\right\}\boldsymbol{\nabla}\cdot\mathbb{P}_s = \left\{\frac{eNU}{L_\perp}\right\}q_sn_s\mathbf{E}+\left\{eNV_\perp B\right\}q_sn_s\mathbf{u}_s\times\mathbf{B} \tag{A.34}$$

$$\parallel\quad\left\{\frac{m_im_s/m_iNV_\parallel}{\tau}\right\}\frac{\partial\left(m_sn_s\mathbf{u}_s\right)}{\partial t}+\left\{\frac{NT}{L_\parallel}\right\}\boldsymbol{\nabla}\cdot\mathbb{P}_s = \left\{\frac{eNU}{L_\parallel}\right\}q_sn_s\mathbf{E}+\left\{0\right\}q_sn_s\mathbf{u}_s\times\mathbf{B} \tag{A.35}$$

The terms in brackets $\{\}$ indicate the order of the associated contributions. Since these equations are written without collisional contributions or source terms, they are homogeneous in the density N. In the drift ordering, one considers that:

$$\begin{aligned}\frac{NT}{L_\perp} &= \frac{eNU}{L_\perp}=eNV_\perp B\\ U &= \frac{T}{e}\\ V_\perp &= \frac{T}{e\ B\ L_\perp}=\rho_*C\end{aligned} \tag{A.36}$$

where $m_iC^2=T$, $\rho_*=\rho_c/L_\perp$ and $\rho_cC=T/(eB)$. It is to be noted that this expression is species independent. Combining these expressions and definitions, one then finds that:

$$\frac{m_im_s/m_iNV_\perp}{\tau eNV_\perp B}=\frac{m_s}{m_i}\frac{1}{\Omega_i\tau} \tag{A.37}$$

Since $\Omega_e\gg\Omega_i\gg1/\tau$ for all relevant transport times τ, one thus finds that the transverse momentum evolution term is small compared to the other terms. Hence all species are in quasi mechanical equilibrium in the transverse direction. This is the well known force balance condition.
Let us now consider the ordering of the particle balance:

$$\begin{aligned}\frac{N}{\tau} &= \frac{NV_\perp}{L_\perp}=\frac{NV_\parallel}{L_\parallel}\\ \Omega_i\tau &= \frac{\Omega_iL_\perp}{V_\perp}=\frac{\Omega_iL_\parallel}{V_\parallel}=\rho_*^{-2}\\ L_\parallel &= L_\perp M_\parallel\rho_*^{-1}\end{aligned} \tag{A.38}$$

Since one considers that in the drift ordering $k_\parallel \approx 1/L_\parallel \approx k_\perp \rho_* \approx 1/L_\perp$, one finds that in the low Mach number limit, $M_\parallel \ll 1$, the parallel contribution to the particle balance is small. This would correspond to a case in the core plasma. For the edge plasma, one usually considers that $M_\parallel$ is of order unity so that the parallel transport is comparable to the transverse transport, this possible balance then governs the equilibrium SOL width. The evolution contribution to the parallel momentum balance equation is determined by:

$$\begin{aligned} \frac{m_i m_s / m_i N V_\parallel}{\tau} &= \frac{m_s}{m_i}\frac{NCM_\parallel}{\Omega_i \tau} m_i \Omega_i \\ &= \frac{NT}{L_\parallel}\frac{m_s}{m_i}\frac{CM_\parallel}{\Omega_i\tau}\frac{\Omega_i L_\parallel}{C^2} = \frac{NT}{L_\parallel}\frac{m_s}{m_i}M_\parallel^2 \end{aligned} \tag{A.39}$$

One thus finds that the evolution contribution is negligible for electrons due to the mass ratio as well as for the ions in the low Mach number limit. In these cases the parallel mechanical equilibrium is reached. This is the case for the ions in the core plasma. The condition is generally met for the electrons: this is the so-called adiabatic electron limit that yields the generalised Ohm's law.

A.4 Ordering of the contributions to the total pressure tensor

The pressure tensor Eq.(A.4) is split in four different contributions with the following ordering:

$$\begin{aligned} \frac{1}{NT}\mathbb{P}_s &= \frac{p_{\perp s}}{NT}\mathbb{I} + \frac{(p_{\parallel s} - p_{\perp s})}{NT}\mathbf{b}\otimes\mathbf{b} \\ &\quad + \frac{\{m_s/m_i NVV' m_i\}}{NT} m_s n_s \mathbf{u}_s \otimes \mathbf{u}_s + \frac{1}{NT}\Pi_s \\ &= \{1\}\frac{p_{\perp s}}{NT}\mathbb{I} + \{1\}\frac{(p_{\parallel s} - p_{\perp s})}{NT}\mathbf{b}\otimes\mathbf{b} \\ &\quad + \left\{m_s/m_i MM'\right\} m_s n_s \mathbf{u}_s \otimes \mathbf{u}_s + \frac{1}{NT}\Pi_s \end{aligned} \tag{A.40}$$

One thus finds that the two first contributions are of order one, except the second one which is equal to zero in the limit $p_{\parallel s} = p_{\perp s}$. In the third contribution V and V' stand for the characteristic values of the components of $\mathbf{u}_s$. When normalised by C they yield the Mach numbers M and M' with values ρ_* and $M_\parallel$ for the transverse and parallel components respectively. For the ions, the perpendicular-perpendicular component then yields a contribution of order $\rho_*^2 NT/L_\perp$, which is comparable to that of the evolution term in the transverse direction. The parallel-parallel ion component leads to a contribution of order $M_\parallel^2 NT/L_\parallel$ which is again comparable to that of the evolution term in the parallel direction. The parallel-perpendicular component is of order $\rho_* M_\parallel NT/L_\parallel \approx \rho_*^2 NT/L_\perp$ and thus leads to the same order as the perpendicular-perpendicular contribution in the transverse balance equation. The perpendicular-parallel component, $\rho_* M_\parallel NT/L_\perp \approx M_\parallel^2 NT/L_\parallel$, is therefore also found to be of the same order as the evolution contribution of the parallel mechanical balance equation. Finally, the tensor Π depending on the correlation of different components of the fluctuating velocities will be considered to be small, $\{\Pi\}/(NT) \ll 1$.

A.5 Transverse current

Equation (A.9a) allows one to determine the plasma current $\mathbf{j}$ that will be inserted in Eq.(A.7):

$$\begin{aligned}\mathbf{j}_\perp &= \frac{\mathbf{B}}{B^2}\times\left(\frac{\partial\left(m_i n\ \mathbf{u}_i\right)}{\partial t}+\boldsymbol{\nabla}\cdot\left(m_i n\mathbf{u}_i\otimes\mathbf{u}_i\right)\right)\\ &+\frac{\mathbf{B}}{B^2}\times\left(\boldsymbol{\nabla}p_\perp+\mathbf{b}\left(\mathbf{b}\cdot\boldsymbol{\nabla}\right)\left(p_\parallel-p_\perp\right)\right)\\ &+\frac{\mathbf{B}}{B^2}\times\left(\left(p_\parallel-p_\perp\right)\left(\mathbf{b}\cdot\boldsymbol{\nabla}\right)\mathbf{b}+\left(p_\parallel-p_\perp\right)\mathbf{b}\left(\boldsymbol{\nabla}\cdot\mathbf{b}\right)\right)\end{aligned}\tag{A.41}$$

In this expression the cross product by $\mathbf{B}$ of colinear terms drop out so that one obtains:

$$\begin{aligned}\mathbf{j}_\perp &= \frac{\mathbf{B}}{B^2}\times\left(\frac{\partial\left(m_i n\ \mathbf{u}_i\right)}{\partial t}+\boldsymbol{\nabla}\cdot\left(m_i n\mathbf{u}_i\otimes\mathbf{u}_i\right)\right)\\ &+\frac{\mathbf{B}}{B^2}\times\boldsymbol{\nabla}p_\perp+\frac{\mathbf{B}}{B^2}\times\left(\left(p_\parallel-p_\perp\right)\left(\mathbf{b}\cdot\boldsymbol{\nabla}\right)\mathbf{b}\right)\end{aligned}\tag{A.42}$$

The ordering of the various contribution yields:

$$\begin{aligned}\mathbf{j}_\perp\left\{eNC\rho_*\right\} &= \frac{\mathbf{B}}{B^2}\times\left(\frac{\partial\left(m_i n\ \mathbf{u}_i\right)}{\partial t}+\boldsymbol{\nabla}\cdot\left(m_i n\mathbf{u}_i\otimes\mathbf{u}_i\right)\right)\left\{\rho_*^2\frac{NT}{BL_\perp}\right\}\\ &+\frac{\mathbf{B}}{B^2}\times\boldsymbol{\nabla}p_\perp\left\{1\times\frac{NT}{BL_\perp}\right\}\\ &+\frac{\mathbf{B}}{B^2}\times\left(\left(p_\parallel-p_\perp\right)\left(\mathbf{b}\cdot\boldsymbol{\nabla}\right)\mathbf{b}\right)\left\{\frac{L_\perp}{R}\frac{NT}{BL_\perp}\right\}\end{aligned}\tag{A.43}$$

where $eNC\rho_* = NT/(BL_\perp)$. At this stage, terms of various orders are retained. Let us now proceed to a couple of operator permutations:

$$\begin{aligned}\mathbf{j}_\perp &= \partial_t\left(\frac{m_i n}{B^2}\ \mathbf{B}\times\mathbf{u}_i\right)+\boldsymbol{\nabla}\cdot\left(\frac{m_i n}{B^2}\mathbf{u}_i\otimes\left(\mathbf{B}\times\mathbf{u}_i\right)\right)\\ &+\mathbf{B}\times\frac{\boldsymbol{\nabla}p_\perp}{B^2}+\frac{\mathbf{1}}{B}\left(p_\parallel-p_\perp\right)\left(\mathbf{b}\times\left(\mathbf{b}\cdot\boldsymbol{\nabla}\right)\mathbf{b}\right)\\ &+\left(m_i n\ \mathbf{u}_i\right)\times\left(\partial_t\left(\frac{\mathbf{B}}{B^2}\right)+\left(\mathbf{u}_i\cdot\boldsymbol{\nabla}\right)\left(\frac{\mathbf{B}}{B^2}\right)\right)\end{aligned}\tag{A.44}$$

A.6 Divergence of the transverse current

The divergence of the transverse current is then given by:

$$\begin{aligned}\boldsymbol{\nabla}_\perp\cdot\mathbf{j}_\perp &= \partial_t\boldsymbol{\nabla}_\perp\cdot\left(\frac{m_i n}{B^2}\ \mathbf{B}\times\mathbf{u}_i\right)+\left(\boldsymbol{\nabla}_\perp\otimes\boldsymbol{\nabla}\right):\left(\frac{m_i n}{B^2}\mathbf{u}_i\otimes\left(\mathbf{B}\times\mathbf{u}_i\right)\right)\\ &+\boldsymbol{\nabla}_\perp\cdot\left(\mathbf{B}\times\frac{\boldsymbol{\nabla}p_\perp}{B^2}\right)\\ &+\boldsymbol{\nabla}_\perp\cdot\left(\frac{\mathbf{1}}{B}\left(p_\parallel-p_\perp\right)\left(\mathbf{b}\times\left(\mathbf{b}\cdot\boldsymbol{\nabla}\right)\mathbf{b}\right)\right)\\ &+\boldsymbol{\nabla}_\perp\cdot\left(\left(m_i n\ \mathbf{u}_i\right)\times\left(\partial_t\left(\frac{\mathbf{B}}{B^2}\right)+\left(\mathbf{u}_i\cdot\boldsymbol{\nabla}\right)\left(\frac{\mathbf{B}}{B^2}\right)\right)\right)\end{aligned}\tag{A.45}$$

We then split the second term to obtain the divergence of a flux:

$$\begin{aligned}
\boldsymbol{\nabla}_\perp \cdot \mathbf{j}_\perp &= \partial_t \left(\boldsymbol{\nabla}_\perp \cdot \left(\frac{m_i n}{B^2}\, \mathbf{B} \times \mathbf{u}_i \right) \right) \\
&+ \boldsymbol{\nabla} \cdot \left(\mathbf{u}_i \left(\boldsymbol{\nabla}_\perp \cdot \left(\frac{m_i n}{B^2} \mathbf{B} \times \mathbf{u}_i \right) \right) \right) \\
&+ \boldsymbol{\nabla} \cdot \left(\left(\left(\frac{m_i n}{B^2} \mathbf{B} \times \mathbf{u}_i \right) \cdot \boldsymbol{\nabla}_\perp \right) \mathbf{u}_i \right) \\
&+ \boldsymbol{\nabla}_\perp \cdot \left(\mathbf{B} \times \frac{\boldsymbol{\nabla} p_\perp}{B^2} \right) \\
&+ \boldsymbol{\nabla}_\perp \cdot \left(\frac{\mathbf{1}}{B} (p_\parallel - p_\perp) \left(\mathbf{b} \times (\mathbf{b} \cdot \boldsymbol{\nabla})\, \mathbf{b} \right) \right) \\
&+ \boldsymbol{\nabla}_\perp \cdot \left((m_i n\ \mathbf{u}_i) \times \left(\partial_t \left(\frac{\mathbf{B}}{B^2} \right) + (\mathbf{u}_i \cdot \boldsymbol{\nabla}) \left(\frac{\mathbf{B}}{B^2} \right) \right) \right)
\end{aligned} \tag{A.46}$$

We then introduce the vorticity W as the divergence of the polarisation density $n\ \boldsymbol{\sigma}_\perp$ defined as:

$$\boldsymbol{\sigma}_\perp = \frac{m_i}{B^2}\, \mathbf{B} \times \mathbf{u}_i \qquad ; \qquad W = \boldsymbol{\nabla}_\perp \cdot \left(n\ \boldsymbol{\sigma}_\perp \right) \tag{A.47}$$

so that one obtains:

$$\begin{aligned}
\boldsymbol{\nabla}_\perp \cdot \mathbf{j}_\perp &= \partial_t W + \boldsymbol{\nabla} \cdot (\mathbf{u}_i\ W) + \boldsymbol{\nabla}_\perp \cdot \left(\frac{\mathbf{B}}{B^2} \times \boldsymbol{\nabla} p_\perp \right) \\
&+ \boldsymbol{\nabla} \cdot \left((n \boldsymbol{\sigma}_\perp \cdot \boldsymbol{\nabla}_\perp)\, \mathbf{u}_i \right) \\
&+ \boldsymbol{\nabla}_\perp \cdot \left((p_\parallel - p_\perp) \left(\frac{\mathbf{B}}{B^2} \times (\mathbf{b} \cdot \boldsymbol{\nabla})\, \mathbf{b} \right) \right) \\
&+ \boldsymbol{\nabla}_\perp \cdot \left((m_i n\ \mathbf{u}_i) \times \left(\partial_t \left(\frac{\mathbf{B}}{B^2} \right) + (\mathbf{u}_i \cdot \boldsymbol{\nabla}) \left(\frac{\mathbf{B}}{B^2} \right) \right) \right)
\end{aligned} \tag{A.48}$$

Taking into account the relations in Appendix **??**, we now reconsider the divergence of the transverse current:

$$\begin{aligned}
\boldsymbol{\nabla}_\perp \cdot \mathbf{j}_\perp &= \partial_t W + \mathbf{B} \times \left(-\mathbf{E}_\perp + \frac{\boldsymbol{\nabla} p_{\perp i}}{q_i n} \right) \cdot \boldsymbol{\nabla} \left(\frac{W}{B^2} \right) + \boldsymbol{\nabla} \cdot \left(\mathbf{b} u_{\parallel i}\ W \right) \\
&+ \left(\frac{W}{B^2} \right) \boldsymbol{\nabla} \cdot (\mathbf{E}_\perp \times \mathbf{B}) + \left(\frac{W}{B^2} \right) \boldsymbol{\nabla} \cdot \left(\mathbf{B} \times \left(\frac{\boldsymbol{\nabla} p_{\perp i}}{n\ q_i} \right) \right) \\
&+ \frac{\mu_0}{B^2}\, \mathbf{j} \cdot \boldsymbol{\nabla} p_\perp + \mathbf{B} \cdot \left(\boldsymbol{\nabla} p_\perp \times \boldsymbol{\nabla} \frac{1}{B^2} \right) \\
&+ \boldsymbol{\nabla} \cdot \left((n \boldsymbol{\sigma}_\perp \cdot \boldsymbol{\nabla}_\perp)\, \mathbf{u}_i \right) \\
&+ \boldsymbol{\nabla}_\perp \cdot \left((p_\parallel - p_\perp) \left(\frac{\mathbf{B}}{B^2} \times (\mathbf{b} \cdot \boldsymbol{\nabla})\, \mathbf{b} \right) \right) \\
&+ \boldsymbol{\nabla}_\perp \cdot \left((m_i n\ \mathbf{u}_i) \times \left(\partial_t \left(\frac{\mathbf{B}}{B^2} \right) + (\mathbf{u}_i \cdot \boldsymbol{\nabla}) \left(\frac{\mathbf{B}}{B^2} \right) \right) \right)
\end{aligned} \tag{A.49}$$

In the electrostatic limit $\mathbf{E} = -\boldsymbol{\nabla}\Phi$, one can then write:

$$\begin{aligned}
\boldsymbol{\nabla}_\perp \cdot \mathbf{j}_\perp &= \partial_t W + \mathbf{B} \times \left(\boldsymbol{\nabla}_\perp \Phi + \frac{\boldsymbol{\nabla} p_{\perp i}}{q_i n} \right) \cdot \boldsymbol{\nabla} \left(\frac{W}{B^2} \right) + \boldsymbol{\nabla} \cdot \left(\mathbf{b} u_{\parallel i}\, W \right) \\
&+ \frac{W \mu_0}{B^2}\, \mathbf{j} \cdot \boldsymbol{\nabla} \Phi \\
&+ \frac{W}{n\ q_i} \frac{\mu_0}{B^2}\, \mathbf{j} \cdot \boldsymbol{\nabla} p_{\perp i} + \frac{W}{n^2\ q_i}\ \frac{\mathbf{B}}{B^2} \cdot (\boldsymbol{\nabla} n \times \boldsymbol{\nabla} p_{\perp i}) \\
&+ \frac{\mu_0}{B^2}\, \mathbf{j} \cdot \boldsymbol{\nabla} p_\perp + \mathbf{B} \cdot \left(\boldsymbol{\nabla} p_\perp \times \boldsymbol{\nabla} \frac{1}{B^2} \right) \\
&+ \boldsymbol{\nabla} \cdot \left((n \boldsymbol{\sigma}_\perp \cdot \boldsymbol{\nabla}_\perp)\, \mathbf{u}_i \right) \\
&+ \boldsymbol{\nabla}_\perp \cdot \left((p_\parallel - p_\perp) \left(\frac{\mathbf{B}}{B^2} \times (\mathbf{b} \cdot \boldsymbol{\nabla})\, \mathbf{b} \right) \right) \\
&+ \boldsymbol{\nabla}_\perp \cdot \left((m_i n\ \mathbf{u}_i) \times \left(\partial_t \left(\frac{\mathbf{B}}{B^2} \right) + (\mathbf{u}_i \cdot \boldsymbol{\nabla}) \left(\frac{\mathbf{B}}{B^2} \right) \right) \right)
\end{aligned} \tag{A.50}$$

It is then convenient to introduce the Poisson Bracket defined as:

$$[F, G] = \frac{\mathbf{B}}{B^2} \cdot (\boldsymbol{\nabla}_\perp F \times \boldsymbol{\nabla}_\perp G) \tag{A.51}$$

so that:

$$\begin{aligned}
\boldsymbol{\nabla}_\perp \cdot \mathbf{j}_\perp &= \partial_t W + B^2 \left[\Phi, \frac{W}{B^2} \right] + \frac{B^2}{q_i n} \left[p_{\perp i}, \frac{W}{B^2} \right] + \boldsymbol{\nabla} \cdot \left(\mathbf{b} u_{\parallel i}\, W \right) \\
&+ \frac{W}{q_i n^2}\ [n, p_{\perp i}] + B^2 \left[p_\perp, \frac{1}{B^2} \right] \\
&+ \frac{\mu_0}{B^2}\, \mathbf{j} \cdot \left(W \boldsymbol{\nabla} \Phi + \frac{W}{n\ q_i} \boldsymbol{\nabla} p_{\perp i} + \boldsymbol{\nabla} p_\perp \right) \\
&+ \boldsymbol{\nabla} \cdot \left((n \boldsymbol{\sigma}_\perp \cdot \boldsymbol{\nabla}_\perp) \left(u_{\parallel i} \mathbf{b} + \frac{1}{m_i}\ \boldsymbol{\sigma}_\perp \times \mathbf{B} \right) \right) \\
&+ \frac{(p_\parallel - p_\perp) \mu_0}{B^2}\, \mathbf{j} \cdot (\mathbf{b} \cdot \boldsymbol{\nabla})\, \mathbf{b} - \frac{\mathbf{B}}{B^2} \cdot \left(\boldsymbol{\nabla}_\perp (p_\parallel - p_\perp) \times (\mathbf{b} \cdot \boldsymbol{\nabla})\, \mathbf{b} \right) \\
&+ (p_\parallel - p_\perp) \mathbf{B} \cdot \left((\mathbf{b} \cdot \boldsymbol{\nabla})\, \mathbf{b} \times \boldsymbol{\nabla}_\perp \frac{1}{B^2} \right) \\
&+ (p_\parallel - p_\perp) \frac{\mathbf{B}}{B^2} \left(\boldsymbol{\nabla}_\perp \times (\mathbf{b} \cdot \boldsymbol{\nabla})\, \mathbf{b} \right) \\
&+ \boldsymbol{\nabla}_\perp \cdot \left((m_i n\ \mathbf{u}_i) \times \left(\partial_t \left(\frac{\mathbf{B}}{B^2} \right) + (\mathbf{u}_i \cdot \boldsymbol{\nabla}) \left(\frac{\mathbf{B}}{B^2} \right) \right) \right)
\end{aligned} \tag{A.52}$$

This expression can then be written as: Retaining only the contributions with power 1 in ρ_* and power zero in β, one obtains a strong simplification of the expression of $\boldsymbol{\nabla}_\perp \cdot \mathbf{j}_\perp$:

$$\begin{aligned}\boldsymbol{\nabla}_\perp \cdot \mathbf{j}_\perp &= \left\{\frac{NeC\rho_*}{L_\perp}\right\}\left(\partial_t W + B^2\left[\Phi, \frac{W}{B^2}\right] + \frac{B^2}{q_i n}\left[p_{\perp i}, \frac{W}{B^2}\right]\right) \\ &+ \left\{\frac{NeC\rho_*}{L_\perp}\right\}\frac{W}{q_i n^2}\ [n, p_{\perp i}] + \left\{\frac{NeC\rho_* L_\perp}{RL_\perp}\right\} B^2\left[p_\perp, \frac{1}{B^2}\right] \\ &- \left\{\frac{NeC\rho_* L_\perp}{L_\perp R}\right\}\frac{\mathbf{B}}{B^2}\cdot\left(\boldsymbol{\nabla}_\perp(p_\parallel - p_\perp)\times(\mathbf{b}\cdot\boldsymbol{\nabla})\,\mathbf{b}\right) \\ &+ \left\{\frac{NeC\rho_* L_\perp^2}{L_\perp R^2}\right\}(p_\parallel - p_\perp)\mathbf{B}\cdot\left((\mathbf{b}\cdot\boldsymbol{\nabla})\,\mathbf{b}\times\boldsymbol{\nabla}_\perp\frac{1}{B^2}\right) \\ &+ \left\{\frac{NeC\rho_* L_\perp^2}{L_\perp R^2}\right\}(p_\parallel - p_\perp)\frac{\mathbf{B}}{B^2}\left(\boldsymbol{\nabla}_\perp\times(\mathbf{b}\cdot\boldsymbol{\nabla})\,\mathbf{b}\right)\end{aligned} \tag{A.53}$$

A.7 Simplified expressions of the divergence of the transverse current

Expression Eq.(A.53) at order ρ_* and in the asymptotic limit of vanishing β is already strongly simplified. Considering that the three last terms are derived from a single term, that allows one to weigh its contribution in terms of the inverse aspect ratio $L_\perp/R$, a more compact expression of $\boldsymbol{\nabla}_\perp \cdot \mathbf{j}_\perp$ is readily obtained by stepping back with respect to that expansion.

$$\begin{aligned}\boldsymbol{\nabla}_\perp \cdot \mathbf{j}_\perp &= \left(\partial_t W + B^2\left[\Phi, \frac{W}{B^2}\right] + \frac{B^2}{q_i n}\left[p_{\perp i}, \frac{W}{B^2}\right] + \frac{W}{q_i n^2}\ [n, p_{\perp i}]\right) \\ &+ B^2\left[p_\perp, \frac{1}{B^2}\right] \\ &+ \boldsymbol{\nabla}_\perp\cdot\left((p_\parallel - p_\perp)\left(\frac{\mathbf{B}}{B^2}\times(\mathbf{b}\cdot\boldsymbol{\nabla})\,\mathbf{b}\right)\right)\end{aligned} \tag{A.54}$$

When comparing this expression to Eq.(A.43), one can readily see where the three different contributions in Eq.(A.54) stem from. In particular one can see that the lowest order contribution to $\mathbf{j}_\perp$ now contributes at the same order of magnitude as the two diamagnetic contributions (the currents driven by the two pressure terms), see Eq.(A.53). This justifies the fact that all contributions have been retained in the calculation at that initial step. In order to recover the TOKAM2D equation for the vorticity we first assume pressure equipartition, hence $p_\perp = p_\parallel$ so that:

$$\begin{aligned}\boldsymbol{\nabla}_\perp \cdot \mathbf{j}_\perp &= \partial_t W + B^2\left[\Phi, \frac{W}{B^2}\right] + \frac{B^2}{q_i n}\left[p_{\perp i}, \frac{W}{B^2}\right] + \frac{W}{q_i n^2}\ [n, p_{\perp i}] \\ &+ B^2\left[p_\perp, \frac{1}{B^2}\right]\end{aligned} \tag{A.55}$$

In the cold ion limit $T_i \ll T_e$, hence $p_{\perp i} \ll p_\perp$, and neglecting $B^2 W[\Phi, 1/B^2]$ with respect to $[\Phi, W]$, which holds in the large aspect ratio limit $L_\perp \ll R$, one then obtains finally:

$$\boldsymbol{\nabla}_\perp \cdot \mathbf{j}_\perp = \partial_t W + [\Phi, W] + B^2\left[p_\perp, \frac{1}{B^2}\right] \tag{A.56}$$

where the vorticity is also simplified with respect to Eq.(A.47), since $\mathbf{u}_i \approx \boldsymbol{\nabla}\Phi \times \mathbf{B}/B^2$ in the cold ion approximation, so that:

$$\boldsymbol{\sigma}_\perp = \frac{m_i}{B^2}\boldsymbol{\nabla}_\perp\Phi \qquad ; \qquad W = \boldsymbol{\nabla}_\perp \cdot \left(\frac{n\, m_i}{B^2}\boldsymbol{\nabla}_\perp\Phi\right) \tag{A.57}$$

A.8 Particle balance equation at lowest order in ρ_*

The analysis of the particle balance equation is readily obtained by considering Eq.(A.1) for the electrons at lowest order in $\mathbf{u}_{\perp e}$

$$\frac{\partial\, n}{\partial t} + \boldsymbol{\nabla}_\perp \cdot (n\mathbf{u}_{\perp e}) + \boldsymbol{\nabla}_\parallel \cdot \left(n\mathbf{u}_{\parallel e}\right) \;=\; 0 \tag{A.58}$$

In this expression, we thus consider:

$$\mathbf{u}_{\perp e} \;=\; \frac{1}{B^2}\left(\mathbf{E}_\perp + \frac{\boldsymbol{\nabla} p_{\perp e}}{en}\right)\times\mathbf{B} = \frac{1}{B^2}\left(-\boldsymbol{\nabla}_\perp\Phi + \frac{\boldsymbol{\nabla} p_{\perp e}}{en}\right)\times\mathbf{B} \tag{A.59}$$

so that the calculation of the divergence of the transverse particle flux is very similar to that of the divergence of the transverse current, except that the evolution terms are squeezed out in the limit of a small aspect ratio.

$$\begin{aligned}
\boldsymbol{\nabla}_\perp \cdot (n\mathbf{u}_{\perp e}) \;&=\; \boldsymbol{\nabla}_\perp\left(\frac{1}{B^2}\left(-n\boldsymbol{\nabla}_\perp\Phi\times\mathbf{B}\right)\right) + \frac{1}{e}\boldsymbol{\nabla}_\perp\cdot\left(\frac{1}{B^2}\boldsymbol{\nabla} p_{\perp e}\times\mathbf{B}\right)\\
&=\; n\frac{\mu_0}{B^2}\mathbf{j}\cdot\boldsymbol{\nabla}_\perp\Phi + \frac{\mathbf{B}}{B^2}B^2\cdot\left(\boldsymbol{\nabla}_\perp\Phi\times\boldsymbol{\nabla}_\perp\frac{n}{B^2}\right)\\
&\quad -\frac{1}{e}\frac{\mu_0}{B^2}\mathbf{j}\cdot\boldsymbol{\nabla} p_{\perp e} + \frac{\mathbf{B}}{B^2}\frac{B^2}{e}\cdot\left(\boldsymbol{\nabla}_\perp\frac{1}{B^2}\times\boldsymbol{\nabla} p_{\perp e}\right)\\
&=\; B^2\left[\Phi,\frac{n}{B^2}\right] - \frac{B^2}{e}\left[p_{\perp e},\frac{1}{B^2}\right]\\
&\quad +\frac{\mu_0}{B^2}\mathbf{j}\cdot\left(n\boldsymbol{\nabla}_\perp\Phi - \frac{1}{e}\boldsymbol{\nabla}_\perp p_{\perp e}\right)
\end{aligned} \tag{A.60}$$

In the zero β asymptotic limit, one then obtains:

$$\boldsymbol{\nabla}_\perp \cdot (n\mathbf{u}_{\perp e}) = B^2\left[\Phi,\frac{n}{B^2}\right] - \frac{B^2}{e}\left[p_{\perp e},\frac{1}{B^2}\right] \tag{A.61}$$

Finally, in the large aspect ratio limit, hence for:

$$\frac{B^2}{e}\left[p_{\perp e},\frac{1}{B^2}\right] \ll [\Phi, n] \tag{A.62a}$$

$$nB^2\left[\Phi,\frac{1}{B^2}\right] \ll \left[\Phi, n\right] \tag{A.62b}$$

one recovers the particle balance equation used in TOKAM2D.

$$\boldsymbol{\nabla}_\perp \cdot (n\mathbf{u}_{\perp e}) \;=\; [\Phi, n] \tag{A.63}$$

and therefore:

$$\frac{\partial\, n}{\partial t} + [\Phi, n] + \boldsymbol{\nabla}_\parallel \cdot \left(n\mathbf{u}_{\parallel e}\right) \;=\; 0 \tag{A.64}$$

Appendix B

Quasilinear analysis

Using a generic transport equation, akin to the particle balance equation of TOKAM2D, in the quasilinear framework allows one to identify the key assumptions that pave the way towards determining an effective diffusive transport to describe turbulent transport.

$$\frac{\partial f}{\partial \tau} + \left[\phi, f\right] - D\Delta f = -\sigma f \tag{B.1}$$

For the sake of simplicity we consider 2D turbulent transport in the plane transverse to the magnetic field, the parallel transport being taken into account via a small loss term proportional to σ. The equation is normalised, time to $1/\Omega_i$, transverse scale to ρ_s and the potential to T_e/e so that the diffusion coefficient is normalised by the Bohm diffusion coefficient $D_B = \rho_s^2\Omega_i$. The equation is homogeneous in f so that the normalisation of f is arbitrary.

B.1 Average procedure.

In a first step one assumes that f can be split into a mean and fluctuating part, $f = \bar{f} + \tilde{f}$. This initial procedure is never discussed in terms of its actual implications, the usual trick being to invoke an averaging procedure based on a series of independent realisations of the same experiment. However, in actual experiments or large simulation runs, this procedure is not applicable. Furthermore, in simulations, the same run conditions will lead to the same simulation unless one allows generating independent realisations of the same numerical experiment via a stochastic process amplified by chaotic sensitivity to initial conditions. The averaging procedure is then governed by the chosen stochastic process and not some "Deus ex machina" determination of independent realisations. The averaging process, symbolised by brackets, $\bar{f} = \left\langle f \right\rangle$, which governs the separation will be further discussed in the following. It leads to two coupled equations replacing (B.1).

$$\frac{\partial \bar{f}}{\partial \tau} + \left[\bar{\phi}, \bar{f}\,\right] + \left\langle \left[\tilde{\phi}, \tilde{f}\,\right] \right\rangle - D\Delta \bar{f} = -\sigma \bar{f} \tag{B.2a}$$

$$\frac{\partial \tilde{f}}{\partial \tau} + \left[\bar{\phi}, \tilde{f}\,\right] + \left[\tilde{\phi}, \bar{f}\,\right] + \left[\tilde{\phi}, \tilde{f}\,\right] - \left\langle \left[\tilde{\phi}, \tilde{f}\,\right] \right\rangle - D\Delta \tilde{f} = -\sigma \tilde{f} \tag{B.2b}$$

sectionOrdering of the fluctuations. We introduce the parameter $\varepsilon = \tilde{f}|/|\bar{f}|$ where the symbol $|f|$ is an appropriate norm allowing one to characterise the magnitude of the

fluctuations with respect to the mean. Introducing ε in (B.2) to characterise the magnitude of all the fluctuating terms with respect to the mean terms, one obtains:

$$\frac{\partial \bar{f}}{\partial \tau} + [\bar{\phi}, \bar{f}\,] + \varepsilon^2 \Big\langle [\tilde{\phi}, \tilde{f}\,] \Big\rangle - D\Delta \bar{f} = -\sigma \bar{f} \tag{B.3a}$$

$$\varepsilon \frac{\partial \tilde{f}}{\partial \tau} + \varepsilon [\bar{\phi}, \tilde{f}\,] + \varepsilon [\tilde{\phi}, \bar{f}\,] + \varepsilon^2 [\tilde{\phi}, \tilde{f}\,] - \varepsilon^2 \Big\langle [\tilde{\phi}, \tilde{f}\,] \Big\rangle - \varepsilon D\Delta \tilde{f} = -\varepsilon\sigma \tilde{f} \tag{B.3b}$$

Multiscale analysis. It is now important to introduce appropriate scaling factors for the parameters and variables τ, x, y in this set of equations to obtain consistent results. Given a variable S we introduce two dimensionless variables z and Z characterised by the scales ℓ_z and L_Z so that:

$$S = \ell_z z + L_Z Z \qquad ; \qquad s = \frac{S}{\ell_s} = \frac{\ell_z}{\ell_s} z + \frac{L_Z}{\ell_s} Z \tag{B.4}$$

where ℓ_s is the chosen normalisation scale of the variable S that defines the normalised variable s in (B.4). Let us now assume that the variables z and Z are independent, one then has the chain rule for the derivative:

$$\ell_s \frac{\partial}{\partial S} = \frac{\partial}{\partial s} = \frac{\partial z}{\partial s}\,\frac{\partial}{\partial z} + \frac{\partial Z}{\partial s}\,\frac{\partial}{\partial Z} = \frac{\ell_s}{\ell_z}\,\frac{\partial}{\partial z} + \frac{\ell_s}{\ell_Z}\,\frac{\partial}{\partial Z} \tag{B.5}$$

Consistently, for the normalised time variable one then has:

$$\frac{\partial}{\partial \tau} = \frac{1}{\Omega_i \tau_t}\,\frac{\partial}{\partial t} + \frac{1}{\Omega_i \tau_T}\,\frac{\partial}{\partial T} \tag{B.6}$$

where τ_t is the relevant time scale of the turbulent fluctuations, hence $\rho_* = 1/(\Omega_i \tau_t)$, and τ_T is the relevant time scale of the diffusive transport determined by this quasilinear analysis.

Regarding the length scales one proceeds in a similar fashion with ρ_s the turbulent length scale, which is also used as normalising parameter, and a for the transport scale one must then replace ∂_x and ∂_y by $\partial_x + \rho_* \partial_X$ and $\partial_y + \rho_* \partial_Y$ respectively. We reuse the variables x and y to simplify the writing. This ordering modifies the Poisson bracket [.] and Laplacian Δ operators.

$$[\,.\,] = [\,.\,]_{x,y} + \rho_* [\,.\,]_{X,y} + \rho_* [\,.\,]_{x,Y} + \rho_*^2 [\,.\,]_{X,Y} \tag{B.7a}$$

$$\Delta = \Delta_{x,y} + 2\,\rho_* \Big(\partial_x \partial_X + \partial_y \partial_Y \Big) + \rho_*^2 \Delta_{X,Y} \tag{B.7b}$$

B.2 Multiscale and averaging

We now define the averaging process as an average over the high frequency variables, namely t, x, y, so that the mean fields only depend on T, X, Y. One then obtains for the mean field equation:

$$\rho_* \,\frac{\tau_t}{\tau_T}\,\frac{\partial \bar{f}}{\partial T} + \rho_*^2 [\bar{\phi}, \bar{f}\,]_{X,Y} + \varepsilon^2 \Big\langle [\tilde{\phi}, \tilde{f}] \Big\rangle - D\rho_*^2 \Delta_{X,Y} \bar{f} = -\sigma \bar{f} \tag{B.8}$$

Given the expression of the Poisson bracket:

$$[\phi, f] = \partial_x \Big(f\big(-\partial_y \phi \big) \Big) + \partial_y \Big(f\ \partial_x \phi \Big) \tag{B.9}$$

One readily obtains:

$$\Big\langle \big[\phi, f\big] \Big\rangle = -\rho_* \partial_X \Big\langle f \big(\partial_y + \rho_* \partial_Y\big)\phi \Big\rangle + \rho_* \partial_Y \Big\langle f \big(\partial_x + \rho_* \partial_X\big)\phi \Big\rangle \tag{B.10}$$

hence,

$$\begin{aligned} \rho_* \, \frac{\tau_t}{\tau_T} \frac{\partial \bar{f}}{\partial T} + \rho_*^2 \big[\bar{\phi}, \bar{f}\,\big]_{X,Y} - \varepsilon^2 \rho_* \, \partial_X \Big\langle \tilde{f} \, \partial_y \tilde{\phi} \Big\rangle + \varepsilon^2 \rho_* \, \partial_Y \Big\langle \tilde{f} \, \partial_x \tilde{\phi} \Big\rangle \\ -\varepsilon^2 \rho_*^2 \, \partial_X \Big\langle \tilde{f} \, \partial_Y \tilde{\phi} \Big\rangle + \varepsilon^2 \rho_*^2 \, \partial_Y \Big\langle \tilde{f} \, \partial_X \tilde{\phi} \Big\rangle - D \rho_*^2 \Delta_{X,Y} \bar{f} = -\sigma \bar{f} \end{aligned} \tag{B.11}$$

In order to complete this ordering, one must determine the appropriate scaling properties of the diffusion coefficient D and of the parallel loss term σ. Regarding $\sigma = 1/(\Omega_i \tau_f)$ where τ_f is the characteristic life-time, one thus obtains:

$$\sigma = \frac{1}{\Omega_i \tau_f} = \frac{a}{\tau_f c_s} \rho_* \tag{B.12a}$$

$$D = \nu_D \rho_*^{\alpha} D_c \tag{B.12b}$$

Since the diffusion coefficient D is normalised by the Bohm diffusion coefficient D_B, $\alpha = 0$ corresponds to a Bohm-like diffusive transport while $\alpha = 1$ will lead to a gyro-Bohm like diffusive contribution to the transport. The parameter ν_D takes into account the smallness of the diffusive transport process. For collisional diffusion one has $\nu_D = \nu_*$ and $\alpha = 1$. Since $\tau_t = a/c_s$ as determined by the turbulence growth rate, the mean transport equation takes the form:

$$\begin{aligned} \frac{\partial \bar{f}}{\partial T} + \frac{\varepsilon^2}{\tau_t/\tau_T} \Bigg(- \; \partial_X \Big\langle \tilde{f} \, \partial_y \tilde{\phi} \Big\rangle + \partial_Y \Big\langle \tilde{f} \, \partial_x \tilde{\phi} \Big\rangle \Bigg) \\ + \frac{\varepsilon^2 \rho_*}{\tau_t/\tau_T} \Bigg(- \partial_X \Big\langle \tilde{f} \, \partial_Y \tilde{\phi} \Big\rangle + \partial_Y \Big\langle \tilde{f} \, \partial_X \tilde{\phi} \Big\rangle \Bigg) \\ + \frac{\rho_*}{\tau_t/\tau_T} \Bigg(- \partial_X \Big(\bar{f} \, \partial_Y \bar{\phi} \Big) + \partial_Y \Big(\bar{f} \, \partial_X \bar{\phi} \Big) \Bigg) \\ - \frac{\nu_D \rho_*^{1+\alpha}}{\tau_t/\tau_T} \, D_c \Delta_{X,Y} \bar{f} = -\frac{\tau_t/\tau_f}{\tau_t/\tau_T} \bar{f} \end{aligned} \tag{B.13}$$

One can then readily show that the convective contribution of the second line, proportional to $\varepsilon^2 \rho_* \tau_T / \tau_t$ will be negligible at order one. One can then identify two transport regimes:

1. *Small fluctuations:* $\varepsilon^2 \ll \rho_* \ll 1$, so that one can set $\tau_t/\tau_T = \rho_*$, and consequently:

$$\frac{\partial \bar{f}}{\partial T} - \partial_X \Big(\bar{f} \partial_Y \bar{\phi} \Big) + \partial_Y \Big(\bar{f} \partial_X \bar{\phi} \Big) - \nu_D \rho_*^{\alpha} \, D_c \Delta_{X,Y} \bar{f} = -\frac{\tau_t/\tau_f}{\rho_*} \bar{f} \tag{B.14a}$$

   In this regime the mean fields are decoupled from the fluctuations. The characteristic time scale of the parallel transport τ_f must be large enough, $\tau_T \leq \tau_f$, so that the transverse transport is adiabatic with respect to the parallel transport.

2. *Large fluctuations:* $\rho_*^{1/2} \ll \varepsilon$ so that one can set $\tau_t/\tau_T = \varepsilon^2$. The order one mean transport equation is then:

$$\frac{\partial \bar{f}}{\partial T} - \partial_X \Big\langle \tilde{f} \partial_y \tilde{\phi} \Big\rangle + \partial_Y \Big\langle \tilde{f} \partial_x \tilde{\phi} \Big\rangle - \frac{\nu_D \rho_*^{1+\alpha}}{\varepsilon^2} \, D_c \Delta_{X,Y} \bar{f} = -\frac{\tau_t/\tau_f}{\varepsilon^2} \bar{f} \tag{B.14b}$$

with the same condition on τ_f, $\tau_T \leq \tau_f$. In this regime, the mean field convective transport is governed by the coherent interferences between the fluctuations of f and of the electric drift velocities.

3. Order one fluctuation transport: $\varepsilon^2 = 1$. This case is in the same regime than defined by the previous idem, however the condition $\tau_t/\tau_T = 1$ means that one cannot make a separation between turbulent and transport time scales $t \equiv T$. The lowest order mean transport equation then takes the form:

$$\frac{\partial \bar{f}}{\partial t} - \partial_X \Big\langle \tilde{f}\, \partial_y \tilde{\phi} \Big\rangle + \partial_Y \Big\langle \tilde{f}\, \partial_x \tilde{\phi} \Big\rangle - \nu_D \rho_*^{1+\alpha}\, D_c \Delta_{X,Y} \bar{f} = -\frac{\tau_t}{\tau_f} \bar{f} \tag{B.14c}$$

Note that when the large scale fields do not depend on the poloidal coordinate Y one only finds the large fluctuation regime, however with no constraint on ε. Let us now consider the evolution equation for the fluctuating field:

$$\begin{aligned}
&\frac{\partial \tilde{f}}{\partial t} + \partial_X \bar{\phi} \partial_y \tilde{f} - \partial_Y \bar{\phi} \partial_x \tilde{f} + \partial_x \tilde{\phi} \partial_Y \bar{f} - \partial_y \tilde{\phi} \partial_X \bar{f} \\
&\quad + \frac{\varepsilon}{\rho_*} \big[\tilde{\phi}, \tilde{f}\, \big]_{x,y} \\
&\quad + \varepsilon \Big(\big[\tilde{\phi}, \tilde{f}\, \big]_{X,y} + \partial_X \Big\langle \tilde{f} \partial_y \tilde{\phi} \Big\rangle \Big) \\
&\quad + \varepsilon \Big(\big[\tilde{\phi}, \tilde{f}\, \big]_{x,Y} - \partial_Y \Big\langle \tilde{f} \partial_x \tilde{\phi} \Big\rangle \Big) \\
&\quad + \varepsilon\, \rho_* \Big(\big[\tilde{\phi}, \tilde{f}\, \big]_{X,Y} - \Big\langle \big[\tilde{\phi}, \tilde{f}\, \big]_{X,Y} \Big\rangle \Big) \\
&\quad - \nu_D \rho_*^{\alpha-1} D_c \Delta_{x,y} \tilde{f} - 2\, \nu_D \rho_*^{\alpha} D_c \big(\partial_X \partial_x + \partial_Y \partial_y \big) \tilde{f} - \nu_D \rho_*^{\alpha+1} D_c \Delta_{X,Y} \tilde{f} \\
&\qquad = -\frac{\tau_t}{\tau_f} \tilde{f}
\end{aligned} \tag{B.15}$$

B.3 Quasilinear framework, small amplitude fluctuations.

Within the quasilinear framework, one neglects the quadratic terms with respect to the fluctuations. One thus requires that $\varepsilon \ll \rho_*$. Furthermore, to avoid issues regarding the ordering of the diffusive transport we shall assume that $\alpha = 1$, namely that the diffusion is gyro-Bohm. At lowest order one then obtains:

$$\frac{\partial \tilde{f}}{\partial t} + \partial_X \bar{\phi} \partial_y \tilde{f} - \partial_Y \bar{\phi} \partial_x \tilde{f} + \partial_x \tilde{\phi} \partial_Y \bar{f} - \partial_y \tilde{\phi} \partial_X \bar{f} - \nu_D D_c \Delta_{x,y} \tilde{f} = -\frac{\tau_t}{\tau_f} \tilde{f} \tag{B.16}$$

which is by construction linear with respect to the fluctuations and can therefore conveniently be Fourier expanded with respect to the high frequency variables, with no mode coupling, so that one can determine $\tilde{f}$ in terms of $\tilde{\phi}$.

$$\hat{f}_{\omega,k_x,k_y} = -\frac{k_y \partial_X \bar{f} - k_x \partial_Y \bar{f}}{\omega + k_x \bar{V}_{Ex} + k_y \bar{V}_{Ey} + i \Big(\nu_D D_c k^2 + \frac{\tau_t}{\tau_f} \Big)} \hat{\phi}_{\omega,k_x,k_y} \tag{B.17}$$

In this expression we have introduced the following notations: $k^2 = k_x^2 + k_y^2$ and $\bar{V}_{Ex} = -\partial_Y \bar{\phi}$, $\bar{V}_{Ey} = \partial_X \bar{\phi}$ so that $k_x \bar{V}_{Ex} + k_y \bar{V}_{Ey} = \boldsymbol{k} \cdot \bar{\boldsymbol{V}}_E$ and therefore:

$$\hat{f}_{\omega,k_x,k_y} = -\frac{\omega + \boldsymbol{k} \cdot \bar{\boldsymbol{V}}_E - i\, \eta}{\big(\omega + \boldsymbol{k} \cdot \bar{\boldsymbol{V}}_E \big)^2 + \eta^2} \Big(k_y \partial_X \bar{f} - k_x \partial_Y \bar{f} \Big) \hat{\phi}_{\omega,k_x,k_y} \tag{B.18}$$

with $\eta = \nu_D D_c k^2 + \tau_t/\tau_f$.

This expression can then be used to compute the non-linear contribution in (B.14b), hence the fluxes

$$\Gamma_X = \left\langle \tilde{f}\partial_y \tilde{\phi} \right\rangle = \sum_{\omega',k'_x,k'_y} \sum_{\omega'',k''_x,k''_y} \hat{f}_{\omega',k'_x,k'_y}(i\ k''_y)\hat{\phi}_{\omega'',k''_x,k''_y} \left\langle e^{i(\varphi'+\varphi'')} \right\rangle \tag{B.19a}$$

$$\Gamma_Y = -\left\langle \tilde{f}\partial_x \tilde{\phi} \right\rangle = - \sum_{\omega',k'_x,k'_y} \sum_{\omega'',k''_x,k''_y} \hat{f}_{\omega',k'_x,k'_y}(i\ k''_x)\hat{\phi}_{\omega'',k''_x,k''_y} \left\langle e^{i(\varphi'+\varphi'')} \right\rangle \tag{B.19b}$$

where:

$$\varphi' + \varphi'' = t(\omega' + \omega'') + x(k'_x + k''_x) + y(k'_y + k''_y) \tag{B.20}$$

The average on the high frequency phases then readily yields:

$$\Gamma_X = -i \sum_{\omega,k_x,k_y} k_y\ \hat{\phi}^*_{\omega,k_x,k_y}\ \hat{f}_{\omega,k_x,k_y} \tag{B.21a}$$

$$\Gamma_Y = i \sum_{\omega,k_x,k_y} k_x\ \hat{\phi}^*_{\omega,k_x,k_y}\ \hat{f}_{\omega,k_x,k_y} \tag{B.21b}$$

Given the expression of $\hat{f}$ (B.18), one then finds the fluxes:

$$\Gamma_X = \sum_{\omega,k_x,k_y} |\hat{\phi}_{\omega,k_x,k_y}|^2\ \frac{i\big(\omega + \boldsymbol{k}\cdot\bar{\boldsymbol{V}}_E\big) + \eta}{\big(\omega + \boldsymbol{k}\cdot\bar{\boldsymbol{V}}_E\big)^2 + \eta^2} \Big(+ k_y^2 \partial_X \bar{f} - k_x k_y \partial_Y \bar{f}\ \Big) \tag{B.22a}$$

$$\Gamma_Y = \sum_{\omega,k_x,k_y} |\hat{\phi}_{\omega,k_x,k_y}|^2\ \frac{i\big(\omega + \boldsymbol{k}\cdot\bar{\boldsymbol{V}}_E\big) + \eta}{\big(\omega + \boldsymbol{k}\cdot\bar{\boldsymbol{V}}_E\big)^2 + \eta^2} \Big(- k_x k_y \partial_X \bar{f} + k_x^2 \partial_Y \bar{f}\ \Big) \tag{B.22b}$$

The symmetry in the sum when changing ω, k_x, k_y to $-\omega, -k_x, -k_y$ then yields the quasi-linear expression of the fluxes:

$$\boldsymbol{\Gamma} = \mathbb{D}_{QL} \cdot \boldsymbol{\nabla} \bar{f} \tag{B.23a}$$

$$\mathbb{D}_{QL} = \sum_{\omega,k_x,k_y} |\hat{\phi}_{\omega,k_x,k_y}|^2\ \frac{\eta}{\big(\omega + \boldsymbol{k}\cdot\bar{\boldsymbol{V}}_E\big)^2 + \eta^2} \begin{pmatrix} k_y^2 & -k_x k_y \\ -k_x k_y & k_x^2 \end{pmatrix} \tag{B.23b}$$

The mean field evolution equation is then:

$$\frac{\partial \bar{f}}{\partial T} - \boldsymbol{\nabla} \cdot \Big(\mathbb{D}_{QL} \cdot \boldsymbol{\nabla} \bar{f} \Big) = -\frac{\tau_t/\tau_f}{\varepsilon^2} \bar{f} \tag{B.24}$$

Given the evolution with T the diffusion coefficient is normalised by $\rho_* D_B$ and is therefore gyro-Bohm. One also finds that for the SOL case, such that $\tau_f = \tau_t$, one must have ε of order 1, hence very large fluctuations which contradicts the quasilinear assumption regarding the quadratic contribution to the fluctuation evolution. Conversely, if the fluctuations are small, one must ensure that $\tau_t \ll \tau_f$, hence adiabatic transverse transport with respect to a slow parallel transport contribution.

Appendix C

The rescaled equation of TOKAM2D

C.1 Linearized sheath losses

We consider here the following set of equations where the sheath terms have been linearized in such a way as to retain the key physics. Modifying the sheath expression provides significant margin to determine a new normalization of the system. We have included explicitly the linear term $-\partial_y\phi\partial_x\bar{n}$ to see how gradient driven systems vary with respect to flux driven systems with a radially localized source $S = S_0\mathcal{S}(x)$ where the radial integral of $\mathcal{S}(x)$ and S_0 is therefore the magnitude of the source term.

$$\partial_t n + [\phi, n] - \partial_y\phi\partial_x\bar{n} - D_\perp\Delta_\perp n + \sigma_n n = S_0\mathcal{S}(x) \tag{C.1a}$$

$$\partial_t W + [\phi, W] + \ g\partial_y n - \nu_\perp\Delta_\perp W - \sigma_\phi\phi = 0 \tag{C.1b}$$

C.2 Normalization coefficients

Let A_n, A_ϕ, A_t, A_L be the normalization constants, we then have:

$$\partial_t n + \frac{A_t\ A_\phi\ A_n}{A_n\ A_L^2}[\phi, n] - \frac{A_t\ A_\phi}{A_n\ A_L}\partial_y\phi\ \partial_x\bar{n} - D_\perp\frac{A_t\ A_n}{A_n\ A_L^2}\Delta_\perp n + \frac{A_t\ A_n}{A_n}\sigma_n n = \frac{A_t}{A_n}S_0\mathcal{S}(A_L\ x) \tag{C.2a}$$

$$\partial_t W + \frac{A_t\ A_\phi^2\ A_L^2}{A_\phi\ A_L^4}[\phi, W] + \ \frac{A_t\ A_n\ A_L^2}{A_\phi\ A_L}g\partial_y n - \frac{A_t\ A_\phi\ A_L^2}{A_\phi\ A_L^4}\nu_\perp\Delta_\perp W - \frac{A_t\ A_\phi\ A_L^2}{A_\phi}\sigma_\phi\phi = 0 \tag{C.2b}$$

C.3 Universal transport equation

Normalizing-out the parameters of the transport equation

As a rule for this normalization we choose to remove coefficients from the particle balance equation. The Poisson bracket control term can be set to 1 with the constraint $A_t\ A_\phi = A_L^2$.

hence:

$$\partial_t n + [\phi, n] - \frac{A_t\ A_\phi}{A_n\ A_L}\partial_y\phi\ \partial_x\bar{n} - D_\perp\frac{A_t}{A_L^2}\Delta_\perp n + A_t\sigma_n n = \frac{A_t}{A_n}S_0\mathcal{S}(A_L\ x) \tag{C.3a}$$

$$\partial_t W + [\phi, W] + \frac{A_t\ A_n\ A_L}{A_\phi}g\ \partial_y n - \frac{A_t}{A_L^2}\nu_\perp\Delta_\perp W - A_t A_L^2\sigma_\phi\ \phi = 0 \tag{C.3b}$$

Setting $D_\perp A_t = A_L^2$ then leads to:

$$\partial_t n + [\phi, n] - \frac{A_L}{A_n}\partial_y\phi\ \partial_x\bar{n} - \Delta_\perp n + \frac{A_L^2\sigma_n}{D_\perp}\ n = \frac{A_L^2\ S_0}{D_\perp\ A_n}\ \mathcal{S}(A_L\ x) \tag{C.4a}$$

$$\partial_t W + [\phi, W] + \frac{A_n\ A_L^3}{D_\perp^2}g\ \partial_y n - \frac{\nu_\perp}{D_\perp}\Delta_\perp W - \frac{\sigma_\phi A_L^4}{D_\perp}\ \phi = 0 \tag{C.4b}$$

Finally, in the SOL, $\sigma_n \neq 0$, so that one can set: $A_L^2\sigma_n = D_\perp$, $A_t = 1/\sigma_n$, and $A_\phi = D_\perp$.

$$\partial_t n + [\phi, n] - \frac{(D_\perp\sigma_n)^{1/2}}{A_n\ \sigma_n}\partial_y\phi\ \partial_x\bar{n} - \Delta_\perp n + \ n = \frac{S_0}{\sigma_n\ A_n}\ \mathcal{S}(A_L\ x) \tag{C.5a}$$

$$\partial_t W + [\phi, W] + \frac{A_n}{(D_\perp\sigma_n)^{1/2}\ \sigma_n}\ g\ \partial_y n - \frac{\nu_\perp}{D_\perp}\Delta_\perp W - \frac{\sigma_\phi D_\perp}{\sigma_n^2}\ \phi = 0 \tag{C.5b}$$

Universal transport, flux driven SOL equations

Considering the flux driven case, $S_0 \neq 0$ and $\partial_x\bar{n} = 0$, one can then define A_n such that $A_n\sigma_n = S_0$.

$$\partial_t n + [\phi, n] - \Delta_\perp n + n - \mathcal{S}(A_L\ x) = 0 \tag{C.6a}$$

$$\partial_t W + [\phi, W] + G_f\ \partial_y n - S_c\ \Delta_\perp W - \Sigma_\phi\ \phi = 0 \tag{C.6b}$$

where:

$$G_f = \frac{S_0\ g}{\left(\sigma_n\ D_\perp\right)^{1/2}\sigma_n^2} \tag{C.6c}$$

$$S_c = \frac{\nu_\perp}{D_\perp} \tag{C.6d}$$

$$\Sigma_\phi = \frac{\sigma_\phi\ D_\perp}{\sigma_n^2} \tag{C.6e}$$

This system depends on 4 control parameters to be compared to the 7 control parameters in Eq.(C.1). It is also to be noted that all control parameters have not been removed from the particle balance equation given the radial dependence of the source term. the other three control parameters are: G_f that characterizes the instability and its magnitude, as well as S_c, Σ_ϕ, Eq.(C.6d, C.6e), that control the instability spectrum via the long wave length damping governed by the Schmidt number and the short wave length damping via Σ_ϕ.

Universal transport, gradient driven SOL equations

Considering now the gradient driven case, $S_0 = 0$ and $\partial_x\bar{n} \neq 0$, one can then define A_n such that $A_n\sigma_n = -(D_\perp\ \sigma_n)^{1/2}\ \partial_x\bar{n}$.

$$\partial_t n + [\phi, n] - \partial_y\phi - \Delta_\perp n + \ n = 0 \tag{C.7a}$$

$$\partial_t W + [\phi, W] + G_g\ \partial_y n - S_c\Delta_\perp W - \Sigma_\phi\ \phi = 0 \tag{C.7b}$$

where:

$$G_g \;=\; \frac{-\partial_x \bar{n}\; g}{\sigma_n^2} \tag{C.7c}$$

In this case 3 control parameters are retained, G_g that characterizes the instability and its magnitude, as well as S_c, Σ_ϕ, Eq.(C.6d, C.6e), that control the instability spectrum via the long wave length damping governed by the Schmidt number and the short wave length damping via Σ_ϕ.

C.4 Universal vorticity equation

Normalizing-out the parameters of the vorticity equation

An alternative is to remove the control parameters from the vorticity equation, hence given Eq.(C.2), one now sets: $A_t\nu_\perp = A_L^2 = A_t\; A_\phi$ so that $A_\phi = \nu_\perp$ and $A_t = A_L^2/\nu_\perp$. Therefore:

$$\partial_t n + [\phi, n] - \frac{A_L}{A_n}\partial_y\phi\;\partial_x\bar{n} - \frac{D_\perp}{\nu_\perp}\Delta_\perp n + A_t\;\sigma_n\;n = \frac{A_L^2\;S_0}{A_n\;\nu_\perp}\;\mathcal{S}(A_L\;x) \tag{C.8a}$$

$$\partial_t W + [\phi, W] + \;\frac{A_n\;A_L^3}{\nu_\perp^2}\;g\;\partial_y n - \Delta_\perp W - \frac{A_L^4\;\sigma_\phi}{\nu_\perp}\;\phi = 0 \tag{C.8b}$$

Let $\bar{k} = 1/A_L = (\sigma_\phi/\nu_\perp)^{1/4}$, $A_t = 1/(\nu_\perp\sigma_\phi)^{1/2}$, one then has:

$$\partial_t n + [\phi, n] - \frac{\partial_x\bar{n}}{\bar{k}\;A_n}\;\partial_y\phi - \frac{D_\perp}{\nu_\perp}\Delta_\perp n + \frac{\sigma_n}{(\nu_\perp\sigma_\phi)^{1/2}}\;n = \frac{S_0}{A_n\;(\nu_\perp\sigma_\phi)^{1/2}}\mathcal{S}(A_L\;x) \tag{C.9a}$$

$$\partial_t W + [\phi, W] + \;\frac{\bar{k}\;A_n\;g}{\nu_\perp\sigma_\phi}\;\partial_y n - \Delta_\perp W - \phi = 0 \tag{C.9b}$$

In a last step one sets $A_n = \nu_\perp\sigma_\phi/(g\bar{k})$ so that:

$$\partial_t n + [\phi, n] - \frac{g\;\partial_x\bar{n}}{\sigma_\phi\;\nu_\perp}\;\partial_y\phi - \frac{D_\perp}{\nu_\perp}\Delta_\perp n + \frac{\sigma_n}{(\nu_\perp\sigma_\phi)^{1/2}}\;n = \frac{g\;\bar{k}\;S_0}{(\nu_\perp\sigma_\phi)^{3/2}}\mathcal{S}(A_L\;x) \tag{C.10a}$$

$$\partial_t W + [\phi, W] + \;\partial_y n - \Delta_\perp W - \phi = 0 \tag{C.10b}$$

Universal vorticity, flux driven SOL equations

Considering the flux driven case, $S_0 \neq 0$ and $\partial_x\bar{n} = 0$, one readily finds:

$$\partial_t n + [\phi, n] - \frac{1}{S_c}\Delta_\perp n + \Sigma_n\;n = Z_s\;\mathcal{S}(A_L\;x) \tag{C.11a}$$

$$\partial_t W + [\phi, W] + \;\partial_y n - \Delta_\perp W - \phi = 0 \tag{C.11b}$$

where:

$$\Sigma_n \;=\; \frac{\sigma_n}{(\nu_\perp\sigma_\phi)^{1/2}} \tag{C.11c}$$

$$Z_s \;=\; \frac{g\;\bar{k}\;S_0}{(\nu_\perp\sigma_\phi)^{3/2}} \tag{C.11d}$$

Universal vorticity, gradient driven SOL equations

Considering the gradient driven case, $S_0 = 0$ and $\partial_x \bar{n} \neq 0$, one readily finds:

$$\partial_t n + [\phi, n] + \frac{1}{\Lambda_n}\,\partial_y \phi - \frac{1}{S_c}\Delta_\perp n + \Sigma_n\, n = 0 \tag{C.12a}$$

$$\partial_t W + [\phi, W] + \partial_y n - \Delta_\perp W - \phi = 0 \tag{C.12b}$$

where:

$$\frac{1}{\Lambda_n} = -\frac{g\,\partial_x \bar{n}}{\sigma_\phi\,\nu_\perp} \tag{C.12c}$$

C.5 Universal transport equation with sheath contribution

Normalizing-out the parameters of the transport equation with sheath

$$\partial_t n + [\phi, n] - \frac{(D_\perp \sigma_n)^{1/2}}{A_n\,\sigma_n}\partial_y \phi\,\partial_x \bar{n} - \Delta_\perp n + n\exp(-D_\perp\,\phi) = \frac{S_0}{\sigma_n\,A_n}\,\mathcal{S}(A_L\,x) \tag{C.13a}$$

$$\partial_t W + [\phi, W] + \frac{A_n}{(D_\perp \sigma_n)^{1/2}\,\sigma_n}\,g\,\partial_y n - \frac{\nu_\perp}{D_\perp}\Delta_\perp W - \frac{\sigma_\phi}{\sigma_n^2}\left(1 - \exp(-D_\perp\,\phi)\right) = 0 \tag{C.13b}$$

Universal transport, flux driven SOL equations with sheath

Considering the flux driven case, $S_0 \neq 0$ and $\partial_x \bar{n} = 0$, one can then define A_n such that $A_n \sigma_n = S_0$.

$$\partial_t n + [\phi, n] - \Delta_\perp n + n\exp(-D_\perp\,\phi) - \mathcal{S}(A_L\,x) = 0 \tag{C.14a}$$

$$\partial_t W + [\phi, W] + G_f\,\partial_y n - S_c\,\Delta_\perp W - \frac{\Sigma_\phi}{D_\perp}\left(1 - \exp(-D_\perp\,\phi)\right) = 0 \tag{C.14b}$$

where G_f, S_c and Σ_ϕ are defined in Eq.(C.6c, C.6d, C.6e).

Universal transport, gradient driven SOL equations with sheath

Considering now the gradient driven case, $S_0 = 0$ and $\partial_x \bar{n} \neq 0$, one can then define A_n such that $A_n \sigma_n = -(D_\perp\,\sigma_n)^{1/2}\,\partial_x \bar{n}$.

$$\partial_t n + [\phi, n] - \partial_y \phi - \Delta_\perp n + n\exp(-D_\perp\,\phi) = 0 \tag{C.15a}$$

$$\partial_t W + [\phi, W] + G_g\,\partial_y n - S_c \Delta_\perp W - \frac{\Sigma_\phi}{D_\perp}\left(1 - \exp(-D_\perp\,\phi)\right) = 0 \tag{C.15b}$$

In this case 3 control parameters are retained, G_g Eq.(C.7c) that characterizes the instability and its magnitude, as well as S_c, Σ_ϕ, Eq.(C.6d, C.6e), that control the instability spectrum via the long wave length damping governed by the Schmidt number and the short wave length damping via Σ_ϕ.

Universal transport, SOL scaling with fixed length scale

The length scale appears the less convenient parameter to change since it modifies both the box size and the source radial dependence. To maintain the length scale, one must keep $A_L^2 = D_\perp/\sigma_n$ constant. Let us recall the control parameters used in the linearized case, removing the dependence on $D_\perp$ that is replaced by $A_L^2\ \sigma_n$.

$$G_f = \frac{S_0\ g}{A_L \sigma_n^3} \quad ; \quad G_g = \frac{-\partial_x \bar{n}\ g}{\sigma_n^2} \quad ; \quad \Sigma_\phi = \frac{\sigma_\phi\ A_L^2}{\sigma_n} \tag{C.16}$$

A scan of the SOL width at constant box size and source width will thus depend on three parameters, the Schmidt number, either G_f or G_g depending on the driving mechanism and Σ_ϕ. It is interesting to note that these three parameters have a well known impact on the turbulence spectrum so that a scaling law would readily be interpreted as the synergy between changes in the spectrum properties and the characteristic SOL scale.

Appendix D

Linear benchmark in GYSELA

The calculation of the linear perturbation is carried out for different modes keeping constant all the parameters as in Lapillone paper [LMG+10]. GYSELA coordinates are not field-alligned and that requires a more fine mesh in order to describe the modes in the $\theta - \phi$ plane. In the table below, the number of points used in the mesh grid for each simulation is listed.

Table D.1:

n	5	10	15	20	25	30	35	40
N_θ	256	256	256	256	512	512	512	512
N_ϕ	128	128	128	128	256	256	256	256

Regarding the number of point in radial direction N_r, in parallel velocity N_v and in μ, there were no changes in the simulations, therefore the fixed parameter of all the simulations are

Table D.2:

N_r	N_v	N_μ	eps
256	64	16	10^{-6}

other parameters that were set constant for all the simulation are $1/\rho* = 180$, the aspect ratio $a = 0.36$ and the mass of the element. In this case it is Hidrogen, $m_s = 1$, we can therefore define the quantities c_s, ω_s and ρ_s. Their definition is crucial for the normalization between the different codes.

D.1 The different procedure to define growth rate

Here we show how the growthrate has been computed for the case $n = 30$, fig.D.1.

The fit method is the most used but it strongly depends on the interval of time taken in account, fig.D.2(a). The steps to calculate the instability growthrate via the fitting procedure are:

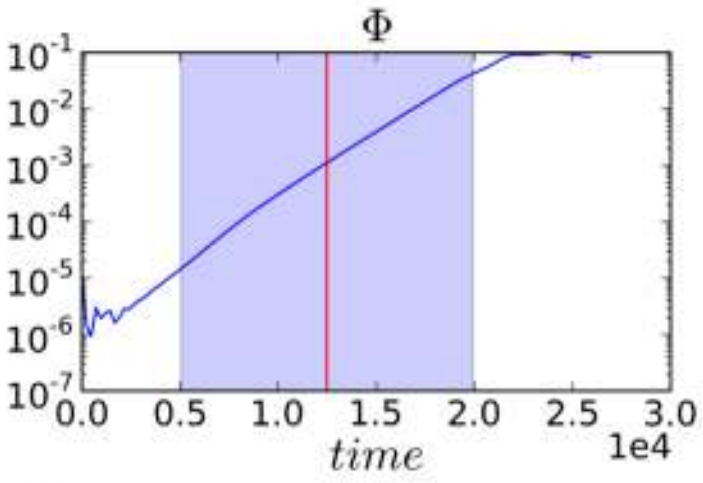

Figure D.1: growth of the potential

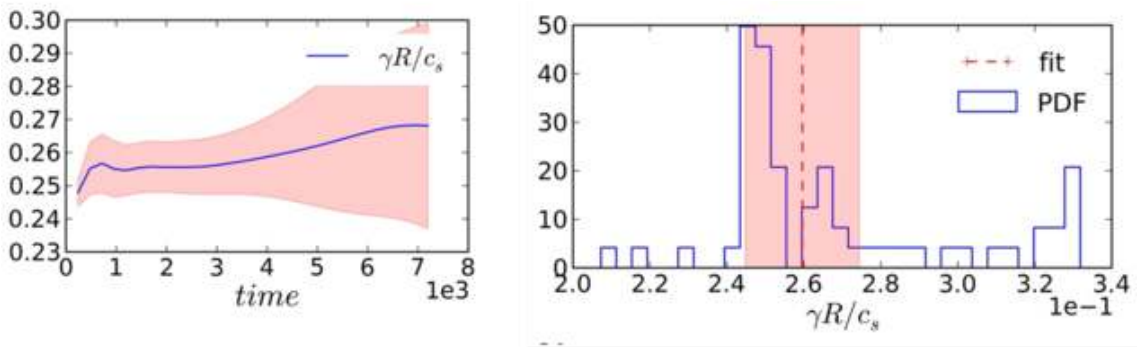

Figure D.2: the two approach to define the growth rate

- $t_0 = (t_{max} - t_{min})/2$ and the interval of time Δt where γ is calculated, i.e. $t_1 = t_0 - \Delta t$ to $t_2 = t_0 + \Delta t$, is defined.
- the growth rate γ is defined as $\gamma =< \partial_t \Phi^2 >_{\Delta_t} /2$.
- the errorbar is defined as $\sigma(\partial_t \Phi^2)_{\Delta t}/2$, where σ is the standard deviation

The only problem relative to this method is the definition of Δt, that can strongly impact on the value of γ and on the size of the errorbar. Another approach is using the probability distribution function to define γ, fig.D.2(b). The steps to calculate γ are:

- the maximum and minimum value reached by $\gamma = \partial_t \Phi^2/2$ and the number of intervals between these two points are defined.
- γ is defined as the highest probable point of the PDF.
- by definition the errorbar is represented by the size of the chosen interval.

The disadvantage is that to have a statistically meaningful results, a good time resolution is needed.

In the fig.D.2(b), the two approaches are compared. It looks clear that in the PDF approach, the size of the errorbar can be strongly reduced. On the other hand, we can still notice that the results are sensitive to:

- The chosen interval t_1, t_2.
- The size of the PDF intervals, such sensitivity should strongly decrease if we increase the diagnostic time

In fig.D.3, the time evolution of ϕ and the PDF distribution for different poloidal wave vectors k_θ are displayed. The table below summarizes the growthrate and frequency.

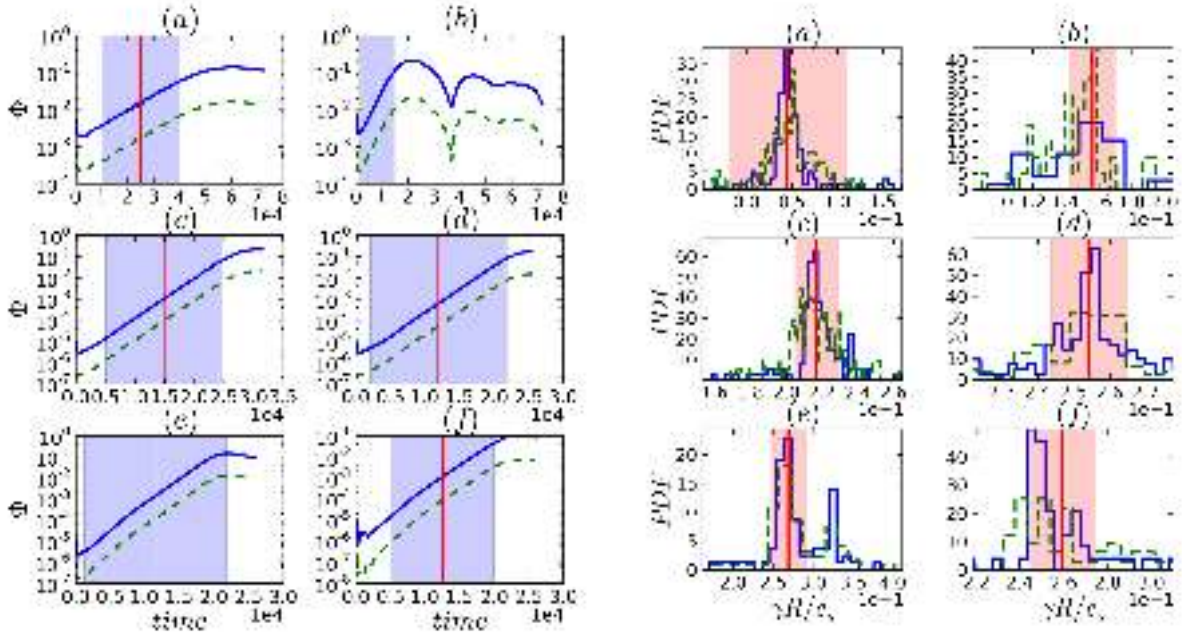

Figure D.3: (a)ϕ^2 in function of time, (b)γ PDFs

Table D.3:

n0	-5.	-10.	-15.	-20.	-25.	-30.
k_θ	-0.078	-0.156	-0.233	-0.311	-0.389	-0.467
γ	0.045	0.158	0.217	0.257	0.271	0.253
err	0.00258	0.00690	0.00123	0.00127	0.00468	0.00200
ω	0.106	0.238	0.476	0.636	0.827	0.978

D.1.1 Higher toroidal modes growthrate: can be really significant?

For the mode $n = 40$, it was not possible to recover a linear growthrate. In the mode evolution, one can observe this characteristic biting. Such results give us a series of problem in the definition of the linear phase that is why we focused our analysis to the modes below $n = 40$. It will be interesting to understand why a second mode is interfering with the mode $n = 40$.

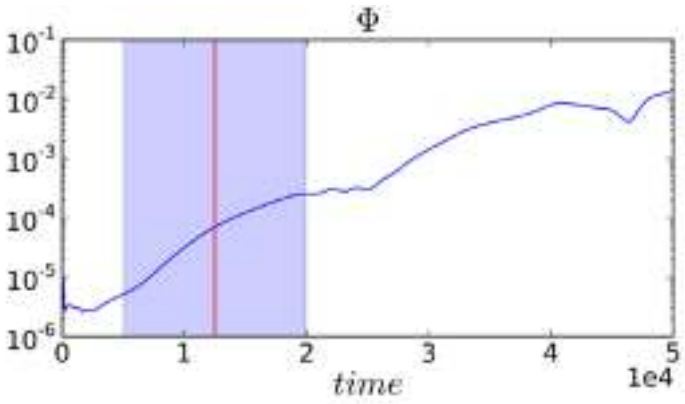

D.2 Envelope dependence on shear and temperature profile

In order to understand how much the choice of the parameters can impact on the linear analysis, a comparison is carried out between the standard CBC (A) and two other cases, where the safety factor (B) or the temperature gradient profile (C) is modified. The envelope growthrate and shape vary with q and L_T profile, despite $q(r_{peak})$ and $L_T(r_{peak})$ is not varied from the reference case.

In fig.5.4, the potential distribution for the three cases is compared. In the no shear case (case B), the eddy structures tend to keep the same size, while in the standard case (case A), we can see a clear difference in size between the low and high field side. Additionally, one can readily observe that the shear also causes the structures different orientation between the top and bottom, while in the slab-like configuration, they all have the same orientation. For the case C, one can observe a different radial distribution of the potential modes.

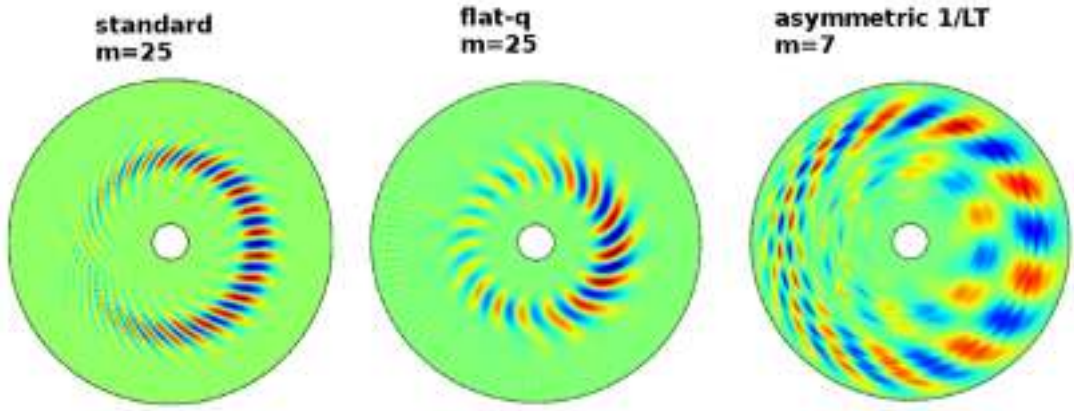

Figure D.4: the potential distribution along $r - \theta$

Case B: q profile variation

In fig.D.5(g)(h) we compare how the envelope for a fixed toroidal mode $n = 20$ changes if we consider a parabolic (fig.D.5(a))or flat q (fig.D.5(b)).We can observe that for flat-

q case, i.e. case with no shear, the eigenmode is mostly defined by a single poloidal contribution that spread on the all unstable region, namely from $r = 0.4$ to $r = 0.6$, its size is constrained by the temperature gradient profile and boundary condition, in agreement with the uniformity of the structures. On the parabolic-q case, the eigenmodes is formed by many poloidal contributions and each mode is localized around the resonance surface, because of the shear effect.

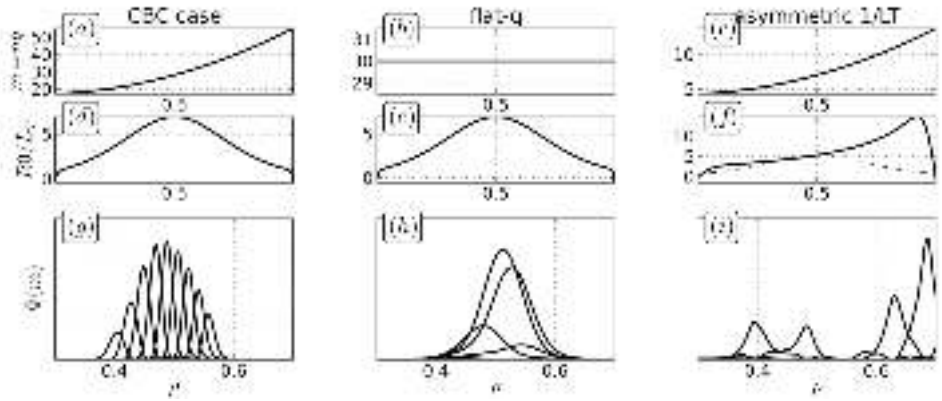

Figure D.5: (a) R/L_T, (d) safety factor profile, (g) envelope distribution in the CBC case for $n = 20$,(b) R/L_T, (e) safety factor profile, (i) envelope distribution for the flat-q profile case for $n = 20$,(c) R/L_T, (l) safety factor profile, (c) envelope distribution for the asymmetric $1/L_T$ case for $n = 5$,

Case C: temperature profile variation

To study the dependence of the envelope growthrate and shape from the temperature distribution, we consider another possible initial temperature profile from the standard CYCLONE case (fig.D.5(f)), where at the midplane the temperature gradient is equivalent to the standard case and the maximum value of $1/LT$ is localized at the edge.Changing the temperature gradient maximum position, we firstly can observe a clear response on the shape of the global eigen-mode despite the same initial condition, see fig.D.5(i).

If we compare the growthrate at the midplane with the standard case, even if the reorganization time interval is increased, the two cases converge to the same order of growthrate. Such observation rise new questions in the definition of the growthrate. If from one side, we can see that the system reorganizes to find the most unstable eigenvalues, it appears that the growthrate of this eigenmode is not impacted by the change of shape, suggesting that the drive is not influenced by a localised variation of the profile: if in a region of the profile temperature gradient is stable, the envelope growthrate could not be influenced by the region. The peak of the temperature gradient localised on the edge seems not to influence the growthrate amplitude of the envelope, but it impacts its shape, a clear correspondence between the temperature gradient profile and the envelope is confirmed.

Appendix E

The ZF-dominated regime in the SOL

In the TOKAM2D SOL region, one can observe that, increasing the forcing, the system moves from (1) a regime dominated by large scale structures recalling a jet like patterns to (2) a turbulence dominated regime.

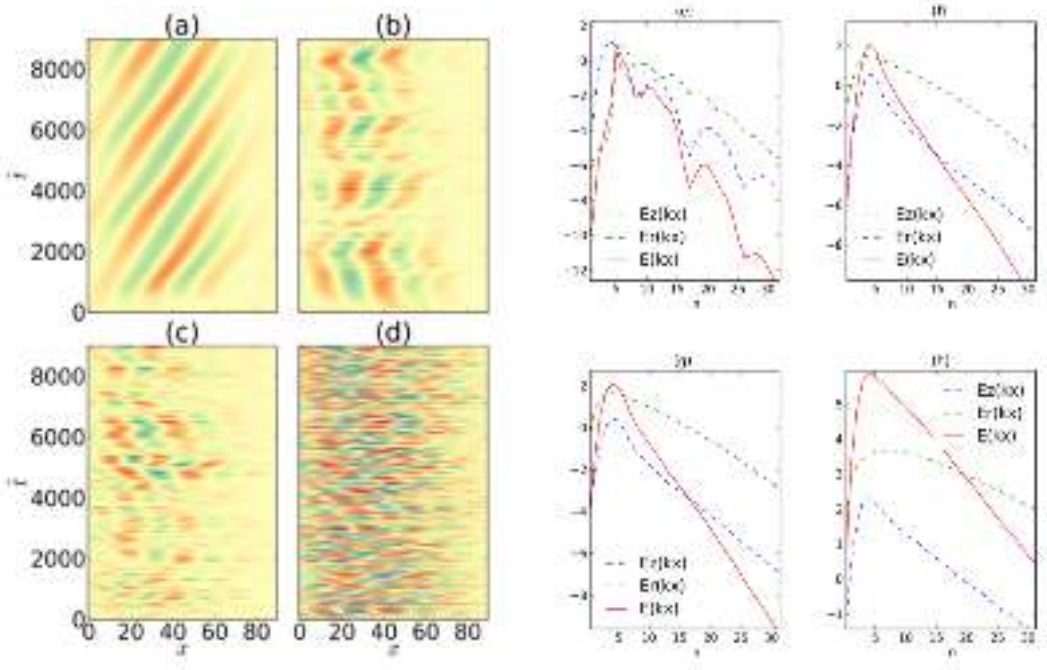

Figure E.1: (a)-(d) potential averaged along y in function of time and radial direction for different value of g ((a)$g = 1.5\ 10^{-4}$, (b)$g = 2.\ 10^{-4}$,(c)$g = 5\ 10^{-4}$, (d) $g = 10\ 10^{-4}$), (e)-(h) the potential spectrum of the zonal and turbulence modes in function of k_y for different value of g ((e)$g = 1.5\ 10^{-4}$, (f)$g = 2.\ 10^{-4}$,(g)$g = 5\ 10^{-4}$, (h) $g = 10\ 10^{-4}$)

Watching at the energy spectrum slope in TOKAM2D defined as $E_Z(k_x), E_r(k_x)$ in fig.E.1(e)-(h), one can observe how the zonal and residual energy spectra change with the forcing.

The system access the zonostrophic regime only for the case where $g = 1.5\ 10^{-4}$, where

we could observe the presence of big convective cells and the turbulence is extremely reduced.
Criticality plays a key role in favoring the self organization, namely the large scale structures dominate the system only close to the marginal stability.
Decreasing the g-term, we actually damp the turbulence linearly in order to access the zonation regime (first case) and the two characteristic slopes of residual and zonal modes are observed. For the other cases, the residual modes dominate the spectrum.
Let us affirm one can access the zonation regime only if the turbulence is linearly suppressed acting on the curvature term.

One can readily understand that also in this region our results are in conflict with the HMB case, namely we can observe that increasing g, we move towards higher values of R_β, but we depart from the zonation regime moving towards a fully turbulent regime. The index to define the transition from turbulence to zonation regime in the HMB framework is no more consistent with the transition also in the SOL.

This discrepancy can be related to the different kinds of forcing used in the two models. On one hand, by defining R_β, Galperin assumes that the injection scale is much smaller and independent from the spectrum, this assumption appears to be crucial to define R_β and favor the anysotropization of the inverse cascade. on the other hand, in our model the forcing is coupled with the density equation and the energy rate ϵ is not an independent parameter but is controlled by the interchange instability and can vary in time and space.

Bibliography

[BBFC+07] P Beyer, S Benkadda, G Fuhr-Chaudier, X Garbet, Ph Ghendrih, and Y Sarazin. Turbulence simulations of transport barrier relaxations in tokamak edge plasmas. *Plasma Physics and Controlled Fusion*, 49(4):507, 2007.

[BH07] A. J. Brizard and T. S. Hahm. Foundations of nonlinear gyrokinetic theory. *Rev. Mod. Phys.*, 79:421–468, Apr 2007.

[CAR+11] G. D. Conway, C. Angioni, F. Ryter, P. Sauter, and J. Vicente. Mean and oscillating plasma flows and turbulence interactions across the *l*-*h* confinement transition. *Phys. Rev. Lett.*, 106:065001, Feb 2011.

[CFG+04] J.W. Connor, T. Fukuda, X. Garbet, C. Gormezano, V. Mukhovatov, M. Wakatani, the ITB Database Group, the ITPA Topical Group on Transport, and Internal Barrier Physics. A review of internal transport barrier physics for steady-state operation of tokamaks. *Nuclear Fusion*, 44(4):R1, 2004.

[CLL+15] G M Cao, Y D Li, Q Li, X D Zhang, P J Sun, G J Wu, L Q Hu, and the EAST Team. Characterization of core microturbulence in l-mode and h-mode regimes on the east superconducting tokamak. *Physica Scripta*, 90(2):025603, 2015.

[CM15] Thomas Cartier-Michaud. *PhD Thesis "Verification de Codes et Reduction de Modeles : Application au Transport dans les Plasmas Turbulents"*. 2015.

[CMGS+14] T Cartier-Michaud, P Ghendrih, Y Sarazin, G Dif-Pradalier, T Drouot, D Esteve, X Garbet, V Grandgirard, G Latu, C Norscini, and C Passeron. Staircase temperature profiles and plasma transport self-organisation in a minimum kinetic model of turbulence based on the trapped ion mode instability. *Journal of Physics: Conference Series*, 561(1):012003, 2014.

[CNLD96] B. A. Carreras, D. Newman, V. E. Lynch, and P. H. Diamond. A model realization of self-organized criticality for plasma confinement. *Physics of Plasmas (1994-present)*, 3(8):2903–2911, 1996.

[CW03] J. Candy and R.E. Waltz. An eulerian gyrokinetic-maxwell solver. *Journal of Computational Physics*, 186(2):545 – 581, 2003.

[DBB+00] A. M. Dimits, G. Bateman, M. A. Beer, B. I. Cohen, W. Dorland, G. W. Hammett, C. Kim, J. E. Kinsey, M. Kotschenreuther, A. H. Kritz, L. L. Lao, J. Mandrekas, W. M. Nevins, S. E. Parker, A. J. Redd, D. E. Shumaker, R. Sydora, and J. Weiland. Comparisons and physics basis of tokamak transport models and turbulence simulations. *Physics of Plasmas (1994-present)*, 7(3):969–983, 2000.

[DH95] P. H. Diamond and T. S. Hahm. On the dynamics of turbulent transport near marginal stability. *Physics of Plasmas (1994-present)*, 2(10):3640–3649, 1995.

[DHCS91] W. D. D'haeseleer, W. N. G. Hitchon, J. D. Callen, and J. L. Shohet. *Flux Coordinates and Magnetic Field Structure*. Springer-Verlag, Berlin, 1991.

[DIIH05] P H Diamond, S-I Itoh, K Itoh, and T S Hahm. Zonal flows in plasma:a review. *Plasma Physics and Controlled Fusion*, 47(5):R35, 2005.

[DPDG+10] G. Dif-Pradalier, P. H. Diamond, V. Grandgirard, Y. Sarazin, J. Abiteboul, X. Garbet, Ph. Ghendrih, A. Strugarek, S. Ku, and C. S. Chang. On the validity of the local diffusive paradigm in turbulent plasma transport. *Phys. Rev. E*, 82(2):025401–, August 2010.

[DPHG+15] G. Dif-Pradalier, G. Hornung, Ph. Ghendrih, Y. Sarazin, F. Clairet, L. Vermare, P.H. Diamond, J. Abiteboul, T. Cartier-Michaud, C. Ehrlacher, D. Esteve, X. Garbet, V. Grandgirard, O.D. Gurcan, P. Hennequin, Y. Kosuga, G. Latu, P. Maget, P. Morel, C. Norscini, R. Sabot, and A. Storelli. Finding the elusive $\mathbf{E} \times \mathbf{B}$ staircase in magnetized plasmas. *Phys. Rev. Lett.*, 114:085004, Feb 2015.

[DWBC96] A. M. Dimits, T. J. Williams, J. A. Byers, and B. I. Cohen. Scalings of ion-temperature-gradient-driven anomalous transport in tokamaks. *Phys. Rev. Lett.*, 77:71–74, Jul 1996.

[EHH+10] T. Estrada, T. Happel, C. Hidalgo, E. Ascasíbar, and E. Blanco. Experimental observation of coupling between turbulence and sheared flows during l-h transitions in a toroidal plasma. *EPL (Europhysics Letters)*, 92(3):35001, 2010.

[FCG+13] E Floriani, G Ciraolo, Ph Ghendrih, R Lima, and Y Sarazin. Self-regulation of turbulence bursts and transport barriers. *Plasma Physics and Controlled Fusion*, 55(9):095012, 2013.

[FGH+13] N Fedorczak, Ph Ghendrih, P Hennequin, G R Tynan, P H Diamond, and P Manz. Dynamics of tilted eddies in a transversal flow at the edge of tokamak plasmas and the consequences for l–h transition. *Plasma Physics and Controlled Fusion*, 55(12):124024, 2013.

[FLP+08] I. Furno, B. Labit, M. Podestà, A. Fasoli, S. H. Müller, F. M. Poli, P. Ricci, C. Theiler, S. Brunner, A. Diallo, and J. Graves. Experimental observation of the blob-generation mechanism from interchange waves in a plasma. *Phys. Rev. Lett.*, 100:055004, Feb 2008.

[FSA+08] G L Falchetto, B D Scott, P Angelino, A Bottino, T Dannert, V Grandgirard, S Janhunen, F Jenko, S Jolliet, A Kendl, B F McMillan, V Naulin, A H Nielsen, M Ottaviani, A G Peeters, M J Pueschel, D Reiser, T T Ribeiro, and M Romanelli. The european turbulence code benchmarking effort: turbulence driven by thermal gradients in magnetically confined plasmas. *Plasma Physics and Controlled Fusion*, 50(12):124015, 2008.

[GAB+15] Virginie Grandgirard, Vndgirard, Jérémie Abiteboul, Julien Bigot, Thomas Cartier-Michaud, Nicolas Crouseilles, Charles Erhlacher, Damien Esteve, Guilhem Dif-Pradalier, Xavier Garbet, Philippe Ghendrih, Guillaume Latu, Michel Mehrenberger, Claudia Norscini, Chantal Passeron, Fabien Rozar, Yanick Sarazin, Antoine Strugarek, Eric Sonnendrücker, and David Zarzoso. A 5d gyrokinetic full-f global semi-lagrangian code for flux-driven ion turbulence simulations. Jul 2015.

[GDPN+14] Philippe Ghendrih, Guilhem Dif-Pradalier, Claudia Norscini, Thomas Cartier-Michaud, Damien Estève, Xavier Garbet, Virginie Grandgirard, Guillaume Latu, Chantal Passeron, and Yanick Sarazin. Self organisation of plasma turbulence: impact on radial correlation lengths. *Journal of Physics: Conference Series*, 561(1):012008, 2014.

[GFC+99] X. Garbet, C. Fenzi, H. Capes, P. Devynck, and G. Antar. Kelvin-helmholtz instabilities in tokamak edge plasmas. *Physics of Plasmas*, 6(10):3955–3965, 1999.

[GHP+06] O E Garcia, J Horacek, R A Pitts, A H Nielsen, W Fundamenski, J P Graves, V Naulin, and J Juul Rasmussen. Interchange turbulence in the tcv scrape-off layer. *Plasma Physics and Controlled Fusion*, 48(1):L1, 2006.

[GIVW10] X. Garbet, Y. Idomura, L. Villard, and T.H. Watanabe. Gyrokinetic simulations of turbulent transport. *Nuclear Fusion*, 50(4):043002, 2010.

[GLB+11] Tobias Gorler, Xavier Lapillonne, Stephan Brunner, Tilman Dannert, Frank Jenko, Sohrab Khosh Aghdam, Patrick Marcus, Ben F. McMillan, Florian Merz, Olivier Sauter, Daniel Told, and Laurent Villard. Flux- and gradient-driven global gyrokinetic simulation of tokamak turbulence. *Physics of Plasmas*, 18(5):056103, 2011.

[GLRS91] X. Garbet, L. Laurent, J.-P. Roubin, and A. Samain. A model for the turbulence in the scrape-off layer of tokamaks. *Nuclear Fusion*, 31(5):967, 1991.

[GNCM+14] Philippe Ghendrih, Claudia Norscini, Thomas Cartier-Michaud, Guilhem Dif-Pradalier, Jérémie Abiteboul, Yue Dong, Xavier Garbet, Ozgür Gürcan, Pascale Hennequin, Virginie Grandgirard, Guillaume Latu, Pierre Morel, Yanick Sarazin, Alexandre Storelli, and Laure Vermare. Phase space structures in gyrokinetic simulations of fusion plasma turbulence. *The European Physical Journal D*, 68(10), 2014.

[GNH+12] Ph Ghendrih, C Norscini, F Hasenbeck, G Dif-Pradalier, J Abiteboul, T Cartier-Michaud, X Garbet, V Grandgirard, Y Marandet, Y Sarazin, P Tamain, and D Zarzoso. Thermodynamical and microscopic properties of turbulent transport in the edge plasma. *Journal of Physics: Conference Series*, 401(1):012007, 2012.

[GPR+11] M Groth, G D Porter, T D Rognlien, S Wiesen, M Wischmeier, M N A Beurskens, X Bonnin, B D Bray, S Brezinsek, N H Brooks, D P Coster, T Eich, M E Fenstermacher, C Fuchs, R A Groebner, D Harting, A Huber, S Jachmich, A Kallenbach, C J Lasnier, A W Leonard, A Meigs, H W Müller, M E Rensink, D L Rudakov, J G Watkins, E Wolfrum, the DIII-D, ASDEX Upgrade Teams, and JET EFDA Contributors. Poloidal distribution of recycling sources and core plasma fueling in diii-d, asdex-upgrade and jet l-mode plasmas. *Plasma Physics and Controlled Fusion*, 53(12):124017, 2011.

[GRB+95] K. W. Gentle, W. L. Rowan, R. V. Bravenec, G. Cima, T. P. Crowley, H. Gasquet, G. A. Hallock, J. Heard, A. Ouroua, P. E. Phillips, D. W. Ross, P. M. Schoch, and C. Watts. Strong nonlocal effects in a tokamak perturbative transport experiment. *Phys. Rev. Lett.*, 74(18):3620–3623, May 1995.

[Gro87] TFR Group. Pellet injection experiments on the tfr tokamak. *Nuclear Fusion*, 27(12):1975, 1987.

[GSD08] Boris Galperin, Semion Sukoriansky, and Nadejda Dikovskaya. Zonostrophic turbulence. *Physica Scripta*, 2008(T132):014034, 2008.

[GSD10] Boris Galperin, Semion Sukoriansky, and Nadejda Dikovskaya. Geophysical flows with anisotropic turbulence and dispersive waves: flows with a beta-effect. *Ocean Dynamics*, 60(2):427–441, 2010.

[HH76] F. L. Hinton and R. D. Hazeltine. Theory of plasma transport in toroidal confinement systems. *Rev. Mod. Phys.*, 48:239–308, Apr 1976.

[Hor99] W. Horton. Drift waves and transport. *Rev. Mod. Phys.*, 71:735–778, Apr 1999.

[HR99] F L Hinton and M N Rosenbluth. Dynamics of axisymmetric exb and poloidal flows in tokamaks. *Plasma Physics and Controlled Fusion*, 41(3A):A653, 1999.

[HRG+15] Felix Hasenbeck, Dirk Reiser, Philippe Ghendrih, Yannick Marandet, Patrick Tamain, Annette Moeller, and Detlev Reiter. Multiscale modeling approach for radial particle transport in large-scale simulations of the tokamak plasma edge. *Procedia Computer Science*, 51:1128 – 1137, 2015. International Conference On Computational Science, {ICCS} 2015Computational Science at the Gates of Nature.

[ITT+13] S. Inagaki, T. Tokuzawa, N. Tamura, S.-I. Itoh, T. Kobayashi, K. Ida, T. Shimozuma, S. Kubo, K. Tanaka, T. Ido, A. Shimizu, H. Tsuchiya, N. Kasuya, Y. Nagayama, K. Kawahata, S. Sudo, H. Yamada, A. Fujisawa, K. Itoh, and the LHD Experiment Group. How is turbulence intensity determined by macroscopic variables in a toroidal plasma? *Nuclear Fusion*, 53(11):113006, 2013.

[IUAT09] Y. Idomura, H. Urano, N. Aiba, and S. Tokuda. Study of ion turbulent transport and profile formations using global gyrokinetic full- f vlasov simulation. *Nuclear Fusion*, 49(6):065029, 2009.

[jKD03] Eun jin Kim and P. H. Diamond. Mean shear flows, zonal flows, and generalized kelvin–helmholtz modes in drift wave turbulence: A minimal model for l –¿ h transition. *Physics of Plasmas*, 10(5):1698–1704, 2003.

[KD03] Eun-jin Kim and P. H. Diamond. Zonal flows and transient dynamics of the *l-h* transition. *Phys. Rev. Lett.*, 90:185006, May 2003.

[KDK+14] Taras Khapko, Yohann Duguet, Tobias Kreilos, Philipp Schlatter, Bruno Eckhardt, and DanS. Henningson. Complexity of localised coherent structures in a boundary-layer flow. *The European Physical Journal E*, 37(4), 2014.

[KDM08] S.. I. Krasheninnkov, D. A. D'ippolito, and J. R. Myra. Recent theoretical progress in understanding coherent structures in edge and sol turbulence. *Journal of Plasma Physics*, 74:679–717, 10 2008.

[KKM+94] Y. Koide, M. Kikuchi, M. Mori, S. Tsuji, S. Ishida, N. Asakura, Y. Kamada, T. Nishitani, Y. Kawano, T. Hatae, T. Fujita, T. Fukuda, A. Sakasai, T. Kondoh, R. Yoshino, and Y. Neyatani. Internal transport barrier on q =3 surface and poloidal plasma spin up in jt-60u high-β_p discharges. *Phys. Rev. Lett.*, 72:3662–3665, Jun 1994.

[KR12] Sumire Kobayashi and Barrett N. Rogers. The quench rule, dimits shift, and eigenmode localization by small-scale zonal flows. *Physics of Plasmas (1994-present)*, 19(1):–, 2012.

[LEHT02] Z. Lin, S. Ethier, T. S. Hahm, and W. M. Tang. Size scaling of turbulent transport in magnetically confined plasmas. *Phys. Rev. Lett.*, 88:195004, Apr 2002.

[LHL+99] Z. Lin, T. S. Hahm, W. W. Lee, W. M. Tang, and P. H. Diamond. Effects of collisional zonal flow damping on turbulent transport. *Phys. Rev. Lett.*, 83:3645–3648, Nov 1999.

[LMG+10] X. Lapillonne, B. F. McMillan, T. Gorerler, S. Brunner, T. Dannert, F. Jenko, F. Merz, and L. Villard. Nonlinear quasisteady state benchmark of global gyrokinetic codes. *Physics of Plasmas (1994-present)*, 17(11):–, 2010.

[LSS+03] A Loarte, G Saibene, R Sartori, D Campbell, M Becoulet, L Horton, T Eich, A Herrmann, G Matthews, N Asakura, A Chankin, A Leonard, G Porter, G Federici, G Janeschitz, M Shimada, and M Sugihara. Characteristics of type i elm energy and particle losses in existing devices and their extrapolation to iter. *Plasma Physics and Controlled Fusion*, 45(9):1549, 2003.

[MBS05] Nikolai A. Maximenko, Bohyun Bang, and Hideharu Sasaki. Observational evidence of alternating zonal jets in the world ocean. *Geophys. Res. Lett.*, 32(12):L12607–, 2005.

[MCT+07] D.C. McDonald, J.G. Cordey, K. Thomsen, O.J.W.F. Kardaun, J.A. Snipes, M. Greenwald, L. Sugiyama, F. Ryter, A. Kus, J. Stober, J.C. DeBoo, C.C. Petty, G. Bracco, M. Romanelli, Z. Cui, Y. Liu, Y. Miura, K. Shinohara, K. Tsuzuki, Y. Kamada, T. Takizuka, H. Urano, M. Valovic, R. Akers, C. Brickley, A. Sykes, M.J. Walsh, S.M. Kaye, C. Bush, D. Hogewei, Y.R. Martin, A. Cote, G. Pacher, J. Ongena, F. Imbeaux, G.T. Hoang, S. Lebedev, A. Chudnovskiy, and V. Leonov. Recent progress on the development and analysis of the itpa global h-mode confinement database. *Nuclear Fusion*, 47(3):147, 2007.

[MDH+12] C.F. Maggi, E. Delabie, N. Hawkes, M. Lehnen, G. Calabro, F. Rimini, E.R. Solano, and JET EFDA Contributors*. Experimental study of h-l transitions in jet. In *40th EPS Conference on Plasma Physics*, 2012.

[MJT+08] B. F. McMillan, S. Jolliet, T. M. Tran, L. Villard, A. Bottino, and P. Angelino. Long global gyrokinetic simulations: Source terms and particle noise control. *Physics of Plasmas*, 15(5):052308, 2008.

[mPTDWGpbTT04] ITPA H mode Power Threshold Database Working Group presented by T Takizuka. Roles of aspect ratio, absolute b and effective z of the h-mode power threshold in tokamaks of the itpa database. *Plasma Physics and Controlled Fusion*, 46(5A):A227, 2004.

[MTtICHmTDWG08] Y R Martin, T Takizuka, and the ITPA CDBM H-mode Threshold Database Working Group. Power requirement for accessing the h-mode in iter. *Journal of Physics: Conference Series*, 123(1):012033, 2008.

[MWS+03] R. J. Maqueda, G. A. Wurden, D. P. Stotler, S. J. Zweben, B. LaBombard, J. L. Terry, J. L. Lowrance, V. J. Mastrocola, G. F.

Renda, D. A. D'Ippolito, J. R. Myra, and N. Nishino. Gas puff imaging of edge turbulence (invited). *Review of Scientific Instruments*, 74(3):2020–2026, 2003.

[Nau07] V. Naulin. Turbulent transport and the plasma edge. *Journal of Nuclear Materials*, 363–365(0):24 – 31, 2007. ¡ce:title¿Plasma-Surface Interactions-17¡/ce:title¿.

[NGC+15] C. Norscini, P. Ghendrih, T. Cartier-Michaud, G. Dif-Pradalier, X. Garbet, N. Nace, Y. Sarazin, and P. Tamain. Transport barrier generation at the interface of regions with different zonal flows dynamics. 2015.

[NGCM+14] C Norscini, P Ghendrih, T Cartier-Michaud, G Dif-Pradalier, D Milelli, Y Sarazin, J Abiteboul, D Estève, X Garbet, V Grandgirard, and G Latu. Turbulent transport close to marginal instability: role of the source driving the system out of equilibrium. *Journal of Physics: Conference Series*, 561(1):012013, 2014.

[OM99] M. Ottaviani and G. Manfredi. The gyro-radius scaling of ion thermal transport from global numerical simulations of ion temperature gradient driven turbulence. *Physics of Plasmas*, 6(8):3267–3275, 1999.

[PK13] Jeffrey B. Parker and John A. Krommes. Zonal flow as pattern formation. *Physics of Plasmas (1994-present)*, 20(10):–, 2013.

[RB90] F. Romanelli and S. Briguglio. Toroidal semicollisional microinstabilities and anomalous electron and ion transport. *Physics of Fluids B*, 2(4):754–763, 1990.

[RBM+02] D L Rudakov, J A Boedo, R A Moyer, S Krasheninnikov, A W Leonard, M A Mahdavi, G R McKee, G D Porter, P C Stangeby, J G Watkins, W P West, D G Whyte, and G Antar. Fluctuation-driven transport in the diii-d boundary. *Plasma Physics and Controlled Fusion*, 44(6):717, 2002.

[RDK00] B. N. Rogers, W. Dorland, and M. Kotschenreuther. Generation and stability of zonal flows in ion-temperature-gradient mode turbulence. *Phys. Rev. Lett.*, 85:5336–5339, Dec 2000.

[RH98] M. N. Rosenbluth and F. L. Hinton. Poloidal flow driven by ion-temperature-gradient turbulence in tokamaks. *Phys. Rev. Lett.*, 80:724–727, Jan 1998.

[RM11] J. Rolland and P. Manneville. Ginzburg–landau description of laminar-turbulent oblique band formation in transitional plane couette flow. *The European Physical Journal B*, 80(4):529–544, 2011.

[RRO+13] F. Ryter, S.K. Rathgeber, L. Barrera Orte, M. Bernert, G.D. Conway, R. Fischer, T. Happel, B. Kurzan, R.M. McDermott, A. Scarabosio, W. Suttrop, E. Viezzer, M. Willensdorfer, E. Wolfrum, and

the ASDEX Upgrade Team. Survey of the h-mode power threshold and transition physics studies in asdex upgrade. *Nuclear Fusion*, 53(11):113003, 2013.

[SCM+07] M. Shimada, D.J. Campbell, V. Mukhovatov, M. Fujiwara, N. Kirneva, K. Lackner, M. Nagami, V.D. Pustovitov, N. Uckan, J. Wesley, N. Asakura, A.E. Costley, A.J.H. Donné, E.J. Doyle, A. Fasoli, C. Gormezano, Y. Gribov, O. Gruber, T.C. Hender, W. Houlberg, S. Ide, Y. Kamada, A. Leonard, B. Lipschultz, A. Loarte, K. Miyamoto, V. Mukhovatov, T.H. Osborne, A. Polevoi, and A.C.C. Sips. Chapter 1: Overview and summary. *Nuclear Fusion*, 47(6):S1, 2007.

[SG98] Y. Sarazin and Ph. Ghendrih. Intermittent particle transport in two-dimensional edge turbulence. *Physics of Plasmas*, 5(12):4214–4228, 1998.

[SGA+10] Y. Sarazin, V. Grandgirard, J. Abiteboul, S. Allfrey, X. Garbet, Ph. Ghendrih, G. Latu, A. Strugarek, and G. Dif-Pradalier. Large scale dynamics in flux driven gyrokinetic turbulence. *Nuclear Fusion*, 50(5):054004, 2010.

[SGA+11] Y. Sarazin, V. Grandgirard, J. Abiteboul, S. Allfrey, X. Garbet, Ph. Ghendrih, G. Latu, A. Strugarek, G. Dif-Pradalier, P.H. Diamond, S. Ku, C.S. Chang, B.F. McMillan, T.M. Tran, L. Villard, S. Jolliet, A. Bottino, and P. Angelino. Predictions on heat transport and plasma rotation from global gyrokinetic simulations. *Nuclear Fusion*, 51(10):103023, 2011.

[SGD02] Semion Sukoriansky, Boris Galperin, and Nadejda Dikovskaya. Universal spectrum of two-dimensional turbulence on a rotating sphere and some basic features of atmospheric circulation on giant planets. *Phys. Rev. Lett.*, 89:124501, Aug 2002.

[SMC+03] W Suttrop, M Maraschek, G D Conway, H-U Fahrbach, G Haas, L D Horton, T Kurki-Suonio, C J Lasnier, A W Leonard, C F Maggi, H Meister, A Mück, R Neu, I Nunes, Th Pütterich, M Reich, A C C Sips, and the ASDEX Upgrade Team. Elm-free stationary h-mode plasmas in the asdex upgrade tokamak. *Plasma Physics and Controlled Fusion*, 45(8):1399, 2003.

[SP08] R. K. Scott and L. M. Polvani. Equatorial superrotation in shallow atmospheres. *Geophys. Res. Lett.*, 35(24):n/a–n/a, 2008.

[SSZ+13] A Strugarek, Y Sarazin, D Zarzoso, J Abiteboul, A S Brun, T Cartier-Michaud, G Dif-Pradalier, X Garbet, Ph Ghendrih, V Grandgirard, G Latu, C Passeron, and O Thomine. Ion transport barriers triggered by plasma polarization in gyrokinetic simulations. *Plasma Physics and Controlled Fusion*, 55(7):074013, 2013.

[SXP05] M. G. Shats, H. Xia, and H. Punzmann. Spectral condensation of turbulence in plasmas and fluids and its role in low-to-high phase transitions in toroidal plasma. *Phys. Rev. E*, 71:046409, Apr 2005.

[SZR+12] L. Schmitz, L. Zeng, T. L. Rhodes, J. C. Hillesheim, E. J. Doyle, R. J. Groebner, W. A. Peebles, K. H. Burrell, and G. Wang. Role of zonal flow predator-prey oscillations in triggering the transition to h-mode confinement. *Phys. Rev. Lett.*, 108:155002, Apr 2012.

[TFR87] TFR Group. Pellet injection experiments on the tfr tokamak. *Nuclear Fusion*, 27(12):1975, 1987.

[TM13] S. M. Tobias and J. B. Marston. Direct statistical simulation of out-of-equilibrium jets. *Phys. Rev. Lett.*, 110:104502, Mar 2013.

[VAB+04] L. Villard, S.J. Allfrey, A. Bottino, M. Brunetti, G.L. Falchetto, V. Grandgirard, R. Hatzky, J. Nuhrenberg, A.G. Peeters, O. Sauter, S. Sorge, and J. Vaclavik. Full radius linear and nonlinear gyrokinetic simulations for tokamaks and stellarators: zonal flows, applied exb flows, trapped electrons and finite beta. *Nuclear Fusion*, 44(1):172, 2004.

[VM93] Geoffrey K. Vallis and Matthew E. Maltrud. Generation of mean flows and jets on a beta plane and over topography. *J. Phys. Oceanogr.*, 23(7):1346–1362, July 1993.

[VS05] Ashwin R Vasavada and Adam P Showman. Jovian atmospheric dynamics: an update after galileo and cassini. *Reports on Progress in Physics*, 68(8):1935, 2005.

[Wag07] F Wagner. A quarter-century of h-mode studies. *Plasma Physics and Controlled Fusion*, 49(12B):B1, 2007.

[WBB+82] F. Wagner, G. Becker, K. Behringer, D. Campbell, A. Eberhagen, W. Engelhardt, G. Fussmann, O. Gehre, J. Gernhardt, G. v. Gierke, G. Haas, M. Huang, F. Karger, M. Keilhacker, O. Klüber, M. Kornherr, K. Lackner, G. Lisitano, G. G. Lister, H. M. Mayer, D. Meisel, E. R. Müller, H. Murmann, H. Niedermeyer, W. Poschenrieder, H. Rapp, H. Röhr, F. Schneider, G. Siller, E. Speth, A. Stäbler, K. H. Steuer, G. Venus, O. Vollmer, and Z. Yü. Regime of improved confinement and high beta in neutral-beam-heated divertor discharges of the asdex tokamak. *Phys. Rev. Lett.*, 49:1408–1412, Nov 1982.

[X.L] X.Lapillone. *PhD Thesis 'Local and global Eulerian gyrokinetic simulations of microturbulence in realistic geometry with applications to the TCV Tokamak'.*

[XSL+14] G.S. Xu, L.M. Shao, S.C. Liu, H.Q. Wang, B.N. Wan, H.Y. Guo, P.H. Diamond, G.R. Tynan, M. Xu, S.J. Zweben, V. Naulin, A.H. Nielsen, J. Juul Rasmussen, N. Fedorczak, P. Manz, K. Miki, N. Yan, R. Chen, B. Cao, L. Chen, L. Wang, W. Zhang, and X.Z. Gong. Study of the lh transition with a new dual gas puff imaging system in the east superconducting tokamak. *Nuclear Fusion*, 54(1):013007, 2014.

[ZGG+00] X L Zou, A Géraud, P Gomez, M Mattioli, J L Ségui, F Clairet, C De Michelis, P Devynck, T Dudok de Wit, M Erba, C Fenzi, X Garbet, C Gil, P Hennequin, F Imbeaux, E Joffrin, G Leclert, A L Pecquet, Y Peysson, R Sabot, and T F Seak. Edge cooling experiments and non-local transport phenomena in tore supra. *Plasma Physics and Controlled Fusion*, 42(10):1067, 2000.

[ZMB+90] MC Zarnstorff, K McGuire, MG Bell, B Grek, D Johnson, D McCune, H Park, A Ramsey, and G Taylor. Parallel electric resistivity in the tftr tokamak. *Physics of Fluids B Plasma Physics*, 2(8):1852, 1990.

[Zwe89] S.J. Zweben. *Visible Imaging of Edge Fluctuations in TFTR*. Plasma Physics Laboratory, Princeton University, 1989.